Towards High-Precision Spectroscopy of Alkaline, Alkaline-Earth-Like, and Antimatter Atomic Systems

Doctor of Philosophy Dissertation

by

Adam Ryszard Linek

Nicolaus Copernicus University in Toruń

Institute of Physics

National Laboratory of Atomic, Molecular, and Optical Physics

Supervisor

dr hab. Michał Zawada, prof. NCU
Institute of Physics
National Laboratory of AMO Physics
Nicolaus Copernicus University

Co-supervisor

dr Marcin Witkowski
Institute of Physics
National Laboratory of AMO Physics
Nicolaus Copernicus University

Toruń, 2025

This page is left blank intentionally.

Podziękowania

Pragnę podziękować mojemu promotorowi, dr. hab. Michałowi Zawadzie, prof. UMK, za wsparcie, życzliwe rady i umożliwienie mi realizacji projektu doktorskiego w Krajowym Laboratorium Fizyki Atomowej, Molekularnej i Optycznej w Toruniu, a także w ramach kolaboracji Antimatter Experiment: gravity, Interferometry, Spectroscopy w Europejskiej Organizacji Badań Jądrowych w Genewie.

Najszczersze podziękowania kieruję do mojego promotora pomocniczego, dr. Marcina Witkowskiego, za wprowadzenie mnie w świat fizyki *na poważnie*, nieustanne wsparcie zarówno w życiu naukowym, jak i prywatnym, inspirujące dyskusje oraz ogromne zaangażowanie. Jestem wdzięczny za zaufanie, otwartość i osiem lat wspólnej pracy, które ukształtowały moje podejście do świata fizyki eksperymentalnej.

Dziękuję całemu zespołowi laboratorium HgRb, a w szczególności Rodolfo Muñoz-Rodriguezowi, który wspierał mnie od moich pierwszych dni w KL FAMO, a także moim kolegom: Archicie Sahu, Indrajitowi Nandi i Matejowi Veis. Wyrazy wdzięczności składam również wszystkim studentom: Jackowi Pyszce, Władysławowi Lewickiemu i Wiktorii Jóźwickiej. Jestem także wdzięczny prof. Romkowi Ciuryle za nieustające wsparcie i pozytywne nastawienie.

Podziękowania kieruję również do moich kolegów: Mateusza Narożnika, Marcina Bobra, Sławka Bilickiego, Piotra Morzyńskiego, Adama Ledzińskiego, Mariusza Piwińskiego, Łukasza Kłosowskiego oraz Małgorzaty Grosbart. Szczególnie wdzięczny jestem Januszowi Dejewskiemu za nieocenioną pomoc techniczną w realizacji projektu.

Najgorętsze podziękowania kieruję do moich Rodziców oraz brata Kamila za nieustające wsparcie i miłość. Z wdzięcznością wspominam także moich nauczycieli, którzy zaszczepili we mnie pasję do fizyki: dr Katarzynę Książek, dr. Ireneusza Książka, Joannę Kędzierską, Ilonę Hajduk oraz Krystynę Bąk. Wyrazy wdzięczności kieruję także do Tadeusza i Tytusa, którzy towarzyszyli mi każdego dnia przy przygotowaniu tej rozprawy.

Останнє, але найважливіше спасибі. Дякую Тобі, Юліє, моя Любов, за Твою відданість і турботу. Дякую за те, що підтримуєш мене на кожному кроці та надихаєш постійно працювати над собою. Дякую за Твоє піклування, за смачні обіди й за терпіння. Дякую за те, що відкрила мені очі на світ, за всі наші подорожі та пригоди. Дякую за віру в мене й за те, що Ти є поруч. Без Тебе я б не зміг довести цей проєкт до кінця.

The research presented in this dissertation was supported by the Polish National Science Centre Project No. 2023/49/N/ST2/03620 (PRELUDIUM 22). I acknowledge the Polish National Science Centre Project No. 2021/41/B/ST2/ 00681 (OPUS 21) support. I acknowledge the Polish National Science Centre Project No. 2021/42/E/ST2/00046 (SONATA BIS 11) support. The research was a part of the 20FUN01 TSCAC project, which has received funding from the EMPIR programme co-financed by the Participating States and from the European Union's Horizon 2020. This research has received funding from the NLPQT- Narodowe Laboratorium Fotoniki i Technologii Kwantowych/ POIR.04.02.00-00-B003/18-00 programme. The research was performed at the National Laboratory FAMO (KL FAMO) in Toruń, Poland, and was supported by a subsidy from the Polish Ministry of Science and Higher Education. During PhD studies, I was a member of the consortium AE$\bar{g}$IS-PL, supported by the Ministry of Education and Science, Agreement no. 2022/WK/06.

Contents

List of Figures

List of Tables

List of Abbreviations

ADEV Allan deviation,

AE$\bar{g}$IS Antimatter Experiment: gravity, Interferometry, Spectroscopy,

AGH AGH University of Kraków,

AOM acousto-optic modulator,

AVAR Allan variance,

BBR blackbody radiation,

BDU beatnote detection unit,

CAD computer-aided design,

CTE coefficient of thermal expansion,

CW continuous-wave,

DDS direct digital synthesiser,

ECDL extended-cavity diode laser,

eDOF effective number of degrees of freedom,

EOM electro-optic phase modulator,

FM frequency modulation,

FNC fibre-noise cancellation,

FP Fabry–Pérot,

FSR free spectral range,

FWHM full width at half maximum,

GCOV Groslambert Covariance,

GEANT pan-European research and education network,

Hg mercury,

LO local oscillator,

MDEV modified Allan deviation,

MOT magneto-optical trap,

MVAR modified Allan variance,

NPBS non-polarising beam splitter,

NPBS-P non-polarising beam splitter plate,

o-Ps ortho-positronium,

OADEV overlapping Allan deviation,

OAVAR overlapping Allan variance,

OFC optical frequency comb,

OI optical isolator,

p-Ps para-positronium,

PBS polarising beam splitter,

PDH Pound–Drever–Hall,

PER polarisation extinction ratio,

PIONIER Polish National Research and Education Network,

PLL phase-locked loop,

PM polarisation-maintaining,

Ps positronium,

PSD power spectral density,

PSNC Poznań Supercomputing and Networking Center,

PTB Physikalisch–Technische Bundesanstalt,

PZT piezoelectric transducer,

QED quantum electrodynamics,

RAM residual amplitude modulation,

Rb rubidium,

RF radio-frequency,

ROC radius of curvature,

SHG second-harmonic generation,

SNR signal-to-noise ratio,

SSPALS single-shot positron annihilation lifetime spectroscopy,

TA tapered amplifier,

TCH Three–Cornered Hat,

TEC thermoelectric cooler,

UHV ultra-high vacuum,

ULE ultra-low expansion,

UV ultraviolet,

VCO voltage-controlled oscillator.

Chapter 1

Introduction

"If it disagrees with experiment, it's wrong. In that simple statement is the key to science."
— Richard P. Feynman, Messenger Lectures *(1964)*

Precision spectroscopy turns this maxim into practice by translating faint physical effects into frequency shifts, the quantity we can measure with the highest precision. With cavity-stabilised lasers, Doppler-free interrogation, and optical frequency comb (OFC) referencing, minute relativistic, many-body and radiative corrections appear as resolvable differences in optical frequencies. In this way, spectroscopy serves a double purpose: it delivers enabling technology for next-generation timekeeping and, at the same time, subjects the Standard Model to stringent experimental tests.

This thesis pursues that programme on two deliberately different platforms, mercury (Hg) and positronium (Ps), with complementary roles. Hg is a heavy, many-electron atom in which relativistic and nuclear effects are naturally enhanced. Selected transitions, notably the ultra-narrow $^1S_0 - {}^3P_0$ transition, exhibit strong sensitivity to potential variations of fundamental constants and to certain beyond-Standard-Model couplings. The same transition underpins optical atomic clock development, linking fundamental tests directly to practical metrology.

Ps is a purely leptonic, hydrogen-like bound state without nuclear structure. Its theory is exceptionally clean, and higher-order bound-state quantum electrodynamics (QED) terms, including recoil and annihilation contributions, can be confronted with high-precision spectroscopic data. Therefore, Ps provides sharp tests of QED and matter–antimatter symmetries with minimal hadronic uncertainty.

This dissertation mainly focuses on developing and applying two complementary high-precision spectroscopy platforms: $^1S_0 - {}^3P_0$ transition in Hg and $1^3S_1 - 2^3S_1$ transition in Ps. The work integrates narrow-linewidth continuous-wave (CW) lasers, OFC referencing for traceability to the SI, and power-enhancement cavities. Together, these platforms pursue frequency-metrology performance needed to confront novel theory, constrain systematics, and enable future ultra-precise measurements.

The thesis is structured as follows:

- **Within Chapter 1**, the remaining sections are organised as follows. *Section 1.1* motivates Hg from metrology and fundamental-physics perspectives, outlines the working transitions, and identifies the dominant systematic shifts. *Section 1.2* motivates Ps as a nucleus-free testbed for high-purity QED and matter–antimatter symmetry tests, indicating the target transitions and the experimental challenges.

- **Chapter 2** introduces neutral Hg as strong candidate for the best optical frequency standard and reviews the lowest-lying levels and relevant transitions: the $^1S_0 - {}^3P_1$ cooling line, the ultra-narrow $^1S_0 - {}^3P_0$ clock transition, and the repumping $^3P_0 - {}^3S_1$ and $^3P_2 - {}^3S_1$ routes from metastable states. A brief note on hyperfine-induced state mixing in $^3P_0$ sets the metrological context for fermionic isotopes.

- **Chapter 3** summarises Ps properties, level structure up to $n = 2$, and the spectroscopy and cooling landscape. Emphasises two-photon access to $1^3S_1 - 2^3S_1$ transition at 486 nm and the opportunities for Doppler-free interrogation in a nucleus-free, QED-clean system.

- **Chapter 4** introduces the Fabry–Pérot (FP) resonator model used throughout, including reflection/transmission, realistic mirror considerations, and intra-cavity intensity. Also, it provides the noise-analysis toolkit (phase/frequency-noise, N-sample and two-sample variances, Three–Cornered Hat (TCH) and Groslambert Covariance (GCOV) methods, and counter models) used to assess stability in later chapters.

- **Chapter 5** details the end-to-end Hg apparatus: ultra-high vacuum (UHV) system and Hg source, laser systems for the magneto-optical trap (MOT) operating at 253.7 nm, and a room-temperature ultra-stable optical reference cavity, including spacer and mount design, thermal stabilisation and zero-crossing characterisation, and finesse ring-down. The chapter then presents the clock spectroscopy chain, including OFC referencing, light distribution, optical amplification and frequency quadrupling to 265.6 nm, and fibre-noise cancellation (FNC) architectures with stability evaluation. Auxiliary systems for repumping and the optical lattice with a new main vacuum chamber design conclude the platform build-out.

- **Chapter 6** describes the Ps formation and UHV environment, the 486 nm laser system, and the cavity design for power-enhancement at the spectroscopy wavelength. A digital frequency-lock implementation, detection methods, and a struc-

tured uncertainty budget are provided to prepare precision $1^3S_1 - 2^3S_1$ measurements.

- **Chapter 7** collects the main outcomes and outlines next steps: deploying the characterised ultra-stable reference for clock-line spectroscopy in Hg, implementing the power-enhancement cavity for Ps two-photon interrogation, and leveraging both platforms for precision tests and metrology.

1.1 Mercury Clock Transition Spectroscopy

The ultra-narrow $^1S_0 - {}^3P_0$ transition in neutral ^{199}Hg is used as a frequency reference in optical lattice clocks, with broad significance in fundamental physics and quantum technology [1, 2]. Spectroscopy of this forbidden transition, referenced as a clock line, enables some of the most precise tests of nature's symmetries and fundamental physical constants. For instance, comparisons of optical clock frequencies over time or orientation provide stringent Lorentz invariance tests [3, 4]. Long-term monitoring of a Hg clock against other species can reveal potential drifts in fundamental constants like the fine-structure constant α [5–7], or coupling to dark matter fields [8, 9]. The heavy Hg atom, with the atomic number $Z = 80$, also amplifies subtle effects of QED, allowing high-precision spectroscopy to probe electroweak interactions and refine nuclear charge radii [10]. In parallel, Hg's two-electron atomic structure, analogous to strontium or ytterbium, offers a platform for quantum simulation and computation [11–13]. The metastable states and the nearly decoupled nuclear spin can be used as long-lived qubit levels or to realise many-body spin models with SU(N) symmetry [11, 14]. The theoretical schemes propose using such alkaline-earth-like atoms for quantum information processing, exploiting independent optical lattices for $^1S_0$ and $^3P_0$ states and nuclear-spin encoding for qubits [15]. Beyond the laboratory, Hg clock transitions play a role in novel networks of atomic clocks used as sensors. For example, comparisons between Hg and Sr [16] or Al^+ [5] have been performed at the 10^{-17} level, enabling improved searches for variations in fundamental constants and even facilitating gravitational wave detection via correlated clock readouts [17]. In space-based experiments, such ultra-stable optical clocks could detect space-time perturbations or violations of General Relativity by monitoring frequency ratios between different atomic species [18, 19].

Mercury's clock transition also has uniquely low blackbody radiation (BBR) sensitivity [1, 20, 21], reducing a major systematic uncertainty for optical atomic clocks. This, combined with its high sensitivity to a possible Higgs-like scalar force, makes precision Hg spectroscopy a promising test of the Standard Model [22, 23]. In particular, by measuring isotope shifts in the $^1S_0 - {}^3P_0$ and $^1S_0 - {}^3P_2$ transitions across multiple Hg isotopes and constructing King plots [24], one can search for nonlinearity that would signal physics beyond the Standard Model [10, 23, 25]. A deviation

from linearity in such a plot could indicate a new boson mediating a Yukawa-type Higgs force between neutrons and electrons [26]. The Hg clock transition is a record-setting frequency standard, providing an incisive probe into Lorentz symmetry, gravitational wave detection, possible variations in fundamental constants, and new subatomic forces.

Experimental and theoretical efforts to realise and measure the $^1S_0 - {}^3P_0$ optical clock transition frequency in neutral Hg have steadily progressed over several decades. Early attempts date back to the 1980s. Working with hot Hg vapour, Wexler et al.[27] observed the 265.6 nm transition and determined the $^3P_0$ state's radiative A coefficient along with collisional broadening coefficients. Such initial spectroscopy confirmed the transition's existence and laid the groundwork for later precision studies.

The full exploitation of the ^{199}Hg clock line had to await the development of laser-cooling and ultraviolet (UV) laser technology in the 2000s. Mercury's steep technical challenges, notably the need for deep-UV 253.7 nm and 265.6 nm light for cooling and clock transition excitation, delayed its exploration compared to lighter alkaline-earth elements. By the mid-2000s, Hg was identified as an exceptional clock candidate due to theoretical predictions of its low BBR shift, two orders of magnitude smaller than in strontium, and large sensitivity to α-variation ($K_\alpha^{\mathrm{Hg}} = \partial \ln\left(\nu_{\mathrm{Hg}}\right) / \partial \ln\left(\alpha\right) = 0.81$ [28]) due to the large atomic mass. In 2008, two independent groups made seminal breakthroughs. In Japan, Hachisu et al. [1] achieved the first MOT of neutral Hg and outlined a lattice clock scheme. They trapped six stable isotopes, four bosonic and two fermionic, making Hg the heaviest atom laser-cooled at that time. Their work proposed operating the clock transition in an optical lattice at the magic wavelength, calculated then to be in the 360 nm range, and anticipated an accuracy better than 10^{-18} after cancelling lattice Stark shifts.

Meanwhile, in France, Petersen et al. [2, 29, 30] performed the first direct laser spectroscopy of the $^1S_0 - {}^3P_0$ line in laser-cooled Hg. Using fermionic ^{199}Hg (nuclear spin $I = 1/2$) and ^{201}Hg ($I = 3/2$) atoms confined in a MOT, they observed the highly forbidden clock transition at 265.6 nm via Doppler-free two-photon spectroscopy of the recoil doublet. This measurement yielded absolute optical frequencies for both isotopes with uncertainties 4–5 orders of magnitude lower than prior indirect values. Petersen reported the ^{199}Hg clock frequency with sub-MHz precision and highlighted Hg's exceptionally low BBR sensitivity as a key advantage for next-generation clocks. These studies firmly established neutral Hg as a viable optical clock species and set the stage for rapid progress in the next decade.

After the initial observation of the clock transition, experimental focus turned to improving spectroscopic resolution and clock stability. By 2010–2012, the SYRTE team in Paris had developed an enhanced setup with Hg atoms confined in a 1-D optical lattice at the magic wavelength, around 362 nm, as later measured [31–33]. Lattice confinement in the Lamb–Dicke regime eliminated Doppler broadening, enabling

ultra-narrow resonances. McFerran et al. [33] locked an ultra-stable laser to the ^{199}Hg clock transition and achieved a spectral linewidth of 15 Hz, transform-limited by the interrogation time. The laser's fractional frequency instability reached 5.4×10^{-15} at 1s averaging, demonstrating the potential of Hg to reach state-of-the-art stability. Around the same time, the magic lattice wavelength for Hg was experimentally determined to be ≈ 362.5 nm, in agreement with refined theoretical predictions (earlier estimates had ranged from 342 nm to 360 nm [31, 34]). With a magic lattice and high-stability laser, researchers in 2013–2014 were able to perform high-resolution spectroscopy of ^{199}Hg and begin evaluating systematic shifts. In 2014, McFerran et al. [35] reported absolute frequency measurements of the ^{199}Hg clock transition over a three-month campaign, referenced to the SI second via primary Cs fountains. Repeated measurements yielded a statistically averaged frequency with fractional uncertainty 2.5×10^{-16}, limited primarily by the fountain reference and statistical noise. This represented the most precise optical frequency measurement in Hg at that time. Furthermore, no significant frequency drift was observed, constraining any time-variation of fundamental constants on the 10^{-16}/year level.

The culmination of these efforts was the first accuracy evaluation of a Hg lattice clock at the 10^{-16} level. Tyumenev et al. [36, 37] compared an improved ^{199}Hg optical lattice clock against both microwave and optical standards. They measured the absolute clock frequency as $\nu_{\mathrm{Hg}} = 1\,128\,575\,290\,808\,154.62$ Hz with an uncertainty of 0.19 Hz (statistical) and 0.38 Hz (systematic) dominated by the realisation of the SI second. This corresponds to a fractional uncertainty of 1.7×10^{-16}, placing the Hg clock among the world's most accurate frequency references. The evaluation accounted for systematic shifts such as lattice Stark, BBR, Zeeman, and density shifts. In that work, the Hg clock was directly compared to a Cs fountain, yielding the absolute frequency, and also to an ^{87}Sr optical lattice clock via an OFC. The ratio $\nu_{\mathrm{Hg}}/\nu_{\mathrm{Sr}}$ was determined with 1.8×10^{-16} uncertainty and found in excellent agreement with a parallel measurement in Japan. Such cross-comparisons between two optical species and between optical and microwave standards serve not only to verify clock accuracy but also to test fundamental physics. For example, the consistency of the Hg/Sr frequency ratio across laboratories constrains any present-day variation in α or other constants. By 2016, the Hg clock transition had thus been measured and re-measured to extraordinary precision, with reproducible results at the 10^{-16} level. Mercury's low BBR shift of -2.4×10^{-16} at 300 K [38] means its uncertainty budget can be improved further by relatively straightforward thermal control. ^{199}Hg is regarded as a prime candidate for pushing optical clock accuracy into the low 10^{-18} range.

In recent years, there have been additional developments by other groups and on other isotopes. In 2015, Paul at the University of Arizona, implemented and characterised a MOT for the ^{199}Hg and performed a precision spectroscopy of the $^1\mathrm{S}_0 - {}^3\mathrm{P}_0$ transition [39]. In 2018, a team in China at Shanghai Institute of Optics and Fine Mechanics reported the observation of the ^{199}Hg clock transition in a MOT, indepen-

dently confirming the transition frequency and basic spectroscopic features [40]. Using a free-running hydrogen maser and OFC for reference, they measured $\nu(^{199}\mathrm{Hg}) = 1\,128\,575\,290.819(14)$ MHz, in agreement with the previously established value. Their experiment achieved over 95% depletion of a ^{199}Hg MOT when the clock laser was on resonance, and observed a Doppler-broadened linewidth of $\sim$ 450 kHz at 60 μK. A weak Doppler-free peak was also detected by using a "free-of-field" detection scheme, hinting at the recoil doublet structure. This result underscores the growing international interest in Hg lattice clocks, alongside established Sr and Yb systems.

On the theoretical front, attention has turned to the yet-unmeasured even isotopes of Hg (with nuclear spin $I = 0$) for clock operation. Since the $^1\mathrm{S}_0 - {}^3\mathrm{P}_0$ transition in bosonic isotopes is strictly forbidden absent perturbations, one proposal is to induce a weak transition via a magnetic field, as done in Sr clocks. To guide future experiments, Schelfhout and McFerran [41] performed state-of-the-art relativistic calculations to predict the clock transition frequencies for all naturally occurring Hg isotopes. Their multiconfiguration Dirac-Hartree-Fock computations, combined with known isotope shifts of the 253.7 m $^1\mathrm{S}_0 - {}^3\mathrm{P}_1$ line, allowed them to estimate the unknown $^1\mathrm{S}_0 - {}^3\mathrm{P}_0$ frequencies in ^{198}Hg, ^{200}Hg, ^{202}Hg, and ^{204}Hg to within a few GHz. Notably, by including an experimental value for ^{198}Hg's clock transition from early spectroscopy, they constructed a King plot using the $^1\mathrm{S}_0 - {}^3\mathrm{P}_1$ and $^1\mathrm{S}_0 - {}^3\mathrm{P}_0$ transitions across the Hg isotopic chain. No significant nonlinearity was found beyond Standard Model expectations, but the analysis refines nuclear charge radii and highlights the sensitivity of Hg isotope shifts to a potential new force.

These theoretical and experimental advances on Hg's clock transition, from initial lifetime measurements, to laser cooling and magic-trapping demonstrations, to high-precision spectroscopy at the 10^{-16} level, collectively pave the way for a Hg-based optical clock with unprecedented accuracy. Such a clock would not only enrich the global timekeeping system but also strengthen probes of new physics like Higgs-related forces or ultralight dark matter, through continued comparisons of Hg against other top-performing clocks. In this dissertation, I address my own attempt to join this pursuit by taking the first steps towards realising the Hg optical atomic clock in our laboratory.

1.2 Positronium Spectroscopy

Positronium, the bound state of an electron and positron, is the lightest atom and a uniquely pure leptonic system. As such, it provides an ideal platform for testing bound-state QED with no complications from nuclear structure [42, 43]. In contrast to hydrogen (where the heavy proton suppresses recoil effects), Ps consists of two equal-mass leptons and demands a fully relativistic two-body treatment. The equal masses lead to large recoil corrections, and the possibility of e^+e^- annihilation into photons introduces additional QED terms not present in ordinary atoms. A com-

plete description of Ps, therefore, requires calculating high-order QED contributions, beyond the simple Coulomb potential, making it a sensitive probe of the QED theory. Early theoretical work by Caswell and Lepage and by Barbieri and Remiddi formulated rigorous two-body QED formalisms for Ps, enabling the computation of energy levels up to $\mathcal{O}(\alpha^6)$, including one- and two-loop radiative corrections, recoil, and annihilation terms [44, 45]. These calculations predict notably large higher-order corrections for the 1S–2S interval in Ps, on the order of tens of MHz. Ps's simplicity, i.e., point-like constituents and only electromagnetic interactions, and these enhanced QED effects have long motivated precision measurements of the Ps spectrum as stringent tests of QED theory. Moreover, being a particle–antiparticle bound state, Ps is an important system for fundamental symmetry tests, such as CPT invariance, and for searches of physics beyond the Standard Model [46, 47]. The specific transition between the 1^3S_1 ground state and the 2^3S_1 excited state has played a central role in this context.

The $1^3S_1 - 2^3S_1$ transition in Ps is a highly forbidden single-photon transition. Instead, it can be excited via two-photon absorption at $\lambda \approx 243$ nm, i.e. two 486 nm photons in combination. Using two photons offers the added advantage of a Doppler-free configuration: two counter-propagating photons can excite 1S–2S without first-order Doppler shifts, a crucial benefit given the thermal velocities of Ps. This two-photon approach was first realised experimentally in the early 1980s. In 1982, Chu and Mills achieved the first laser excitation of the Ps 1S–2S transition [48]. They employed pulsed dye lasers at 486 nm to drive the two-photon resonance and introduced a detection scheme based on photoionisation. The laser-excited Ps atoms in the 2S state were photoionised, and the resulting free positrons counted. Chu and Mills's 1982 experiment thus demonstrated the feasibility of Ps two-photon spectroscopy, albeit with modest precision.

By 1984, rapid progress enabled a much more precise measurement. Chu, Mills and Hall reported a Doppler-free two-photon spectrum of Ps [49]. They measured the $1^3S_1 - 2^3S_1$ interval to be $1\,233\,607\,185(15)$ MHz, corresponding to a relative uncertainty of 1.2×10^{-8}. This was an enormous improvement in accuracy, owing to innovations such as a bunched positron beam, improved laser stabilisation, and frequency calibration against a Te_2 reference line. The result agreed with QED predictions and established the Ps 1S–2S line as a benchmark in exotic-atom spectroscopy. Nonetheless, systematic uncertainties in the pulsed-laser approach, notably frequency chirp, ultimately limited further progress. After subsequent recalibrations of the Te_2 reference and corrections for laser frequency offsets, the Ps interval was known to about ± 10.7 MHz by the late 1980s [50].

Theoretical calculations in this period provided further motivation for improved precision. By the early 1990s, Ps energy levels were known through $\mathcal{O}(\alpha^6)$, with the next order, $\mathcal{O}(\alpha^7)$, expected to contribute on the order of 10 MHz to the 1S–2S interval [51]. This meant that a few-MHz measurement could directly test higher-order QED terms. In 1993, Fee, Chu, Mills and collaborators achieved such a measurement

using CW two-photon spectroscopy [50, 51]. A narrow-band CW dye laser at 486 nm was power enhanced in a high-finesse FP cavity, reaching ∼2.5 kW circulating power. Ps atoms passing through the cavity were excited to the 2S state and subsequently photoionised by a delayed 532 nm pulse. A detailed Monte Carlo simulation incorporating velocity distributions, second-order Doppler shifts, and AC Stark effects was used to extract the line centre. The result achieved a relative uncertainty of 2.6×10^{-9}. This landmark experiment provided a stringent test of QED. The result agreed with theory within 2.5 MHz and directly probed the size of uncalculated $\mathcal{O}(\alpha^7)$ terms [50, 51]. The measurement remains the most precise determination of the Ps 1S–2S interval to date.

Despite its success, the 1993 work underscored experimental challenges: second-order Doppler effects, AC Stark shifts from high intra-cavity power, pulsed-laser chirp in earlier work, and Ps's short lifetime, which limits interaction time. Next-generation measurement must address these systematic issues, either through direct velocity control, chirp correction, or new detection strategies.

After two decades of relative inactivity, Ps spectroscopy has recently experienced a revival. Advances in laser technology have enabled new approaches. In 2024, Heiss *et al.* at ETH Zürich reported a modern remeasurement using pulsed two-photon excitation combined with Rydberg-state detection [47]. Ps atoms were excited to the 2S state and then promoted to the 20P Rydberg level, which was field-ionised in a controlled electric field. Measuring the time-of-flight of the ionised positrons allowed a determination of the Ps velocity distribution, enabling a direct correction of the second-order Doppler shift. Furthermore, an optical heterodyne method was used to measure and correct the chirp of the pulsed 486 nm laser on each shot. After detailed Monte Carlo modelling, Heiss *et al.* obtained $1\,233\,607\,210.5(49.6)$ MHz, with 40×10^{-9} fractional uncertainty. This result is consistent with the value from 1993 within uncertainties and demonstrates powerful new techniques for managing Doppler and chirp effects. While less precise, the measurement from 2024 paves the way for future CW or hybrid experiments that could surpass the state-of-the-art accuracy.

In summary, the Ps $1^3\mathrm{S}_1 - 2^3\mathrm{S}_1$ transition has been a central focus of precision spectroscopy for over four decades. Its measurement history, from the pioneering work of Chu and Mills to the CW breakthrough of Fee *et al.*, and most recently to the modern pulsed experiments with Rydberg detection, exemplifies the synergy between experimental innovation and theoretical QED advances. The comparison between experiment and theory has so far shown excellent agreement, validating QED predictions up to $\mathcal{O}(\alpha^6)$ and probing the scale of $\mathcal{O}(\alpha^7)$ contributions. Our recent developments in Ps laser-cooling within Antimatter Experiment: gravity, Interferometry, Spectroscopy (AE$\bar{g}$IS) collaboration [52] suggest that sub-MHz precision, approaching the natural linewidth, may be achievable in the future, enabling even more stringent tests of bound-state QED. In this dissertation, I propose an experimental setup design to be implemented within the AE$\bar{g}$IS apparatus, which enables the precision spectroscopy

of Ps.

Chapter 2

About Mercury

In this section, I discuss the fundamental properties of neutral Hg and its suitability as a frequency reference for optical atomic clocks. I begin by exploring Hg's unique physical characteristics and closed-shell electronic structure. Next, I discuss Hg's lowest-lying electronic energy levels and transitions, particularly focusing on transitions important for laser cooling and trapping, such as the intercombination $^1\mathrm{S}_0 - {}^3\mathrm{P}_1$ transition, and the doubly forbidden $^1\mathrm{S}_0 - {}^3\mathrm{P}_0$ transition relevant for optical clock operation. I also discuss repumping schemes using transitions to short-lived states to maintain continuous clock operation.

Furthermore, I elaborate on the state mixing in the hyperfine structure of the $\mathrm{P}_{0,1,2}$ state, especially for fermionic isotopes. This mixing, induced by hyperfine interactions, weakly enables otherwise forbidden transitions, significantly influencing their transition probabilities. Finally, I address the Zeeman effect on the clock transitions.

2.1 Mercury Properties

Mercury, atomic number 80 is an alkaline-earth-like element with a closed-shell electronic configuration of $[\mathrm{Xe}]\, 4f^{14}5d^{10}6s^2$. This structure results in two valence electrons in the $6s$ orbital, which give rise to low-energy singlet and triplet electronic states. The presence of long-lived metastable states makes neutral Hg an attractive candidate for high-precision optical frequency standards [53, 54].

A distinguishing physical property of Hg is its liquid state at room temperature, with a melting point of $-38.83\ ^\circ\mathrm{C}$ and a boiling point of $356.73\ ^\circ\mathrm{C}$ at atmospheric pressure [55]. At 300 K, Hg exhibits a vapour pressure of approximately 0.3 Pa [56], orders of magnitude higher than other commonly used clock species, such as strontium [57] or ytterbium [58]. This high vapour pressure enables the generation of atomic beams or vapour samples without needing high-temperature ovens. Cooled Hg-droplet atom sources and atom sources and MOTs are thus readily implemented [59].

Hg possesses seven stable isotopes, comprising five bosonic ^{196}Hg, ^{198}Hg, ^{200}Hg, ^{202}Hg and ^{204}Hg, with nuclear spin $I = 0$, and two fermionic ^{199}Hg and ^{201}Hg, with nuclear spin respectively $I = 1/2$ and $I = 3/2$, species [60]. The isotope ^{199}Hg is commonly used in optical lattice clock experiments due to its relatively high natural abundance (Table 2.1) and simple atomic structure. Also, Hg has the lowest susceptibility to BBR (-16×10^{-17} at 300 K [37]) compared to the neutral species most commonly used in optical atomic clocks, i.e. Sr (-550×10^{-17} at 300 K [54]) and Yb (-270×10^{-17} at 300 K [54]), making it a strong candidate for the best optical frequency standard [1, 31].

Table 2.1: List of natural isotopes of Hg.

Isotope	Abundance	Nuclear spin
196	0.15%	0
198	9.97%	0
199	16.87%	1/2
200	23.10%	0
201	13.18%	3/2
202	29.86%	0
204	6.87%	0

Beyond its metrological applications, Hg's rich isotopic structure, significant mass and two narrow transitions, $^1S_0 - {}^3P_0$ and $^1S_0 - {}^3P_2$, also make it an excellent system for probing fundamental physics, such as possible violations of the King plot linearity or new interactions beyond the Standard Model [10, 23–25]. The combination of favourable spectroscopic properties, high natural vapour pressure, and low environmental sensitivities underscores the potential of neutral Hg as a next-generation optical clock candidate.

2.2 Neutral Mercury Lowest Lying Energy Levels and Transitions

Mercury has an electronic structure similar to that of alkaline-earth atoms such as magnesium, strontium, or ytterbium. Its lowest energy levels include the ground state $^1S_0$, the triplet states ^3P_J, and the singlet state $^1P_1$. The only electric dipole-allowed transition from the ground state to these excited states is the $^1S_0 - {}^1P_1$ transition. However, singlet-triplet transitions are commonly used in experiments, as their transition probabilities are non-zero due to the mixing of pure LS states. This phenomenon is discussed in Section 2.2.4.

Alkaline-earth and alkaline-earth-like atoms share a similar energy level structure and are widely used in optical atomic clocks. Owing to its high transition probability and broad spectral width γ, the strong $^1S_0 - {}^1P_1$ transition is used to cool and trap atoms in MOT. The short lifetime of the $^1P_1$ state sets a limit on the Doppler temperature, $T_D = \hbar\gamma/2k_B$, where k_B is the Boltzmann constant. Therefore, atoms are typically transferred to a MOT operating on the weaker and spectrally narrower intercombination transition $^1S_0 - {}^3P_1$, which enables cooling to lower temperatures.

The doubly forbidden by the spin and total angular momentum rules, spectrally narrow $^1S_0 - {}^3P_0$ transition exhibits zero magnetic moment in both states, making it highly suitable as an optical frequency reference. It also finds use in various scientific applications, including quantum simulation [11, 61–64], quantum computation [12, 13, 15, 65], and gravitational wave detection [17, 66, 67]. The $^1S_0 - {}^3P_2$ transition, although also doubly forbidden, is less suitable for frequency metrology due to the non-zero magnetic moment of the excited $^3P_2$ state, which increases sensitivity to systematic uncertainties from static magnetic fields. Continuous operation of an optical atomic clock benefits from repumping atoms from the metastable $^3P_0$ state back to the ground $^1S_0$ state. This can be achieved using optical transitions to higher-lying, short-lived states such as $^3S_1$ or $^3D_3$.

The energy level structure of relevant Hg optical transitions is shown in Figure 2.1.

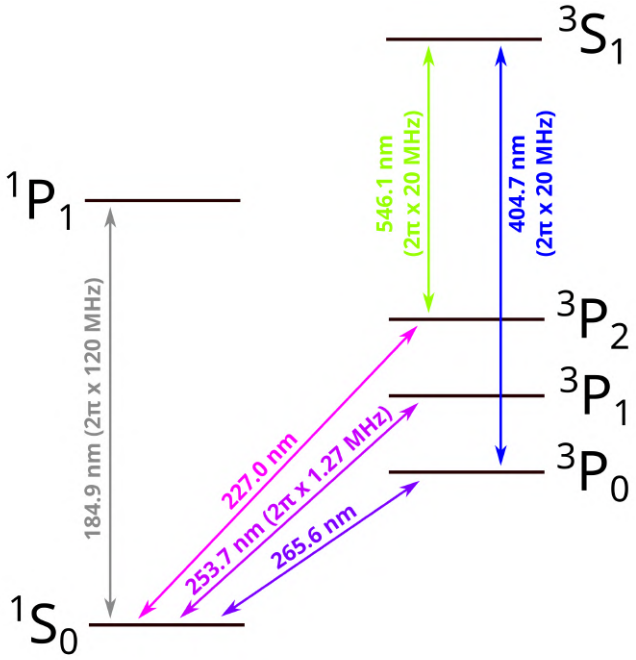

Figure 2.1: The lowest lying energy levels of neutral Hg relevant for this work.

2.2.1 Cooling Transition $^1S_0 - ^3P_1$

Alkaline-earth(-like) atoms are typically slowed and cooled using the strong dipole transition $^1S_0 - {}^1P_1$. For Hg, this transition lies in the deep UV at a wavelength of 184.9 nm, beyond the reach of commercially available laser systems. A significant challenge in implementing such a laser is that 184.9 nm light is strongly absorbed by air. As a result, the output mirror of the laser system would need to serve as a viewport of the vacuum science chamber.

On the other hand, the 253.7 nm intercombination transition $^1S_0 - {}^3P_1$, with a natural linewidth of $\gamma = 2\pi \times 1.27$ MHz, is strong enough to allow efficient trapping of Hg in a MOT with the Doppler temperature limit of $T_D = 31$ μK [1, 29, 59, 68–73]. The saturation intensity of

$$I_s = \frac{\pi h c \gamma}{3\lambda^3} = 10.2 \, \frac{\text{mW}}{\text{cm}^2}, \tag{2.2.1}$$

where h is the Planck constant, and c is the speed of light, allows for the experimentally feasible saturated absorption with less than 1 mW of 253.7 nm light power. The absolute frequency of the $^1S_0 - {}^3P_1$ intercombination transition has been precisely measured in a hot vapour cell by S. Gravina [74] and by us [10, 75] using Doppler-free saturation spectroscopy. The spectrum of the $^1S_0 - {}^3P_1$ transition in Hg is shown in Figure 2.2. The isotopic shift measurements of the $^1S_0$–$^3P_1$ transition, when combined

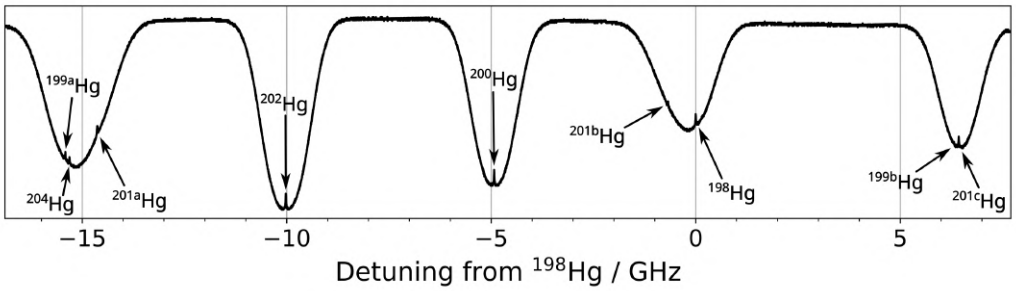

Figure 2.2: The saturation spectroscopy of the $^1S_0 - {}^3P_1$ transition in the room-temperature Hg vapour cell. Five Doppler-broadened profiles of the Hg isotopes with sub-Doppler Lamb peaks are visible. At room temperature, the Doppler-broadened profiles are of ~1 GHz widths, much more than the isotopic shifts of some Lamb peaks. The overlapping leads to situating the sub-Doppler spectral lines at the slopes. The a, b, and c letters refer to hyperfine transitions in fermions.

with measurements from other transitions, such as the $^3P_2$–$^3S_1$ transition at 546 nm, can be used to form the King plot [24]. The analysis of the King plot allows for the determination of the changes in nuclear charge radii and testing atomic structure theories [10].

Despite Doppler-free saturation spectroscopy providing high-resolution access to the intercombination line, sub-Doppler features often appear on the sloped background of Doppler-broadened profiles. This leads to systematic shifts in the measured line centre. To address this, we developed the background-free locking scheme. That involves alternate acquisition of signal with and without the pump beam, enabling direct subtraction of the Doppler background and minimising frequency offset errors [75].

The $^1S_0$–$^3P_1$ transition can be employed in Doppler broadening thermometry. By measuring the Doppler width of the absorption line in a thermal vapour, one can determine the temperature of the gas with high accuracy. This method offers a primary thermometric technique traceable to fundamental constants, contributing to the realisation of the kelvin in the International System of Units [76].

2.2.2 Clock Transition $^1S_0$—$^3P_0$

The doubly forbidden $^1S_0 - {}^3P_0$ transition at 265.6 nm features a narrow natural linewidth of approximately $\delta\nu = 100$ mHz in fermions, enabling high quality factors $Q = f/\delta\nu$ exceeding 10^{15} [54]. Owing to the absence of angular momentum in both the ground and excited states, the transition is weakly allowed only in fermionic isotopes due to hyperfine interaction-induced state mixing [1]. In bosonic isotopes, the transition remains forbidden under electric dipole selection rules. The transition probability can be increased by using magnetic quenching [77, 78], i.e., the interaction of Hg atoms with a magnetic field by the Zeeman effect.

A key advantage of Hg, compared to other alkaline-earth-like atoms such as strontium or ytterbium, lies in its reduced sensitivity to external perturbations. Studies show that the BBR shift in Hg is one of the lowest among Group II elements of the periodic table [20]. This reduced sensitivity relaxes the thermal shielding requirements of the experimental system and simplifies systematic uncertainty budgets. Furthermore, the $^1S_0 - {}^3P_0$ transition exhibits a negligible first-order Zeeman shift due to the absence of a magnetic moment in both states. The second-order Zeeman effect, while present, is both measurable and controllable [79].

The scalar and tensor components of the AC Stark shift can also be precisely evaluated. This makes the transition well-suited for operation in optical lattices, particularly at the so-called magic wavelength, where the differential scalar AC Stark shift between the two states involved in the $^1S_0 - {}^3P_0$ transition vanishes to first order [80]. The magic wavelength for Hg has been identified near 362.5 nm, enabling confinement of atoms in an optical lattice with minimal perturbation to the clock frequency [31]. Operating in the Lamb-Dicke regime suppresses motional broadening and recoil effects, thus permitting spectroscopic interrogation with sub-hertz resolution [54].

The $^1S_0 - {}^3P_0$ transition's insensitivity to BBR and external electromagnetic fields makes Hg a strong candidate for next-generation optical frequency standards [1, 31]. Recent work has demonstrated a direct frequency ratio measurement between ^{199}Hg

and ^{171}Yb optical lattice clocks with a total fractional uncertainty of 8.8×10^{-17} and short-term instability reaching $2.0 \times 10^{-15}/\sqrt{\tau}$ [81], where τ is the averaging time in seconds. The systematic uncertainty of the Hg clock alone was evaluated at 7.5×10^{-17}, limited primarily by residual effects such as BBR, lattice Stark shifts, and collisional interactions.

2.2.3 Metastable States Repumping Transitions $^3\mathrm{P}_0 - ^3\mathrm{S}_1$, $^3\mathrm{P}_2 - ^3\mathrm{S}_1$

The operation of optical lattice clocks based on fermionic Hg requires efficient repumping from the long-lived metastable $^3\mathrm{P}_0$ and $^3\mathrm{P}_2$ states back to the ground $^1\mathrm{S}_0$ state. The repumping is necessary for the determination of the fraction of atoms excited to the $^3\mathrm{P}_0$ state during the clock cycle.

The $^3\mathrm{P}_0 - {}^3\mathrm{S}_1$ (404.7 nm) and $^3\mathrm{P}_2 - {}^3\mathrm{S}_1$ (546.1 nm) transitions serve as viable optical pathways for repumping [82], due to their allowed electric dipole character and relatively short lifetimes of the $^3\mathrm{S}_1$ state of $8.0(7)$ ns [83]. Light at these repumping wavelengths efficiently excites atoms to the $^3\mathrm{S}_1$ state, from which they can decay into the $^3\mathrm{P}_\mathrm{J}$ manifold. Atoms in the $^3\mathrm{P}_2$ and $^3\mathrm{P}_0$ states are thus cyclically pumped up to the $^3\mathrm{S}_1$ state. Atoms in $^3\mathrm{P}_1$ state quickly decay back down to the $^1\mathrm{S}_0$ ground state. The choice of repumping wavelength must take into account not only the transition strength, but also the branching ratios of decay from $^3\mathrm{S}_1$, to ensure efficient population transfer back to the ground state. In addition, narrow-linewidth lasers are not required for these transitions because of their relatively broad natural linewidths. This relaxes the demands on the laser frequency stabilisation systems.

2.2.4 State Mixing in Hyperfine Structure of $^3\mathrm{P}_0$ State

In bosonic isotopes, the $^1\mathrm{S}_0 - {}^3\mathrm{P}_0$ transition is strictly forbidden under electric dipole (E1) selection rules because both states have total electronic angular momentum $J = 0$, and the $J = 0 \to J = 0$ transitions are E1-forbidden [54]. Moreover, within the LS coupling, also the $\Delta S \neq 0$ transition is forbidden [84]. However, in fermionic isotopes (which have non-zero nuclear spin $I \neq 0$), hyperfine interactions introduce a small amount of state mixing that makes this transition weakly allowed [85].

The hyperfine interaction arises from the coupling between the nuclear magnetic moment and the magnetic field generated by the electrons [86]. As the $\mathbf{J}^2$ does not commute with the Hamiltonian, this interaction can mix electronic states of different total angular momentum J, particularly mixing the $^3\mathrm{P}_0$ state with nearby $J = 1$ states, such as $^3\mathrm{P}_1$ and $^1\mathrm{P}_1$. The mixing allows for a non-zero E1 transition probability between the mixed $^3\mathrm{P}_0$ state and the $^1\mathrm{S}_0$ ground state.

The perturbed $^3\mathrm{P}_0$ state can be expressed as [87]

$$\left|{}^3\mathrm{P}_0^{(1)}\right\rangle = \left|{}^3\mathrm{P}_0\right\rangle + \sum_n \frac{\langle n \left|H_{\mathrm{hf}}\right| {}^3\mathrm{P}_0\rangle}{E_{^3\mathrm{P}_0} - E_n} \left|n\right\rangle , \tag{2.2.2}$$

where H_{hf} is the hyperfine interaction Hamiltonian, E_n are the energies of the intermediate states $|n\rangle$, and the sum runs over states with $J = 1$ that can mix with $^3\mathrm{P}_0$. The dominant contributions to the mixing come from the $^3\mathrm{P}_1$ and $^1\mathrm{P}_1$ states due to their proximity in energy to the $^3\mathrm{P}_0$ state. The mixing coefficients can be approximated using first-order perturbation theory [88]

$$\alpha_{^3\mathrm{P}_1} = \frac{\langle ^3\mathrm{P}_1 \left| H_{\mathrm{hf}} \right| ^3\mathrm{P}_0 \rangle}{E_{^3\mathrm{P}_0} - E_{^3\mathrm{P}_1}}, \quad \beta_{^1\mathrm{P}_1} = \frac{\langle ^1\mathrm{P}_1 \left| H_{\mathrm{hf}} \right| ^3\mathrm{P}_0 \rangle}{E_{^3\mathrm{P}_0} - E_{^1\mathrm{P}_1}}. \tag{2.2.3}$$

These coefficients quantify the admixture of $^3\mathrm{P}_1$ and $^1\mathrm{P}_1$ character into the $^3\mathrm{P}_0$ state,

$$\left| ^3\mathrm{P}_0^{(1)} \right\rangle = \left| ^3\mathrm{P}_0 \right\rangle + \alpha_{^3\mathrm{P}_1} \left| ^3\mathrm{P}_1 \right\rangle + \beta_{^1\mathrm{P}_1} \left| ^1\mathrm{P}_1 \right\rangle . \tag{2.2.4}$$

The presence of $J = 1$ components in the mixed state allows for a weakly allowed E1 transition to the $^1\mathrm{S}_0$ ground state.

The transition rate A for the $^1\mathrm{S}_0 - {}^3\mathrm{P}_0$ transition can be estimated by [36],

$$A = \frac{4}{3}\alpha\omega^3 \left| \left\langle ^1\mathrm{S}_0 \middle\| \mathbf{D} \middle\| ^3\mathrm{P}_0^{(1)} \right\rangle \right|^2, \tag{2.2.5}$$

where α is the fine-structure constant, ω is the angular frequency of the transition, and $\mathbf{D}$ is the electric dipole operator. The reduced matrix element [89] $\left\langle ^1\mathrm{S}_0 \middle\| \mathbf{D} \middle\| ^3\mathrm{P}_0^{(1)} \right\rangle$ is non-zero due to the admixture of $J = 1$ states in $^3\mathrm{P}_0^{(1)}$. The transition rate is dependent on the isotope due to the different values of the nuclear spin. Calculations by [1] lead to

$$A\left(^{199}\mathrm{Hg}\right) = 1.3 \times 10^{-2}\,\mathrm{s}^{-1} \quad \text{and} \quad A\left(^{201}\mathrm{Hg}\right) = 8.8 \times 10^{-3}\,\mathrm{s}^{-1}. \tag{2.2.6}$$

Hyperfine structure is characterised by total angular momentum **F**, which is equal to the vector sum of the total electronic angular momentum **J** and nuclear spin **I**

$$\mathbf{F} = \mathbf{J} + \mathbf{I}. \tag{2.2.7}$$

An external magnetic field will remove the degeneracy of the atom's total angular momentum **F**. Magnetic field will split energy levels with total angular momentum **F** in $2F + 1$ sub-levels characterised by projection of total angular momentum on quantisation axis M_F. The first-order Zeeman shift is proportional to the magnetic field

$$\Delta E_{\text{Zeeman}} = \mathbf{M} \cdot \mathbf{B}. \tag{2.2.8}$$

The **M** is the magnetic moment of an atom

$$\mathbf{M} = g_F \mu_B M_F, \tag{2.2.9}$$

where g_F is the Lande factor, and μ_B is the Bohr magneton. The atomic magnetic moment can be decomposed into

$$\mathbf{M} = \frac{\mu_B}{\hbar} \left(g_L \mathbf{L} + g_S \mathbf{S} - g_I \mathbf{I} \right), \tag{2.2.10}$$

where $g_L = 1$ is the angular momentum Lande factor, $g_S \approx 2$ is the spin momentum Lande factor, and g_I is the nuclear Lande factor. For ^{199}Hg $I = 1/2$ and both, ^{1}S$_0$ and ^{3}P$_0$ states, split into two sublevels characterised by $M_F = \pm 1/2$. For ^{201}Hg $I = 3/2$, and the states split into four sublevels characterised by $M_F = \pm 1/2, \pm 3/2$. The transitions with $\Delta M_F = 0$, called π-transitions, are coupled with linearly polarised light, if the polarisation vector is collinear with the magnetic field **B**. The transitions with $\Delta M_F = -1$, and $\Delta M_F = 1$ are coupled with circular left polarisation, σ^-, and circular right polarisation, σ^+, respectively. Due to the higher abundance and simpler energy spectrum, the ^{199}Hg isotope is the preferred candidate for the optical atomic clock. Hence, the ^{199}Hg isotope is studied within this thesis. The Zeeman splitting of the ^{1}S$_0$ − ^{3}P$_0$ transition in ^{199}Hg is shown in the Figure 2.3.

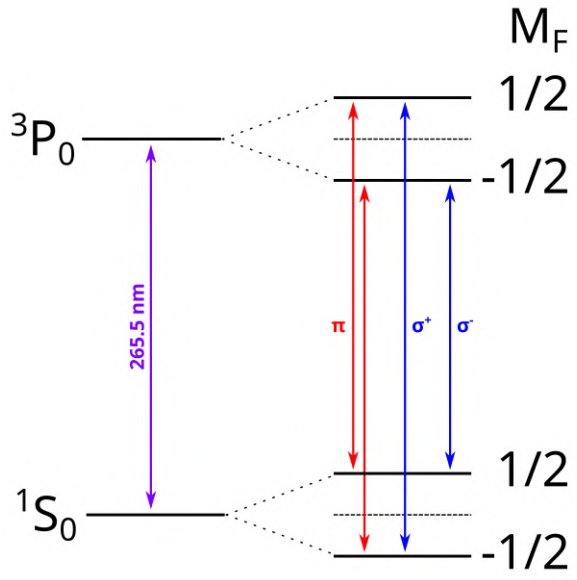

Figure 2.3: The Zeeman splitting of the clock ^{1}S$_0$ − ^{3}P$_0$ transition for ^{199}Hg isotope. The red lines indicate the π-transitions, while the blue lines indicate the $\sigma^{\pm}$ transitions.

Chapter 3

About Positronium

In this section, I discuss the fundamental properties of Ps and its role as a clean test system for bound-state QED. I describe the Ps annihilation channels and introduce the lowest-lying electronic energy levels and optical transitions.

Finally, I discuss the spectroscopic relevance of selected transitions, such as the Lyman-α line and the two-photon $1^3S_1 - 2^3S_1$ interval, which are central to high-precision experimental studies.

3.1 Positronium Properties

Positronium is a purely leptonic bound state formed by an electron and its antiparticle, the positron [90]. The two particles are held together by their mutual Coulomb attraction, creating the lightest known atom-like system. Unlike conventional atoms, Ps has no nucleus and is thus free from nuclear structure effects. This makes it a unique testbed for QED, in which all theoretical contributions arise solely from electromagnetic interactions [91].

Ps is unstable due to electron–positron annihilation, and its decay channels are tightly constrained by charge-conjugation symmetry. Since Ps is made from a particle-antiparticle pair, it has no net additive quantum numbers, and is therefore an eigenstate of the charge-conjugation operator C. The operator converts particles into antiparticles. Since applying this operator twice must return a particle to its original state, C eigenvalues must be ± 1. Since Ps has no net additive quantum numbers, the charge-conjugation invariance determines the number of gamma rays emitted in Ps decay. The C eigenstate of a state of orbital angular momentum l and total spin S is [46]

$$C = (-1)^{l+S}. \tag{3.1.1}$$

The number N of emitted γ photons is defined by

$$(-1)^{l+S} = (-1)^N. \tag{3.1.2}$$

Para-positronium (p-Ps), the singlet $^1S_0$ configuration with antiparallel spins, has eigenvalue $C = +1$ and decays predominantly into two 511 keV photons. Ortho-positronium (o-Ps), the triplet $^3S_1$ configuration with parallel spins, has $C = -1$ and decays mainly into three photons [92].

At the microscopic level, the annihilation probability is proportional to the modulus squared of the wavefunction at the origin, $|\psi(0)|^2$. Since annihilation requires the electron and positron to coincide spatially, only S-wave states contribute significantly. The overlap enhancement in S-states also implies that excited states with orbital angular momentum ($L > 0$) are strongly suppressed in their annihilation channels [93]. However, the symmetry of the wavefunction dictates that annihilation processes contribute directly to the self-energy of the atom, giving rise to an imaginary component of the energy (and thus a finite lifetime) for every state. Table 3.1 lists the annihilation and fluorescence lifetimes for selected $n = 1$ and $n = 2$ states of Ps.

Table 3.1: Annihilation ($\tau_{\text{ann.}}$) and fluorescence ($\tau_{\text{fl.}}$) lifetimes for selected $n = 1$ and $n = 2$ states of Ps.

Level	$\tau_{\text{ann.}}$ / ns	Ref.	$\tau_{\text{fl.}}$ / ns	Ref.
1^1S_0	0.125	[94]	N/A	N/A
1^3S_1	142	[95]	$\gtrsim 10^{16}$	[96]
2^1S_0	1	[94]	$\simeq 243\,100\,000$	[97]
2^3P_0	100 000	[98]	3.19	[99]
2^3P_1	$\approx \infty$	[98]	3.19	[99]
2^1P_1	3 330 000	[100]	3.19	[99]
2^3P_2	384 000	[98]	3.19	[99]
2^3S_1	1 136	[95]	$\simeq 243\,100\,000$	[97]

At leading order, the annihilation rate of p-Ps into two photons is

$$\Gamma_{2\gamma} = \frac{1}{2}\alpha^5 \frac{m_e c^2}{\hbar} \approx 7.989 \times 10^9 \text{ s}^{-1}, \tag{3.1.3}$$

corresponding to a mean lifetime of $\tau_{p\text{-Ps}} \approx 0.125$ ns. For o-Ps, the three-photon decay rate is

$$\Gamma_{3\gamma} = \frac{2(\pi^2 - 9)}{9}\alpha^6 \frac{m_e c^2}{\hbar} \approx 7.204 \times 10^6 \text{ s}^{-1}, \tag{3.1.4}$$

leading to a lifetime of $\tau_{o\text{-Ps}} \approx 142$ ns [101]. Thus, the triplet state lives nearly three orders of magnitude longer than the singlet.

Although the two- and three-photon channels dominate, higher-order decays are also permitted. p-Ps can decay into four photons and o-Ps into five photons, both with branching ratios on the order of 10^{-6}[102]. Even rarer processes, such as decays into

neutrino–antineutrino pairs, are allowed by the Standard Model but occur with vanishingly small probability ($< 10^{-17}$)[103]. These extremely suppressed channels, along with searches for invisible or non-standard decays, make Ps a sensitive probe for physics beyond the Standard Model.

Both Ps constituents have identical mass; hence, recoil effects are much larger in Ps than in hydrogen. For hydrogen, these effects are suppressed by the large proton-to-electron mass ratio (1836), whereas in Ps they are maximal (ratio = 1). QED calculations for Ps are therefore particularly demanding, requiring inclusion of high-order terms and annihilation loop diagrams[101]. The absence of nuclear structure effects eliminates one of the main sources of theoretical uncertainty present in ordinary atoms. For this reason, Ps has long been recognised as one of the cleanest systems for precision tests of bound-state QED [92, 104].

3.2 Neutral Positronium Lowest Lying Energy Levels and Transitions

The energy spectrum of Ps is hydrogen-like in structure but modified by the reduced mass $m_e/2$. As a consequence, the Bohr radius is twice that of hydrogen ($a_{\mathrm{Ps}} = 2a_0$), while the binding energy is halved. The ground state has a binding energy of 6.8 eV, in contrast to hydrogen's 13.6 eV. All transition frequencies are therefore reduced by a factor of two compared with hydrogen, with the Lyman-α transition occurring at 243 nm instead of 122 nm [86]. The next order of corrections makes the similarity between Ps and hydrogen disappear [105]. The energy level structure up to $n = 2$ of Ps is shown in Figure 3.1.

The ground-state hyperfine interval $1^1\mathrm{S}_0 - 1^3\mathrm{S}_1$ is exceptionally large compared with hydrogen, about 203 GHz [92]. This hyperfine splitting is dominated by spin–spin interactions but also receives contributions from relativistic recoil and higher-order annihilation corrections. Its accurate determination, both theoretically and experimentally, represents one of the most stringent tests of QED in bound states [106].

The fine structure of the $n = 2$ manifold is also important. The three $2^3\mathrm{P}_{0,1,2}$ states are split by spin–orbit and tensor interactions, while the $2^3\mathrm{S}_1$ state lies nearby in energy. Theoretical predictions for these splittings include terms up to $\mathcal{O}(m_e\alpha^6)$ and higher logarithmic contributions [107]. Experimentally, the $2^3\mathrm{S}_1$–$2^3\mathrm{P}_{0,1,2}$ intervals have been measured using microwave spectroscopy and optical two-photon excitation [108], and while most results agree with theory, persistent discrepancies at the few MHz level in the $2^3\mathrm{S}_1$–$2^3\mathrm{P}_2$ splitting remain unresolved [104].

Of particular spectroscopic interest is the two-photon $1^3\mathrm{S}_1$–$2^3\mathrm{S}_1$ transition. This interval at 243 nm has been the subject of several precision measurements using pulsed and CW laser sources. Recent work achieved fractional uncertainties on the order of 2.6×10^{-9}[50, 51], in agreement with QED predictions yet still leaving room for im-

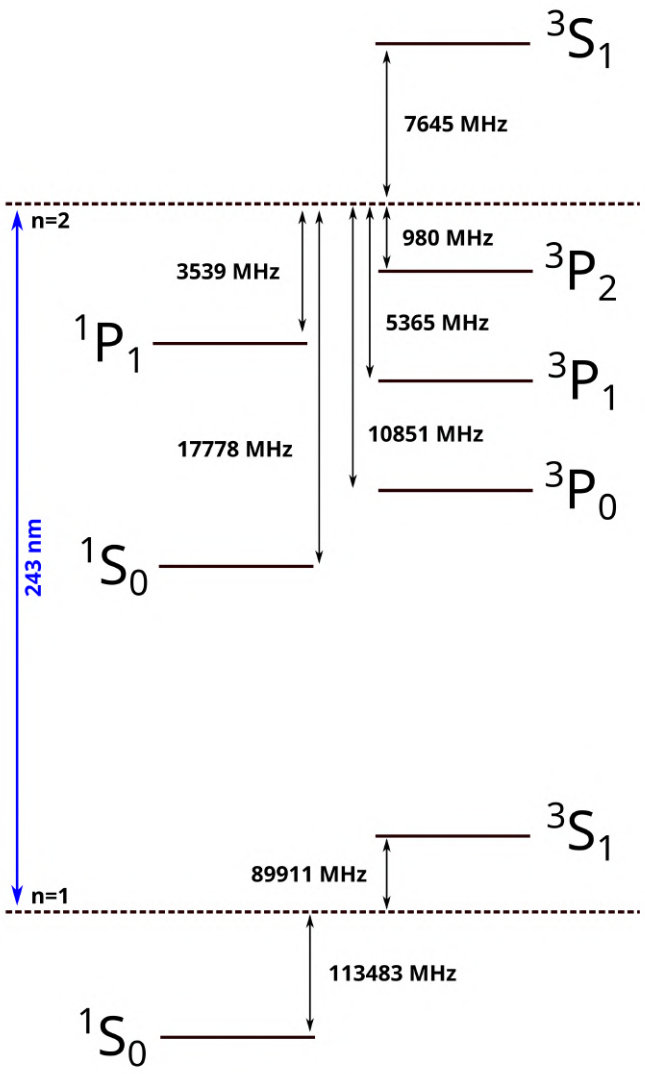

Figure 3.1: The lowest lying energy levels up to $n = 2$ of Ps. The blue line indicates the Lyman-α transition, the black lines indicate the levels' intervals, and the dashed lines indicate the positions of the non-relativistic Bohr energy levels.

provement since the theoretical uncertainty is about 0.8×10^{-9}[109]. Since the 2^3S_1 state is metastable, with a lifetime of about 1.1 μs, it is well suited for high-accuracy spectroscopy. Achieving 100 kHz precision in the 1^3S_1–2^3S_1 transition would enable tests of bound-state QED at the order of $\alpha^7 me^+$ [91], allow a determination of the me^+/m_{e^-} mass ratio to high accuracy[110], and even test the equivalence principle with a purely leptonic system by observing any gravitation-induced redshift of this transition [111].

Taken together, the lowest-lying levels of Ps thus provide a rich arena for experimental tests of QED [42]. The interplay of hyperfine structure, fine structure, and radiative shifts makes this purely leptonic atom a stringent laboratory for theory. Ongoing improvements in both theoretical calculations and spectroscopic techniques continue to push the sensitivity of Ps towards uncovering possible deviations from QED and hints of new physics [112].

3.2.1 Positronium Laser Cooling

Ps, as a bound state of an electron and a positron, has long attracted attention because it is a purely leptonic matter–antimatter system. Experimental studies to date have typically produced Ps ensembles with broad velocity distributions on the order of 10^4 m/s [113–115]. Such high velocities cause large Doppler broadening, which has in turn limited the accuracy of spectroscopic measurements [50, 51]. The prospect of reducing this velocity spread by applying laser cooling was first put forward in the late 1980s [116], only a few years after the pioneering demonstrations of laser cooling in neutral atoms [117]. Nevertheless, despite numerous efforts [118], the experimental realisation of positronium laser cooling remained unfeasible until very recently.

The first detailed theoretical treatment was provided by Liang and Dermer in 1988 [116], who considered the feasibility of driving the $1^3\mathrm{S}_1$–$2^3\mathrm{P}_{0,1,2}$ Lyman-α transitions at 243 nm. They pointed out that because of the extremely small mass of Ps, the photon recoil is unusually large, and the standard Doppler cooling limit does not apply. Their calculations suggested that temperatures in the millikelvin range could be achieved within the o-Ps lifetime of about 142 ns, thereby opening the possibility of Bose–Einstein condensation at densities as low as 10^{15} cm^{-3}. They also highlighted the potential for Doppler-free annihilation spectroscopy and even the prospect of stimulated γ-ray emission.

Despite the theoretical promise, early experimental attempts faced formidable challenges. The generation of sufficiently intense and spectrally tailored 243 nm radiation, the extremely short timescale for cooling compared with the o-Ps lifetime, and the large initial thermal velocities of Ps emitted from converter materials all presented significant obstacles. Work by Kumita *et al.* [118], for example, demonstrated the technical difficulty of coupling UV radiation to positronium ensembles, and no clear evidence of cooling could be obtained at the time.

Only in the last year has laser cooling of Ps been successfully demonstrated. Breakthrough experiments by Shu *et al.* [119] provided the first unambiguous evidence of cooling, and, in parallel, we, the AE$\bar{g}$IS collaboration, achieved an independent realisation of the effect [52]. These results confirm long-standing theoretical predictions and establish a new experimental regime in which cold positronium can be prepared. Such ensembles pave the way for ultra-precise spectroscopy, more stringent tests of bound-state QED, and the future exploration of collective quantum behaviour, including the

Bose–Einstein condensation of positronium [120, 121].

Chapter 4

Theory and Methods

4.1 Fabry–Pérot Interferometer

Fabry–Pérot interferometers are essential tools for optical lattice clocks. In its canonical form, an FP interferometer comprises two parallel mirrors. Many of its properties also hold for two-mirror optical cavities that are non-planar. Accordingly, although the two-mirror cavities discussed in this thesis are non-planar, I refer to them as FP cavities to emphasise the shared properties.

The optical cavity can be designed to fulfil i.a. the role of a short-time frequency reference for the probing laser [122], or to produce a high-power periodic trapping potential for atoms in the optical dipole trap called optical lattice [54, 123]. In this section, I will discuss the properties and characteristics of the FP interferometer.

4.1.1 Light Reflection and Transmission

A FP interferometer employed in typical experimental setups often comprises one or two concave mirrors to maintain optical stability within the cavity [124, 125]. This configuration compensates for the fact that experiments deal with Gaussian laser beams, which naturally experience divergence or convergence, rather than ideal plane waves [126]. Nevertheless, many properties relevant to experiments can be derived by analysing a simplified model of a FP interferometer with plane mirrors.

A plane wave enters a FP cavity formed by two parallel, planar mirrors spaced by a distance. The intensity of light transmitted by the FP cavity is given by [127]

$$I_T = I_0 \frac{T_1 T_2}{(1-R)^2} \frac{1}{1 + F \sin^2\left(\frac{\Delta\phi'}{2}\right)}, \tag{4.1.1}$$

where I_0 is the incident intensity, T_1 and T_2 are the transmissions of the mirrors, R is the geometric mean value of the mirrors' reflection, which includes their losses L_1 and

L_2, and $\Delta\phi'$ is the phase accumulated during the round-trip. For clarity, the equation is written with the use of the coefficient of finesse F

$$F = \frac{4R}{(1-R)^2}. \tag{4.1.2}$$

The reflected light intensity I_R is given by [126]

$$I_R = I_0 \frac{R_1 + (1-L_1)\left(R^2 - 2R + 4R\sin^2\left(\frac{\Delta\phi'}{2}\right)\right) + T_1\left(R^2 + T_1 R_2\right)}{(1-R)^2 + 4R\sin^2\left(\frac{\Delta\phi'}{2}\right)}, \tag{4.1.3}$$

where R_1 and R_2 are the reflections of the mirrors, and L_1 describes the losses of the in-coupling mirror. The full derivations of Eqs. (4.1.1) and (4.1.3) are provided in Appendix A.

Figure 4.1 depicts the transmission of an identical mirrors FP interferometer as a function of the phase difference for different values of $T = T_1 = T_2$ and $L = L_1 = L_2$ following the Eq. (4.1.1). The transmitted spectrum consists of regularly spaced

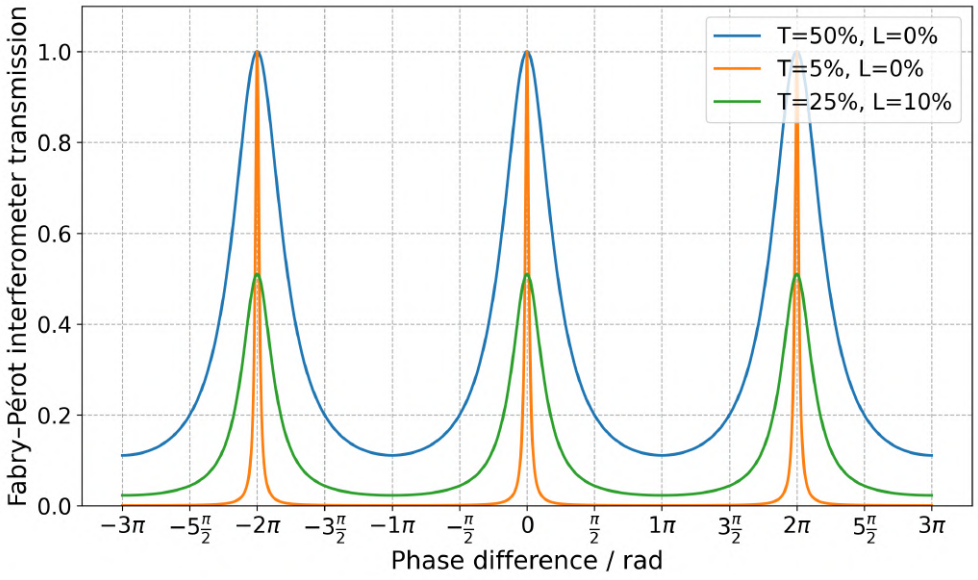

Figure 4.1: Simulated transmission of a FP interferometer with identical mirrors as a function of the phase difference, for different values of mirror transmission $T = T_1 = T_2$ and losses $L = L_1 = L_2$, based on Eq. (4.1.1).

maxima located at points where $\Delta\phi'$ is a multiple of 2π. These are called the optical cavity resonances. The free spectral range (FSR) between adjacent resonances is given by [128]

$$\text{FSR} \equiv \Delta\nu = \frac{c}{2d}, \tag{4.1.4}$$

which, for a cavity length of 10 centimetres, yields approximately 1.5 GHz.

The full width at half maximum (FWHM) of the resonance expressed in phase domain can be derived from Eq. (4.1.1) as

$$\varepsilon = 4 \arcsin\left(\frac{1-R}{2\sqrt{R}}\right). \tag{4.1.5}$$

For high reflectivity mirrors ($R \approx 1$), this expression can be approximated as

$$\varepsilon = \frac{2(1-R)}{\sqrt{R}} = \frac{4}{\sqrt{F}}. \tag{4.1.6}$$

In frequency units, the FWHM of the resonance $\delta\nu$ is given by [129]

$$\delta\nu = \frac{2\Delta\nu}{\pi\sqrt{F}}. \tag{4.1.7}$$

An important parameter characterising the FP interferometer is the finesse $\mathcal{F}$ [130]

$$\mathcal{F} = \frac{\Delta\nu}{\delta\nu} = \frac{\pi\sqrt{F}}{2} = \frac{\pi\sqrt{R}}{1-R}. \tag{4.1.8}$$

A high-finesse FP cavity can be employed as a short-term frequency reference for laser systems [54]. The optical signal reflected from the cavity may be utilised to generate an error signal via the Pound–Drever–Hall (PDH) technique [131], which is suitable for incorporation into a servo loop. The electronic servo loop stabilises the laser frequency to the cavity resonance. A sufficiently fast servo loop enables narrowing of the laser spectral width below that of the FP resonance [132]. For instance, a cavity of length 10 cm with a finesse of 400000 exhibits resonance linewidths of approximately 3.75 kHz, allowing spectral narrowing of the laser to below 100 Hz. More about the PDH error generation can be found in [122, 131, 133–135].

4.1.2 Realistic Mirror Model

The mirror model described in the previous section was simplified, lacking any internal structure. In contrast, a realistic FP interferometer intended for power-enhancement applications requires a more advanced representation.

The model assumes that each mirror consists of a multi-layer dielectric coating deposited on an optical substrate. These coatings are designed to exhibit specific reflectance and transmittance properties, but also introduce losses due to absorption and scattering. These losses are generally different for reflected and transmitted light. Moreover, internal reflections within the substrate are usually suppressed using wedged substrates or anti-reflection coatings [136].

When accounting for these effects, the standard transmission and reflection formulas of a FP interferometer must be modified to include the effective transmission, reflection, and loss factors. The resulting transmitted intensity is

$$I_T = I_0 \frac{\tilde{T}_1 \tilde{T}_2}{(1-\tilde{R})^2} \frac{1}{1 + \tilde{F} \sin^2\left(\frac{\Delta\phi}{2}\right)}, \tag{4.1.9}$$

where $\tilde{F}$ is the generalised finesse that depends on the mirror reflectivities and losses.

Similarly, the reflected intensity becomes

$$I_R = I_0 \frac{\tilde{R}_1 + (\tilde{R}_1 + \tilde{T}_1)\left(\tilde{R}_2 - 2\tilde{R} + 4\tilde{R}\sin^2\left(\frac{\Delta\phi}{2}\right)\right) + \tilde{T}_1\left(\tilde{R}^2 + \tilde{T}_1\tilde{R}_2\right)}{(1-\tilde{R})^2 + 4\tilde{R}\sin^2\left(\frac{\Delta\phi}{2}\right)}. \tag{4.1.10}$$

These expressions reduce to those in the ideal case when mirror losses vanish. The full derivation, including the definitions of effective coefficients and generalised finesse, is provided in Appendix B.

4.1.3 Light Intensity Inside The Cavity

The electromagnetic field inside a FP interferometer comprises two counter-propagating components: a forward-travelling wave E_{circ} and a backwards-travelling wave $E_{\text{b-circ}}$, originating from reflection at the second mirror. These two waves form an interference pattern along the cavity axis, resulting in a standing wave. The superposition of these two fields gives rise to spatial modulation of the intra-cavity intensity

$$I_{\text{ins}}(x) \propto 1 + \cos\left(\frac{4\pi}{\lambda}x\right), \tag{4.1.11}$$

leading to periodic maxima and minima of intensity, known as an optical lattice [137]. The nodes are separated by $\lambda/2$.

Typically, optical lattices are used as red-detuned optical dipole traps, where atoms are attracted towards maxima of light intensity, i.e. lattices' anti-nodes, due to a high intensity gradient along the axis [138]. The light intensity at the anti-node is

$$I^{\text{anti-node}} = I_0 \frac{\tilde{T}_1}{(1-\tilde{R})^2} \frac{1}{1 + \tilde{F}\sin^2\left(\frac{\Delta\phi}{2}\right)} \left(1 + \tilde{R}_2 + \sqrt{\tilde{R}_2}\right). \tag{4.1.12}$$

The intra-cavity power strongly depends on the phase $\Delta\phi$. Hence, to obtain the maximum intensity, the FP interferometer is pumped with the light of frequency matching the cavity resonance, or the cavity length is stabilised to the incoming beam wavelength. In both cases, the light intensity at the anti-node is

$$I_{\text{max}}^{\text{anti-node}} = I_0 \frac{\tilde{T}_1}{(1-\tilde{R})^2} \left(1 + \tilde{R}_2 + \sqrt{\tilde{R}_2}\right). \tag{4.1.13}$$

Maximising the intra-cavity power with respect to the mirror transmission leads to the condition of impedance matching, also known as critical coupling. Under typical assumptions of identical mirrors and small losses, the transmission, for which the intra-cavity power is maximised, is approximately equal to the mirror losses

$$T'_{\text{opt}} \approx L'. \tag{4.1.14}$$

More about the critical coupling can be found in [139–142] also including asymmetrical mirrors [143, 144].

The derivation of these results, including detailed expressions for circulating fields and intensity build-up, is provided in Appendix C. This includes expressions for the forward- and backwards-propagating waves and the resulting standing-wave intensity profile. The dependence of the power enhancement factor $I_{\text{max}}^{\text{anti-node}}/I_0$ on the mirrors' transmission T' for various L' values is presented in Figure 4.2. The above analysis con-

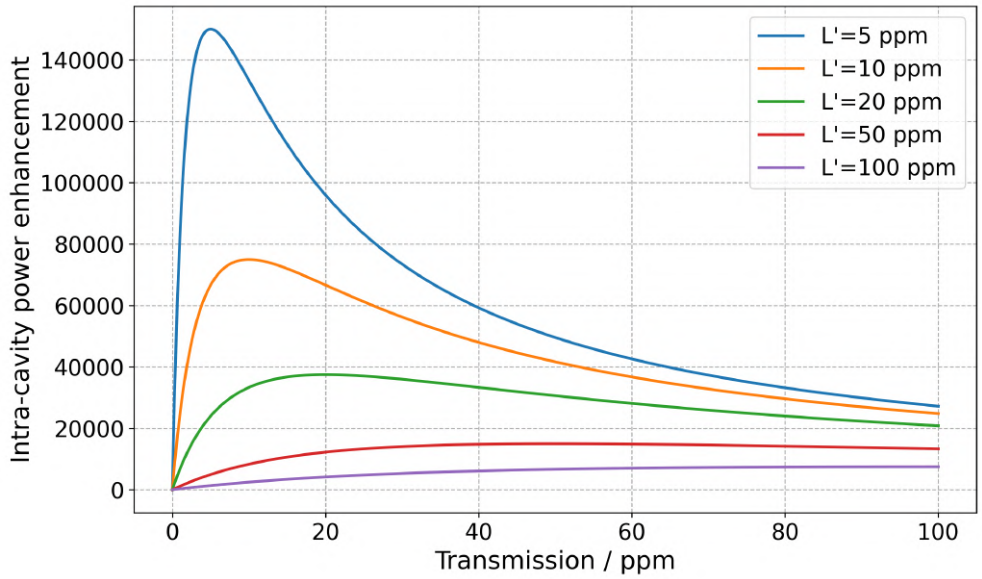

Figure 4.2: The dependence of intra-cavity power enhancement factor on the mirrors' transmission $T' = 1 - R'$ for different values of the losses L'.

cludes that the maximum intra-cavity power highly depends on the losses, both scattering and absorption, introduced by the mirrors' coatings.

4.2 Phase Noise, Frequency Counters, and Variances in Frequency Stability Analysis

This section presents an overview of the key concepts I use for frequency stability analysis. I begin by discussing phase and frequency noise, describing their

physical origins and statistical properties. I then explain the limitations of the standard N-sample variance and introduce two-sample approaches, such as the Allan variance (AVAR) and its variants. Next, I describe methods for isolating the stability of individual oscillators, focusing on the TCH method and the GCOV technique. Finally, I detail the operating principles of Π- and Λ-type frequency counters and their impact on stability measurements.

4.2.1 Phase and Frequency Noise

A sinusoidal signal influenced by both amplitude modulation and phase modulation noise can be expressed as [145]

$$V(t) = V_0 \left(1 + \alpha(t)\right) \cos\left(2\pi\nu_0 t + \varphi(t)\right), \tag{4.2.1}$$

where V_0 is the nominal amplitude, ν_0 is the carrier frequency, $\alpha(t)$ represents the fractional amplitude fluctuations and $\varphi(t)$ accounts for the random phase deviations (Figure 4.3). In most practical systems, the magnitude of $|\alpha|$ is much smaller than unity,

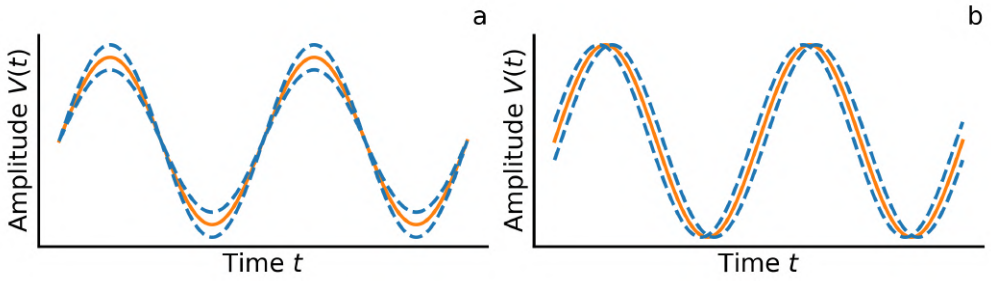

Figure 4.3: Simulated sinusoidal signal affected by (a) amplitude modulation and (b) phase modulation noises. The orange line represents the unmodulated signal, and the blue dashed lines represent the signal modulated arbitrarily.

typically on the order of 10^{-7} to 10^{-4}, particularly in quartz oscillators and frequency synthesisers [146]. The absolute value of $\varphi(t)$ is generally of limited relevance, as it becomes meaningful primarily in two-port systems [147], where $\varphi(t)/2\pi\nu_0$ corresponds to fluctuations in the propagation delay between input and output [148]. Greater attention is given to the time derivative of the phase $\dot{\varphi}/2\pi\nu_0$, characterising frequency instability [149]. The parameter can reach values as low as 8×10^{-19} in state-of-the-art optical atomic clocks [150], serving as the prototype realisations of frequency standards. The time derivative of the instantaneous phase defines the fractional instantaneous frequency deviation from a nominal value ν_0

$$y(t) \equiv \frac{d\varphi}{dt} \frac{1}{2\pi\nu_0}. \tag{4.2.2}$$

The stability of the $y(t)$ is most important in characterising the frequency source, including radio-frequency (RF) oscillators, ultra-stable lasers, and atomic clocks [151]. Typically, the noise present in $y(t)$ has various sources [152]. Widely used phase noise model, the polynomial law or the power law, distinguishes five noise types presented in Table 4.1 [153]. The total noise in the system is the sum of the contributions.

Table 4.1: The most common noise types distinguished by the polynomial law. Each noise type is proportional to a frequency or averaging time in different powers.

Noise type	$S_y(f)$	$\sigma_y(\tau)$
White phase noise	$h_2 f^2$	$a_2 h_2 \tau^{-3/2}$
Flicker phase noise	$h_1 f$	$a_1 h_1 \tau^{-1}$
White frequency noise	h_0	$a_0 h_0 \tau^{-1/2}$
Flicker frequency noise	$h_{-1} f^{-1}$	$a_{-1} h_{-1}$
Frequency random walk	$h_{-2} f^{-2}$	$a_{-2} h_{-2} \tau^{1/2}$

In the frequency domain, the noise can be characterised using power spectral density (PSD) $S_y(f)$ [154]. The total noise can be written as

$$S_y(f) = \sum_{n=-2}^{2} h_n f^n, \tag{4.2.3}$$

where h_n is the scaling factor, and f is the frequency. In the time domain, PSD can be transformed into variance

$$\sigma_y^2(\tau) = \sum_{n=-2}^{2} a_{-n}^2 h_{-n}^2 \tau^{n-1}, \tag{4.2.4}$$

where a_{-n}^2 are scaling parameters used to distinguish the h_n parameters used in PSD, and τ is the averaging time. For the optical frequencies, it is more common to present the signal's relative stability y using variances σ_y^2 or its square root, deviations σ_y [155]. Hence, this method will be used in this thesis to characterise the signals present in the experimental setup.

4.2.2 N-sample and Two-sample Variances

The conventional N-sample variance

$$\widehat{\sigma_y^2} = \frac{1}{N-1} \sum_{i=1}^{N} (y_i - \bar{y})^2, \tag{4.2.5}$$

where y_i are consecutive measurements of the fractional frequency and

$$\bar{y} = \frac{1}{N} \sum_{i=1}^{N} y_i \tag{4.2.6}$$

is the average frequency, is generally unsuitable for assessing frequency stability. This is mainly because N-sample variance fails to converge for certain noise types frequently encountered in frequency sources, such as flicker frequency modulation (FM) noise, and is inadequate for processes exhibiting time-diverging behaviour. A more appropriate approach involves introducing the averaging time τ and evaluating only two frequency samples $N = 2$. This leads to formulating the AVAR, a two-sample modification of the standard variance [155]. The AVAR of the fractional frequency deviation y is defined as

$$\sigma_y^2(\tau) = \mathbb{E}\left\{ \frac{1}{2} \left[\bar{y}_2 - \bar{y}_1 \right]^2 \right\}, \tag{4.2.7}$$

where $\mathbb{E}\{\}$ denotes the expectation value, and $\bar{y_1}$ and $\bar{y_2}$ are average fractional frequencies computed over successive time intervals of duration τ. In practical measurements, the expectation $\mathbb{E}\{\}$ is replaced by a statistical estimator,

$$\widehat{\sigma_y^2} = \frac{1}{2(M-1)} \sum_{k=1}^{M-1} \left[\bar{y}_{k+1} - \bar{y}_k \right]^2, \tag{4.2.8}$$

which averages over $M - 1$ realisations of $\bar{y}_2 - \bar{y}_1$. This estimator requires M contiguous measurements of $\bar{y}$. It is worth noting that even though the Eq. (4.2.8) is the estimation of AVAR, it is common to use it as the definition [156]. The AVAR results presented in this thesis are calculated using such an approach. The direct comparison of standard N-sample variance and AVAR is shown in Figure 4.4. For this purpose, I generated the flicker FM noise [157] and calculated the deviation σ_y using N-sample deviation and non-overlapping two-sample Allan deviation (ADEV). The N-sample deviation changes significantly with the number of samples, while the non-overlapping Allan deviation (ADEV) converges.

A practical and commonly adopted approach to estimating the AVAR involves using overlapping sample pairs, forming overlapping Allan variance (OAVAR) and overlapping Allan deviation (OADEV). This method leverages all possible combinations of data points separated by the averaging time $\tau = m\tau_0$, where m is a positive integer and τ_0 represents the inverse of the sampling frequency. A proof of principle of OADEV is presented in Figure 4.5. Employing overlapping samples enhances the statistical confidence of the stability estimate at the cost of increased computational demand. Although these overlapping intervals are not entirely independent, they contribute more

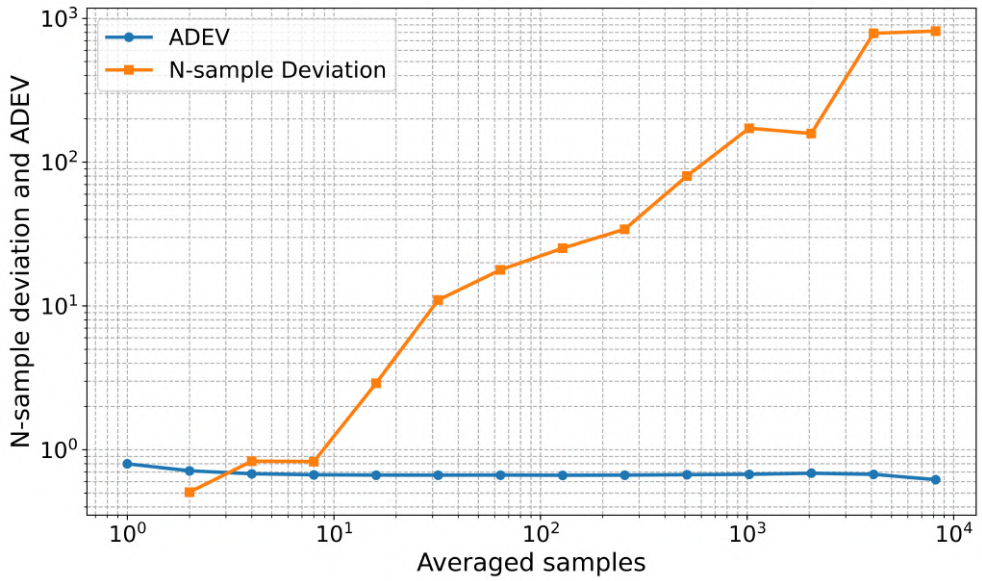

Figure 4.4: Comparison of convergence of the N-sample deviation (orange) and the non-overlapping ADEV (blue) for the generated flicker FM noise.

degrees of freedom. When adopting an estimation-based definition, the OAVAR is expressed as [158]

$$\sigma_y^2(m\tau_0) = \frac{1}{2m^2(M-2m+1)} \sum_{j=1}^{M-2m+1} \left\{ \sum_{i=j}^{j+m-1} (y_{i_m} - y_i) \right\}^2 . \tag{4.2.9}$$

This approach yields a tighter confidence interval than the non-overlapping AVAR. The comparison between the non-overlapping ADEV and the OADEV is shown in Figure 4.6. The deviations are calculated for the generated flicker FM noise. Due to the higher number of degrees of freedom, the OADEV exhibits smaller confidence intervals than the non-overlapping approach.

Due to the definition of the AVAR, it cannot distinguish between white phase noise ($\propto \tau^{-3/2}$) and flicker phase modulation noise ($\propto \tau^{-1}$). The modified Allan variance (MVAR) and modified Allan deviation (MDEV) are capable of doing so due to an additional phase averaging operation [159]

$$\text{Mod}\,\sigma_y^2(m\tau_0) = \frac{1}{2m^4(M-3m+2)} \sum_{j=i}^{M-3m+2} \left\{ \sum_{i=j}^{j+m-1} \left[\sum_{k=i}^{i+m-1} (y_{k+m} - y_k) \right] \right\}^2 . \tag{4.2.10}$$

The difference between OADEV and MDEV is illustrated in Figure 4.7. To generate the plot, I simulated a signal composed of a white phase modulation noise and a flicker

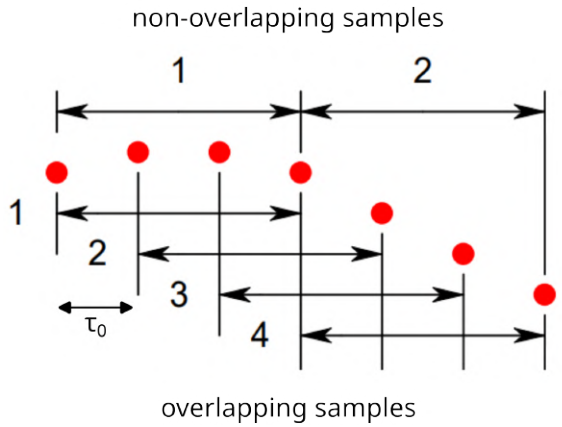

Figure 4.5: Comparison between non-overlapping samples and overlapping samples. The red circles represent the measured frequency sampled in the constant interval τ_0. For the averaging time $\tau = 3\tau_0$, the non-overlapping sampling allows only two points for estimating the AVAR, while the overlapping sampling allows for using four frequency measurements.

phase modulation noise. I then calculated both the OADEV and MDEV for the signal. As shown in the figure, the OADEV (orange curve) maintains a constant slope on the log-log scale and cannot distinguish between the two noise types. In contrast, the MDEV (blue curve) reveals two distinct noise regimes. For short averaging times τ, the steeper slope corresponds to white phase modulation noise, while for longer τ, the curve flattens, indicating the transition to flicker phase modulation noise. To emphasise this, I fitted a function proportional to τ^{-1} (dashed black line) to the last few points of the MDEV. This example demonstrates the advantage of using MDEV when analysing experimental signals containing white PM and flicker phase modulation noise.

Selecting the appropriate type of variance for analysis is not straightforward, especially given other variance types commonly used in noise characterisation, such as Hadamard variance, Total variance, and Parabolic variance [158]. AVAR is generally the preferred method for evaluating $\sigma_y^2(\tau)$ across the full range of τ values, up to $\tau = \mathcal{T}/2$, for a data record lasting $\mathcal{T}$. This scenario is typical for atomic clock time scales, where oscillators are continuously monitored and attention is mainly on slower processes [160]. Conversely, the MVAR becomes more suitable when dealing with wideband noise associated with faster processes. Originating from optics, MVAR was developed to allow precise and efficient measurement of white phase modulation noise. It is also important to mention that due to differences in normalisation, MVAR provides more optimistic noise estimation in comparison to AVAR [149]. This effect is evident in Figure 4.7, where the flicker phase modulation noise ($\propto \tau^{-1}$) appears lower when estimated with MDEV rather than non-modified ADEV.

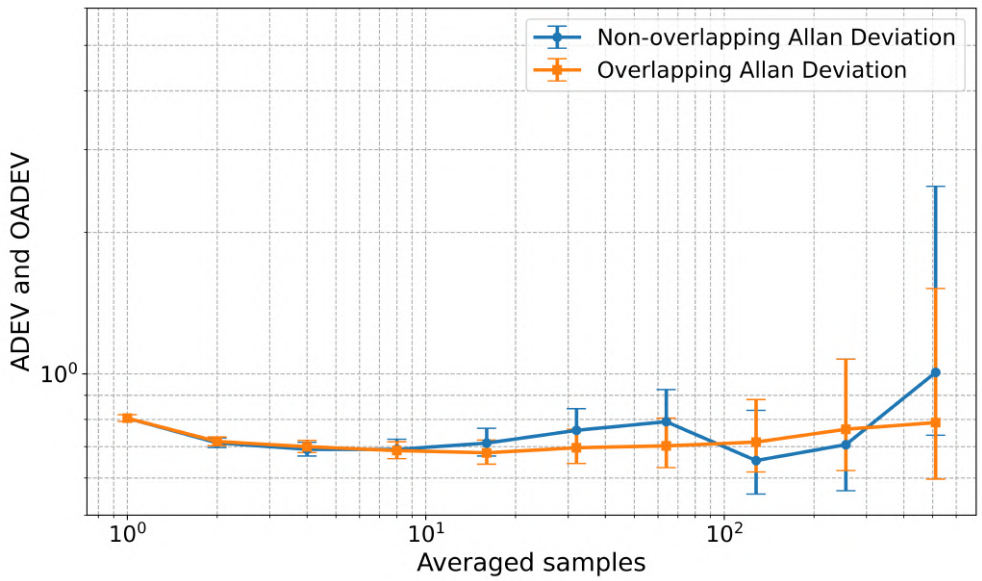

Figure 4.6: Comparison of confidence interval $\pm 1\sigma$ for non-overlapping ADEV (blue) and OADEV (orange). The deviations are calculated for the generated flicker FM noise.

Some oscillators exhibit ageing or linear drift of frequency over time. When estimating the stability of the oscillator, the trend should be calculated and removed before estimating $\sigma_y^2(\tau)$ [155]. This approach is applied in the thesis when analysing the frequency stability of ultra-stable optical cavities.

It is generally insufficient to just calculate a stability statistic such as the Allan deviation and thereby obtain an estimate of its expected value. Any such determination should be accompanied by an indication of the statistical confidence in this estimate, expressed by upper and lower bounds at a specified confidence level. The confidence limits of a variance estimate depend on the variance type, the number of available data points and averaging factor, the chosen statistical confidence factor, and the underlying noise type. A simple approximation to the confidence interval, without considering the noise characteristics, sets the $\pm 1\sigma$ (68.3%) error bars at $\pm\sigma_y(\tau)/\sqrt{N}$, where N is the number of data pairs used in calculating the Allan deviation. Although straightforward, this estimate is often overly optimistic, particularly in the presence of correlated noise processes.

A more rigorous approach is obtained by applying the chi-squared (χ^2) statistic to variance estimators. Chi-squared methods allow one to calculate single- or double-sided confidence intervals at any desired confidence level. These calculations require a determination of the effective number of degrees of freedom (eDOF), which depends on the number of averaging intervals, the degree of data overlap, and the spectral character of the underlying noise.

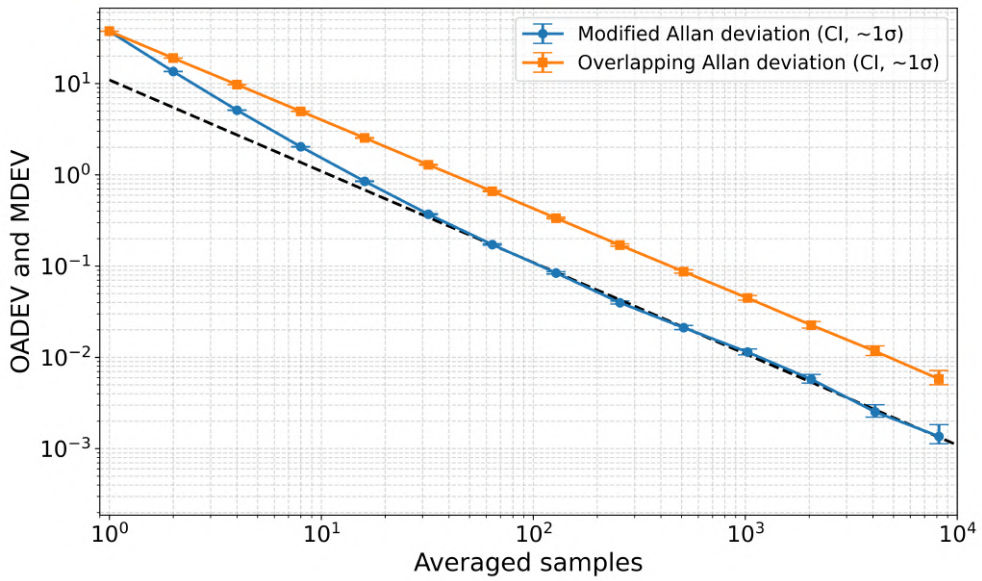

Figure 4.7: Comparison of OADEV (orange) and MDEV (blue). The deviations are calculated for the generated signal characterised by a sum of white phase modulation noise and flicker phase modulation noise. The dashed black line, $\propto \tau^{-1}$, is fit to the latest points of MDEV to show the difference between the white phase modulation noise and the flicker phase modulation noise.

Sample variances are distributed according to

$$\chi^2 = \frac{\text{eDOF} \cdot s^2}{\sigma^2}, \tag{4.2.11}$$

where χ^2 is the chi-squared variable, s^2 is the sample variance, and σ^2 is the true variance. The eDOF encapsulates the statistical efficiency of the estimator, accounting for both the number of available samples and the noise type [145, 158]. The eDOF is therefore the key quantity for determining confidence intervals of Allan-type variances. It is not equal to the raw number of samples, since successive averages are statistically correlated. The eDOF depends on the type of variance estimator, the number of available data points N, the averaging factor $m = \tau/\tau_0$, the degree of overlap, and the power-law noise type.

For overlapping Allan deviation, the eDOF can be determined analytically from Greenhall's expressions based on the generalised autocovariance function [161]. For other estimators, such as the modified Allan deviation or the Hadamard deviation, similar expressions exist. The rigorous use of eDOF together with chi-squared statistics is now the standard method for computing confidence intervals of frequency stability measures.

Once the eDOF has been established, the true variance is bounded by chi-squared statistics. For a sample variance s^2 the double-sided confidence limits are obtained as

$$\sigma^2_{\text{min}} = \frac{\text{eDOF} \cdot s^2}{\chi^2\left(1 - \frac{p}{2},\, \text{eDOF}\right)}, \qquad \sigma^2_{\text{max}} = \frac{\text{eDOF} \cdot s^2}{\chi^2\left(\frac{p}{2},\, \text{eDOF}\right)}, \tag{4.2.12}$$

where $\chi^2(p, \text{eDOF})$ denotes the p-quantile of the chi-squared distribution with eDOF degrees of freedom, and p is the selected confidence level. The confidence interval on the Allan deviation itself is then obtained by taking the square root of these bounds,

$$\sigma_{\text{min}} = \sqrt{\sigma^2_{\text{min}}}, \qquad \sigma_{\text{max}} = \sqrt{\sigma^2_{\text{max}}}. \tag{4.2.13}$$

In practice, the $\pm 1\sigma$ confidence level ($p \approx 68.3\%$) is commonly reported, although higher confidence factors such as 95% or 99% may also be used.

In the present work, these confidence intervals were calculated using the AllanTools Python package[156], which implements Greenhall's eDOF expressions and the chi-squared statistics described above.

4.2.3 Three-Cornered Hat Method and Groslambert Covariance

Determining the frequency stability of an oscillator requires comparing its output to that of one or more reference oscillators. Such a comparison inherently captures the test oscillator's and the reference's instabilities. As a result, measurements typically reflect the combined stability of oscillators, while the goal is often to assess the performance of a single oscillator. One widely used technique for isolating the stability of an individual oscillator is the Three-Cornered Hat (TCH) method, which involves simultaneously comparing the frequencies of three or more independent oscillators [162].

Considering three oscillators, A, B, and C, one can measure three combined variances σ^2_{AB}, σ^2_{AC}, and σ^2_{BC}. Assuming that the oscillators are uncorrelated, each combined variance can be written as a sum of the variances of individual oscillators

$$\sigma^2_{AB} = \sigma^2_A + \sigma^2_B, \tag{4.2.14}$$
$$\sigma^2_{AC} = \sigma^2_A + \sigma^2_C, \tag{4.2.15}$$
$$\sigma^2_{BC} = \sigma^2_B + \sigma^2_C. \tag{4.2.16}$$

These equations can be solved for the variance of the individual oscillator being investigated. For example [163]

$$\sigma^2_A = \frac{1}{2}\left(\sigma^2_{AB} + \sigma^2_{AC} - \sigma^2_{BC}\right). \tag{4.2.17}$$

The TCH method can help compare the stability of units with similar performance levels. However, it may yield negative variance when applied to units with significantly

different stabilities, correlated units, or insufficient available data. Therefore, this method should be applied carefully and not be seen as a replacement for a low-noise reference. It works best when used to evaluate units with comparable stability, helping to identify the superior one. The appearance of negative variances indicates that the method breaks down, typically due to limited measurement data, stability differences or correlations between the units. Such issues are more likely to occur at longer averaging times. If the TCH method fails, an approach proposed by Groslambert can be used [164]. It is based on the two-sample covariance, typically called Allan Covariance or Groslambert Covariance (GCOV). The GCOV method offers an alternative way of assessing the stability of individual oscillators by exploiting the covariance between successive frequency measurements. Unlike the TCH method, which estimates variances through combinations of measured variances, the Groslambert approach directly calculates a two-sample covariance between oscillators. A key advantage of this method is its ability to eliminate biases introduced by measurement noise, especially white and flicker phase noise originating from the measurement instrumentation. By construction, the GCOV does not square the measurement noise, which otherwise introduces positive biases into the variance estimations when using the TCH.

For two oscillators A and B, the GCOV is defined as [165]

$$\mathrm{GCOV}_{A,B}(\tau) = \frac{1}{2}\mathbb{E}\left[z_A z_B\right], \tag{4.2.18}$$

where z_A and z_B represent the time-differential frequency fluctuations of oscillators A and B, respectively. This definition requires synchronous measurements of the involved signals. Importantly, when applying the GCOV method, the variance of an oscillator, say B, can be retrieved through a combination of cross-covariances [166]

$$\sigma_B^2(\tau) = -\mathrm{GCOV}_{AB,BC}(\tau), \tag{4.2.19}$$

where AB and BC denote the beat measurements between oscillators A and B, and B and C, respectively.

One of the significant strengths of the GCOV method is its immunity to measurement noise. This property makes the technique particularly powerful when dealing with ultra-stable oscillators, where the measurement noise can dominate at short averaging times. Consequently, GCOV is especially beneficial when measuring stability at very short integration times (below 1 second), where classical methods like the TCH would suffer from high bias and increased uncertainty.

Nonetheless, the GCOV method also has limitations. It demands strict synchronisation between the measurement channels, which may not always be feasible, especially in older or less sophisticated measurement systems. Furthermore, at longer averaging times, where the measurement noise becomes negligible compared to the oscillator noise, the advantages of GCOV diminish, and its results converge to those obtained using the TCH.

4.2.4 Frequency Counters

Frequency counters are widely utilised instruments for measuring the stability of oscillators. The internal measurement principle significantly influences the output data and thus must be carefully considered during stability analysis. Two principal types of frequency counters are commonly encountered: the Π-type and the Λ-type counters [158, 167]. The average relative frequency $\bar{y}(\tau)$ measured by the counter during the averaging time τ can be defined as

$$\bar{y}(\tau) = \int_0^\infty y(t) w(t;\tau) dt, \tag{4.2.20}$$

where $w(t;\tau)$ is the weighting function related to the counter type.

A Π-counter operates by counting the number of zero crossings over a fixed gate time τ, corresponding to a uniform rectangular time window. The measured fractional frequency $\bar{y}(t)$ is obtained by simple integration over the gate interval [168]

$$\bar{y}(\tau) = \frac{1}{\tau} \int_0^\infty y(t) dt. \tag{4.2.21}$$

The associated weighting function, $w_\Pi(t;\tau)$, is a rectangular function:

$$w_\Pi(t;\tau) = \begin{cases} \frac{1}{\tau}, & 0 \le t < \tau, \\ 0, & \text{otherwise.} \end{cases} \tag{4.2.22}$$

This leads to a low-pass filtering effect on the measured signal. Consequently, Π-counters offer good sensitivity to long-term fluctuations but perform poorly when capturing high-frequency noise such as white or flicker phase modulation [169].

In contrast, the Λ-counter improves upon this principle by using overlapping gate intervals and measuring phase differences continuously. The weighting function in a Λ-counter has a triangular shape

$$w_\Lambda(t;\tau) = \begin{cases} \frac{2t}{\tau^2}, & 0 \le t < \frac{\tau}{2}, \\ \frac{2(\tau - t)}{\tau^2}, & \frac{\tau}{2} \le t < \tau, \\ 0, & \text{otherwise.} \end{cases} \tag{4.2.23}$$

This smoother transition reduces the impact of wideband noise and enhances sensitivity to fast phase variations. In particular, the response to white phase noise decreases as $\tau^{-3/2}$ for a Λ-counter, while it decreases only as τ^{-1} for a Π-counter [170]. An additional factor to consider is the dead time between measurements. Traditional Π-counters often introduce dead time, which can bias the variance estimation and especially degrade the evaluation of short-term stability. In contrast, Λ-counters typically

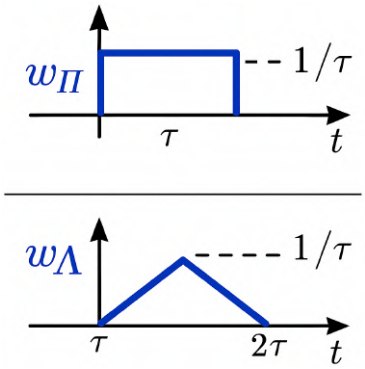

Figure 4.8: Weighting functions for the Π-counter (rectangular) and Λ-counter (triangular).

operate with overlapping measurements and minimal or zero dead time, improving stability analyses' reliability [159].

Moreover, it is crucial to recognise the limitations introduced by the internal timebase of the counter. The internal reference clock's phase noise and frequency instability add directly to the measured signal. Therefore, high-precision measurements require the counter to be synchronised to an external reference of superior stability. Failure to do so results in apparent degradation of the device under test, masking its true performance [169].

Modern frequency counters like the K+K FXE65 offer selectable measurement modes that switch between Π- and Λ-type operations [171].

Chapter 5

Experimental Setup at National Laboratory FAMO

Within this chapter, I present the experimental infrastructure that I developed and implemented at the National Laboratory FAMO for high-precision spectroscopy of the Hg clock transition. I begin with a description of the vacuum apparatus, which provides UHV conditions for the co-trapping of Hg and rubidium (Rb) atoms. I outline the operation of the Hg source and the main science chamber, which form the basis of the experimental system.

I then describe the laser systems required for cooling and trapping Hg atoms at 253.7 nm, including the generation of the UV light through frequency conversion and its stabilisation to an OFC. In the following section, I present the ultra-stable optical reference based on a FP interferometer, detailing its mechanical design, thermal stabilisation, and characterisation.

I then introduce the laser setup for $^1S_0 - {}^3P_0$ spectroscopy at 265.6 nm, explaining the referencing scheme to the optical reference, the implementation of FNC, the amplifier stage, and the frequency conversion chain. I also describe how I evaluated the frequency stability of this system.

In the later sections, I present the repumping laser systems I constructed to deplete atoms from the metastable states, including the digital frequency stabilisation scheme and the design of custom extended-cavity diode lasers (ECDLs). Finally, I outline my design and implementation strategy for the optical lattice at the magic wavelength, together with the new vacuum chamber and magnetic field coils that I developed to accommodate it. These elements together form the technical foundation for my attempt to realise a Hg optical lattice clock in our laboratory.

5.1 Vacuum System and Mercury Source

Our vacuum system allows for experiments with ultra-cold Hg and Rb atoms, a feature which makes it unique. The vacuum setup, presented in Figure 5.1, consists of three parts: the Hg source, the Rb source with the Zeeman slower, and the main scientific chamber, where the two species can be collocated and trapped in a MOT or a dipole trap. The vacuum system was extensively described in [172]. Hence, I will only briefly describe the Hg part.

The Hg part of the vacuum system contains a reservoir with Hg atoms cooled to $-30\,^{\circ}\mathrm{C}$, a cubic chamber, and two gate valves. During the experiment only, the temperature of the Hg source is raised to $-8\,^{\circ}\mathrm{C}$ to increase the vapour pressure of Hg. This reservoir is isolated from the main scientific chamber by a pneumatically actuated gate valve. The valve is opened only during the experiment, which allows for the maintenance of the UHV in the main chamber.

The main chamber is equipped with a 150 l/s ion-sublimation pump. The filaments of the sublimation pump are periodically activated to refresh the titanium layer inside the pump. Active residual gases are permanently bound to the freshly deposited titanium surface.

Differential pumping is implemented between the main chamber and the Hg source. A copper tube with a length of 25 mm and an internal diameter of 1.5 mm is used. The inner side of the tube is conical and coated with a gold layer. The conical surface has a stepped profile, which increases the effective pumping area. Mercury and gold form an amalgam, which allows hot Hg atoms to bind to the gold-coated surface. The cubic chamber between the Hg reservoir and the main chamber is used for optical access for the source diagnostics. The spectroscopy of the Hg vapour enables estimation of the source performance and can indicate the necessity of Hg droplet replacement. The chamber could also be used for a 2D MOT for the atomic beam collimation.

5.1.1 Mercury Source

The source consists of a droplet of Hg stored inside a copper reservoir. The reservoir is cooled to suppress the high vapour pressure of Hg. The cooling system consists of two thermoelectric coolers (TECs) and a glycol-based coolant, maintained at $-18\,^{\circ}\mathrm{C}$ and circulated by a chiller[1]. The temperature of the reservoir is measured using a PT100 resistive sensor.

The reservoir is mounted at the bottom of a six-way cross vacuum chamber. Two of the arms are sealed with CF 35 viewports. The top viewport allows visual inspection of the Hg content inside the reservoir, as shown in Figure 5.2. The side window can be used for optical access for the pushing beam used in the 2D MOT.

[1] Bolid Piccolo

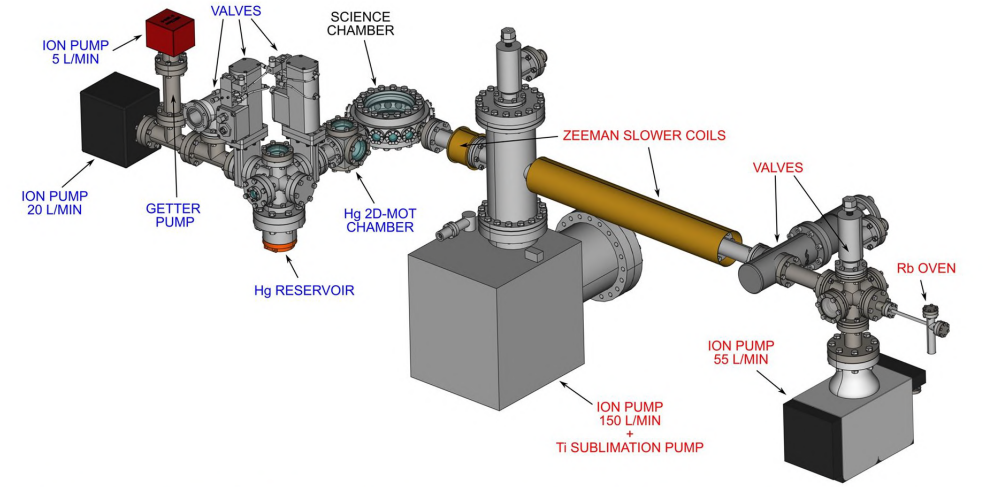

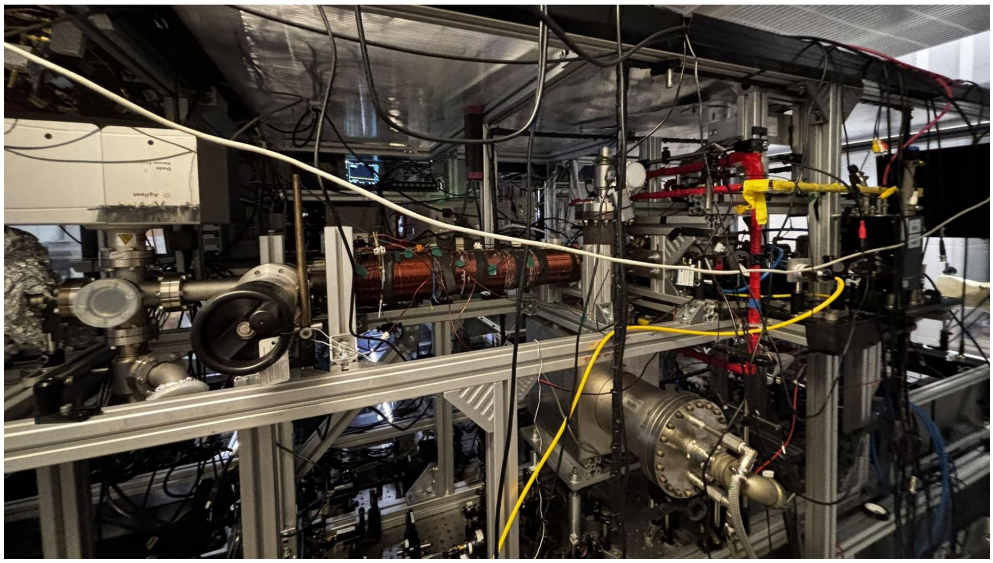

Figure 5.1: **Top:** CAD model of the vacuum system. The vacuum setup consists of three parts: the Hg source, the Rb source with the Zeeman slower, and a main science chamber, labelled in blue, red, and black, respectively. **Bottom:** Photograph of the actual vacuum system. The Rb source is visible on the left and the main science chamber on the right, while the Hg source is hidden behind the main chamber.

The remaining two arms of the six-way chamber are connected to vacuum valves. The first gate valve connects to two T-cross chambers housing a 20 l/s ion-pump[2], a 5 l/s ion-getter pump[3], and a turbo-molecular pump line. The ion pumps maintain a

[2]Agilent Technologies StarCell 20
[3]SAES NEXTorr D 200-5

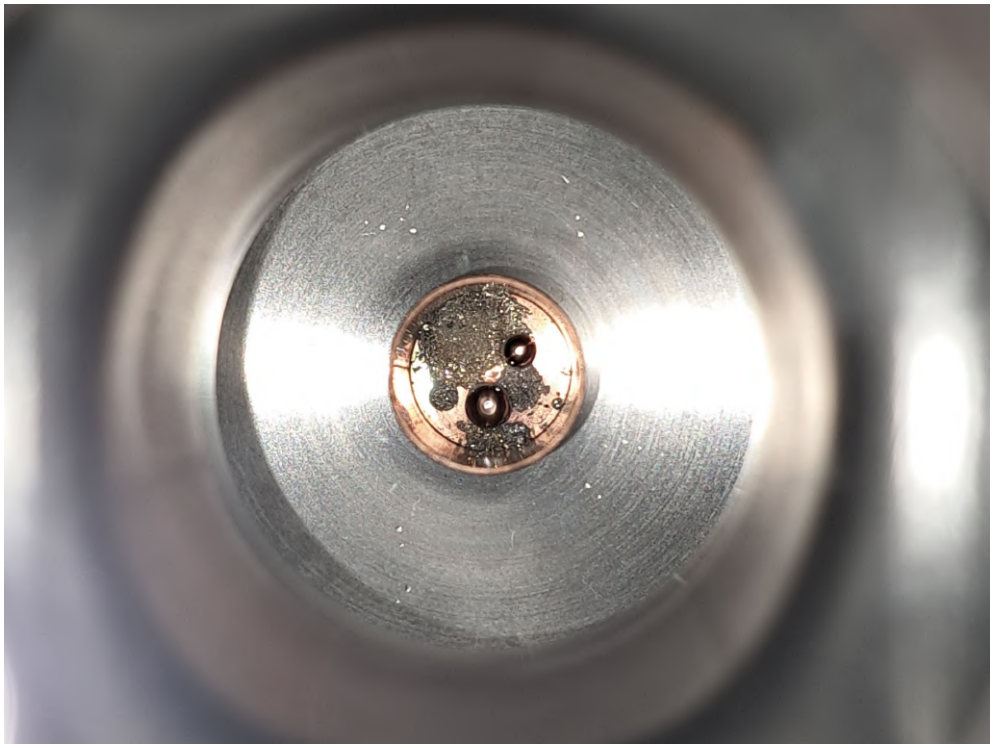

Figure 5.2: Picture of the Hg droplet inside the copper reservoir after refill. The amalgam surrounds two fresh Hg droplets. Photo taken from above using the top viewport.

pressure of 10^{-6} mbar in the reservoir. The second gate valve is connected to a cubic chamber, which is opened during the experiment.

As seen in Figure 5.2, the Hg droplet has formed an amalgam with the reservoir. This amalgamation alters the surface interaction with the fresh Hg and reduces the time between refills. A new Hg source is currently being developed by Matej Veis and Jacek Pyszka and tested in a different experimental setup built by me in the past. The new design is based on a 4-stage TEC[4], which allows cooling the reservoir below -80 °C with a coolant temperature of 19 °C.

Although I did not take part in the construction of the Hg reservoir, I include this section to clarify its operation and to highlight the limitations that have motivated the redesign.

[4]Laird Thermal Systems 9340005-304

5.1.2 Main Scientific Chamber

The main vacuum chamber is connected to a four-way cross equipped with an ion-sublimation pump[5]. The ion pump has a pumping speed of 150 l/s, allowing the system to reach pressures as low as 10^{-9} mbar. The manual valve is connected to the top flange, which allows the turbo-molecular pump to be connected for vacuum recovery.

Within the main vacuum chamber, Hg and Rb atoms can be collocated and trapped in the MOT or the dipole trap, allowing for various experiments, including collisional studies or Hg-Rb photo-association.

The main vacuum chamber is a regular hexadecagon made of stainless steel[6]. The chamber provides optical access via fourteen CF 16 viewports with various anti-reflection coatings, and two CF 160 viewports with anti-reflection coatings designed for 253.7 nm and 780 nm. The CF 16 viewports are used for Hg horizontal MOT beams, Rb horizontal MOT beams, Zeeman slower beams, imaging beams, and a dipole beam. The CF 160 viewports are used for the Hg vertical MOT beam, the Rb vertical MOT beam, a photo-association beam, and a beam resonant to $^1S_0 - {}^3P_1$ transition in Hg overlapped with a beam resonant to a clock $^1S_0 - {}^3P_0$ transition. The $^1S_0 - {}^3P_1$ beam is used as a guide beam for a clock beam. Due to a low transmission of a CF 160 viewports for a 363 nm light, below 80% of total transmission through the chamber, the current configuration does not allow for implementing the optical lattice with enough power enhancement. Also, installing the lattice mirrors inside the current main vacuum chamber is impossible. Hence, I designed a new vacuum chamber tailored for the optical lattice for Hg. More about the new vacuum chamber in Section 5.6.3.

5.2 Laser System for Hg Magneto-Optical Trap

The ability to laser-cool and trap neutral Hg atoms relies on a stable and narrow-linewidth light source at 253.7 nm, resonant with the $^1S_0$– $^3P_1$ transition. This section presents the laser system developed for this task. In the first subsection, I present the optical setup used to generate and distribute the 253.7 nm light. I outline the frequency conversion process based on frequency quadrupling of fundamental light at 1014.8 nm, including successive second-harmonic generation (SHG) stages, frequency shifting using acousto-optic modulators (AOMs), and preparing multiple UV beams. These beams serve different roles within the experiment: laser cooling, saturated absorption spectroscopy, and spatial alignment of the clock transition probe beam.

In the second subsection, I detail the method used to stabilise the frequency of the fundamental laser to an OFC referenced to an ultra-stable 1542 nm cavity. I explain the beatnote detection scheme, signal processing, and feedback control using a PI^{3}D

[5] Agilent Technologies Noble Diode 150

[6] Kimball Physics MCF600-SphHexadecagon-F2A16

servo. I also describe how I characterised the performance of the frequency servo loop by measuring the beatnote spectrum and plotting the ADEV.

5.2.1 Optical Setup for Hg Laser-trapping

Laser cooling and trapping of Hg atoms in a MOT require a stable light at 253.7 nm. A schematic representation of the complete optical setup used for this purpose is shown in Figure 5.3.

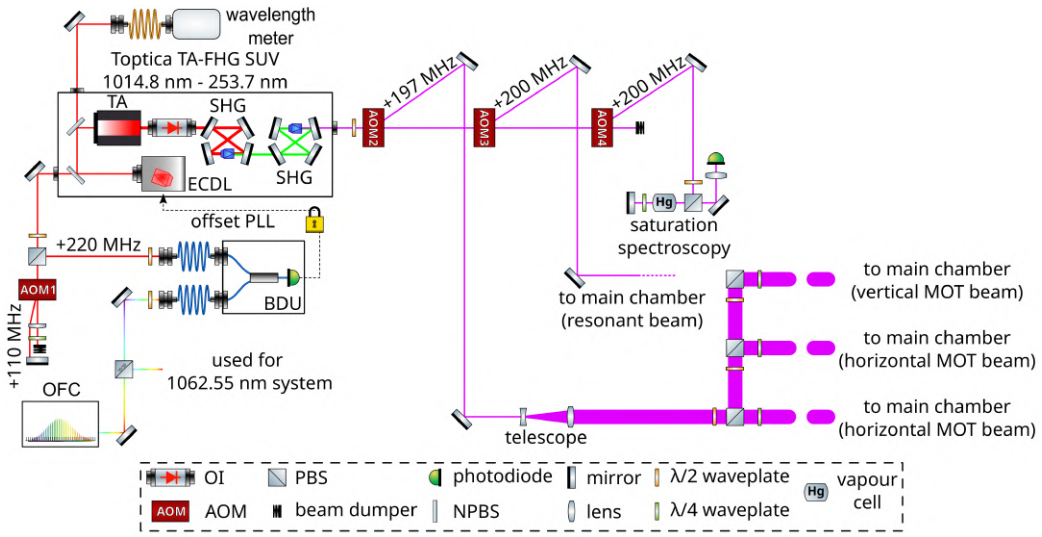

Figure 5.3: Schematic of the laser system used for the generation of 253.7 nm light for the cooling and trapping of Hg atoms. The laser frequency is stabilised via optical beat detection to an OFC.

The UV light at 253.7 nm is produced by a commercial system[7], based on frequency quadrupling of near-infrared radiation at 1014.8 nm, referred to as the fundamental light. The fundamental light is initially generated by an ECDL, and amplified to a power level of approximately 2 W using a tapered amplifier (TA). The fundamental light is injected into a bow-tie enhancement cavity with a Lithium Triborate crystal, stabilised at a temperature of 47 °C. This stage utilises SHG at 507.4 nm, with an optical conversion efficiency of nearly 100%. Efficient phase matching is achieved through careful alignment of the cavity mirrors and optimisation of the input coupling.

The optical cavity is locked to the frequency of the fundamental light using the PDH technique. The phase modulation required for PDH locking is realised via high-frequency modulation of the diode laser current, producing sidebands. Cavity length

[7] Toptica TA-FHG SUV

stabilisation is accomplished using a piezoelectric transducer (PZT) attached to one of the mirrors.

The 507.4 nm light is coupled into a second bow-tie cavity, containing a non-linear crystal held at 41 °C. Although the crystal type remains unspecified, the cavity operates under conditions analogous to the first doubling stage, including phase matching and PDH-based length stabilisation. This final stage generates up to 100 mW of UV light at 253.7 nm. While the system was originally capable of producing over 200 mW of UV power, its output power has decreased over time due to the harmful effects of prolonged UV exposure on the optical components.

The UV light at 253.7 nm is divided into three separate optical paths using AOMs[8], operating as frequency shifters. These components, labelled AOM2–AOM4 in Figure 5.3, were installed and aligned by Archita Sahu, Indrajit Nandi, Marcin Witkowski, and me. AOM4 shifts the frequency of the UV beam by 200 MHz and directs it towards a saturated absorption spectroscopy setup. This arm is used to manually fine-tune the laser frequency to resonance with the $^1S_0 - {}^3P_1$ transition by means of Doppler-free spectroscopy on thermal Hg vapour. The spectroscopy signal is detected using an avalanche photodiode[9]. I constructed the saturation spectroscopy setup myself.

AOM2 shifts the frequency of the laser output beam by 197 MHz, resulting in a red-detuning of 3 MHz relative to the $^1S_0 - {}^3P_1$ transition. This beam is directed into a Galilean telescope, which expands the beam diameter to approximately 10 mm, appropriate for the MOT. After expansion, the beam is split into three power-balanced arms to serve as the vertical and horizontal MOT beams. This part of the optical setup, including the telescope and beam-splitting arrangement, was assembled by Archita Sahu, Indrajit Nandi, and Marcin Witkowski.

The third modulator, AOM3, extracts a low-power portion of the UV light to produce a beam resonant with the $^1S_0 - {}^3P_1$ transition. This beam is used as a spatial reference to align the $^1S_0 - {}^3P_0$ clock transition probe beam, ensuring co-propagation and overlap within the atomic sample. The resonant reference beam was prepared by Matej Veis, while I performed the alignment of the clock transition probe beam myself.

The AOMs used in the setup are based on UV-grade fused silica crystals and exhibit single-pass diffraction efficiencies exceeding 90% when operated with *p*-polarised light, that is, light polarised in the plane of incidence. According to the data sheet, the efficiency for *s*-polarised light is significantly lower, making double-pass configurations based on polarising beam splitters (PBSs) inherently inefficient. In such arrangements, where the incident and diffracted beams are orthogonally polarised and separated via a PBS, the overall diffraction efficiency drops below 25%.

While higher efficiency could be achieved using alternative separation schemes, such as knife-edge mirrors, these approaches demand substantially longer optical paths, which

[8] AA Opto-Electronic MQ200-A1.5-244.300-Br

[9] Thorlabs APD430A2/M

would complicate the layout and stability of the system. Consequently, all AOMs are operated in single-pass configurations. When the RF driving signal is altered, corresponding changes in beam direction are compensated by readjusting the optical path using steering mirrors and guiding irises.

The laser system provides access to two low-power outputs of the fundamental light at 1014.8 nm. One of these beams is frequency-shifted by 220 MHz using AOM1, as indicated in Figure 5.3, configured in a double-pass arrangement. The frequency-shifted beam is coupled into a polarisation-maintaining (PM) optical fibre and directed to a fibre-coupled beatnote detection unit (BDU). The half-wave plate in front of the PM fibre is used for polarisation alignment with the fibre's polarisation axis. I assembled and aligned the double-pass AOM configuration myself, while the injection into the PM fibre was performed by Marcin Witkowski.

The second input of the BDU is seeded by light from an OFC, also delivered via a PM fibre. The OFC is located in a different part of the building. The fibre connecting the OFC and the laboratory is 200 m long. The OFC is stabilised to an ultra-stable optical reference cavity operating at 1542 nm and acts as a transfer oscillator, allowing the frequency stability of the optical reference to be transferred to the 1014.8 nm laser system. The OFC and the 1542 nm ultra-stable laser are part of a project conducted by Marcin Bober and Piotr Morzyński. I personally performed the mode-matching of the OFC beam and injected it into the PM fibre.

The OFC is based on a phase-stabilised femtosecond laser whose spectrum comprises evenly spaced modes, commonly referred to as *teeth*. The frequencies of the OFC modes are described by

$$f = f_{\mathrm{CEO}} + n f_{\mathrm{rep}}, \tag{5.2.1}$$

where f_{CEO} denotes the carrier-envelope offset frequency, f_{rep} is the pulse repetition frequency, and n is an integer representing the mode number. The repetition frequency, f_{rep}, can be phase-locked either to a RF reference or to an optical reference, such as an ultra-stable laser locked to a high-finesse cavity. The offset frequency, f_{CEO}, is stabilised using frequency-doubling techniques combined with f–$2f$ self-referencing interferometry.

The BDU measures the frequency difference, f_{beat}, between the optical frequencies of the two input beams. In the present setup, the repetition rate of the OFC is stabilised to 250 MHz. Consequently, the beatnote signal lies within the RF signal range of DC to 125 MHz. This electronic signal can be used to stabilise the fundamental light frequency arbitrarily.

The optical frequency of the fundamental light at 1014.8 nm can be expressed as

$$f_{1014.8\,\mathrm{nm}} = f_{\mathrm{CEO}} + n f_{\mathrm{rep}} \pm f_{\mathrm{beat}} - 2 f_{\mathrm{AOM1}}, \tag{5.2.2}$$

where f_{AOM1} is the frequency of RF signal driving the AOM1, which operates in a double-pass configuration as shown in Figure 5.3. The sign of $\pm f_{\mathrm{beat}}$ has to be deter-

mined experimentally, e.g. by changing the AOM1 frequency and observing whether the f_{beat} rises or decreases.

The second low-power beam of the fundamental light is delivered to a wavelength meter[10] via a multimode optical fibre. The wavelength meter provides a coarse estimate of the laser frequency, which is sufficient either for initial alignment or for determining the OFC mode number n.

The OFC mode number can be obtained by rounding to the nearest integer

$$n = \left\lfloor \frac{f_{\text{WM}} - f_{\text{CEO}} \mp f_{\text{beat}} + 2f_{\text{AOM1}}}{f_{\text{rep}}} \right\rceil , \tag{5.2.3}$$

where f_{WM} is the optical frequency measured by the wavelength meter.

To unambiguously identify the mode number n, the wavelength meter uncertainty must be smaller than half the OFC modes spacing.

5.2.2 Laser Frequency Stabilisation to Optical Frequency Comb

Historically, lasers were stabilised either directly to atomic transitions using spectroscopic techniques [173–175] or indirectly by referencing them to other lasers with better frequency stability. In such cases, the reference laser had to operate at a frequency sufficiently close, typically within a few gigahertz, to the target laser in order for the frequency difference to be manageable by the servo loop electronics.

When the two lasers operated at significantly different wavelengths, frequency stability could still be transferred using an optical transfer cavity. In this method, the length of a high-finesse optical cavity is actively stabilised to the reference laser using a PZT attached to one of the cavity mirrors. The target laser is then referenced to the same cavity. This approach, however, demands custom-designed cavity mirrors with high reflectivity at both wavelengths involved, making it experimentally complex and wavelength-specific.

The advent of OFCs, a breakthrough recognised with the 2005 Nobel Prize in Physics [176, 177], has revolutionised this process. OFCs allow for robust and broadband transfer of frequency stability between lasers across a wide spectral range.

The OFC employed in this work was referenced to an ultra-stable fibre laser[11] operating at 1542 nm. This fibre laser was, in turn, referenced to an ultra-stable optical cavity that ensures short-term stability. Long-term frequency drift was actively compensated by comparing the OFC repetition rate to a 10 MHz reference signal derived from UTC (AOS) [178–180].

Using this setup, the frequency stability of the ultra-stable laser is transferred to the 1014.8 nm fundamental light used for the generation of 253.7 nm radiation. The

[10] HighFinesse WS7-60

[11] NKT Adjustik

transfer is achieved via optical heterodyne detection. A beatnote between the referenced laser and the nearest OFC mode is generated, and it lies within the RF range. This RF signal is electronically filtered, amplified, and phase-compared to a stable local oscillator (LO). The resulting phase difference provides an error signal that is fed into a feedback servo loop, which stabilises the laser frequency accordingly. The electronic scheme used to reference the 1014.8 nm laser to the OFC is shown in Figure 5.4. The system was originally installed by Marcin Witkowski and later modified and optimised by me.

The beatnote signal is detected using a fibre-coupled commercial BDU[12]. This signal contains the optical frequency difference between the referenced laser and the spectrally closest OFC mode, as well as the 250 MHz signal corresponding to the repetition rate f_{rep}, and spurious components that must be filtered out.

A portion of the filtered signal is tapped by a directional coupler for spectrum analysis. When unused, the coupler output is terminated with a 50 Ω load. The main RF path continues to a level 7 double-balanced mixer. An arbitrary function generator[13], referenced to UTC (AOS), produces a 7 dBm LO signal for the mixer. The mixer shifts the beatnote frequency to match the passband of a narrow bandpass filter centred at 21.5 MHz, which precedes the phase detector. The LO frequency is chosen to satisfy the condition

$$f_{\text{LO}} = \left| f_{\text{beat}} \pm 21.5\,\text{MHz} \right| . \tag{5.2.4}$$

In practice, we fine-tune LO frequency during the optimisation of the MOT.

The frequency-shifted beatnote is then amplified, filtered, and split into two paths. One path is monitored on a spectrum analyser, while the other is directed to a digital phase detector[14] based on field-programmable gate arrays (FPGA). These detectors can track phase differences up to $\pm 256\ \pi$, which provides a broad capture range suitable for locking systems with significant phase changes.

Digital phase detectors are available in at least two distinct architectures. The simpler variant operates by counting zero-crossings of the rectified input signals, incrementing on one channel and decrementing on the other, thereby extracting the phase difference. A more advanced implementation digitises the analogue inputs and computes the phase and amplitude using the CORDIC algorithm [181–183]. Regardless of the specific type, digital phase detectors require highly filtered input signals to function reliably.

The 21.5 MHz reference signal for the phase detector (0 dBm) is also generated using an arbitrary function generator[15] referenced to UTC (AOS). The analogue output of the phase detector serves as the error signal for the feedback loop.

For frequency stabilisation, I implemented a servo loop based on a PI^{3}D controller[16].

[12] Menlo Systems BDU-FF
[13] Rigol DG4102
[14] Mode-Locked Technology
[15] Rigol 4102
[16] Toptica FALC 110

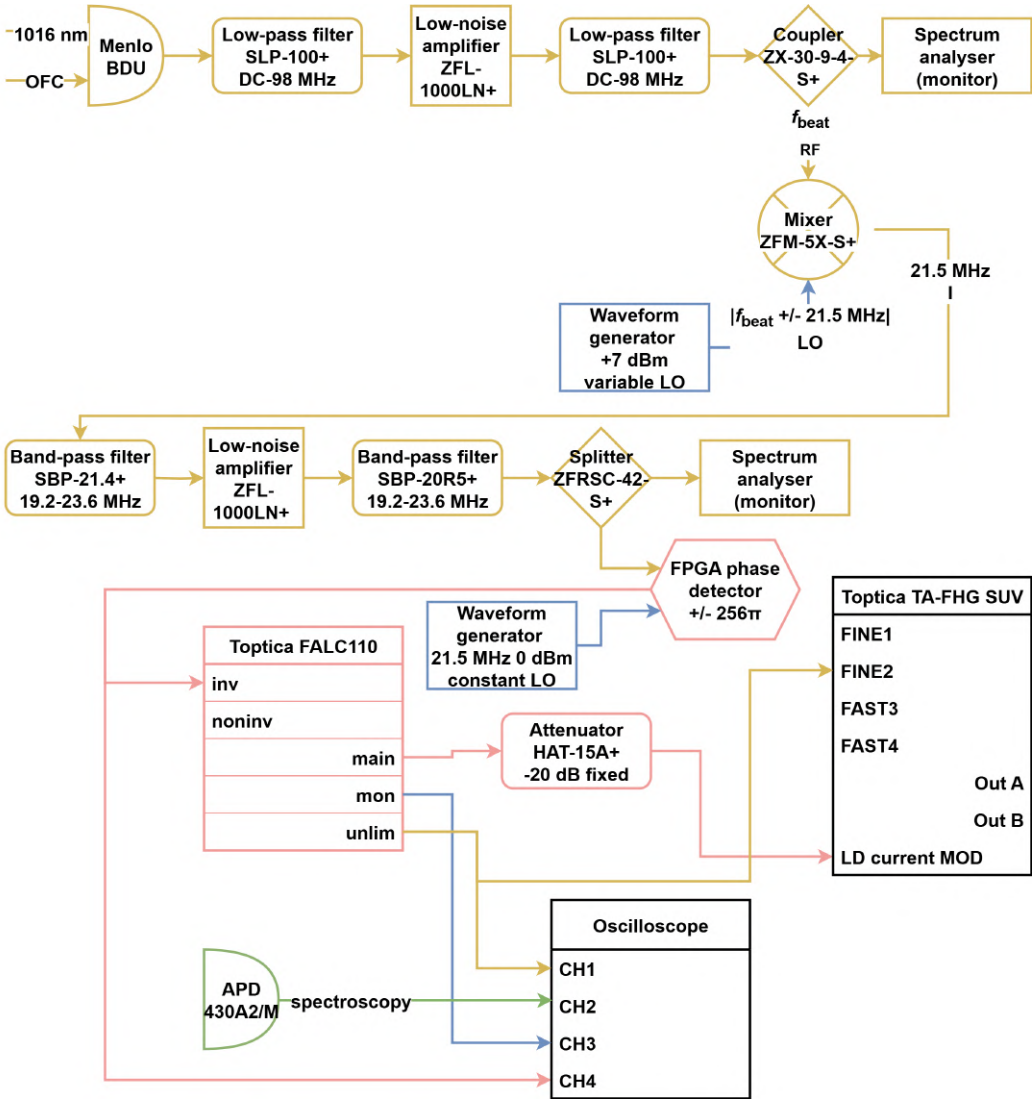

Figure 5.4: Schematic of the electronic setup used to reference the 1014.8 nm laser to the OFC. The beatnote between the laser and the nearest OFC mode is detected, mixed with a LO, and filtered before entering a digital phase detector. The resulting error signal is processed by a Toptica FALC 110 PI^{3}D controller, which drives the diode laser current (fast path) and PZT (slow path). Coloured blocks indicate signal paths: yellow for input signal processing, blue for LOs, and pink for the feedback loop.

The fast output is used to modulate the current of the 1014.8 nm laser diode, while the slow output controls the PZT of the ECDL, enabling coarse frequency stabilisation.

The optimisation of the PI^{3}D controller gain parameters was performed based on the spectral characteristics of the controller's main output. During this procedure, I ex-

perimentally adjusted the parameters to shift the servo bump towards higher frequencies, which is an indicator of increased servo-loop bandwidth. To adjust the main gain, I minimised the phase detector output signal peak-to-peak value observed on the oscilloscope. As a result, I achieved a servo bandwidth exceeding 350 kHz. The spectra of both the controller's main output and the optical beatnote signal, recorded using a spectrum analyser, are shown in Figure 5.5.

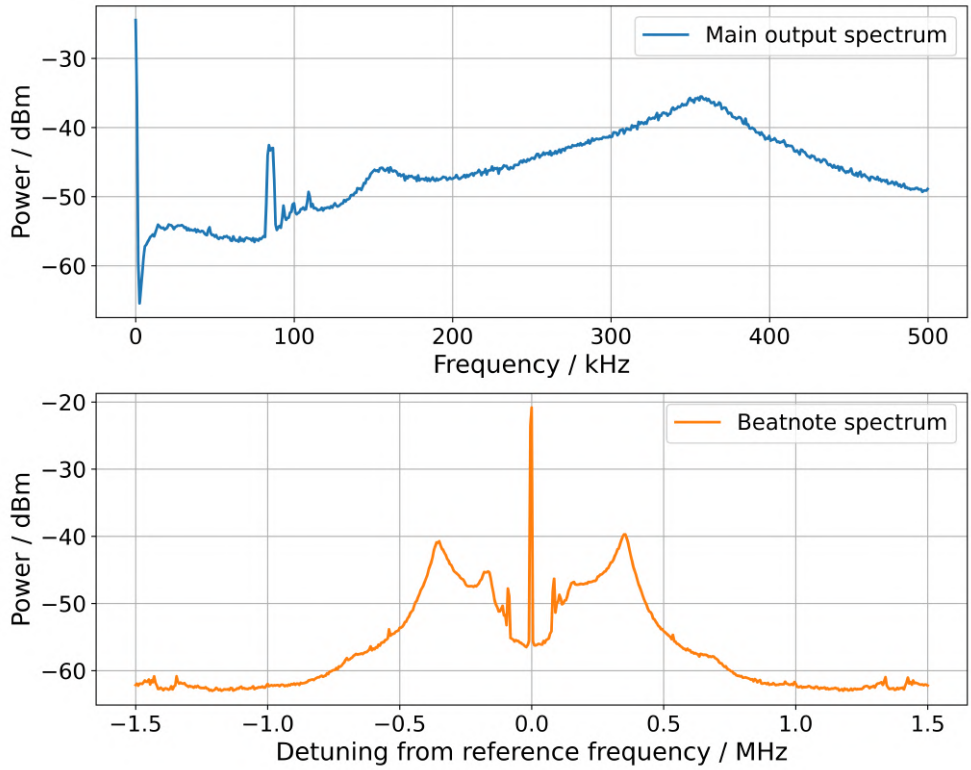

Figure 5.5: Spectral measurements of the servo controller's main output (upper trace) and the optical frequency beatnote signal (lower trace), recorded using a spectrum analyser. The spectrum of the controller output exhibits a servo bump at 356 kHz, corresponding to the bandwidth of the feedback loop. The optical beatnote shows a narrow spectral peak near the reference frequency, surrounded by a suppression dip, indicating that the laser spectrum is being compressed within a narrower frequency range.

To evaluate the frequency stability of the 1014.8 nm laser, I measured the stability of the beatnote signal and calculated the non-overlapping ADEV σ_y, as plotted in Figure 5.6.

For these measurements, I compared the beatnote signal to a reference 10 MHz signal derived from UTC (AOS), which I assumed to be much more stable. This assumption enabled me to extract the stability characteristics of the 1014.8 nm laser without

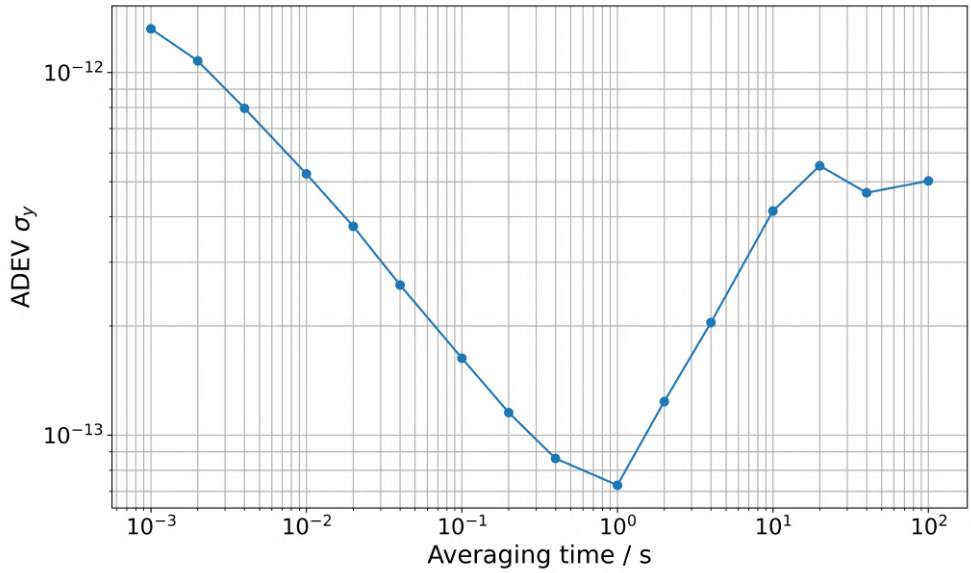

Figure 5.6: Non-overlapping ADEV of the optical beatnote signal between the 1014.8 nm laser and the OFC. The measurement was performed using a commercial phase-noise analyser referenced to UTC (AOS), enabling evaluation of the frequency stability of the laser. The phase-noise analyser does not provide confidence intervals.

requiring more complex techniques such as the TCH method or GCOV analysis.

It is important to note, however, that this measurement does not account for phase noise introduced by the 200 m-long optical fibre connecting the OFC to the laboratory. Since no optical reference is present at the remote end, fibre-induced noise is not visible in the current detection scheme. Based on measurements performed on the $^1S_0 - {}^3P_0$ transition probe laser, I estimate that the fibre-induced instability does not exceed 1×10^{-15} at 1 s of the averaging time. A detailed discussion of fibre-induced noise is provided in Section 5.4.1.

5.3 Ultra-stable Optical Reference

In this section, I discuss the design, construction, and characterisation of the ultra-stable reference system based on a FP cavity. The system serves as a frequency reference for stabilising a narrow-linewidth laser operating near 1062.55 nm, a wavelength corresponding to the optical clock transitions in Hg before the frequency quadrupling.

I begin by describing the mechanical design of the FP cavity, with particular attention paid to reducing sensitivity to environmental vibrations and thermal fluctuations. I then detail the implementation of the UHV system, which ensures long-term stability

of the refractive index inside the cavity. I also discuss the thermal shielding and active temperature stabilisation techniques developed to suppress cavity length variations due to thermal expansion. Next subsections are devoted to the vibration and acoustic isolation systems I developed to attenuate external disturbances. I then present the experimental determination of the cavity's zero-crossing temperature and evaluate the cavity finesse using the cavity ring-down method.

5.3.1 Ultra-stable Optical Cavity Mechanical Design

The optical reference system is based on a notched FP cavity with a spacer made of ultra-low expansion (ULE) glass (Figure 5.7). The cylindrical spacer has a length of

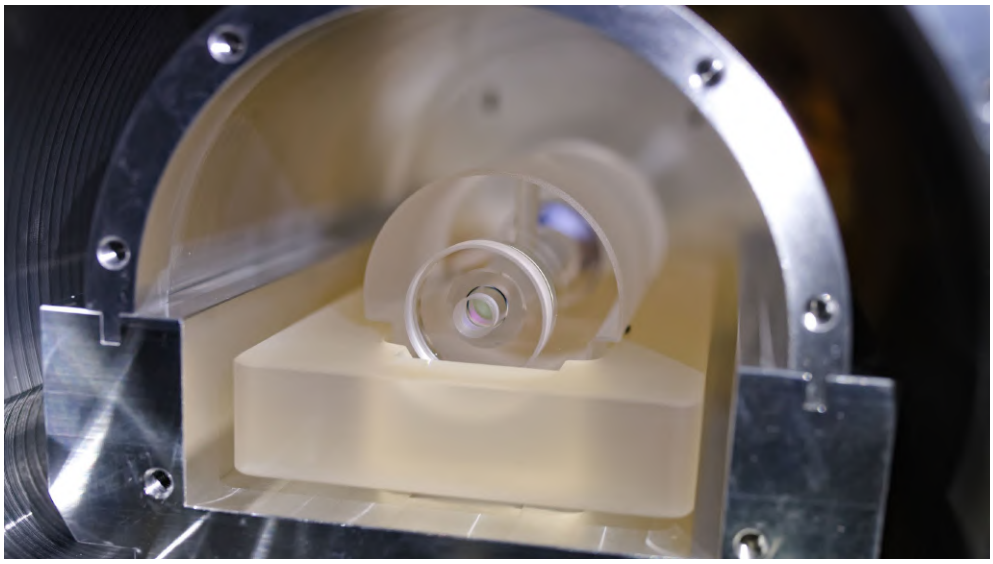

Figure 5.7: Notched FP cavity consisting of a spacer and compensation rings made of ULE glass, with mirrors made of fused silica. The cavity is supported by four Viton balls resting on a Zerodur cradle.

100 mm and a diameter of 50 mm. The cavity employs a standard plano-concave mirror configuration, where one mirror is planar and the other has a radius of curvature (ROC) of 50 cm. Both mirrors are made of fused silica and are optically contacted to the ULE glass spacer. To minimise the influence of the mirror substrates on the overall thermal response of the cavity, ULE glass compensation rings are also optically contacted to the rear surfaces of the mirrors.

The dielectric coatings on the mirrors are designed to provide high reflectivity at both 1062.55 nm and 907.92 nm, corresponding to the $^1S_0 - {}^3P_0$ and $^1S_0 - {}^3P_2$ transitions in Hg, before the frequency quadrupling. The reflective coatings were designed

and deposited by FiveNine Optics, while the spacer, mirror substrates, compensation rings, and optical contacting were supplied by Stable Laser Systems.

Mechanical isolation of the cavity from environmental vibrations and gravitational forces is essential to achieve high stability [184, 185]. Acceleration acting on the cavity introduces two primary effects: sagging of the spacer along the optical axis, which changes the mirrors' separation distance, and deformation of the spacer surfaces, which affects the mirrors' parallelism. These effects can be mitigated by supporting the cavity at optimised positions suited for notched geometry [186, 187]. Finite-element simulation, performed in SolidWorks, is used to determine the optimal support points that minimise deformation under external acceleration. Further refinement can be performed experimentally by adjusting the support positions and observing the resulting improvement in cavity performance.

The support points for the cavity were determined and specified by the manufacturer. The axial spacing between the supports is 54 mm, while the transverse spacing is 43.8 mm. The cavity is supported by four Viton balls with a diameter of 3/32"[17] These supports rest on a cradle machined from Zerodur, offering a mechanically and thermally stable mounting platform. To accurately position the Viton balls, a dedicated alignment fixture with undercut grooves was employed (Figure 5.8), allowing the balls to be slid into place on the surface of the Zerodur cradle. Once the cavity was installed, the fixture was removed.

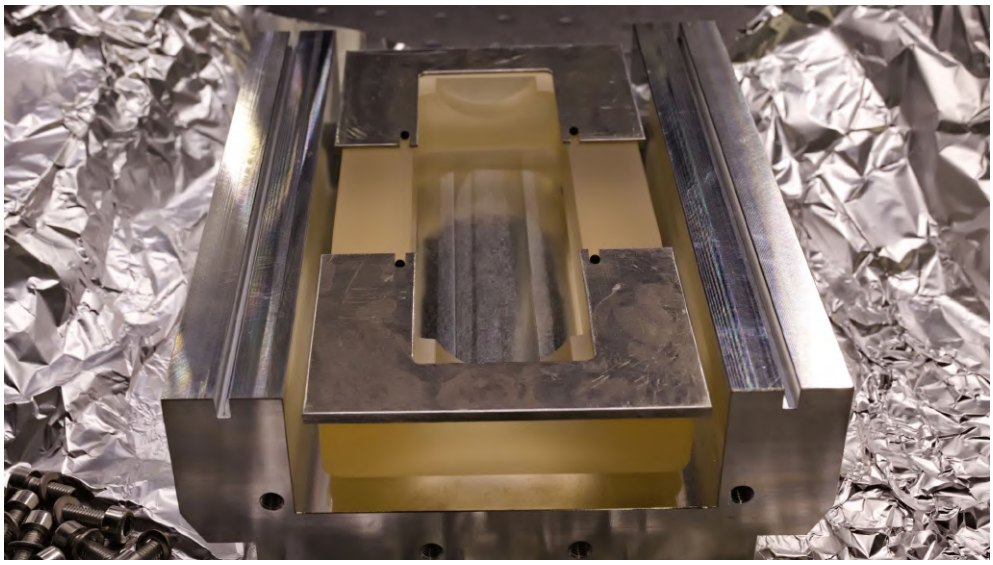

Figure 5.8: Dedicated alignment fixture with undercut grooves used for positioning the Viton balls. The fixture was slid onto the Zerodur cradle to ensure accurate placement of the Viton balls at the manufacturer-specified support points.

[17] Precision Plastic Ball

The stability of the cavity length is related to the spacer's response to temperature fluctuations. The relative change in the optical path length due to thermal expansion can be expressed as

$$\frac{\Delta L}{L} = \alpha(T)\Delta T + \frac{1}{2}\frac{d\alpha}{dT}\Delta T^2 + \mathcal{O}(\Delta T^3), \tag{5.3.1}$$

where $\alpha(T)$ is the temperature-dependent coefficient of thermal expansion (CTE), T is the absolute temperature, and ΔT is a small temperature deviation.

The coefficient $\alpha(T)$ varies with temperature and zeroes at a specific temperature T_0, known as the zero-crossing temperature, for which $\alpha(T_0) = 0$. While the manufacturer provides the nominal zero-crossing temperature of the ULE glass spacer [188], the effective zero-crossing temperature of the entire cavity is shifted due to the influence of the fused silica mirror substrates. To minimise this shift, ULE glass compensation rings are optically contacted to the rear surfaces of the substrates, reducing the thermal mismatch between the spacer and the mirrors [189].

The second-order term, $\frac{d\alpha}{dT}$, typically has a value on the order of $1 \times 10^{-9}\,\mathrm{K}^{-2}$ [188]. Achieving a fractional frequency stability at the level of 10^{-16} requires the temperature of the cavity to be stabilised near the zero-crossing temperature with a stability better than 1 mK.

The optical path length between the cavity mirrors depends not only on their physical separation but also on the refractive index of the medium within the cavity. Variations in the refractive index n due to changes in temperature and pressure directly influence the frequency stability of the optical reference. The temperature- and pressure-dependence of the refractive index of air is described by the corrected Edlén equation [190, 191]

$$n - 1 = \frac{p(n-1)_s\left[1 + 10^{-8}(0.601 - 0.00972T)p\right]}{96095.43\,(1 + 0.0036610T)}, \tag{5.3.2}$$

$$(n-1)_s = 3 \times 10^{-8}\left[8342.54 + \frac{2406147}{130 - 1/\lambda^2} + \frac{15998}{38.9 - 1/\lambda^2}\right], \tag{5.3.3}$$

where λ is the wavelength in micrometres, T is the temperature in degrees Celsius, and p is the pressure in pascals.

The relative frequency stability of the cavity is directly proportional to the relative stability of the refractive index:

$$\frac{\Delta\nu}{\nu} \propto \frac{\Delta n}{n}. \tag{5.3.4}$$

Since the refractive index of air is close to unity ($n \approx 1$), the relation simplifies to

$$\frac{\Delta\nu}{\nu} \propto \Delta n. \tag{5.3.5}$$

From Eq. (5.3.2) and Eq. (5.3.5), achieving a fractional frequency stability at the level of 10^{-16} for 1062.55 nm light necessitates pressure fluctuations below approximately 1.3×10^{-10} mbar. Consequently, the cavity must be housed in an UHV environment. In addition to suppressing refractive index fluctuations, UHV conditions improve thermal stability by eliminating convective heat transport. It should be noted, however, that the critical requirement is not the absolute vacuum pressure, but rather its stability over time. Achieving good vacuum stability is more feasible in a better vacuum, where pressure fluctuations are inherently reduced.

The cavity is housed within a vacuum system comprising three chambers made from aluminium. Due to its significantly higher thermal conductivity than stainless steel, aluminium facilitates a more uniform temperature distribution across the system. The vacuum system was primarily designed by Rodolfo Muñoz-Rodriguez and subsequently modified by me. I assembled the system with Marcin Witkowski.

The outermost chamber is nearly cylindrical, with an external diameter of 306 mm, and functions both as a sealed vacuum enclosure and as a thermal reservoir for regulating the cavity temperature during stabilisation. The chamber is sealed axially at both ends with Viton o-rings and flanges fitted with centrally positioned 1-inch wedged windows[18], which provide optical access to the cavity. Each window is mounted in a slot inclined at an angle of $4°$, ensuring that no two windows are parallel to each other or the cavity mirrors, thereby suppressing the formation of unwanted etalon effects or spurious interferometers. Each window in all chambers' flanges is sealed on both sides using pressed 1 mm-thick indium wire.

Three vacuum ports are integrated into the chamber: one for an all-metal angle valve, one for a T-cross chamber, and one for a 20-pin electrical feedthrough (Figure 5.9). The angle valve facilitates evacuation of the system using a combination of a backing pump and a turbomolecular pump. The T-cross chamber connects to a 20 l/s ion pump[19] to maintain UHV conditions. The electrical feedthrough provides connections for three TECs wired with a common ground, a Pt1000 resistance thermometer in a four-wire configuration for the temperature stabilisation loop, and six Pt100 sensors used to monitor thermal gradients across the middle chamber. We used the monitoring Pt100 sensors in the early stage of the project for diagnostics, but now they remain unconnected. The chamber is supported by four 1-inch, 15 cm long pillars and stands on the optical breadboard.

Since aluminium is significantly softer than stainless steel, it is unsuitable for standard ConFlat connections employing knife edges and copper gaskets. Instead, the vacuum ports were designed to use 1 mm-thick indium wire as a sealing material. The indium wire had to be treated appropriately before installation to ensure reliable vacuum sealing.

[18] Thorlabs WW11050-B

[19] Agilent Technologies StarCell 20

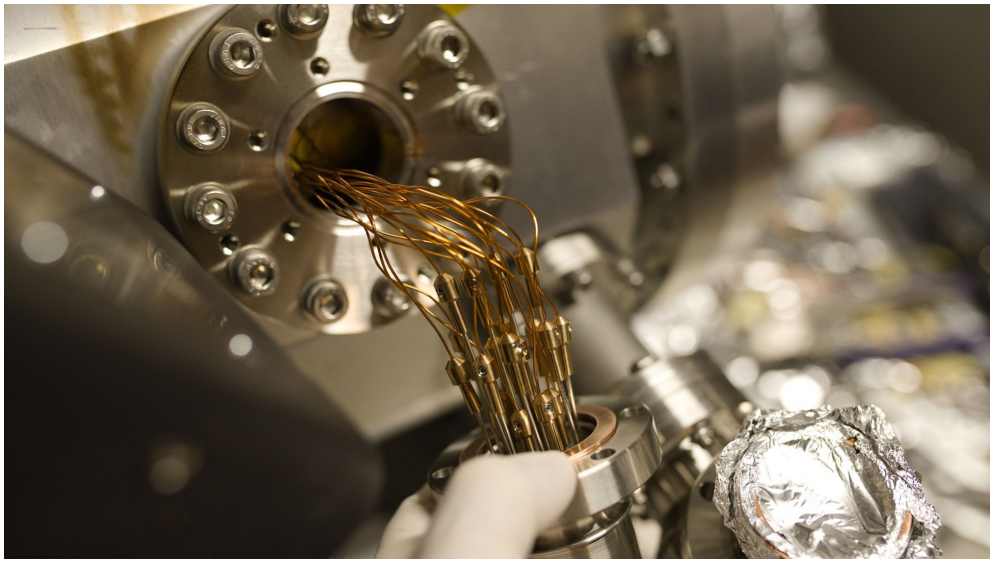

Figure 5.9: Photo of the 20-pin electrical feedthrough before mounting on the vacuum chamber. Vacuum-compatible Kapton-insulated wires are connected to the feedthrough pins using beryllium copper set-screw connectors. The feedthrough provides electrical access to three TECs wired in a common-ground configuration, a Pt1000 sensor in a four-wire arrangement for active temperature stabilisation, and six Pt100 sensors that were initially used to monitor temperature gradients across the middle chamber.

I began by cutting the required lengths of 99.99% purity indium wire and degreasing them in an ultrasonic bath using acetone. I then placed the wires in a 10% hydrochloric acid (HCl) solution for one minute to remove surface oxides. Once dry, the indium wires were ready for installation in the vacuum system.

The middle and inner chambers are nearly cylindrical but are not vacuum-tight. They serve as thermal shields and dampers for vacuum fluctuations. The middle chamber is supported by three TEC modules[20] (Figure 5.10). To ensure vacuum compatibility, I modified the TEC modules by removing the insulation from the connecting wires and eliminating the silicone compound between the ceramic plates. I then cleaned the modules in an ultrasonic bath using a water-detergent solution, rinsed them with demineralised water, and subsequently subjected them to a second ultrasonic bath in 99.5% acetone. To verify that the cleaning procedure did not degrade the thermal performance, I compared the heat transfer efficiency of the treated modules with that of the untreated ones.

The chamber contains machined pockets at the bottom to accommodate the TEC modules. To enhance thermal contact between the TECs and the chamber body, we

[20]CUI Devices CP115559405

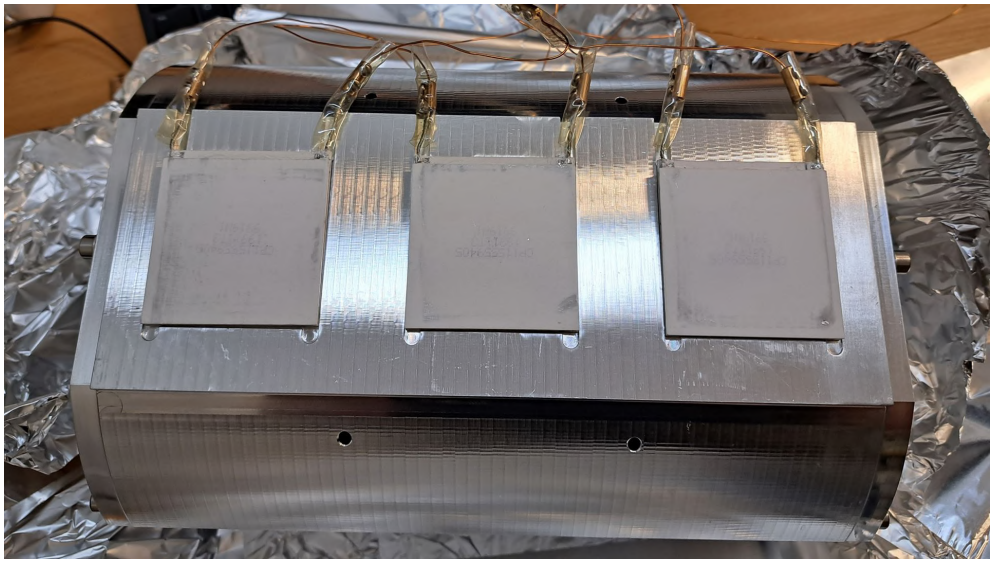

Figure 5.10: Bottom view of the middle chamber with three TEC modules attached. The modules are coupled to the chamber using 1 mm-thick indium sheets. Electrical connections are isolated with vacuum-compatible heat-shrink tubing and extended using Kapton-insulated copper wires.

inserted 1 mm-thick indium sheets at each interface. We isolated the electrical wires from the aluminium chamber using vacuum-compatible heat-shrink tubing. A dedicated milled recess on the top of the chamber allows mounting a Pt1000 resistance thermometer.

Axial sealing of the chamber is achieved via two end flanges, each fitted with a central wedged window inclined at $4°$. These windows are axially rotated relative to those of the outermost chamber, further suppressing the formation of unwanted interferometric paths. To permit chamber evacuation, the flanges are equipped with eight ventilation holes, each 8 mm in diameter and drilled at an angle of $30°$.

The innermost chamber, located within the middle chamber, is supported by four 7/32-inch Viton balls, providing thermal isolation and vibration damping. It is axially sealed by two end flanges similar to those used for the middle chamber. The flanges are fitted with indium-sealed wedged windows inclined at an angle of $4°$, with their orientation rotated relative to the windows of both the outermost and middle chambers to prevent the formation of a parasitic interferometer.

The Zerodur cradle, which supports the FP cavity, is housed within the innermost chamber. It is mounted on four Viton balls with a diameter of 7/32", further minimising mechanical coupling and thermal conduction from the chamber walls.

To characterise the performance of the UHV system, I recorded the pressure measured by the ion pump attached to the outermost vacuum chamber. I retrieved the data

from the ion pump controller using a serial monitor. The average pressure during the measurement period was approximately 5×10^{-8} mbar. I used the recorded data to compute the non-overlapping ADEV, σ_p, using Eq. (4.2.8), with the absolute pressure p instead of the fractional frequency y. In addition, I calculated the PSD of the absolute pressure as a function of frequency. The results are presented in Figure 5.11.

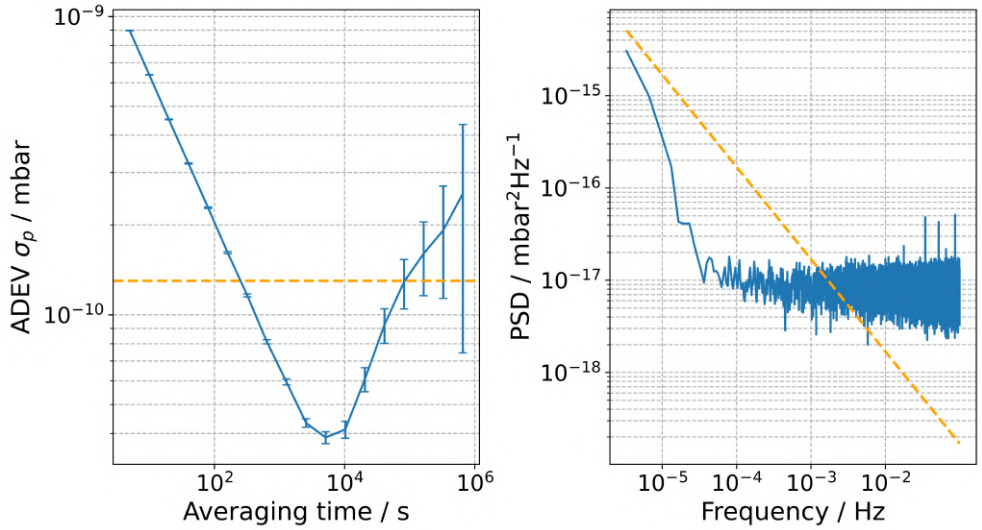

Figure 5.11: Absolute pressure stability, shown as a non-overlapping ADEV (left) and PSD (right). The pressure was monitored using the ion pump and read from the controller via a serial interface. The orange dashed lines in both plots indicate the estimated stability limit of 1.3×10^{-10} mbar, required to support a fractional frequency stability of 10^{-16}. The confidence intervals in the ADEV plot are a simple approximation.

The dashed horizontal line in the plots represents the estimated pressure stability required to achieve a fractional frequency stability of 10^{-16} at a wavelength of 1062.55 nm, corresponding to pressure fluctuations below approximately 1.3×10^{-10} mbar. The results indicate that, without additional vacuum shielding, pressure fluctuations at short averaging times, that is, at higher frequencies, could limit the attainable frequency stability. This highlights the importance of implementing additional vacuum layers, which effectively act as a low-pass filter for pressure fluctuations.

The typical vacuum pressure achieved in chambers housing ULE glass cavities is below 10^{-8} mbar. Although these chambers are usually relatively small in volume, the attainable pressure is limited by the outgassing rates of materials such as Zerodur and ULE glass. In my setup, the slightly elevated pressure may be attributed to the quantity of Kapton tape used for electrical insulation inside the chamber. I applied additional layers of insulation after the standard Kapton-insulated wires were damaged during the installation of the electrical feedthrough.

To improve the isolation of the cavity from vibrations, acoustic noise, and temperature fluctuations in the laboratory, the vacuum system is placed on a passive anti-vibration platform[21]. The platform rests on a custom vibration-damping pillar composed of multiple construction materials, which I designed to attenuate a broad range of mechanical disturbances. The entire assembly is enclosed within an acoustic housing lined with sound-absorbing foam to suppress acoustic noise (Figure 5.12).

Figure 5.12: Photos of the acoustic isolation system before (left) and after (right) the installation of the optical cavity and associated optics. The vacuum system is mounted on a passive anti-vibration platform placed atop a custom-designed vibration-damping pillar composed of layered construction materials. The pillar lies on a 1 cm-thick dense rubber damping mat and incorporates successive layers of concrete, MDF, lead, and marble to attenuate mechanical disturbances. Ceramic slabs with Viton half-balls (not seen in the picture) are placed between the anti-vibration platform and the optical breadboard to provide further mechanical decoupling. The entire setup is enclosed in a cuboid acoustic housing, constructed from 45 mm aluminium profiles and OSB panels, with internal and external acoustic foams for suppression of ambient acoustic noise.

The pillar's base lies on a 1 cm-thick damping mat made of dense rubber. I constructed the pillar as a layered structure, from bottom to top, as follows: 5 cm-thick concrete slabs coated with a bituminous layer, a 1 cm-thick MDF board, 5 cm-thick

[21] Minus K 350BM-1

lead slabs, another 1 cm-thick MDF board, 2 cm-thick marble slabs, a further 1 cm-thick MDF board, and a final 2 cm-thick layer of marble slabs. The anti-vibration platform is mounted on the top surface of this composite base. To further decouple the system, I placed ceramic slabs with Viton half-balls between the anti-vibration platform and the optical breadboard supporting the vacuum system.

I constructed the acoustic-proof chamber in a cuboid shape, incorporating two removable walls that serve as access doors. The chamber is placed on the same damping mat as the vacuum system and has no mechanical contact with other structures or walls in the laboratory, thereby reducing the transmission of external vibrations and acoustic noise.

The structural framework is built from 45 mm aluminium profiles, while the walls and roof are made from 1 cm-thick OSB panels. The exterior surfaces of the walls and roof are covered with 1 cm-thick acoustic foam, while the interior surfaces are lined with 5 cm-thick foam featuring a triangular-profile sound-absorbing sponge to enhance acoustic isolation.

To characterise the effectiveness of the isolation chamber, the pillar, and the anti-vibration platform, Rodolfo Muñoz-Rodriguez performed a vertical acceleration measurement. A one-axis accelerometer was mounted on the optical breadboard, while a high-power speaker was placed on the floor nearby. Using a function generator, the acoustic signals were generated at discrete frequencies ranging from DC to 1 kHz, and the corresponding voltage signals from the accelerometer were recorded.

For comparison, an additional measurement was performed with the accelerometer directly attached to the laboratory floor. For both accelerometer positions, the measurement was repeated without the acoustic signal generated. The results, presented in Figure 5.13, demonstrate that for certain frequencies, the amplitude of the accelerometer signal was reduced by more than 41 dBV. On average, the reduction was more than 11 dBV, confirming the effectiveness of the setup in attenuating mechanical vibrations.

On top of the acoustic-proof chamber, I placed a standard half-inch 90 cm $\times$ 60 cm aluminium breadboard. On this breadboard, I installed the 1062.55 nm fibre laser together with the optical setup used for spectroscopy of the $^1S_0 - {}^3P_0$ transition prior to frequency quadrupling. The breadboard is enclosed in a custom-made protective housing constructed from 30 mm aluminium profiles, with sliding doors made of PVC to shield the optics from dust.

Based on my experience, I do not recommend using such a thin breadboard unless it is firmly secured to a more rigid support structure. In the configuration I used, the breadboard exhibited noticeable flexing when components mounted on it were touched, which made precise alignment of the optical setup considerably more difficult.

Figure 5.13: Accelerometer signal measured on the optical breadboard inside the acoustic isolation system, depicted in blue, and directly on the laboratory floor, depicted in orange, as a function of vibration frequency. For both positions, a reference measurement was also taken without the acoustic signal generated, depicted in green and red. At certain frequencies, the accelerometer signal amplitude was reduced by more than 41 dBV, with an average attenuation exceeding 11 dBV. The data is provided by Rodolfo Muñoz-Rodriguez.

5.3.2 Thermal Stabilisation

The thermal stabilisation of the cavity is implemented using three TEC[22], which allow for both heating and cooling of the middle chamber. Thermal equilibrium between the cavity, the innermost chamber, and the middle chamber is achieved primarily through radiation. The temperature of the middle chamber is measured using a Pt1000 resistance thermometer, which is mounted on the top of the chamber. The Pt1000 sensor is a thin-film ceramic element[23] calibrated to class 1/3B, corresponding to a resistance of $1000\,\Omega$ ($\pm 0.4\,\Omega$) at $0\,^{\circ}\mathrm{C}$.

I selected a Pt1000 over the more commonly used Pt100 due to its higher sensitivity to slight temperature variations, resulting in larger, more easily detected resistance changes. The resistance is measured by applying a known, low current and recording the corresponding voltage drop. Owing to the higher nominal resistance of the Pt1000, a lower current can be used to achieve the same voltage signal, which reduces sensor

[22] CUI Devices CP115559405
[23] Hayashi Denko CRZ1636RE-1000-1/3B

self-heating and thus minimises systematic error. Compared to NTC thermistors (e.g., NTC 10k), the Pt1000 offers a nearly linear resistance–temperature relationship, reducing the uncertainty associated with nonlinear model fitting.

I connected the Pt1000 sensor to a 20-pin electrical feedthrough using 1 mm-thick copper wires in a four-wire configuration. This configuration compensates for the lead resistance during measurement, improving accuracy and stability. The resistance of the Pt1000 is measured using a 6.5-digit multimeter[24] operating in four-wire mode. The device internally converts the measured resistance to temperature and displays the result with a resolution down to 1 mK.

The TEC modules are connected in a common-ground configuration and are powered by a three-channel laboratory power supply[25] operated in constant current mode. I ensure that each TEC module receives the same current. I implemented the stabilisation control using a Python 3 script running on a microcomputer[26]. The microcomputer communicates with the multimeter via USB to read the current temperature using the `PyVISA` library. Based on these readings, the script computes the appropriate current for the TEC modules using a digital proportional–integrating control algorithm. This algorithm adjusts the current flowing through the TEC modules to maintain the temperature of the middle chamber at $34.822\ ^\circ\mathrm{C}$. The computed current is then sent to the laboratory power supply over USB using `PyVISA`. The control loop operates with a 3-second update interval. The script used for temperature stabilisation is provided in [192].

To characterise the performance of the thermal stabilisation control system, I measured the temperature of the middle chamber over an extended period. I used the recorded data to compute the non-overlapping ADEV, $\sigma_{\Delta T/T}$, using Eq. (4.2.8), with the relative temperature $\Delta T/T$ instead of the fractional frequency y. In addition, I calculated the PSD of the relative temperature as a function of frequency. The results are presented in Figure 5.14. The dashed horizontal line in the plots represents the target temperature stability of better than 1 mK, which corresponds to a relative temperature stability of approximately 3×10^{-6}. The results indicate that the thermal stabilisation system is not a limiting factor in achieving the required frequency stability.

It should be noted, however, that the system exhibits sensitivity to mechanical disturbances of the electrical connectors on the multimeter. Accidental contact with the connectors or tension on the cables results in abrupt changes in the measured resistance, leading to spurious spikes in the recorded temperature. I identified and removed these artefacts from the dataset prior to calculating the ADEV and PSD.

[24] Keysight 34465A

[25] Rohde & Schwarz HMP2030

[26] Raspberry Pi 5

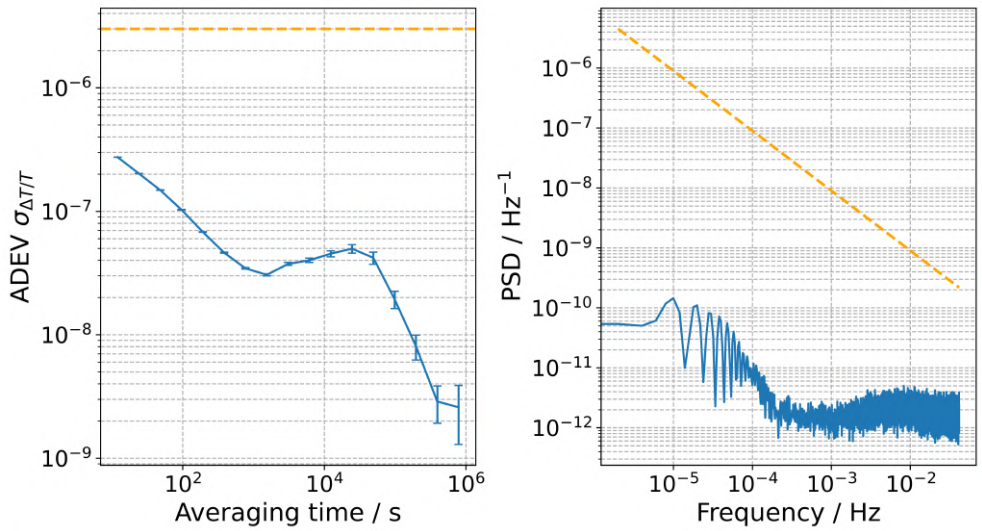

Figure 5.14: Relative temperature stability of the middle chamber, shown as a non-overlapping ADEV (left) and PSD (right). The temperature was monitored using a Pt1000 sensor in a four-wire configuration, read out by a 6.5-digit multimeter. The orange dashed lines in both plots indicate the estimated target temperature stability of 3×10^{-6}, corresponding to a fractional frequency stability of 10^{-16}. The confidence intervals in the ADEV plot are a simple approximation.

5.3.3 Zero-Crossing Temperature

According to Eq. (5.3.1), changes in the length of the cavity spacer due to slight temperature variations are minimised when the temperature-dependent CTE $\alpha(T)$ becomes zero. This condition occurs at a specific temperature T_0, referred to as the zero-crossing temperature, which must be determined experimentally.

A common method for determining T_0 involves measuring the optical frequency of a cavity fringe at different temperatures. A practical approach is to stabilise a laser to the resonance fringe of the optical cavity and to measure its optical frequency via heterodyne detection with an OFC. The resulting beatnote frequency is temperature-dependent and is expected to follow a parabolic trend. The temperature corresponding to the vertex of the fitted parabola is the zero-crossing temperature. Although an approximate value of T_0 is typically provided by the spacer manufacturer, a more precise determination generally requires scanning the cavity temperature over a range of several degrees Celsius around the nominal value.

The dependence of the beatnote frequency on temperature is expected to follow a parabolic trend, provided that the frequency shifts originate solely from the Eq. (5.3.1). To ensure this, it is essential to use an OFC referenced to a stable source, either a stabilised RF signal or a de-drifted optical reference. Furthermore, the temperature varia-

tion must be sufficiently large to distinguish the beatnote shift from the long-term drift of the cavity length.

For cavities with mirrors made of fused silica, it has been observed that alternating increases and decreases in temperature reduce the accuracy of the zero-crossing determination. In such cases, the measurement should be performed in one direction only, either by continuously increasing or decreasing the temperature. This behaviour is not typically observed in cavities with ULE glass mirror substrates. Unfortunately, I was unaware of this limitation when I carried out the measurement on my system and varied the cavity temperature in a random order. To determine the zero-crossing temperature, I stabilised the OFC to a 10 MHz reference signal derived from UTC (AOS), which exhibits a negligible drift. Although the OFC was stable over long time scales, its short-term stabilisation performance was underperforming, resulting in statistical uncertainties in the beatnote frequency no better than 10 kHz.

I measured the beatnote frequency using a spectrum analyser over a temperature range from 28 °C to 45 °C. The results are presented in Figure 5.15. Due to the non-monotonic selection of temperature values, the parabolic fit does not fully agree with the measured data points within their statistical uncertainties. Nonetheless, I estimated the zero-crossing temperature of the cavity to be $34.822(43)$ °C.

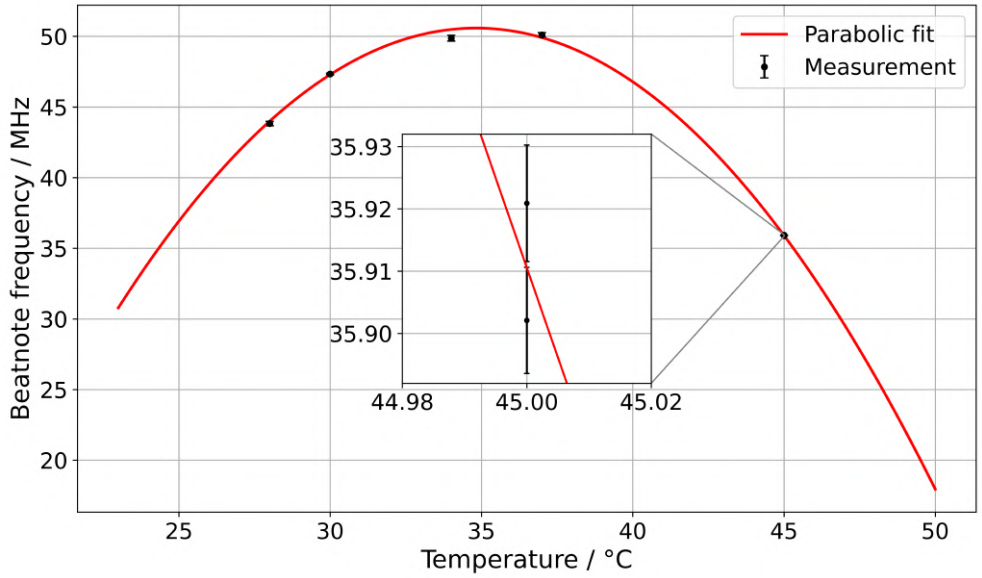

Figure 5.15: The beatnote frequency of the laser stabilised to the optical cavity as a function of cavity temperature. The optical frequency was measured via heterodyne detection with an OFC referenced to a 10 MHz signal derived from UTC (AOS). The parabolic fit reflects the expected cavity length dependence due to thermal expansion. The estimated zero-crossing temperature of the cavity is $34.822(43)$ °C.

5.3.4 Finesse

To evaluate the performance of the optical cavity, I measured its finesse using the cavity ring-down method. This technique is based on observing the exponential decay of the transmitted light intensity after suddenly interrupting the input beam. The decay time constant τ is directly related to the photon lifetime within the cavity, which in turn allows the finesse to be determined.

For this measurement, I modulated the input laser beam using a fibre-coupled AOM, which allowed me to rapidly switch off the light entering the cavity. The transmitted light intensity was monitored using a fast photodetector with a bandwidth of 400 MHz. Once the AOM was switched off, I recorded the decay of the transmission signal. I performed the measurement three times and merged the obtained data. The resulting data was fitted with a single exponential decay function with an offset

$$I(t) = I_0 \exp\left(-\frac{t}{\tau}\right) + \text{offset}, \tag{5.3.6}$$

where I_0 is the initial transmitted intensity at $t = 0$ and τ is the decay constant.

The effective reflectivity R of the cavity mirrors is related to the decay time by [193]

$$R = 1 - \frac{L}{c\tau}, \tag{5.3.7}$$

where L is the cavity length and c is the speed of light. This relation neglects absorption and scattering in the cavity, which is valid for high-finesse cavities. From the reflectivity, I calculated the finesse according to Eq. (4.1.8). The results are shown in Figure 5.16. From the fit, I obtained a decay time of $\tau = 44.432(32)$ µs. Given the cavity length $L = 100$ mm, I calculated the finesse to be $41847(15) \times 10^1$.

5.4 Laser System for Clock Spectroscopy

In this section, I describe the design and implementation of the laser system used for high-resolution spectroscopy of the $^1S_0$–$^3P_0$ clock transition in Hg atoms. The system is designed to provide ultra-stable and narrow-linewidth UV light at 265.6 nm, generated by frequency quadrupling a laser operating at 1062.55 nm.

The section begins with an overview of the optical setup developed to stabilise the infrared fibre laser to an ultra-stable FP cavity using the PDH technique. I then present the free-space light distribution system, which delivers the stabilised light to various subsystems, including the OFC and the frequency conversion stages, while actively suppressing fibre-induced phase noise. Subsequent subsections describe the implementation of the high-power optical amplifier and the frequency quadrupling setup required to generate the UV radiation. I also detail the FNC schemes used in each optical link

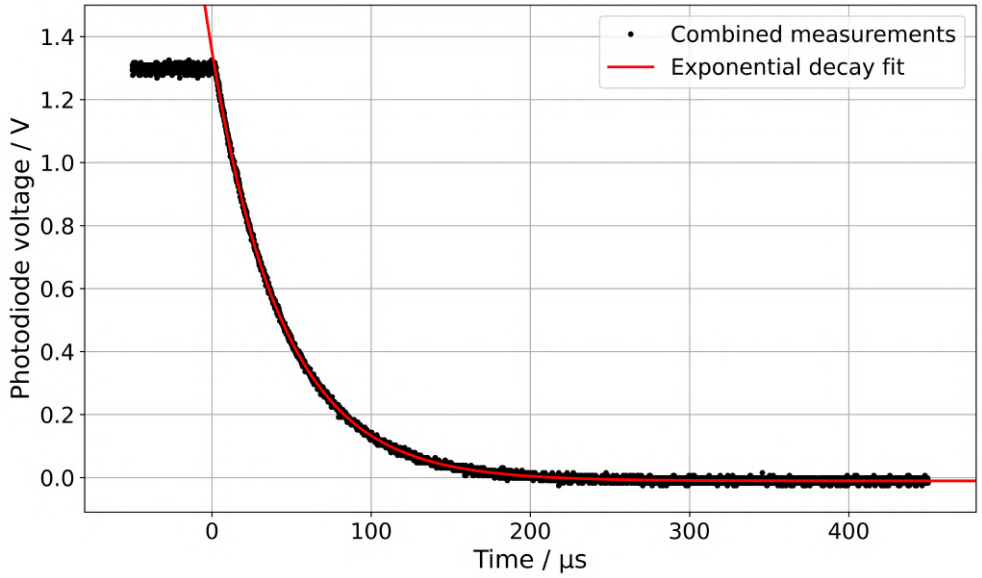

Figure 5.16: Cavity ring-down measurement of the finesse. The transmitted intensity was recorded using a fast photodetector after suddenly switching off the input beam with a fibre-coupled AOM. The dataset shown is a combination of three independent measurements. The decay curve was fitted with a single exponential function to extract the photon lifetime $\tau = 44.432(32)$ µs.

and the tracking oscillator-based method developed to ensure high-accuracy beatnote measurements with the OFC. Finally, I present the results of laser frequency stability measurements, demonstrating the system's performance and its suitability for optical clock interrogation.

5.4.1 Optical Setup for Clock Spectroscopy

Optical Setup for Laser Referencing

Spectroscopy of the $^1S_0$– $^3P_0$ transition requires a highly stable and spectrally narrow laser source operating at 265.6 nm. In my setup, this light is obtained by frequency quadrupling the output of a fibre laser operating at 1062.55 nm, which is referenced to an ultra-stable optical cavity. A schematic of the optical setup used to stabilise the fundamental laser to the reference cavity is shown in Figure 5.17.

I used a Koheras BASIK Y10 fibre laser from NKT Photonics, which emits more than 10 mW of light at 1062.55 nm and features a Lorentzian instantaneous linewidth below 20 kHz. The laser is equipped with both thermal tuning and PZT actuation. The thermal tuning allows wavelength adjustment over ± 240 pm, while the PZT enables fine tuning over a range of approximately 10 GHz with a modulation bandwidth

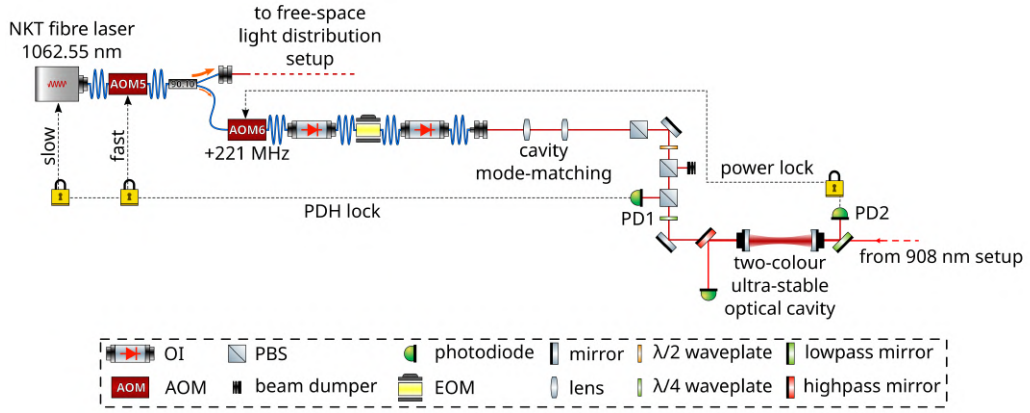

Figure 5.17: Schematic of the optical setup used to reference the 1062.55 nm fibre laser to the ultra-stable optical cavity. The fibre laser is frequency-tuned using a fibre-coupled AOM (AOM5), which enables fast modulation via a VCO. The light is then split, with 10% sent towards the cavity setup. A second AOM (AOM6) provides frequency offset tuning to match the cavity resonance and the optical transition frequency, and also functions within a power stabilisation loop using photodiode PD2. The EOM, installed between two OI, imprints the modulation sidebands required for PDH locking. The beam is mode-matched to the cavity via a lens system and cleaned in polarisation using a PBS. Power is attenuated using a half-wave plate and a second PBS. A quarter-wave plate and another PBS allow separation of the reflected beam, which is detected by photodiode PD1 and used to generate the PDH error signal. A dichroic mirror near the cavity input separates the 1062.55 nm and 907.92 nm paths. The cavity-transmitted signal is detected by PD2 and is used for optical power stabilisation.

of up to 20 kHz. However, this bandwidth is insufficient for the effective transfer of the cavity reference stability. To address this, I implemented a fibre-coupled AOM[27], labelled AOM5 in Figure 5.17, driven by a voltage-controlled oscillator (VCO)[28] capable of fast frequency tuning with sub-microsecond response time.

The output of AOM5 is split using a fibre splitter, 90% of the power is directed to the free-space light distribution system, while the remaining 10% is sent to a second AOM[29] (AOM6) for cavity referencing. AOM6 is driven by a signal generated by a high-resolution direct digital synthesiser (DDS)[30] and provides the necessary frequency offset between the cavity resonance and optical transition frequency, and allows for optical power stabilisation via a feedback loop using the signal from the photodiode

[27] AA Opto-Electronic MT200-IR10-Fio-PM-J1-A-Ic
[28] AA Opto-Electronic DRFA10Y
[29] AA Opto-Electronic MT200-IR10-Fio-PM-J1-A-Ic
[30] Analog Devices AD9912A

PD2[31], which measures the optical power transmitted by the cavity.

The beam then passes through an electro-optic phase modulator (EOM)[32] driven by a 6 MHz sinusoidal signal, which I used to generate modulation sidebands required for the PDH error signal. To minimise optical feedback and reduce residual amplitude modulation (RAM), I placed the EOM between two polarisation-dependent optical isolators (OIs). The output from the EOM is coupled into free space using a triplet fibre collimator[33], which ensures a clean Gaussian spatial mode for optimal coupling into the reference cavity.

To maximise mode-matching to the cavity, I shaped the beam using a system of two spherical lenses. The initial polarisation extinction ratio (PER) of the laser was insufficient for stable operation, so I introduced a PBS to enhance PER and maintain a consistent polarisation axis. Further attenuation of the optical power to the desired level (approximately 1 μW) was achieved using a half-wave plate and an additional PBS.

To separate the reflected and leaked beams from the incident one, I inserted a quarter-wave plate and another PBS. The reflected and leaked light is used to generate the PDH error signal and is detected by an avalanche photodiode[34] (PD1). Just before the cavity, the beam passes through a long-pass dichroic mirror to decouple the 1062.55 nm beam from a beam at 907.92 nm. The light transmitted through the cavity is monitored using a second avalanche photodiode[35] (PD2), which is used in the optical power stabilisation loop.

To optimise the spatial mode-matching to the cavity, I measured the beam profile using a beam profiler[36]. The reference cavity is a plano-concave configuration, with a ROC of 50 cm for the concave mirror. In such cavities, the fundamental transverse electromagnetic mode (TM_{00}) has its waist located at the surface of the plane mirror. The waist radius w_0 is given by [124]

$$w_0^2 = \frac{\lambda L}{\pi} \frac{\sqrt{g_1 g_2 \left(1 - g_1 g_2\right)}}{|g_1 + g_2 - 2 g_1 g_2|}, \quad g_1 = 1 - \frac{L}{R_1}, \quad g_2 = 1 - \frac{L}{R_2}, \tag{5.4.1}$$

where λ is the wavelength, $L = 10$ cm is the cavity length, and $R_1 = \infty$ and $R_2 = 50$ cm are the radii of curvature of the plane and concave mirrors, respectively. For the optical cavity used in my system, this yields a mode waist radius of approximately 260 μm.

Based on the measured divergence of the input beam, I simulated the placement of two spherical lenses, each with a focal length of 100 mm, to achieve the required waist

[31] Thorlabs APD410C/M
[32] Exail NIR-MPX-LN-0.1
[33] Thorlabs TC12APC-1064
[34] Thorlabs APD410C/M
[35] Thorlabs APD410C/M
[36] Cinogy CMOS-1.001-Nano

size of 260 µm at the surface of the cavity's plane mirror. In this setup, the plane mirror serves as the output mirror of the cavity.

I measured the power transmission through the cavity to be approximately 35%. This result indicates that the beam coupling to the cavity is satisfactory but could be further optimised.

Although the optical setup was ultimately implemented using the NKT BASIK Y10 laser, my initial approach relied on the EQ4126 ultra-narrow linewidth fibre laser from OEwaves. This system was based on a high-quality-factor whispering gallery mode micro-resonator, and according to the manufacturer's specification, it offered a Lorentzian spectral linewidth below 10 Hz, an output power of 10 mW, and frequency modulation capability up to 1 MHz. While the datasheet characteristics appeared superior, the laser was malfunctioning since its first use. The issue was its failure to stabilise during the warm-up procedure. Despite that, I was able to reference the laser to the ultra-stable optical cavity.

After several weeks of operation, the laser began lasing in multiple longitudinal modes, and referencing the optical cavity was no longer possible. An inspection by the manufacturer revealed that internal optical components had become detached due to epoxy ageing. The unit had been purchased during the COVID-19 pandemic and remained unused for over two years due to restricted laboratory access under health and safety regulations. By the time the malfunction was revealed, the warranty period had expired, and the manufacturer declined to service the unit unless a payment comparable to the cost of a new laser was made. This unfortunate situation caused an exceptionally long and disruptive delay to the project, as the absence of a light source for the spectroscopy prevented any meaningful progress for an extended period.

Light Distribution System

The free-space light distribution system splits the laser beam into three separate arms, each serving a distinct purpose. A schematic of the optical layout is shown in Figure 5.18 and the photography of the real-life implementation is shown in Figure 5.19.

The free-space coupled beam passes through a half-wave plate and a PBS to improve the PER and stabilise the polarisation axis. It is then modulated by an AOM[37] (AOM7). I use AOM7 for several purposes: as a frequency shifter to match the clock transition frequency and for frequency modulation required for noise cancellation. The latter compensates for phase noise introduced both in the delivery fibre and by the optical amplifier. Further details about the FNC scheme are provided in Section 5.4.1.

I also employ AOM7 as a variable beam splitter. The diffracted beam is coupled into a PM fibre that delivers light to the optical amplifier and the frequency quadrupling stage. The non-diffracted beam is directed towards a 50:50 non-polarising beam splitter (NPBS). A fraction of this beam is internally reflected within the NPBS cube

[37] AA Opto-electronic MT200-A0.5-1064

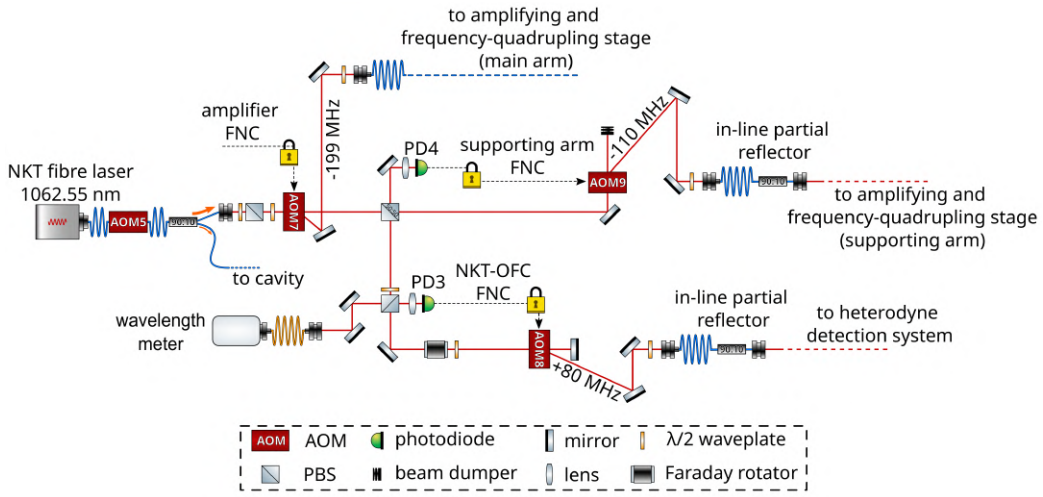

Figure 5.18: Schematic of the free-space optical setup used to distribute the 1062.55 nm light into three dedicated arms. The beam first passes through a half-wave plate and a PBS to improve the PER. It is then modulated by an AOM (AOM7), which serves multiple roles: frequency shifting, fibre noise modulation, and acting as a variable beam splitter. The diffracted beam is coupled into a fibre that leads to the optical amplifier and frequency quadrupling stages. The non-diffracted beam is directed towards a 50:50 NPBS, where a small internally reflected portion is monitored on PD4 as a reference signal. The beam transmitted through the NPBS is frequency-shifted by AOM9 and fibre-coupled to an arm terminating with a partial reflector. The retro-reflected light returns and interferes on PD4 with the reference beam, providing a beatnote for FNC. The main beam reflected by the NPBS continues through polarisation optics, passes through a Faraday rotator, and is modulated by AOM8 before fibre coupling. The back-reflected signal interferes with the reference beam on PD3, yielding another beatnote for FNC. This final arm is used for heterodyne detection with the OFC to determine the absolute frequency of the clock laser.

and directed onto an avalanche photodiode[38] (PD4), where it serves as an optical frequency reference.

The beam transmitted through the NPBS undergoes frequency shifting via another AOM[39] (AOM9) and is coupled into a PM fibre. At the end of the fibre, I installed an in-line partial reflector, which retro-reflects approximately 10% of the optical power. This retro-reflected beam retraces the same path, and upon returning to the NPBS, a portion is directed onto PD4. There, it interferes with the optical frequency reference beam, generating a heterodyne beatnote. The resulting RF signal is used for active

[38] Thorlabs APD430C/M
[39] AA Opto-electronic MT110-A1.5-IR

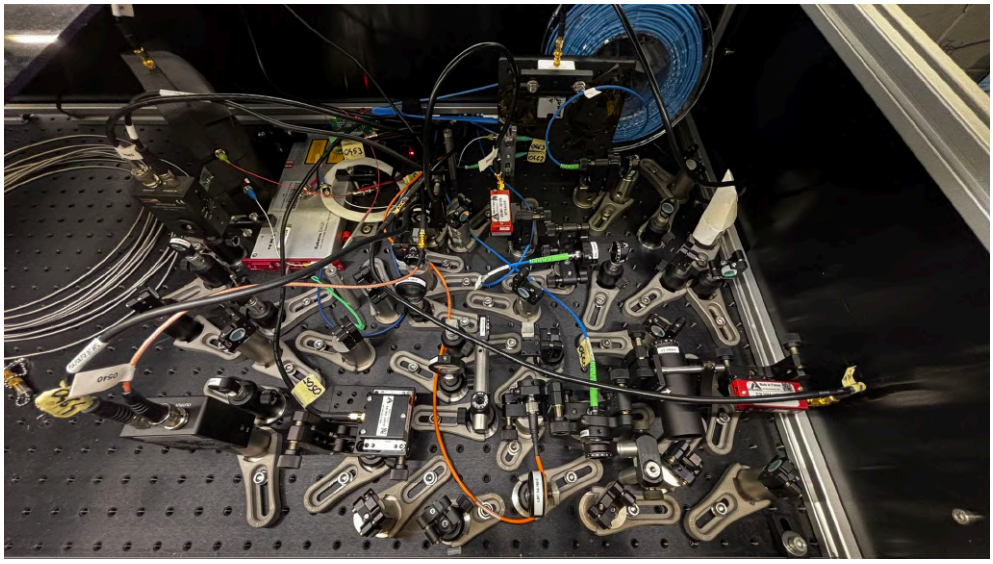

Figure 5.19: Photo of the implemented free-space optical setup for distributing the 1062.55 nm light. The NKT Basik Y10 fibre-laser is visible on the upper left side of the image. The fibre-coupled AOMs are mounted on the small aluminium breadboards, and AOM6 with its fibres is additionally covered with isolation foams to minimise the induced phase noise.

FNC. The noise-compensated output of this fibre serves as the optical frequency reference for the amplifier stage.

The main beam reflected by the NPBS continues through a half-wave plate and a PBS. These components are used to decouple a small fraction of the light for a wavelength meter. The transmitted portion of the beam then passes through a Faraday rotator, which rotates the polarisation axis by $45°$, and subsequently enters another AOM[40] (AOM8). The diffracted beam is coupled into a PM fibre, where an in-line partial reflector is again used to retro-reflect about 10% of the optical power. The retro-reflected light passes back through the Faraday rotator, accumulating a total polarisation rotation of $90°$. This polarisation-rotated beam is reflected by the PBS and directed onto an avalanche photodiode[41] (PD3). The reference beam, formed by the back-reflection of the non-diffracted light, follows a similar path and also reaches PD3. Interference between the frequency-shifted and reference beams at the detector produces a beatnote used for active FNC. The noise-compensated output of this fibre arm is used in heterodyne detection with the OFC, allowing for precise determination of the absolute optical frequency of the clock laser.

[40] AA Opto-electronic MT80-A1-IR

[41] Thorlabs APD430C/M

Optical Amplifier and Frequency Quadrupling Stage

To generate ultra-stable light at 265.6 nm required for $^1S_0 - {}^3P_0$ transition spectroscopy, I implemented an optical amplifier and frequency quadrupling system. A schematic of this setup is presented in Figure 5.20 and the photography of the real-life implementation is shown in Figure 5.21.

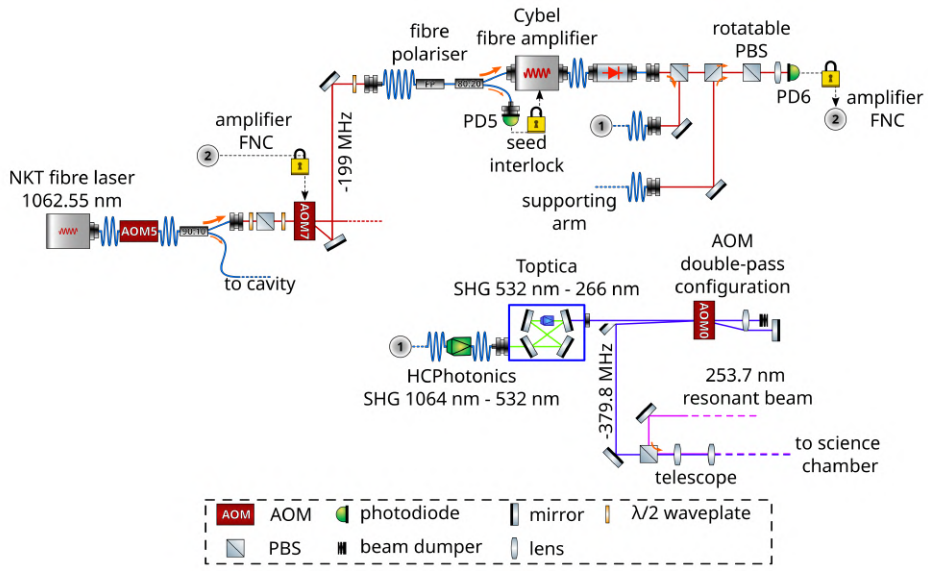

Figure 5.20: Schematic of the optical amplifier and frequency quadrupling system used to generate ultra-stable 265.6 nm light for spectroscopy of the $^1S_0 - {}^3P_0$ transition in Hg. The fundamental 1062.55 nm light is amplified to over 1 W using a fibre amplifier. The amplifier input is protected by a fibre-based interlock system to prevent damage from insufficient seeding. The amplified light is used in two consecutive stages of SHG: first in a PPLN waveguide and then in a bow-tie enhancement cavity, resulting in more than 13 mW of 265.6 nm light. To scan the frequency, I implemented a double-pass AOM configuration based on a D-shaped mirror for efficient spatial separation, avoiding polarisation losses specific to SiO_2-based AOMs. The UV beam is finally overlapped with a guidance beam resonant with the $^1S_0 - {}^3P_1$ transition for proper alignment with the atomic cloud in the MOT.

Frequency quadrupling is achieved through two consecutive stages of SHG. As the efficiency of nonlinear conversion depends strongly on input power, I amplified the fundamental 1062.55 nm light to more than 1 W using a Cybel MAKO-AMP1064 fibre amplifier, which is equipped with a high-power OI .

The amplifier is seeded with more than 1 mW of light delivered via a PM fibre from the light distribution system. Operating the amplifier with insufficient seed power or incorrect polarisation results in permanent damage. Unfortunately, I experienced such

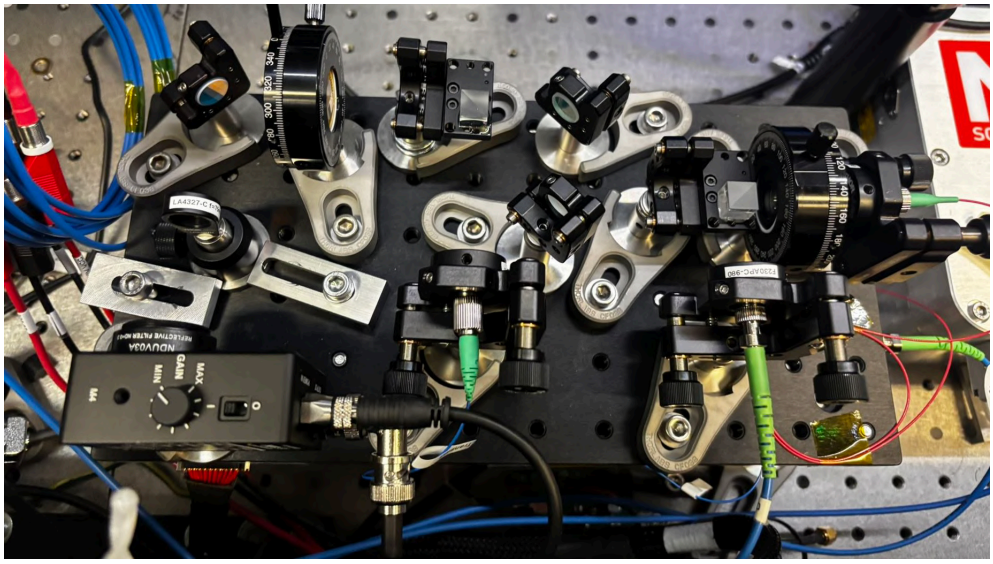

Figure 5.21: Photo of the implemented optical amplifier stage. The free-space setup used for active compensation of phase noise introduced in the seed delivery fibre and the optical amplifier is visible. The fibre-coupled elements and the optical amplifier are secured on the bottom side of the black aluminium breadboard.

amplifier failures on two occasions, significantly delaying the project. To prevent recurrence, I equipped the input with an in-line fibre polariser[42] providing a typical PER of 28 dB, followed by an 80:20 fibre-coupled NPBS. The tapped output is monitored by a photodiode[43] (PD5), and the resulting signal is compared against a reference voltage using an analogue comparator. If the seed power drops, the comparator triggers a MOSFET driver to interrupt the amplifier's internal interlock, shutting it down within tens of nanoseconds and protecting it from damage.

The amplified output is coupled into free space. A small fraction of the beam is extracted using a PBS to generate a heterodyne beatnote with the reference beam from the fibre-noise-compensated supporting arm. I aligned the two beams using a set of PBSs such that their polarisations are projected on the same axis. I then adjusted the power ratio by rotating one PBS to maximise the beatnote signal, which I detected with an avalanche photodiode[44] (PD6). I used this signal in a feedback loop to actively compensate for phase noise introduced in the seed delivery fibre and the amplifier. The correction was applied via frequency modulation of AOM7 in the seed path.

The main beam from the amplifier is fibre-coupled to a first SHG stage based on a

[42] Thorlabs ILP1064PM-APC
[43] Thorlabs PDA20CS2
[44] Thorlabs APD430C/M

single-pass PPLN waveguide mixer[45]. Phase matching is maintained by stabilising the crystal at 22.5 °C. The mixer is mounted on a temperature-controlled breadboard[46] equipped with a TEC, a controller, an internal thermistor, and a heat sink for improved thermal stability. With more than 800 mW of seed light at 1062.55 nm, the output of this stage reaches 185 mW at 531.3 nm. This green light is then sent to the second SHG stage[47], which uses a bow-tie enhancement cavity. The final output provides more than 13 mW of 265.6 nm light in free space.

To enable frequency scanning of the UV light, I implemented a double-pass configuration of an AOM[48] (AOM0). The beam is down-shifted by a total of 379.8 MHz to match the $^1S_0 - {}^3P_0$ transition frequency.

Conventional double-pass AOM setups use a quarter-wave plate and PBS for spatial decoupling of the retro-reflected beam. However, this approach is unsuitable for AOMs based on SiO_2 crystals, which exhibit strong polarisation dependence and only efficiently diffract light polarised parallel to the plane of incidence. To address this, I implemented a long-distance scheme using a D-shaped knife-edge mirror placed more than 1 m from the AOM. By slightly misaligning the retro-reflected beam in the diffraction axis, I was able to spatially separate the down-shifted beam and achieve over 70% total efficiency.

Finally, the 265.6 nm beam is overlapped with a guidance beam resonant with the $^1S_0 - {}^3P_1$ transition using a PBS. The guidance beam ensures proper alignment with the MOT containing Hg atoms. I shaped the beam with two spherical lenses to achieve a waist diameter of 120 μm at the location of the atomic cloud in the vacuum chamber.

Fibre-Noise Cancellation

Transmission of ultra-stable laser light through optical fibres introduces frequency noise, primarily due to environmental perturbations such as mechanical vibrations and thermal fluctuations. These disturbances affect the optical path length of the fibre, resulting in phase noise that degrades the frequency stability of the transmitted light [194, 195]. To mitigate these effects, FNC systems are employed [196].

The technique is based on the self-heterodyne interferometric method. In this approach, the laser beam is split into two paths. One path acts as a local optical frequency reference, while the second is directed through the fibre and subsequently partially retro-reflected. The fibre-coupled beam passes through an AOM twice, which introduces a fixed frequency shift. This shift relocates the beatnote between the two beams to a higher frequency, away from the low-frequency noise region, thereby improving signal stability.

[45] HC Photonics
[46] Thorlabs PTC1/M
[47] Toptica SHG-Pro
[48] AA Optoelectronics MQ200-A1.5-244.300-Br

After reflection, the light returning from the fibre is recombined with the reference beam using a beam splitter. The interference signal is detected on a fast photodetector, producing a beatnote centred at twice the AOM driving frequency. Frequency noise acquired in the fibre manifests as fluctuations in the beatnote phase and frequency.

This beatnote is compared with a LO using a phase detector. The resulting error signal is processed in a feedback loop, which controls the frequency of a VCO driving the AOM. The servo-loop actively compensates for the phase fluctuations introduced by the fibre, thereby stabilising the transmitted light and preserving its spectral coherence.

While the operating principle of FNC is relatively straightforward, its practical implementation can vary significantly. Numerous configurations exist, each offering distinct advantages and limitations depending on the application requirements. Commercial systems typically employ fully fibre-integrated architectures to maximise compactness and reliability. However, the internal designs of such systems are often proprietary and thus not publicly disclosed. In contrast, the development and characterisation of long-distance optical links have been extensively reported in the literature [197–202].

The laboratory-based setups more commonly utilise free-space or hybrid configurations, which offer greater flexibility for prototyping and experimental adjustments. A comparison of schematics for several widely used configurations is presented in Figure 5.22.

A widely adopted approach (Panel A in Figure 5.22) is based on a 50:50 NPBS, which divides the incoming beam into a reference path and a main path that is coupled into the optical fibre. The reference beam is retroreflected and recombined at the NPBS, with half of the returning light directed towards a photodiode to serve as the optical frequency reference, and the other half reflected back towards the laser. In setups lacking optical isolation after the laser, the backward-propagating beam may introduce unwanted feedback, potentially destabilising the laser system.

After transmission through the optical fibre, the main beam is diffracted by an AOM. A fraction of the diffracted light is retroreflected using a non-polarising beam splitter plate (NPBS-P), passes through the AOM a second time, and is recoupled into the fibre. Upon return, the beam recombines at the NPBS and is directed both to the photodiode and, like the reference beam, partially back towards the laser. The photodiode detects the frequency beatnote between the reference and returning beams, which is used for active FNC.

This implementation is cost-effective, as it avoids the use of polarisation-sensitive components. However, it is not power-efficient. The optical throughput—defined as the ratio of output to input power—is typically in the range of 30% to 40%, limited by the 50:50 NPBS, AOM diffraction efficiency, and retroreflection losses at the NPBS-P. Furthermore, optimising the signal-to-noise ratio (SNR) of the beatnote can be challenging, as adjusting the relative powers of the interfering beams is not straightforward in this configuration.

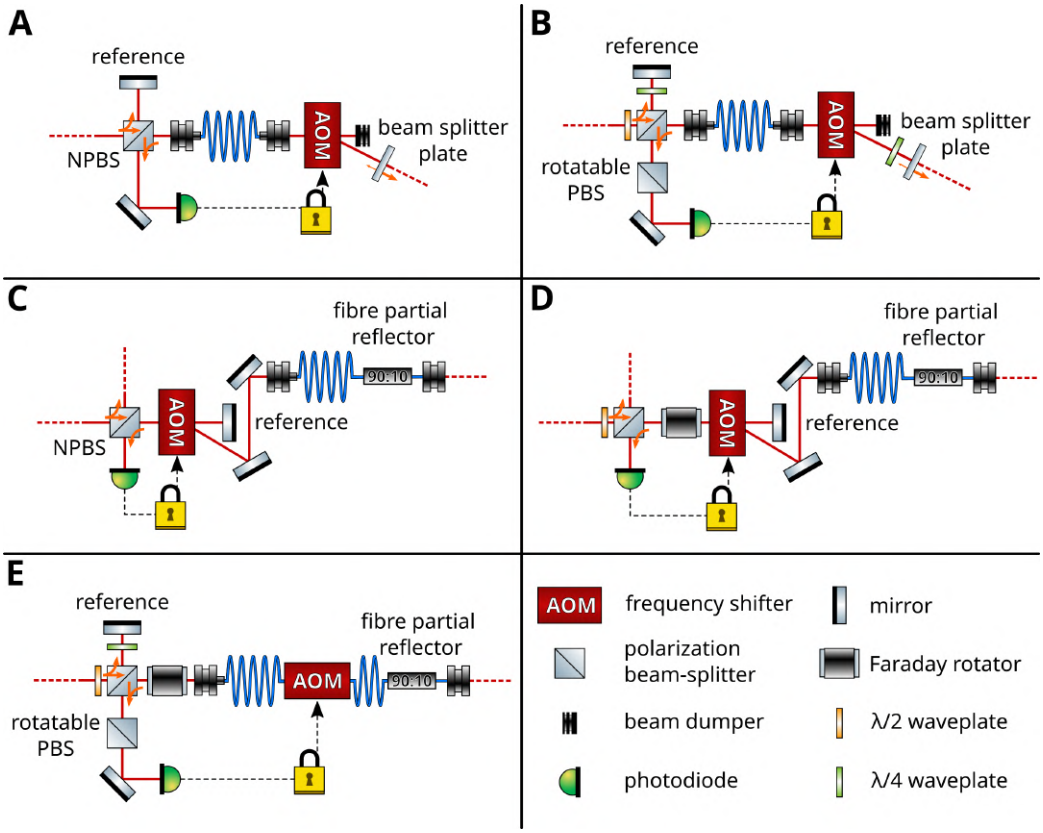

Figure 5.22: Schematics of FNC setups based on the self-heterodyne method. In each case, the laser beam is split into a reference and a fibre-coupled arm, with the retro-reflected light passing twice through an AOM and interfering with the reference on a photodiode. **A:** Basic setup with an NPBS and an NPBS-P. **B:** Power-balanced version using a PBS, wave plates, and a rotatable PBS. **C:** As in A, but with an in-line fibre partial reflector and the AOM placed before the fibre. **D:** Like C, with polarisation-sensitive elements and a Faraday rotator for spatial separation. **E:** Compact version with a fibre-coupled AOM and Faraday rotator. Half-wave plates before AOMs and fibre couplers are omitted for clarity.

The limitations of the basic configuration can be mitigated by replacing the NPBS with a combination of a half-wave plate and a PBS, as illustrated in Panel B of Figure 5.22. This modification enables control over the power ratio between the reference and main beams, improving both performance and flexibility.

To recombine the reference beam and the beam returning from back-reflection after the fibre, quarter-wave plates are inserted in each path. Double-pass propagation through a quarter-wave plate results in a net polarisation rotation of $90°$. For the main beam, it is essential that the quarter-wave plate is placed after the optical fibre and the

AOM, as both components perform optimally with linearly polarised light. As a consequence, the recombined beams emerge with orthogonal linear polarisations. To enable interference on the photodiode, a rotatable PBS is placed before the detector. This component acts as a polariser, projecting both polarisations onto the same axis. By adjusting the rotation angle of the PBS, the relative power contributions of the two beams can be balanced, thereby optimising the SNR of the detected frequency beatnote.

This configuration is considerably more power-efficient than the one shown in Panel A, owing to the elimination of unnecessary losses at the NPBS and the absence of light being back-reflected towards the laser. Additionally, it offers fine control over both optical power distribution and beatnote SNR. However, the use of polarisation-sensitive components introduces increased complexity and cost. In particular, wave plates for non-standard wavelengths typically require custom fabrication, which can significantly increase the overall cost of the setup.

The configuration presented in Panel B offers the greatest flexibility, but it is also the most complex and requires the highest degree of optical alignment. This can pose practical challenges when the optical fibre connects remote locations. Alignment becomes significantly simpler if the NPBS-P at the fibre output is replaced with an in-line fibre partial reflector, as illustrated in Panels C and D of Figure 5.22. Connecting or splicing the partial reflector directly to the optical fibre eliminates the need for precise alignment of the reflected beam and its recoupling into the fibre core. However, this approach necessitates placing the AOM before the fibre rather than at its output.

Installing the AOM in front of the fibre enables the use of the non-diffracted beam as the optical reference by its retro-reflecting. Consequently, the beam previously used as a reference in the configurations shown in Panels A and B can be used for a different purpose, improving the overall power efficiency of the system. The distinction between Panels C and D lies in the use of polarisation-sensitive elements, and the considerations are analogous to those discussed for Panels A and B.

In the configuration shown in Panel D, both the reference and the returning beams share the same polarisation axis. Thus, the use of a rotatable PBS becomes unnecessary. Spatial separation of the beams from the incident path is achieved using a Faraday rotator. Double-pass propagation through the Faraday rotator induces a net polarisation rotation of 90°, enabling reflection from the PBS and beam routing towards the photodetector.

Particular care must be taken to ensure efficient coupling into the optical fibre. Light that is not properly coupled is not only dissipated as heat but is also partially back-reflected from the fibre coupler's surface. This back-reflected light retraces the original optical path and undergoes a double-pass through the AOM, producing an unintended beatnote at the same frequency as the desired signal. This spurious contribution can be identified by observing a persistent beatnote signal even when the in-line fibre partial reflector is disconnected. In an ideal configuration, detaching the reflector should eliminate any beatnote, as no light should be retro-reflected.

Additionally, the performance of AOMs must be considered carefully, as they exhibit non-ideal behaviour. A small fraction of the optical power may remain frequency-unshifted in the diffracted beam, while a minor portion of frequency-shifted light may appear in the non-diffracted beam. These effects can give rise to unintended interference components. It is therefore essential to ensure that the primary contribution to the desired beatnote signal arises from interference between the reference arm and the retro-reflected light at the fibre output, rather than from parasitic paths.

The configuration illustrated in Panel E of Figure 5.22 requires even less alignment effort. In this approach, the free-space AOM is replaced by a fibre-coupled model. The input beam is split by a PBS into a reference arm, analogous to the configuration shown in Panel B, and a main beam, which is fibre-coupled after passing through a Faraday rotator.

The portion of the main beam back-reflected by an in-line fibre partial reflector passes the Faraday rotator twice, undergoing a net polarisation rotation of 90°. This polarisation-rotated beam is reflected by the PBS and directed towards the photodetector. As the returning beam and the reference beam possess orthogonal linear polarisations, a rotatable PBS is placed before the detector to project both polarisation components onto a common axis, thereby enabling effective interference.

This implementation offers the greatest immunity to environmental disturbances and requires the least optical alignment. However, these advantages come at the cost of increased system expense, primarily due to the higher price of fibre-coupled AOMs compared to their free-space counterparts. Additionally, the overall power efficiency is reduced, as fibre-coupled AOMs typically exhibit diffraction efficiencies below 50%, in contrast to efficiencies of typically 80% in free-space AOMs.

It should be noted that the splitting ratio of the in-line fibre partial reflector must be carefully selected. Insufficient power in the retro-reflected beam can significantly degrade the SNR of the beatnote, thereby compromising the effectiveness of the FNC system.

In my system, I implemented the FNC scheme depicted in Panel C for the supporting arm that transfers the optical frequency reference used in the noise cancellation of the optical amplifier. For the fibre link delivering the signal to the OFC, I employed the configuration shown in Panel D.

Implementation and Characterisation of Fibre-Noise Cancellation Systems

To process the beatnote signal in the FNC system for the fibre link connecting the light distribution system to the OFC, I implement the electronic setup shown schematically in Figure 5.23.

The optical frequency beatnote is detected using an avalanche photodiode[49] with a 400 MHz bandwidth. The beatnote is centred at 160 MHz, which is too high for direct

[49] Thorlabs APD430C/M

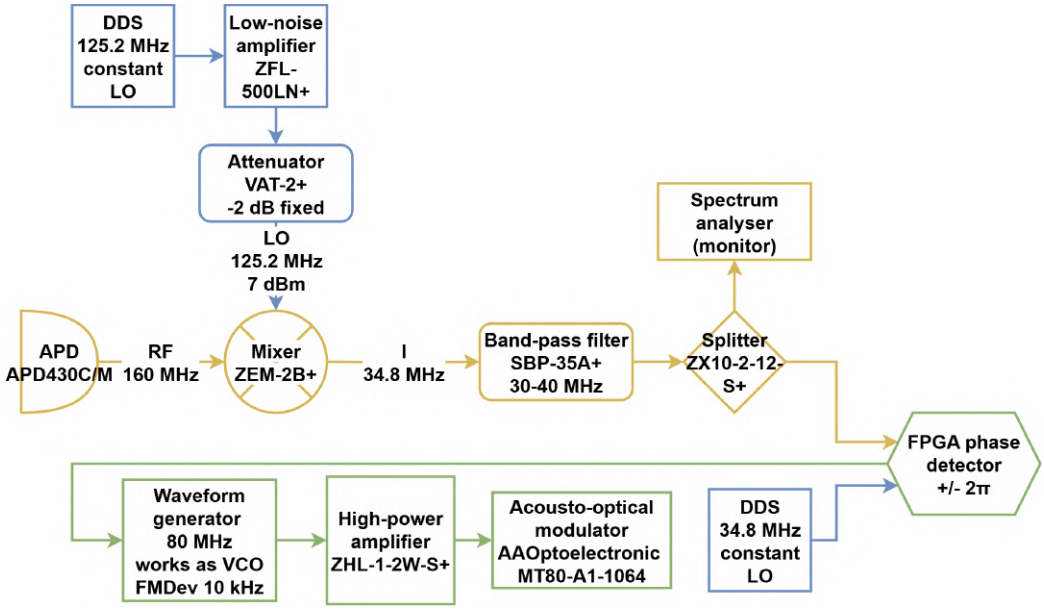

Figure 5.23: The electronic setup used for FNC between the light distribution system and the OFC. The beatnote is downshifted using a frequency mixer and processed by a digital phase detector. A waveform generator acts as a VCO and modulates the AOM to compensate for fibre-induced phase noise. Coloured blocks indicate signal paths: yellow for input signal processing, blue for LOs, and green for the feedback loop.

processing by the digital phase detector. Although a frequency divider could be used, none was available in the laboratory at the time. To overcome this limitation, I downshift the beatnote using a frequency mixer. A 7 dBm LO signal from a DDS[50] mixes with the beatnote and produces a 34.8 MHz intermediate frequency, chosen to match the bandwidth of a narrow bandpass filter centred at 35 MHz and to avoid overlap with spurious RF signals present in the laboratory environment.

The filtered signal is split into two paths. One arm serves as a monitoring output, which can be connected to a spectrum analyser or terminated with a 50 Ω load. The second path is sent to a digital phase detector[51] based on FPGA logic. A reference signal at 34.8 MHz, also generated by the DDS, is supplied to the second input of the phase detector.

Typically, the phase detector output is routed to a servo controller that processes the error signal and drives a VCO. In my implementation, I use a waveform generator[52] as the VCO. The phase detector output is connected to the modulation input of the waveform generator, which applies frequency modulation to its output signal in re-

[50] Analog Devices AD9959
[51] Mode-Locked Technology
[52] Rigol DG4162

sponse to the input voltage. The generator allows for direct setting of the modulation sensitivity in Hz/V, thereby eliminating the need for an additional servo controller.

The RF output of the waveform generator is amplified using a high-power amplifier[53] and drives the AOM, which modulates the optical frequency to actively compensate for fibre-induced phase noise using a phase-locked loop (PLL).

The fibre link between the light distribution system and the OFC spans approximately 200 m and passes through the entire building. In contrast, the other two links, connecting the light distribution system to the optical amplifier and the frequency quadrupling stage, are significantly shorter, each extending roughly 10 m within the laboratory. As these shorter links are subjected to a less noisy environment, I chose to implement analogue phase detectors[54] instead of the more costly FPGA-based detectors.

The schematic diagram of the electronic system used for FNC in the supporting arm is shown in Figure 5.24. The primary difference between the system depicted in Figure 5.23 and that shown in Figure 5.24 lies in the amplification of the down-shifted beatnote and the LO signal to 7 dBm, which is required by the analogue phase detector. The output of the phase detector is filtered with a low-pass filter and connected to the modulation input of a waveform generator[55], which acts as a VCO. The RF output of the waveform generator is then amplified using a high-power amplifier[56], and this amplified signal drives the AOM, which modulates the optical frequency to compensate for fibre-induced phase fluctuations.

The schematic of the electronic system used for noise cancellation of both the fibre and the optical amplifier is presented in Figure 5.25. In this configuration, no frequency mixer is required, as the beatnote frequency is centred at 89 MHz, which lies within the bandwidth of the analogue phase detector. As in the previous system, the phase detector output is connected to the modulation input of a waveform generator[57]. The output signal is subsequently amplified and used to drive the AOM, thereby enabling active cancellation of noise introduced by the fibre and the optical amplifier.

To characterise the performance of the implemented FNC systems, I measured the frequency stability of the beatnote signals for all configurations using the available monitor ports. For comparison, I recorded the stability of the beatnotes with the PLLs both closed and open, as well as the stability of the reference signals themselves. For these measurements, I used the commercial phase-noise analyser[58].

It must be noted, however, that a full evaluation of the FNC system requires the comparison of the stabilised fibre optical output with an optical reference with much

[53] Mini-Circuits ZHL-1-2W-S+
[54] Mini-Circuits ZRPD-1+
[55] Rigol DG4162
[56] Mini-Circuits ZHL-1-2W-S+
[57] Rigol DG4202
[58] Symmetricom TSC5120A

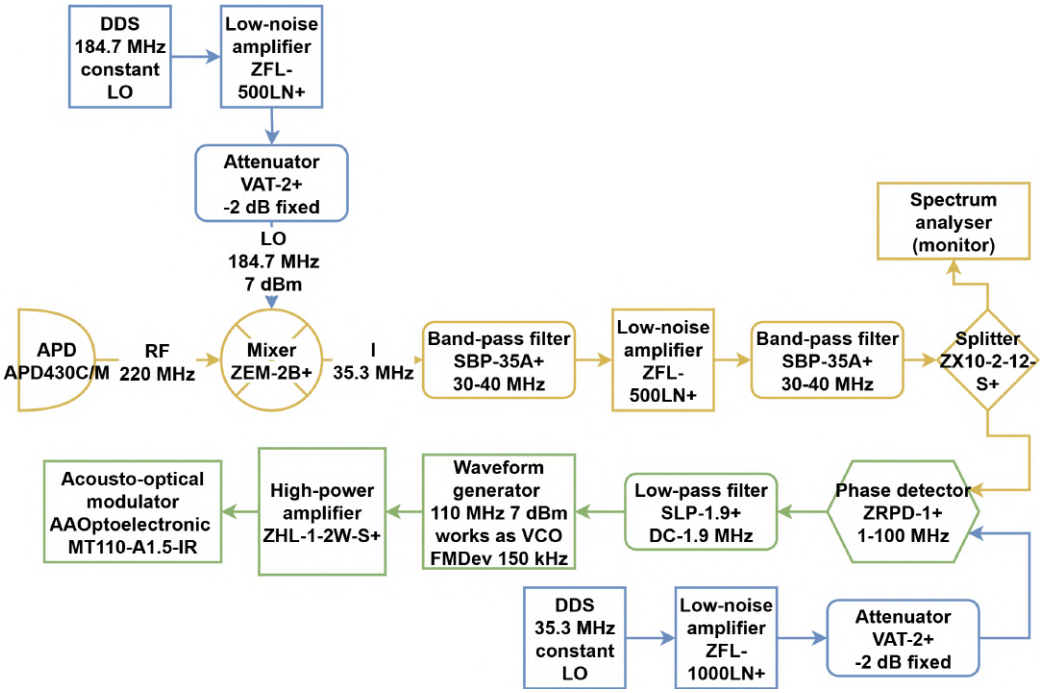

Figure 5.24: The electronic system used for FNC in the supporting arm transfers the stability from the light distribution system for the optical amplifier. The beatnote and LO signals are amplified to 7 dBm for compatibility with the analogue phase detector. The resulting error signal is processed by a waveform generator acting as a VCO, which drives the AOM for active phase noise compensation. Coloured blocks indicate signal paths: yellow for input signal processing, blue for LOs, and green for the feedback loop.

better stability [203]. The approach I used here assumes that all noises are reciprocal [204], and the delay between the forthcoming and returning beams inside the fibre is negligible. If there is phase noise on the transmitted signal from fibre noise, $S_{\text{fibre}}(f)$, then even for perfect cancellation of this noise on the round-trip light, the one-way light will still suffer from delay-unsuppressed fibre phase noise [198]

$$S_{\text{out}}(f) = \frac{1}{3}\left(\frac{2\pi f L}{c_n}\right)^2 S_{\text{fibre}}(f), \tag{5.4.2}$$

where $c_n \approx 2 \times 10^8$ m/s is the speed of light in the fibre.

The results of the stability measurements are presented in Figure 5.26. These data confirm the necessity of employing active noise compensation. Without such systems, the overall relative stability of the optical setup would be significantly compromised and would not reach below 10^{-16}. It is important to note that the phase-noise analyser is equipped with only one input and one reference channel. Therefore, all stability measurements were performed sequentially rather than simultaneously.

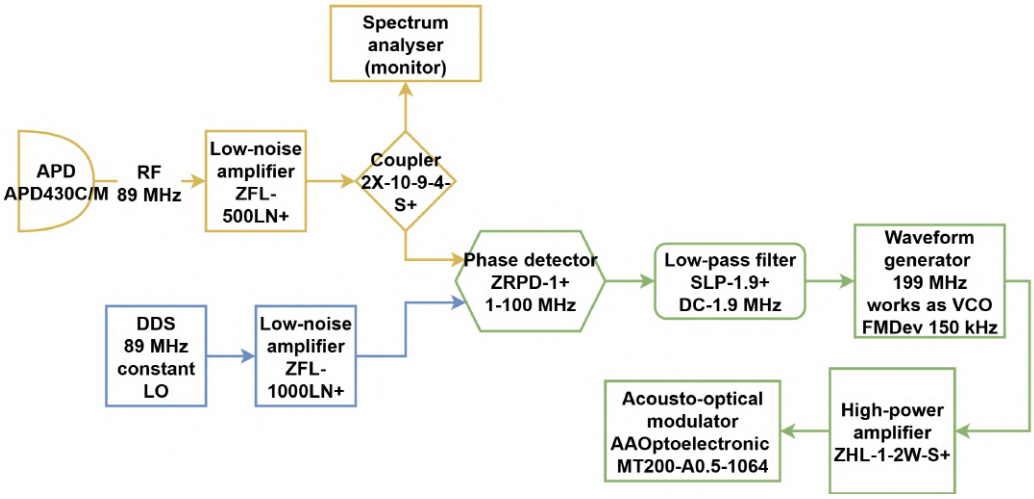

Figure 5.25: The electronic setup used for cancelling noise from both the optical fibre and the optical amplifier. The system omits frequency mixing, as the beatnote lies within the bandwidth of the analogue phase detector. The error signal is fed into a VCO, amplified, and used to drive the AOM for active optical phase noise cancellation. Coloured blocks indicate signal paths: yellow for input signal processing, blue for LOs, and green for the feedback loop.

5.4.2 Laser Frequency Stabilisation to Ultra-stable Optical Cavity

I stabilise the frequency of the fibre laser[59] to the resonance fringe of the ultra-stable optical cavity using the PDH technique. This method involves phase modulation of the input beam and detecting the interference between the reflected and leakage signals from the cavity using an avalanche photodiode. The schematic diagram of the electronic implementation is shown in Figure 5.27.

The interference signal is detected using an avalanche photodiode[60]. The photodiode is mounted on the post, custom-made from polyoxymethylene (Ertacetal) for galvanic isolation and minimisation of the electrical noise. I split the photodiode signal to enable simultaneous monitoring on a spectrum analyser and demodulation using an analogue phase detector[61]. The demodulation is performed using a 6 MHz, 7 dBm sinusoidal signal generated by a two-channel waveform generator[62]. One channel drives the EOM[63], while the other serves as the reference input for the phase detector. I optimise the relative phase between the two signals to maximise the slope of the resulting error signal.

[59] NKT BASIK Y10
[60] Thorlabs APD410C/M
[61] Mini-Circuits ZRPD-1+
[62] Siglent SDG1010
[63] Exail NIR-MPX-LN-0.1

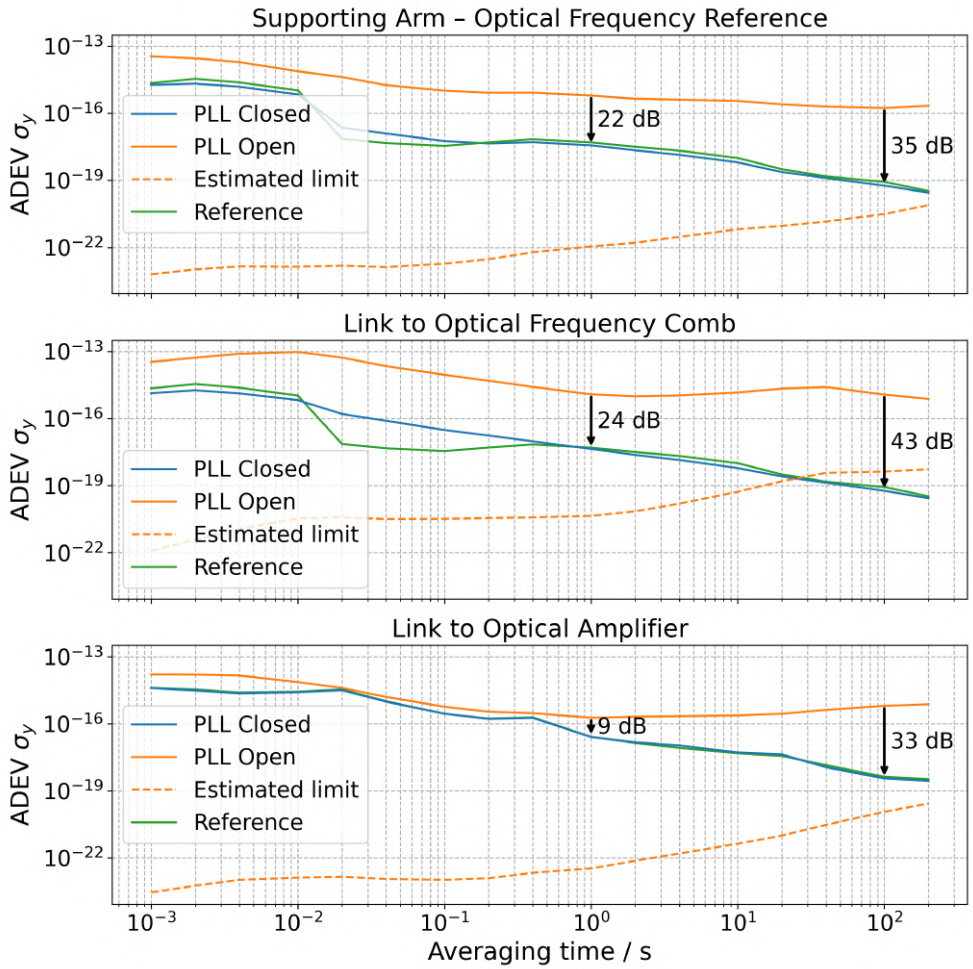

Figure 5.26: Non-overlapping ADEV σ_y of the beatnote signals measured for all fibre links in the system. Each subplot corresponds to a different fibre link: (top) supporting arm; (middle) link to the OFC; (bottom) link to the optical amplifier. For each link, frequency stability is shown with the PLL open (solid orange), closed (blue), and for the frequency reference (green). The solid-dashed lines represent the estimated stability limit of the transmitted light. The improvement in stability at averaging times of 1 s and 100 s is explicitly marked. The measurements were performed using a commercial phase-noise analyser referenced to UTC (AOS). The phase-noise analyser does not provide confidence intervals. The results highlight the necessity of active FNC to reach the fractional stability below 10^{-16}.

The output of the phase detector consists of a DC error signal superimposed with an RF component oscillating at twice the modulation frequency, i.e. 12 MHz. In standard implementations, this RF signal is filtered out to minimise the noise present in

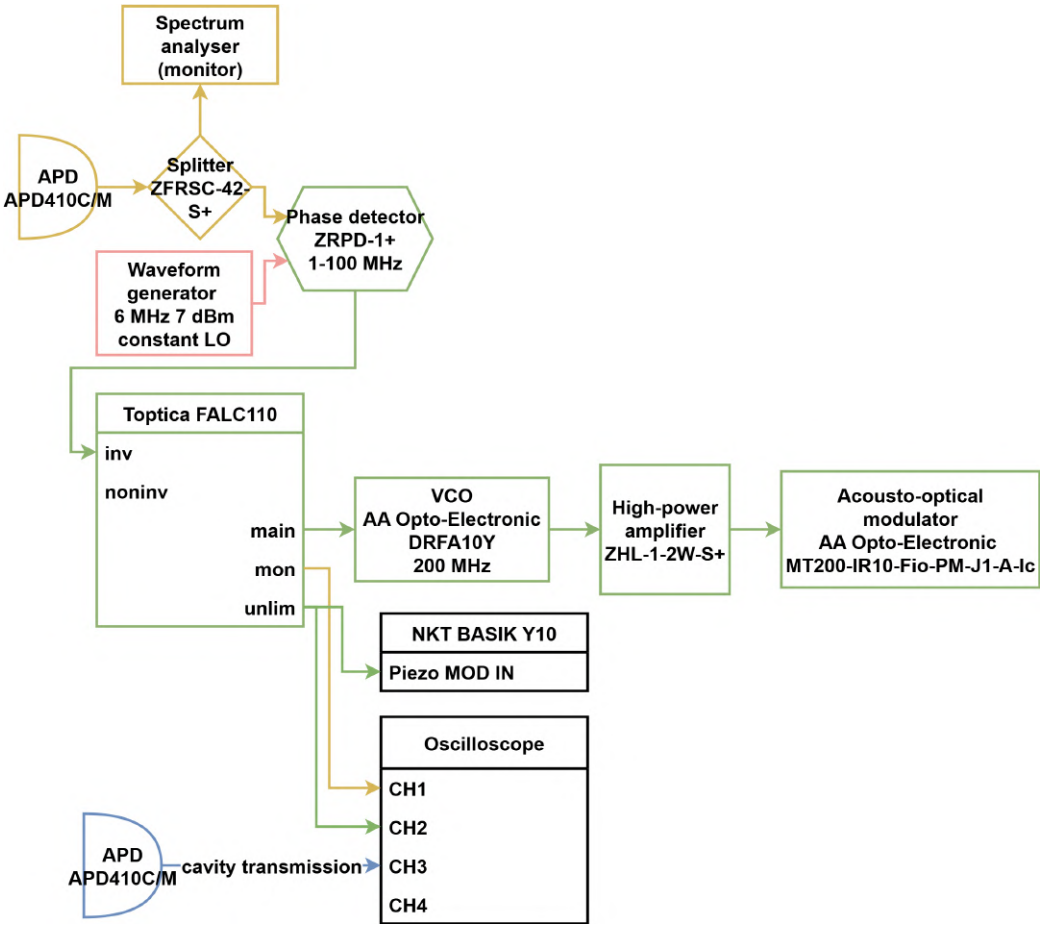

Figure 5.27: Schematic of the electronic setup used to stabilise the 1062.55 nm fibre laser (NKT BASIK Y10) to an ultra-stable optical cavity using the PDH technique. The system includes an EOM driven by a waveform generator, an analogue phase detector for demodulation, and a Toptica FALC 110 PI^{3}D servo controller. The fast feedback loop modulates a VCO driving an AOM, while the slow loop controls the fibre laser's PZT for coarse frequency tuning. Coloured blocks indicate signal paths: yellow for input signal processing, pink for LO, and green for the feedback loop.

the error signal. However, in high-bandwidth laser locking schemes, the low-pass filter introduces a phase delay that significantly limits the achievable loop bandwidth. In my setup, I observed that removing the 1.9 MHz low-pass filter[64] improved the servo-loop bandwidth by almost 200%. This is because the oscillating RF component lies well outside the effective bandwidth of the control loop and is naturally attenuated in the servo chain.

[64] Mini-Circuits SLP-1.9+

The error signal from the phase detector is processed by a PI^{3}D servo controller[65]. The fast output of the controller modulates a VCO[66], which is subsequently amplified and used to drive the fibre-coupled AOM[67]. The slow output of the servo controller feeds back to the PZT integrated into the fibre laser head, enabling coarse frequency tuning.

To optimise the parameters of the servo controller, I monitored the photodiode signal on a spectrum analyser. The recorded spectrum is shown in Figure 5.28. The

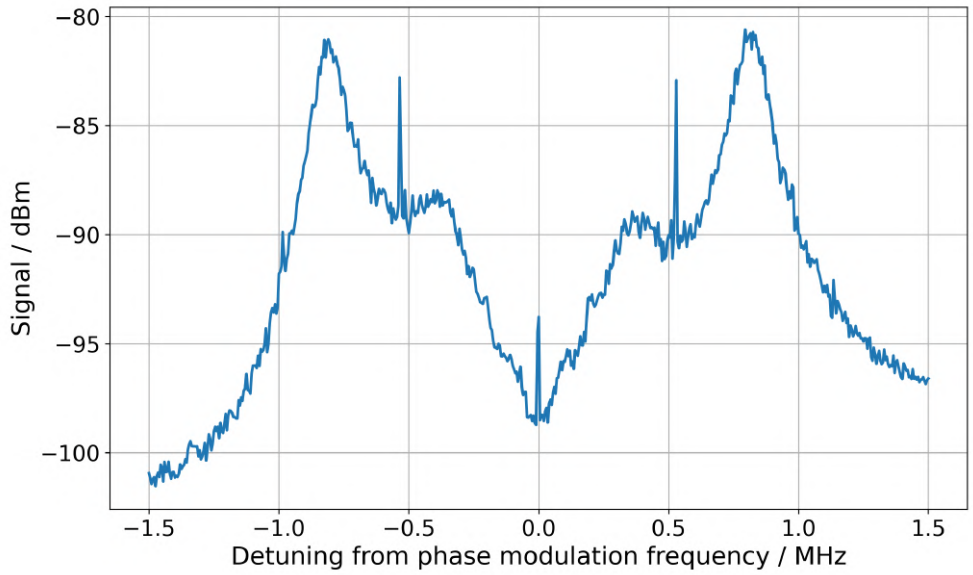

Figure 5.28: Spectrum of the reflection signal from the ultra-stable optical cavity, recorded using a spectrum analyser for the optimisation of the PDH locking loop. The trace is centred at the 6 MHz phase modulation frequency. The servo bump indicates a loop bandwidth exceeding 790 kHz. A residual peak at the carrier frequency originates from electronic cross-talk, imperfect mode matching, and input offset drift in the analogue servo controller.

spectrum is centred at the phase modulation frequency of 6 MHz. The objective of the optimisation process is to push the servo bump, an indicator of the control bandwidth, as far from the carrier as possible and to achieve a deep, flat dip around the centre frequency. A narrow residual peak at 6 MHz remains visible and originates from three sources.

Firstly, it is partly caused by cross-talk between coaxial cables, as the peak persists even when the servo loop is open. Secondly, imperfect optical injection into the cavity

[65] Toptica FALC 110
[66] AA Opto-Electronic DRFA10Y
[67] AA Opto-Electronic MT200-IR10-Fio-PM-J1-A-Ic

may result in a portion of the light being reflected back towards the photodiode. This can arise from non-ideal mode-matching conditions or from an electronic offset in the feedback loop that prevents the laser from locking exactly at the centre of the cavity resonance.

The third and most significant contributor is the drifting input offset of the analogue servo controller itself. This offset variation results in oscillations of the peak amplitude at 6 MHz. I minimise this effect by carefully adjusting the input offset parameter on the controller from time to time.

Based on the observed spectral features, I estimate the servo-loop bandwidth to exceed 790 kHz.

5.4.3 Measurement of Frequency Beatnote with Optical Frequency Comb

Interference between the laser beam and the OFC mode gives rise to a frequency beatnote. This beatnote, typically in the RF domain, is detected using an avalanche photodiode and manifests as an electrical sinusoidal signal. The primary objective is to determine the frequency of this signal, and it can be analysed using either a spectrum analyser or a frequency counter.

In practice, the signal captured by the photodiode often contains not only the desired beatnote but also spurious components resulting from electronic noise or cable crosstalk. The use of a spectrum analyser is advantageous in such cases, as it can reliably identify the spectral peak corresponding to the beatnote, irrespective of the exact spectral shape or the presence of neighbouring signals. However, spectrum analysers are typically limited by their relatively slow measurement rate and single-channel architecture, which restricts the possibility of simultaneously monitoring multiple beatnotes.

For this reason, frequency counters are more widely employed in multi-channel beatnote measurement setups. Further details concerning the operating principles of frequency counters are provided in Section 4.2.4.

Frequency counters, however, are particularly sensitive to unwanted signals in the input spectrum. As such, careful signal conditioning is required before measurement. If an accuracy better than approximately 100 Hz is not required, passive band-pass filtering is generally sufficient. For higher precision measurements, however, the systematic error introduced by the filter must be considered.

This bias arises from the fact that the bandwidth of standard band-pass filters is often much broader than the spectral width of the beatnote signal and may not be centred exactly on the signal frequency. Such misalignment results in an asymmetric transmission profile, which can shift the apparent frequency measured by the counter. This effect becomes evident when the same beatnote signal is routed to different channels of a frequency counter and produces systematically different readings. If the discrepancy

exceeds the expected frequency stability of the system, the influence of filter-induced bias can no longer be neglected.

Such behaviour was present in my system, and I addressed it by implementing a tracking oscillator, also called a phase tracking filter or an adaptive frequency filter [205]. This device generates a clean sinusoidal signal whose frequency follows that of the input beatnote via a PLL. The resulting signal is free from spurious components and is thus well-suited for frequency measurement using a frequency counter. The schematic diagram of the implemented setup is shown in Figure 5.29.

I detect the interference between the laser beam and the OFC mode using an avalanche photodiode[68]. The resulting RF signal passes through a 100 MHz low-pass filter and is amplified with a low-noise amplifier. I then split the signal: one branch is used for monitoring and diagnostics, while the second is further amplified to 7 dBm and fed into an analogue phase detector[69]. This signal serves as the reference input for the PLL, which forces the oscillator to follow the beatnote frequency. This part of the setup is highlighted in yellow in Figure 5.29.

I use the frequency counter[70], which supports input signals up to 60 MHz. Since the beatnote lies at 96 MHz and the OFC is shared with other laboratories, I cannot modify the repetition rate to shift the beatnote. To address this, I implement frequency division within the tracking oscillator system.

I use a waveform generator with frequency modulation capability to produce a sinusoidal signal at 48 MHz, i.e., half the beatnote frequency. I split this signal into two paths: one goes to the frequency counter, while the other goes to a passive frequency doubler[71]. After amplification and filtering, the doubled 96 MHz signal is applied to the second input of the phase detector. This portion of the system is shown in blue in Figure 5.29.

The two signals have similar frequencies, so the phase detector output contains a slowly varying component corresponding to the frequency difference, as well as higher-frequency terms. I filter the output using two low-pass filters: a standard 1.9 MHz filter and a custom-built 40 kHz filter. The filtered signal modulates the frequency of the waveform generator, completing the PLL and enabling the generated signal to track the beatnote frequency accurately. This feedback loop is depicted in green in Figure 5.29.

The use of the tracking oscillator ensures reliable and accurate measurement of the frequency beatnote using the available frequency counter. This solution allows me to eliminate spurious signals, mitigate measurement bias, and accommodate the signal to the frequency counter without relying on changes to the OFC system.

[68] Thorlabs APD430C/M
[69] Mini-Circuits ZRPD-1+
[70] K+K FXE65
[71] Mini-Circuits MK-2

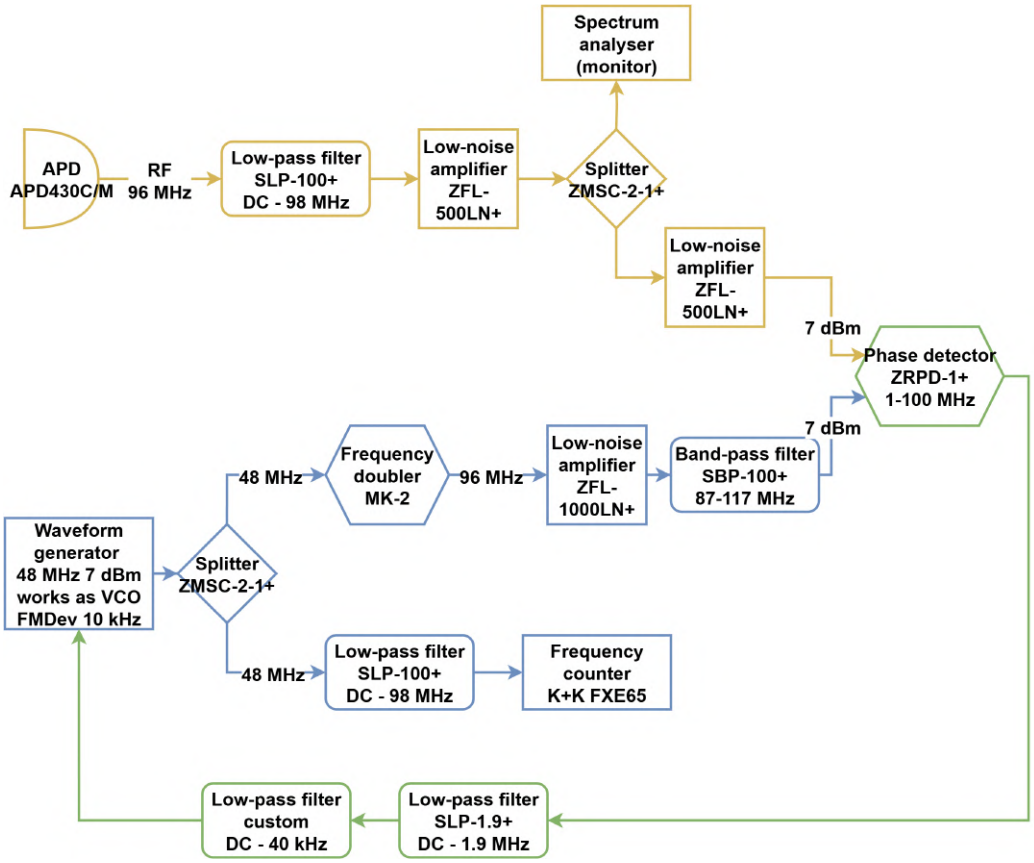

Figure 5.29: Schematic of the tracking oscillator system used to enable accurate measurement of the optical frequency beatnote. The beatnote signal, detected by an avalanche photodiode, is filtered, amplified, and fed into an analogue phase detector as the reference. A waveform generator produces a 48 MHz signal, which is both measured by a frequency counter and frequency-doubled to 96 MHz to match the beatnote. This doubled signal is compared with the input beatnote in the phase detector. The resulting error signal is low-pass filtered and used to modulate the frequency of the waveform generator, forming a closed PLL. Coloured regions indicate signal paths: yellow for input signal processing, blue for oscillator and division, and green for the feedback loop.

5.4.4 Frequency Stability Characterisation

To determine the frequency stability of the ultra-stable 1062.55 nm laser, I had to compare its output with other oscillators exhibiting comparable or superior stability. During the characterisation campaign, I had access to two independent references: an OFC locked to a 1542 nm ultra-stable laser stabilised to a separate high-finesse cavity at FAMO (referred to as the FAMO 1.5 µm cavity), and a fibre-delivered optical sig-

nal referenced to a state-of-the-art ULE glass cavity at Physikalisch–Technische Bundesanstalt (PTB) in Germany [132], denoted as the PTB 1.5 µm cavity. The PTB optical reference was delivered to Toruń via a phase-noise-compensated long-haul fibre link established within the pan-European research and education network (GEANT) Time & Frequency Pathfinder [206, 207], spanning the German GEANT segment and the Polish Polish National Research and Education Network (PIONIER) backbone operated by Poznań Supercomputing and Networking Center (PSNC) [208], and employing ELSTAB-based repeater stations developed at AGH University of Kraków (AGH) [178].

My objective is to characterise the individual frequency stability of each oscillator using either the TCH method or the GCOV approach. Detailed descriptions of these techniques are provided in Section 4.2.3.

The experimental setup allows me to simultaneously record two optical beatnotes using a frequency counter[72] operated in Λ-mode. The data acquisition time was 4300 s. The first beatnote corresponds to the frequency difference between the FAMO 1.5 µm cavity and PTB 1.5 µm cavity. The second beatnote is between my 1062.55 nm laser, stabilised to the FAMO 1 µm cavity, and the OFC[73], which is optically referenced to the FAMO 1.5 µm cavity. In this configuration, the OFC acts as a transfer oscillator.

The specified instability of the OFC does not exceed 1×10^{-16} at 1 s, allowing me to neglect its contribution in the analysis. The missing beatnote between the FAMO 1 µm cavity and the PTB 1.5 µm cavity is obtained by taking the difference between the two measured beatnotes after appropriate frequency scaling. This approach is justified by the negligible contribution of the beat detection system to the overall noise.

To perform the scaling, I convert the beatnote between the FAMO 1 µm and 1.5 µm cavities to the 1542 nm optical frequency basis by multiplying the measured frequency by the ratio $1062.55\ \text{nm}/1542\ \text{nm}$. This allows the calculation of the FAMO 1 µm versus PTB 1.5 µm beatnote by simple subtraction. All beatnote signals are converted to relative frequencies by dividing by $c/1542$ nm, where c is the speed of light. From each resulting dataset, I remove a linear frequency drift and compute the OADEV. The fractional frequency stabilities of all oscillator pairs are shown in Figure 5.30.

I do not expect correlations between the cavities, since the FAMO 1.5 µm and FAMO 1 µm cavities are located in separate parts of the building, and the PTB cavity resides in a facility located in a different country. This allows me to use the TCH method to estimate the individual stabilities of each oscillator. The results of this analysis are presented in the upper panel of Figure 5.31.

From the TCH analysis, I obtain the stability of the FAMO 1 µm and 1.5 µm cavities and PTB 1.5 µm cavity as 7.2×10^{-16}, 2.3×10^{-15}, and 2.8×10^{-15} at 1 s, respectively. Although the method is effective for comparably stable oscillators, it can

[72] K+K FXE65

[73] Menlo FC1500-ULN

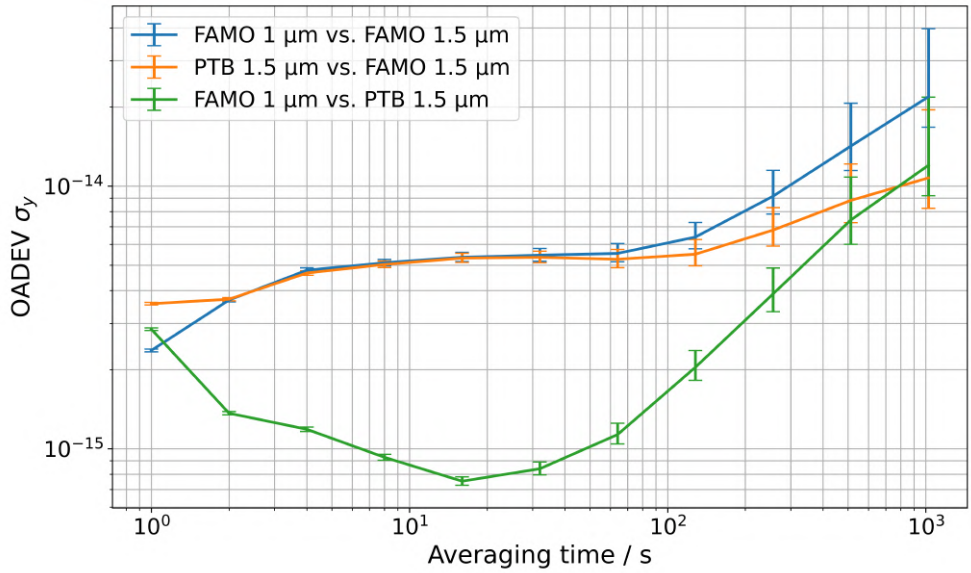

Figure 5.30: OADEV of the relative frequency fluctuations for all measured oscillator pairs: FAMO 1 µm cavity versus FAMO 1.5 µm cavity (blue), FAMO 1.5 µm cavity versus PTB 1.5 µm cavity (orange), and FAMO 1 µm cavity versus PTB 1.5 µm cavity (green). At 1 s averaging time, the respective stabilities are approximately 2.4×10^{-15}, 3.6×10^{-15}, and 2.9×10^{-15}. The data is corrected for linear frequency drifts and converted to fractional frequency units. The confidence intervals of $\pm 1\sigma$ are calculated using the χ^2 statistics.

yield negative variances when applied to combinations with large disparities in performance, correlations, or insufficient averaging. As a result, the TCH method is unable to reliably determine the stability of the PTB 1.5 µm cavity for all considered averaging times.

To address this issue, I apply the GCOV technique, which enables reliable stability estimation even in the presence of a low-noise reference. The results of the GCOV analysis are shown in the lower panel of Figure 5.31.

The GCOV analysis yields values consistent with the TCH method for all cavities at 1 s. At 1 s, the PTB cavity exhibits a stability of 2.8×10^{-15}, which improves to 2.1×10^{-16} at 16 s. This behaviour is expected, as the short-term stability is limited by the performance of the optical fibre link delivering the reference signal from PTB.

The results presented in this section confirm the performance of the FAMO 1 µm cavity and the laser system. This cavity serves as the most stable short-term optical reference currently available within the institute.

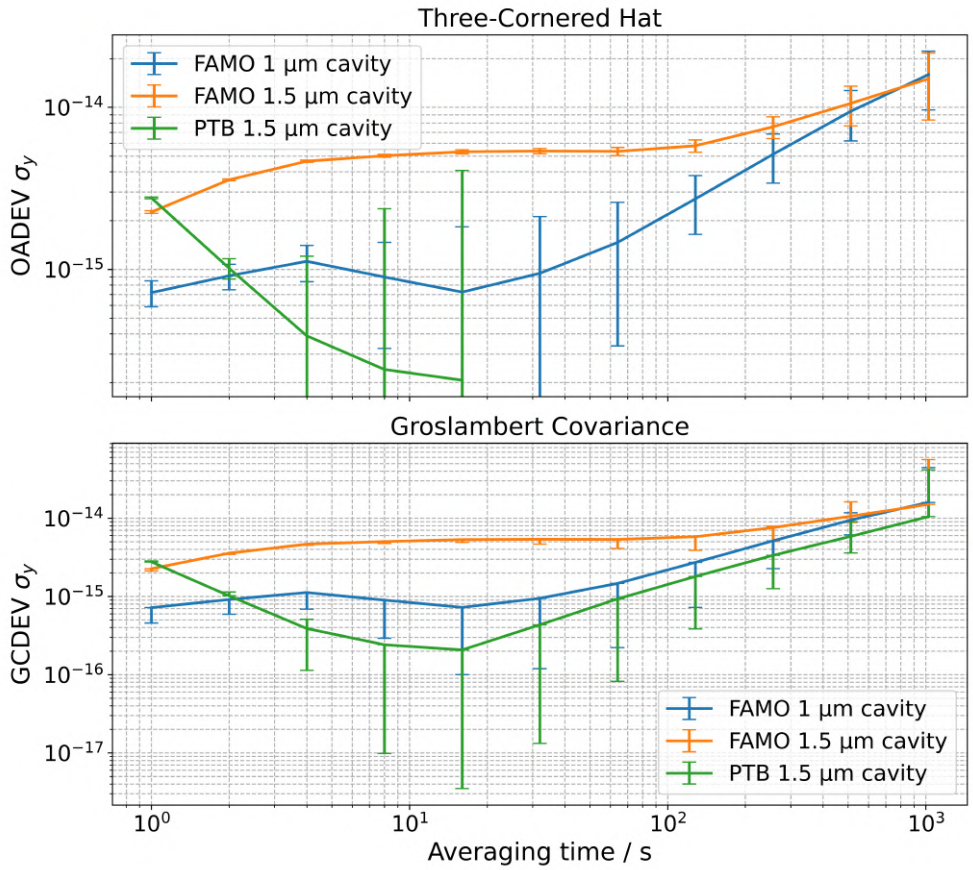

Figure 5.31: Fractional frequency stability of the FAMO 1 µm (blue), FAMO 1.5 µm (orange), and PTB 1.5 µm (green) cavities. **Top panel:** Stability estimated using the TCH method. At 1 s averaging time, the estimated stabilities are 7.2×10^{-16} for the FAMO 1 µm cavity, 2.3×10^{-15} for the FAMO 1.5 µm cavity, and 2.8×10^{-15} for the PTB 1.5 µm cavity. The confidence intervals of $\pm 1\sigma$ are calculated using the propagation of the confidence intervals of the stability of oscillator pairs. **Bottom panel:** Stability estimated using the GCOV method. At 1 s averaging time, the stabilities are 7.2×10^{-16} for the FAMO 1 µm cavity, 2.3×10^{-15} for the FAMO 1.5 µm cavity, and 2.8×10^{-15} for the PTB 1.5 µm cavity. The confidence intervals of $\pm 1\sigma$ are obtained via a Studentised moving-block bootstrap [209, 210]. The GCOV analysis confirms agreement with the TCH results and provides an estimate for the PTB cavity, which exhibits superior stability of 2.1×10^{-16} at 16 s.

5.5 Laser Systems for Metastable States Depopulation

This section describes the design, construction, and characterisation of the laser systems developed for repumping Hg atoms from the metastable $^3P_0$ and $^3P_2$

states to the ground $^1S_0$ state. These repumping transitions are essential for determining the population in the $^3P_0$ state.

I begin by presenting the optical setup of the two repumping lasers: a 404.7 nm ECDL for addressing the $^3P_0$–$^3S_1$ transition, and a 1092.2 nm diode laser system, frequency-doubled to 546.1 nm for addressing the $^3P_2$–$^3S_1$ transition. The section continues with an overview of the digital frequency stabilisation scheme I implemented, which references the laser wavelength to a wavelength meter via a proportional–integral feedback loop. Finally, I describe the mechanical and optical construction of the custom-made ECDLs, including the feedback geometry, thermal control, and integration with digital electronics.

5.5.1 Optical Setup for Metastable States Depopulation

To determine the fraction of atoms excited to the $^3P_0$ state, it is necessary to repump atoms from the metastable $^3P_0$ and $^3P_2$ states back to the ground $^1S_0$ state. This is achieved via the $^3P_0$–$^3S_1$ (404.7 nm) and $^3P_2$–$^3S_1$ (546.1 nm) transitions, both of which have natural linewidths of 20 MHz due to the relatively short lifetime of the $^3S_1$ state, estimated to be $8.0(7)$ ns.

To access these transitions, I constructed and implemented two ECDL systems. One system emits directly at 404.7 nm, while the other operates at 1092.2 nm and is frequency-doubled to produce 546.1 nm. The optical configurations of both systems are illustrated in Figure 5.32.

The 404.7 nm laser system (Panel B in Figure 5.32) delivers approximately 30 mW of optical power after the OI when operating at 100 mA. A small portion of the beam is directed to a wavelength meter using a NPBS-P. The main beam is shaped with a pair of spherical lenses to improve coupling efficiency into a 10 m-long single-mode fibre. At the fibre output, the light is coupled into a large-beam collimator[74], which produces a 5.3 mm diameter beam with approximately 8.5 mW of power. The shape of the beam is shown in Figure 5.33.

The 1092.2 nm laser system (Panel A in Figure 5.32) provides around 300 mW of power after the OI when operating at 455 mA. A small portion of the beam is decoupled towards a wavelength meter. The main beam suffers from astigmatism typical of laser diodes and is corrected in the parallel axis using a pair of cylindrical lenses. The astigmatism-corrected beam is then reshaped with spherical lenses to optimise fibre coupling into a PM fibre connected to a single-pass PPLN waveguide mixer[75]. The phase-matching condition is maintained by stabilising the crystal temperature. With over 200 mW of input power at 1092.2 nm, the system produces more than 12 mW of light at 546.1 nm. The fibre output is collimated using a collimator[76], generating a

[74] Thorlabs F810APC-405
[75] HC Photonics
[76] Thorlabs F810APC-543

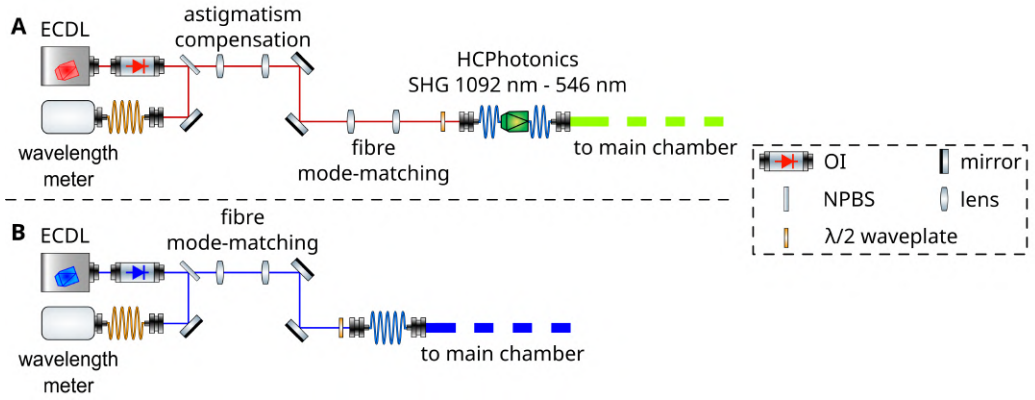

Figure 5.32: Optical layout of the ECDL systems used for depopulating metastable $^3P_0$ and $^3P_2$ states to the ground $^1S_0$ state. Panel A shows the 1092.2 nm ECDL system with astigmatism compensation and frequency doubling in a single-pass PPLN waveguide mixer to generate 546.1 nm light for addressing the $^3P_2$–$^3S_1$ transition. Panel B shows the 404.7 nm ECDL system used for driving the $^3P_0$–$^3S_1$ transition. In both setups, a small portion of the beam is directed to a wavelength meter, while the main beam is coupled into a single-mode optical fibre and subsequently collimated for delivery to the main chamber.

6.4 mm diameter beam.

The saturation intensities for these transitions are given by

$$I_{\text{sat}} = \frac{\pi h c \Gamma}{3\lambda^3}, \tag{5.5.1}$$

where h is Planck's constant, c is the speed of light, Γ is the natural linewidth in radians per second, and λ is the wavelength. For the $^3P_0$–$^3S_1$ transition at 404.7 nm and the $^3P_2$–$^3S_1$ transition at 546.1 nm, the corresponding saturation intensities are approximately $0.39\ \text{mW/mm}^2$ and $0.16\ \text{mW/mm}^2$, respectively. Based on the beam diameters, the estimated minimum optical powers required to reach saturation are approximately 8.7 mW and 5.2 mW for the 404.7 nm and 546.1 nm beams, respectively. The optical powers generated by both systems comfortably exceed these thresholds.

5.5.2 Digital Stabilisation of Laser Frequency to Wavelength Meter

Due to the relatively broad linewidths of the repumping transitions, it is not necessary to stabilise the frequency of the repumping lasers to narrow optical references such as high-finesse cavities, OFCs, or atomic transitions. Instead, I monitor the laser fre-

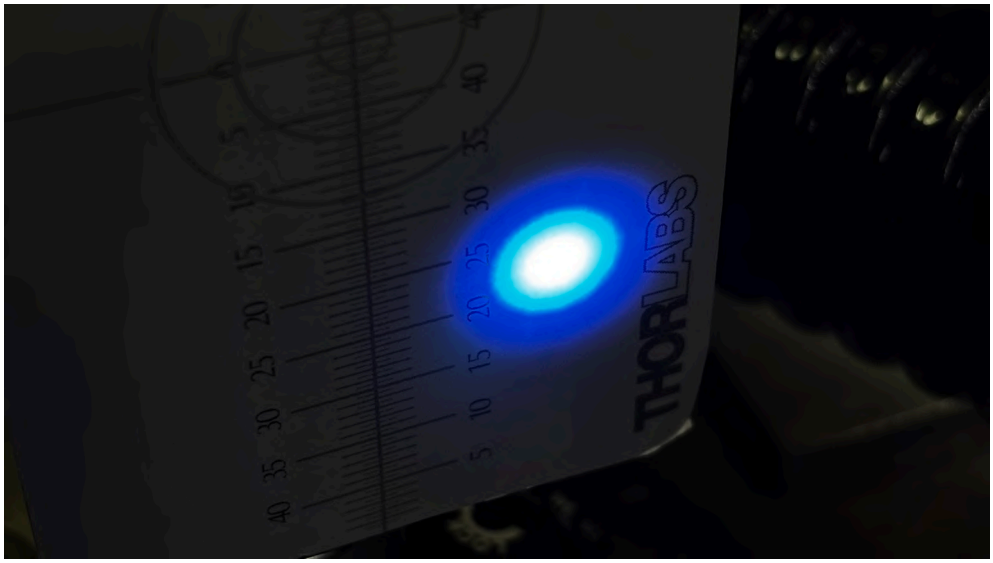

Figure 5.33: Photo of the 404.7 nm laser system output beam after a large-beam collimator. The output beam has a clean Gaussian profile.

quencies using a wavelength meter[77]. The specified absolute accuracy of the calibrated HighFinesse WS7-60 is no worse than tens of megahertz, while its short-term stability is significantly better. These characteristics make it well-suited for implementing a digital frequency stabilisation scheme.

I implement the stabilisation using a Python 3 script running on a PC connected to the wavelength meter via USB. The script continuously compares the measured wavelength with a predefined setpoint, and the resulting difference serves as an error signal. I process this signal using a proportional–integral control algorithm to compute the correction voltage.

The control signal, ranging from 0 to 150 V DC, is applied to a PZT mounted inside the extended cavity of the laser. This voltage is supplied by a high-voltage amplifier[78], which communicates with the control PC via USB. The full source code for the stabilisation routine is provided in [211].

The script communicates with the wavelength meter indirectly, by querying its proprietary control software through the `wlmData.dll` interface. This dynamic link library enables real-time access to wavelength readings from the selected channel without interrupting the wavemeter routines. Upon execution, the script prompts the user to configure key parameters, including the wavemeter channel, the high-voltage amplifier channel, and the target wavelength. The user must also specify the polarity of the control response, which determines whether increasing or decreasing the applied voltage

[77] HighFinesse WS7-60
[78] Vescent SLICE-DHV

results in a higher laser wavelength. Moreover, the correct VISA address of the high-voltage amplifier must be supplied to ensure successful serial communication. Once initialised, the script acquires the current wavelength at fixed time intervals, calculates the error relative to the target, and updates the control voltage accordingly. All relevant quantities—including the measured wavelength, setpoint, and applied voltage—are logged continuously for further analysis and verification.

To assess the performance of the frequency stabilisation system, I measured the wavelength stability of the 1092.2 nm laser with the digital feedback loop enabled and disabled over an extended period. The results of these measurements are shown in Figure 5.34. They clearly demonstrate the necessity of applying digital stabilisation, as without feedback, the laser exhibits a gradual drift from its initial wavelength, corresponding to a detuning from the optical transition and thus a significant reduction in the repumping efficiency. With the loop closed, the stability improves markedly for averaging times exceeding 3 s and reaching an enhancement of 33 dB after one hour. I note, however, that this measurement is performed relative to the wavelength meter and does not account for the stability of the reference itself. A complete characterisation of the laser frequency stability would require, for example, heterodyne detection against a laser of superior frequency stability.

5.5.3 Custom-made Extended-Cavity Diode Laser

I constructed the ECDLs for 1092.2 nm and 404.7 nm based on the design described in [172], which I modified to streamline the construction and significantly simplify the alignment procedure. Each ECDL operates in a Littrow configuration [212], where a reflective diffraction grating acts as a wavelength-selective element. The first-order diffracted beam is directed back into the laser diode, forming the extended cavity, while the zeroth-order reflection serves as the main output beam. A schematic diagram of the ECDL structure is shown in Figure 5.35.

The main modification I introduced compared to the original design in [172] is the implementation of adjustable laser diode collimation tubes fitted with a pre-mounted aspheric lens[79]. The position of the lens can be adjusted by up to 2.5 mm by rotating the end cap of the tube. Importantly, the lens translates without rotating, which improves pointing stability. Owing to the extended travel range, these collimation tubes are compatible with a wide variety of standard laser diodes. The lens is anti-reflection coated across three overlapping spectral bands, covering a combined wavelength range from 350 nm to 1700 nm.

The laser diode (Innolume GC-1030-160-TO-200-B for 1092.2 nm and Toptica LD-0405-0060-2 for 404.7 nm) is mounted inside the collimation package, and I adjusted the lens position to collimate the output beam in the far field. The LD-0405-

[79] Thorlabs LTN330

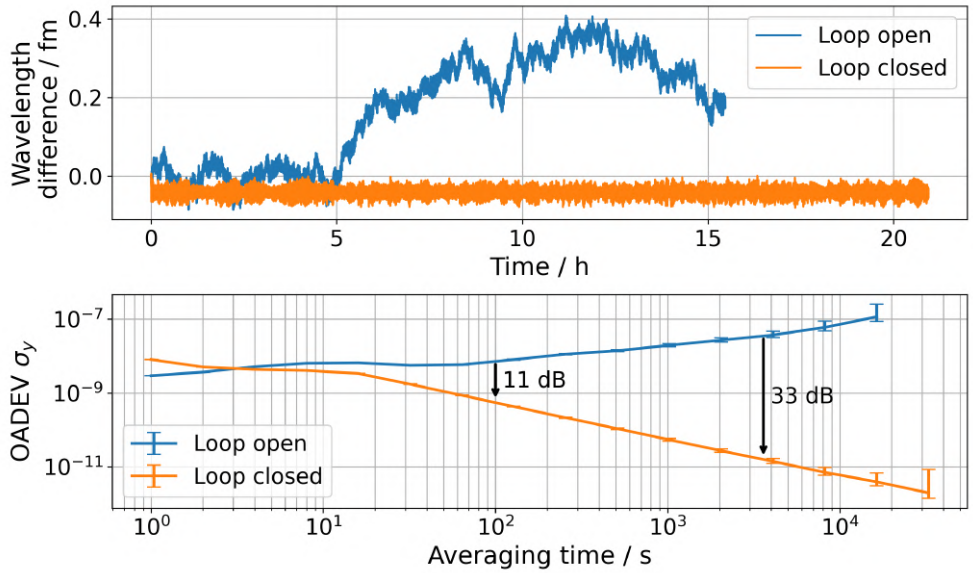

Figure 5.34: Wavelength stability of the 1092.2 nm laser with the digital stabilisation loop open (blue) and closed (orange). The upper panel shows the wavelength difference relative to the initial value, measured over more than 15 hours. Without stabilisation, the laser exhibits significant drift. The lower panel presents the corresponding OADEV σ_y as a function of averaging time. For timescales longer than 3 s, the closed-loop system provides improved stability, with enhancements of 11 dB at 100 s and 33 dB at 3600 s. The measurement is referenced to the wavelength meter and does not include its own instability. The confidence intervals of $\pm 1\sigma$ are calculated using the χ^2 statistics.

0060-2 diode is a transverse single-mode FP type, featuring an internal resonator formed by the facets of the semiconductor chip. This diode is capable of lasing without an external cavity but typically operates in multiple longitudinal modes. In contrast, the GC-1030-160-TO-200-B diode is equipped with an anti-reflection coating on its output facet, effectively suppressing internal feedback. Such diodes, often referred to as gain chips, do not lase within the nominal current range without optical feedback and are therefore particularly well-suited for use with external cavities, as they eliminate resonant competition between internal and external modes and reduce the required level of optical feedback.

The collimated beam is incident on a holographic reflective diffraction grating[80]. The diffraction efficiency of these gratings varies between 10% and 55%, depending on the polarisation of the incoming light, enabling tuning of the optical feedback to optimise the laser's spectral characteristics. I set the polarisation by rotating the collimation package with the diode. For the 1092.2 nm laser, the feedback is set to approximately

[80]Thorlabs GH13-12V for 1092.2 nm and Thorlabs GH13-36U for 404.7 nm

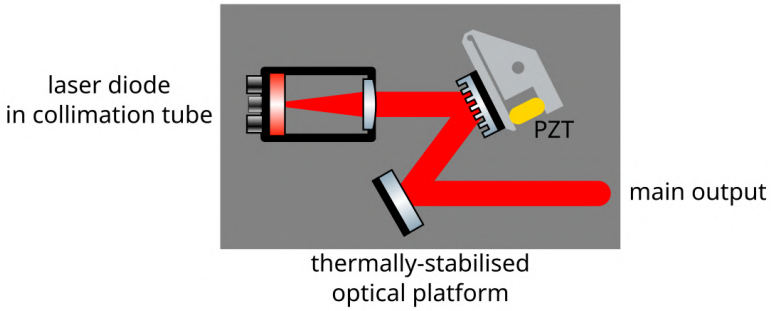

Figure 5.35: Schematic diagram of the optical layout of the ECDL. The system operates in a Littrow configuration, with the first-order diffraction providing optical feedback to the laser diode and the zeroth-order reflection forming the main output. The diffraction grating is mounted on a PZT-controlled arm for fine tuning, and the entire optical path is mounted on a thermally stabilised platform.

10%, while for the 404.7 nm system, the feedback is increased to approximately 30%. The typical distance between the diode facet and the grating is around 25 mm, corresponding to a longitudinal mode spacing of approximately 6 GHz. The grating is mounted on a pivoting arm, which I can rotate to perform coarse wavelength selection. To assist with initial alignment, I used a 3D-printed angular template set to the Littrow angle

$$\alpha = \arcsin\left(\frac{\lambda}{2a}\right), \tag{5.5.2}$$

where λ is the operating wavelength and a is the groove spacing of the grating.

I mounted the diffraction grating on a flexible arm that can be bent using a PZT[81], mechanically supported by a fine-thread adjustment screw. The holder geometry is designed such that the pivot point lies approximately at the intersection of the grating surface and the mirror plane. This configuration is crucial for maintaining the round-trip optical phase independently of the feedback wavelength [213]. In this arrangement, the feedback is synchronous with cavity mode scanning, meaning that the reflected wave retains a constant phase with respect to the incident wave during tuning. It is important to note that, unlike in a conventional optical cavity, the cavity length here determines only the longitudinal mode spacing around the feedback wavelength, not the absolute frequencies of the modes. For this reason, some authors avoid referring to the mode spacing as the cavity FSR .

The zeroth-order reflection from the grating is redirected by a mirror mounted on a secondary arm mechanically linked to the grating holder. This ensures that the mirror remains parallel to the grating, thereby converting the angular movement of the

[81] Thorlabs PC4WM

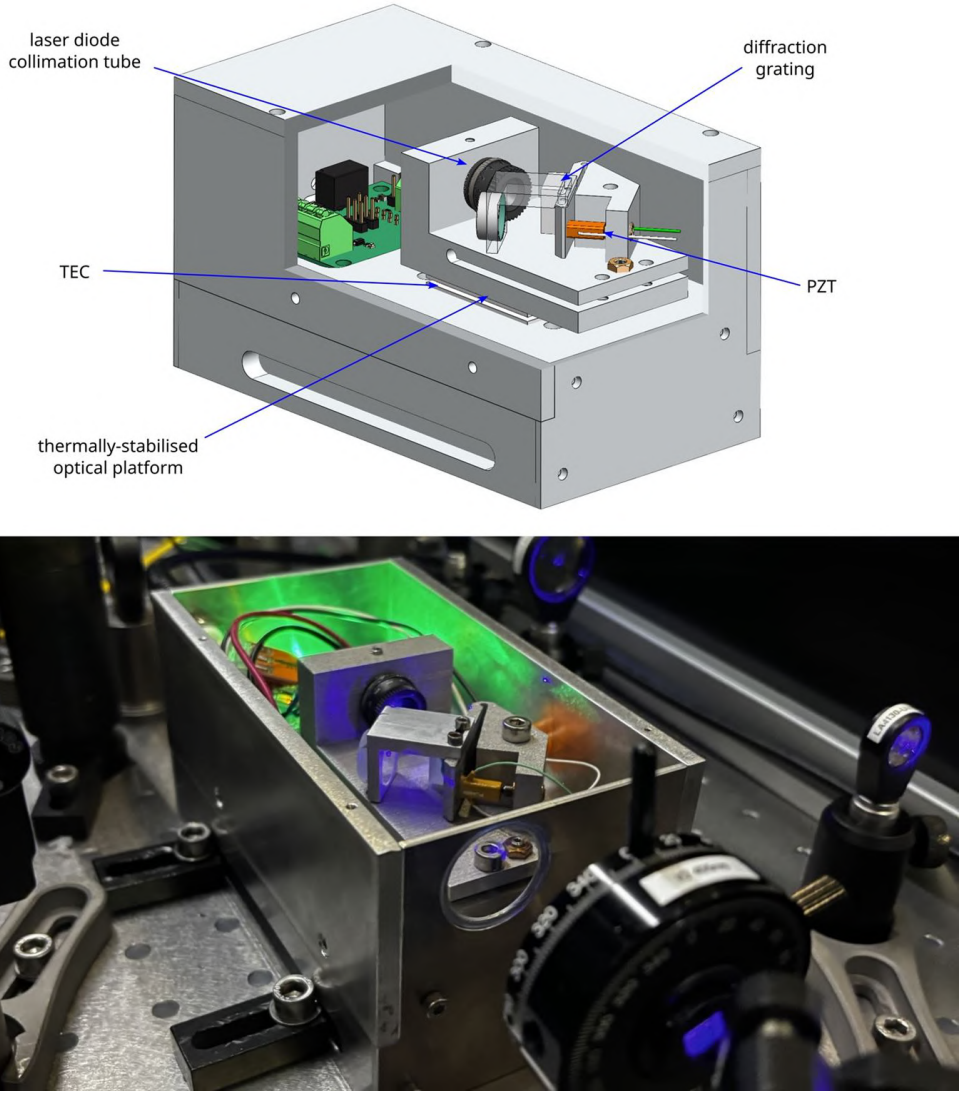

Figure 5.36: **Top image:** CAD model of the ECDL assembly. Key components include the laser diode collimation tube, PZT-driven diffraction grating mount, TEC, and thermally stabilised optical platform. The modular and compact design facilitates stable operation and straightforward alignment. **Bottom image:** Photo of the implemented 404.7 nm ECDL.

diffracted beam into a small lateral displacement. This arrangement significantly enhances pointing stability during frequency tuning. The output beam exits the laser housing through an anti-reflection-coated window. Although the housing is not hermetically sealed, it contains no open apertures, which reduces the cavity's susceptibility to pressure-induced fluctuations.

All of the aforementioned components are mounted on a compact, thermally stabilised optical platform. Temperature is monitored using a 10 kΩ NTC thermistor, which I affixed with thermal adhesive adjacent to the laser diode collimation tube to ensure accurate thermal contact. The platform rests on a TEC, which actively regulates the heat flow to and from the assembly, thereby stabilising both the platform and the laser diode temperature. To minimise parasitic heat conduction, I secure the optical platform using nylon screws. A rectangular cut-out in the platform allows for precise vertical and horizontal adjustment of the feedback beam, facilitating optimal coupling into the laser diode. The TEC itself is mounted onto a large aluminium base, which functions as both the mechanical support and a heat sink. A rendering of the 3D model of the complete laser assembly is shown in Figure 5.36.

I control the laser diode current and temperature using a digital laser diode controller[82], housed within a custom 3D-printed enclosure. Communication with the controller is established via USB from a PC. The PZT is driven by a high-voltage amplifier[83], which I use as part of the digital wavelength stabilisation system described previously.

The complete set of technical drawings, 3D computer-aided design (CAD) models, and a bill of materials is available as a repOD repository [214].

5.6 Optical Lattice and New Main Vacuum Chamber

The optical lattice potential enables the confinement of several thousand neutral atoms over extended periods, typically for a few seconds in a one-dimensional lattice, and up to one minute in a three-dimensional configuration [215]. Such long trapping times permit the use of prolonged interrogation pulses, thereby facilitating the observation of narrow spectroscopic resonances in the optical domain. To confine atoms within the Lamb–Dicke regime, where their motional degrees of freedom are strongly suppressed, a sufficiently intense optical field is required. This field induces an AC Stark shift of the atomic energy levels involved in the clock transition.

The shift of the clock transition frequency arises from the differential AC Stark shift between the two states involved in the $^1S_0 - {}^3P_0$ transition. The idea of the optical lattice clock, proposed by Katori in the early 2000s [123, 216, 217], is that since the AC Stark shift depends on the difference in dynamic polarisabilities of the two states at the lattice laser frequency, it is possible to identify a specific frequency, called the magic wavelength, at which the polarisabilities become equal. At this wavelength, the differential AC Stark shift vanishes to first order, making the clock transition frequency insensitive to fluctuations in the lattice intensity. For a given atomic species, multiple

[82] Koheron CTL200-0
[83] Vescent SLICE-DHV

magic wavelengths may exist. In the case of ^{199}Hg, the most experimentally convenient magic wavelength lies near 362.5 nm.

In this section, I present my design and implementation strategy for integrating the optical lattice into our experimental apparatus. This includes the optical setup of the lattice laser system and its stabilisation scheme, the design of the power-enhancement optical lattice cavity optimised for operation at the magic wavelength, and the development of a new main vacuum chamber capable of accommodating the in-vacuum cavity mirrors. I also describe the design and construction of the custom water-cooled coils required to generate the quadrupole magnetic field for the MOT within the new chamber. Together, these developments form the foundation for the realisation of a Hg optical lattice clock in our laboratory.

5.6.1 Optical Setup for Optical Lattice

The optical lattice will be based on a frequency-doubled titanium sapphire laser, which seeds a power-enhancement optical cavity. The layout of the optical setup is shown in Figure 5.37.

In my proposed design, the laser system will be based on a commercial solution from M Squared Lasers. It consists of a titanium sapphire laser SolsTiS pumped by an Equinox pump laser, and a frequency doubling module ECD-X that extends the accessible output wavelengths of the SolsTiS system into the UV region. The monitor output of the SolsTiS laser will be split into separate paths. One path is intended to be coupled to a wavelength meter[84], while the other is to be delivered via a 200 m PM fibre link to the OFC. The OFC will be stabilised to an ultra-stable optical reference cavity. It will serve as a transfer oscillator, allowing the frequency stability of the optical reference to be transferred to the 725 nm laser system.

The fundamental light at 725 nm will be overlapped with the OFC output beam using an NPBS. A half-wave plate will adjust the polarisation of the fundamental beam relative to the OFC output. The overlapped beams will be directed onto a diffraction grating, acting as a frequency discriminator and enhancing the SNR of the detected signal. An avalanche photodiode will detect the frequency beatnote between the 725 nm beam and the nearest OFC mode. The resulting electronic signal is intended to be used to stabilise the frequency of the 725 nm fundamental light using an offset PLL, a similar approach to that employed for the 1014.8 nm system shown in Figure 5.4.

The laser system is intended to deliver 800 mW of light at 362.5 nm. The beam will pass through an AOM[85], which is planned to serve as an intensity modulator within the power stabilisation servo loop. To maximise diffraction efficiency, the polarisation of the beam will be aligned using a half-wave plate. The first-order diffracted beam will

[84] HighFinesse WS7-60

[85] AA Opto-electronics MQ110-A3-UV

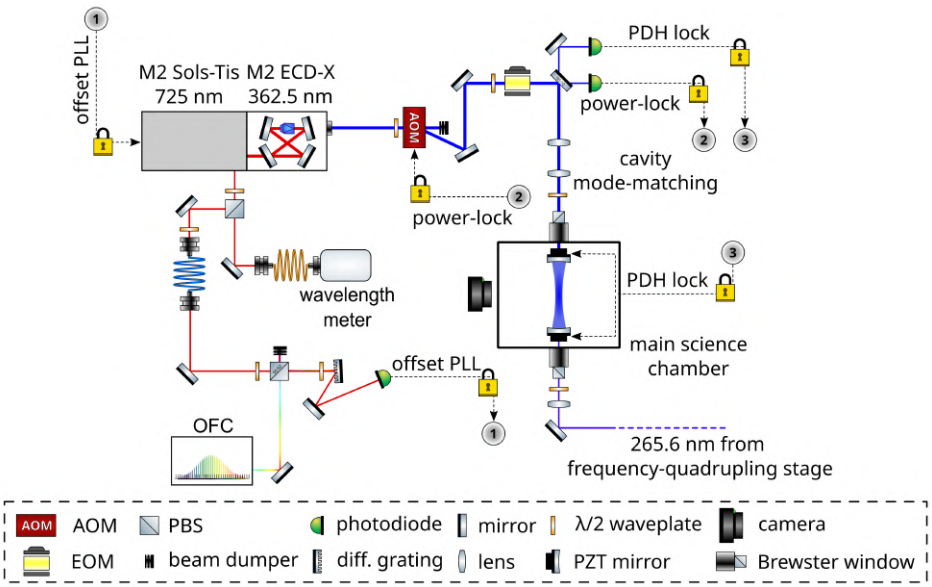

Figure 5.37: Proposed optical layout for the UV laser system designed to drive the optical lattice at 362.5 nm. The laser source is based on a frequency-doubled titanium sapphire laser. The fundamental 725 nm output is stabilised to an OFC via an offset PLL. The 362.5 nm light is intensity- and phase-modulated using an AOM and an EOM, respectively. The beam is mode-matched to a power-enhancement optical cavity inside the main vacuum chamber. A PDH scheme is used to lock the cavity resonance to the laser frequency, while additional servo loops stabilise optical power and suppress RAM. Fluorescence from atoms trapped in the optical lattice is imaged using a CMOS camera.

then be phase modulated using an EOM[86], driven by a 5 MHz RF signal. A second half-wave plate will be used to optimise the polarisation of the beam with respect to the EOM. This modulator includes a DC port to allow active suppression of RAM via feedback on the crystal, and it is also equipped with a temperature sensor[87] and a TEC for active temperature stabilisation.

The phase-modulated beam will be directed towards the main vacuum chamber by a back-polished, UV-enhanced aluminium-coated mirror[88] with a reflectivity of approximately 90% at 362.5 nm. A small portion of light will transmit through the mirror and be detected by a photodetector, which will be used to monitor intensity fluctuations for the power-stabilisation loop. This signal may also serve the active RAM suppression loop after demodulation with a phase-shifted RF signal that drives the EOM.

[86] Qubig PM7-UV-5
[87] NTC10k
[88] Edmund Optics #39-209

The main reflected beam will be shaped using a pair of spherical lenses to maximise coupling into the optical cavity located inside the main vacuum chamber. The vacuum chamber input windows are mounted at the Brewster angle of $58.6°$ to act as polarisers. The p-polarised component of the beam will pass through these windows without loss, whereas the s-polarised component will be partially reflected. To maximise transmission through the Brewster window, a half-wave plate will be used to fine-tune the polarisation of the input beam.

The power-enhancement optical cavity will be formed by a pair of concave mirrors, as described in Section 5.6.2. The light that is back-reflected and leaked by the cavity will retrace the incoming path back towards the back-polished mirror. A fraction of this returning light will again pass through the mirror and be measured by another photodetector. This signal will be used to generate a PDH error signal for actively stabilising the cavity resonance to the laser frequency via control of the cavity length.

On the opposite side, the clock transition spectroscopy beam will be coupled into the main vacuum chamber through an additional Brewster window. The beam will be focused at the centre of the optical lattice trap. A half-wave plate will be used to adjust the beam polarisation relative to the Brewster angle. Fluorescence from the atoms will be detected using a CMOS camera[89].

5.6.2 Optical Lattice Cavity Design

A high-performance optical lattice is essential for confining atoms in the Lamb–Dicke regime and for suppressing motional effects during clock interrogation. In the case of Hg optical lattice clocks, the design of the lattice cavity must overcome specific challenges arising from the relatively small differential polarisability at the magic wavelength $\lambda_L = 362.5$ nm, the requirement for deep trapping potentials, and the limitations imposed by UV optics.

The potential depth of the lattice trap can be estimated based on the circulating intracavity power P_{circ} and the cavity waist radius w_0 as

$$U_0 = \frac{\alpha_{\text{Hg}}(\lambda_L)}{2c\varepsilon_0}\left(\frac{8P_{\text{circ}}}{\pi w_0^2}\right), \tag{5.6.1}$$

where $\alpha_{\text{Hg}}(\lambda_L) \approx 5.3\times10^{-40}$ m^3 is the dynamic polarisability of the ground state [32], c is the speed of light, and ε_0 is the vacuum permittivity. The trap depth is often expressed in units of the recoil energy $E_{\text{rec}} = \hbar^2 k_L^2/2m$, where m is the atomic mass and $k_L = 2\pi/\lambda_L$ is the wave number of the lattice photon. Alternatively, it may be expressed in temperature units as E_{rec}/k_B, with k_B being the Boltzmann constant.

In this section, I present my design of the optical lattice cavity for our experiment, with the goal of obtaining a high achievable trap depth and ensuring long-term operational stability. In my proposed design, I have selected a plano-concave mirror substrate

[89] Cinogy CMOS-1.001-Nano

made from FS-LO-A, with a ROC of 100 mm, to serve as the cavity mirror. To minimise the mass of the optical element, the substrate is only 6.35 mm in diameter and 3 mm in thickness. The plane side of the substrate is coated with an anti-reflection coating specified for high transmission at 362.5 nm ($R < 0.7\%$), 265.6 nm ($R < 0.8\%$), and 227 nm ($R < 1.1\%$). The concave surface features a custom high-reflectivity coating optimised for 362.5 nm, while maintaining maximal transmission at 265.6 nm and 227 nm. This is essential to keep the 362.5 nm light circulating inside the cavity and letting the spectroscopy beams, 265.6 nm and 227 nm, pass undisturbed.

To maximise the intracavity circulating power, the coating reflectivity at 362.5 nm has been carefully designed to satisfy the condition for impedance matching or critical coupling. According to Eq. (4.1.14), this requires the mirror transmission to equal the total losses of the coating, including absorption and scattering. Based on estimates provided by the coating manufacturer[90], absorption losses are expected to be approximately 500 ppm, and scattering losses on the order of 50 ppm for premium-grade substrates. Consequently, the coatings have been specified with a target transmission of $T = 550$ ppm at the lattice wavelength.

Given the challenges associated with producing high-quality coatings in the deep UV, the magnetron sputtering technique was employed to achieve the required specifications. This method offers the best layer uniformity and control over the optical properties. It should be noted, however, that these coatings were produced on a best-effort basis, and detailed characterisation will be necessary to verify their actual performance.

Although the mirrors have been fabricated and delivered, they have not yet been tested. Nevertheless, based on Eq. (4.1.13), the expected power enhancement factor of the optical cavity using these mirrors exceeds 1360, while the finesse exceeds 2850.

In my proposed design, the cavity geometry assumes a mirror separation of $L = 175$ mm. This spacing yields a beam waist radius of approximately 62 μm, comparable to the 69 μm used in the SYRTE implementation [32, 36, 218]. The corresponding cavity stability parameter is $g = 1 - L/\mathrm{ROC} = -0.75$, placing the system well within the stable operational regime with $g^2 = 0.5625 \ll 1$. Such a configuration is expected to ensure robust mode stability, even in the presence of mechanical vibrations or acoustic noise.

Assuming ideal mode matching into the cavity, an input power of 100 mW results in an estimated circulating power exceeding 130 W. This corresponds to a potential well depth of approximately 660 μK or $1800E_{\mathrm{rec}}$ — two orders of magnitude greater than the value achieved in the SYRTE system [32, 36, 218]. However, such high optical intensities raise concerns regarding possible damage to the cavity mirrors. For a circulating power of 130 W, the estimated linear power density at the cavity waist remains below 4 kW/cm. According to the coating manufacturer, the dielectric coatings typically tolerate CW irradiation up to 100 kW/cm before thermal damage becomes signif-

[90] LaserOptik

icant. Nevertheless, in the UV regime, other damage mechanisms must be considered. In particular, outgassing of any polymers or adhesives within the vacuum chamber can lead to the degradation of the coating through carbon-hydroxide deposition and contamination, greatly reducing the power-enhancement factor.

Following the approach adopted in the SYRTE [32, 36, 218] system, my proposed design places the cavity mirrors inside the vacuum chamber. Positioning the mirrors outside the vacuum system would require optical windows within the cavity mode path, which would introduce additional losses and substantially reduce the power-enhancement factor. Integrating the mirrors within the vacuum eliminates this issue and maximises optical performance.

The cavity mirrors will be mounted from the UHV side onto a custom DN35CF–DN40CF vacuum flange. A rendering of the flange design is shown in Figure 5.38. On the air side, the flange incorporates an optical window mounted at the Brewster angle of $58.6°$ to act as a beam polariser. These windows are fabricated from Corning 7980 0A fused silica and feature integrated random nano-textured anti-reflection coatings[91], providing exceptionally low reflectivity in the UV spectral range. The flange is also equipped with four threaded holes compatible with the Thorlabs 30 mm optical cage system. On the vacuum side, it includes two mounting tabs for attaching a vacuum-compatible kinematic mirror mount[92] fitted with PZT. This arrangement will enable coarse alignment via mechanical knobs during installation and fine alignment through PZT actuation once the system is under vacuum.

The cavity mirror substrate will be bonded to a pair of PZT ring chips[93], which will be glued to one another and to a 0.5-inch stainless steel ring mounted in the kinematic holder. Each PZT ring provides a maximum displacement of 2.7 μm with a capacitance of 195 nF. While the first mechanical resonance of the chip is specified at 475 kHz, the additional mass of the mirror will reduce this value to an estimated 330 kHz.

An identical configuration will be implemented on the opposite side of the main vacuum chamber. The two mirrors facing each other form the power-enhancement optical cavity, which will be used as the optical lattice. The cavity length will be tuned by applying a high voltage to the PZT ring chips. To ensure the lattice centre remains in its position, the same high-voltage signal will be applied to both sides of the cavity. Initially, I plan to operate only one pair of PZT within the cavity stabilisation feedback loop. The second pair can be used if the first reaches its displacement limit or if there is a requirement to separate fast and slow modulation. In such a case, slow modulation can be applied to the PZT closer to the mounting structure, while fast modulation can be applied to the PZT directly bonded to the mirror.

The PZT ring chips will be driven by a high-performance amplifier[94], capable of

[91] TelAztec RAR-S
[92] Polaris POLARIS-K05P2
[93] Thorlabs PA44RKW
[94] PiezoDrive MX200

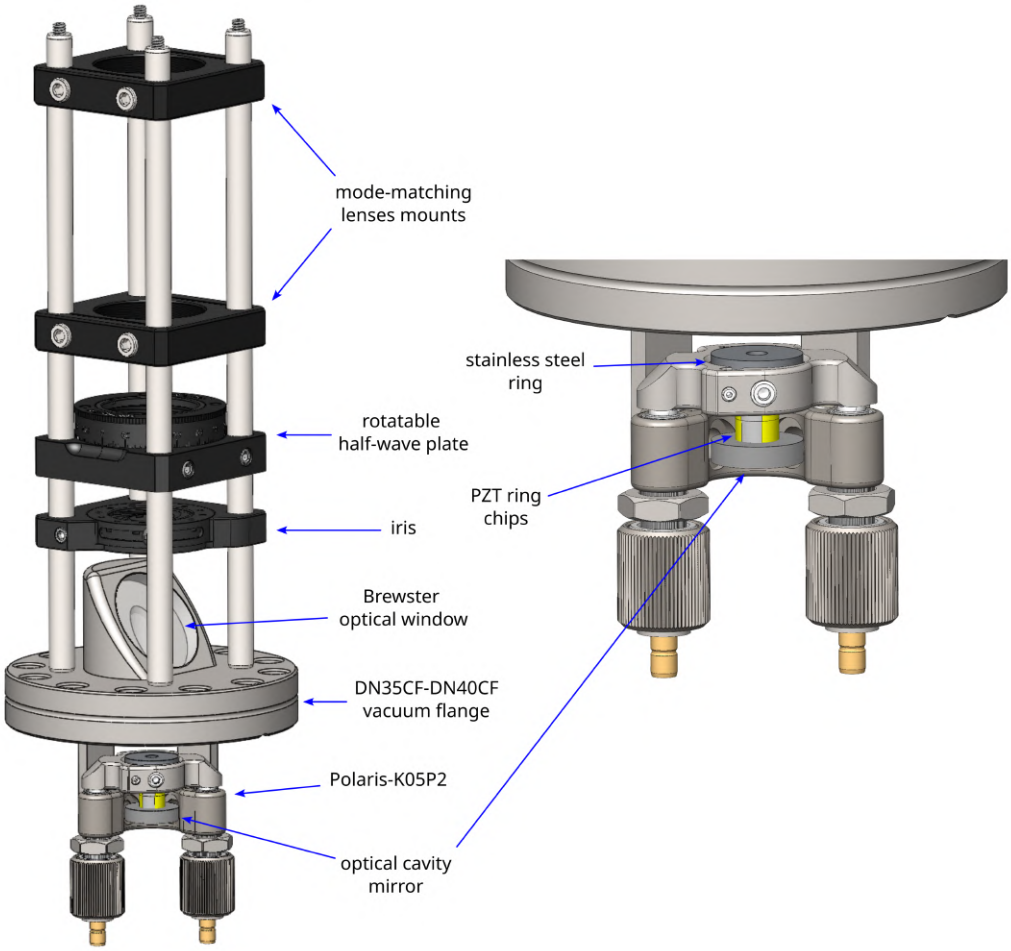

Figure 5.38: Rendering of the vacuum-compatible mirror assembly used in the proposed optical lattice cavity design. The custom DN35CF–DN40CF vacuum flange integrates a Brewster-angle optical window on the air side for polarisation control and is compatible with the Thorlabs 30 mm cage system. On the vacuum side, the cavity mirror is mounted in a Polaris POLARIS-K05P2 kinematic holder equipped with PZT for alignment and resonance tuning. The mirror substrate is bonded to a pair of Thorlabs PA44RKW PZT chips, enabling precise displacement and dynamic control of the cavity length.

delivering 150 mA of average current. This corresponds to a theoretical power bandwidth exceeding 5 kHz and a small-signal bandwidth of more than 120 kHz. The PZT adjusters in the kinematic mounts will be supplied using a three-channel ultra-low noise driver[95], with a specified total noise level below 62 µV RMS (0.03 Hz to 1 MHz).

[95] PiezoDrive PDu150

5.6.3 New Main Vacuum Chamber Design

The implementation of the optical lattice is not feasible with the main vacuum chamber currently used in the experiment. The transmission of 362.5 nm light through the existing chamber viewports is below 80%, making it impractical to form the optical cavity outside the vacuum due to excessive losses. At the same time, the internal geometry of the installed vacuum chamber lacks the mechanical infrastructure required to accommodate cavity mirrors within the vacuum.

To overcome these limitations, I have designed a new main vacuum chamber that enables the in-vacuum installation of the optical lattice cavity mirrors, as described in Section 5.6.2. The design preserves all existing functionalities of the current main chamber while integrating the elements necessary for the clock transition spectroscopy, and offering the flexibility for future integration of new hardware components. A rendering of the designed vacuum chamber is presented in Figure 5.39.

The new chamber is designed as three components: the main body with twelve DN35CF–DN40CF vacuum flanges and two DN200CF vacuum flanges, together with two multi-port hats, each equipped with seven DN35CF–DN40CF flanges and one DN200CF flange. The DN200CF flanges connect the three components to form the chamber. The chamber has a diameter of approximately 300 mm and a height of 220 mm, and is constructed from stainless steel AISI 316LN. The inner walls are polished to a surface roughness of $Ra \leq 0.2$ and coated with a gold layer. The polished surfaces exhibit reduced emissivity, lowering thermal radiation within the chamber and thereby mitigating the BBR. The gold coating further reduces thermal radiation, since the emissivity of gold is several times lower than that of stainless steel [219]. In addition, the gold surface assists in reducing the background pressure, as gold acts as an adsorption pump for Hg through amalgamation processes.

The chamber accommodates eighteen DN35CF–DN40CF custom-made UHV viewports. Each viewport comprises a flange body with a slot for a 1.5-inch optical window fabricated from Corning 7980 0A fused silica and equipped with random nanotextured anti-reflection coatings[96]. On the vacuum side, the window is sealed with a 1 mm-thick indium wire, in the same manner as the windows of the ultra-stable optical cavity chamber. The window and indium seal are held against the viewport body by a clamping element with a rubber gasket. This clamping element additionally incorporates four threaded holes compatible with the Thorlabs 30 mm cage system.

The main body accommodates ten viewports: four are allocated for two orthogonal pairs of co-propagating Hg MOT and Rb MOT beams at 253.7 nm and 780 nm, one is used for the Rb Zeeman slower beam, two are used for absorption imaging with a CMOS camera, one serves for MOT fluorescence detection with a photomultiplier tube, and two are dedicated to a far-detuned optical dipole trap beam. The remaining two DN35CF–DN40CF flanges connect to the existing Rb and Hg sources.

[96] TelAztec RAR-S1, RAR-VL

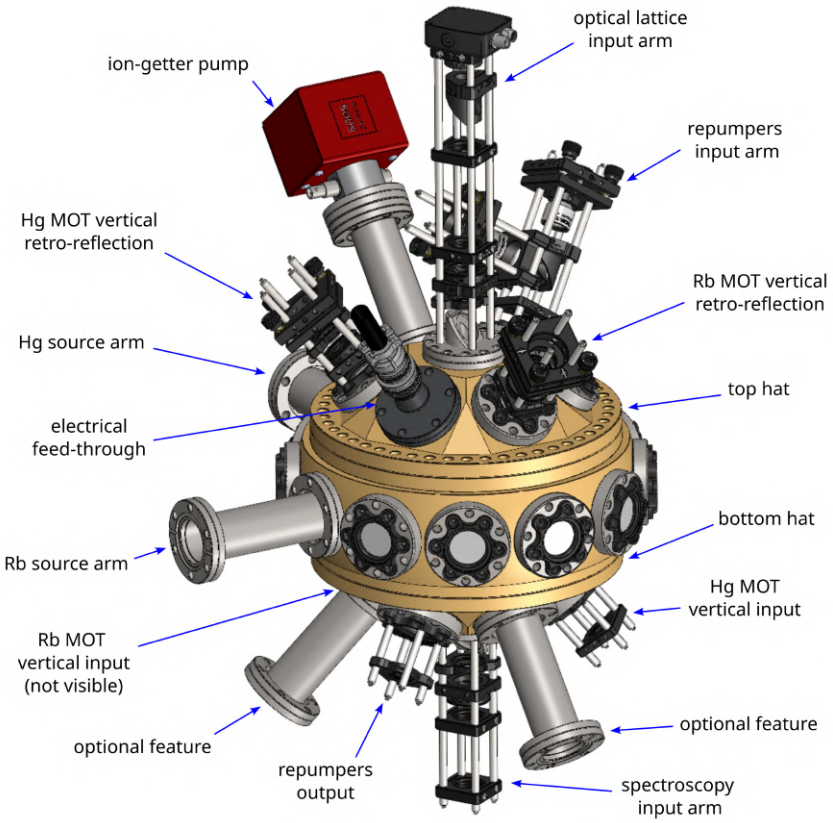

Figure 5.39: Rendering of the newly designed main vacuum chamber with labelled ports and optical access. The chamber consists of the main body and two multi-port hats, providing optical access for the MOT beams, the optical lattice input, repumping beams, spectroscopy arm, and source connections for Rb and Hg. Additional ports accommodate the ion-getter pump, electrical feedthroughs, and optional expansion features.

The top multi-port hat accommodates, at its centre, the custom DN35CF–DN40CF flange for the optical lattice described in Section 5.6.2, together with four custom UHV viewports for 1.5-inch optical windows. Two are used for retro-reflection of the separated, nearly vertical Rb MOT and Hg MOT beams, one for imaging with a CMOS camera, and one for the combined 404.7 nm and 546.1 nm repumping beams. The remaining two flanges connect to an ion-getter pump[97] and a 10-pin electrical feedthrough[98] for supplying high voltage to PZTs inside the chamber.

The bottom multi-port hat provides the second lattice flange, together with three custom UHV viewports for 1.5-inch windows. Two serve as inputs for the separated,

[97] SAES NEXTorr Z200

[98] Kurt J. Lesker IFTAG104103

nearly vertical Rb MOT and Hg MOT beams, while the third is used as the output for the combined 404.7 nm and 546.1 nm repumping beams. One of the residual flanges accommodates a second 10-pin feedthrough for PZT high-voltage supply, while the last two remain unused, allowing future integration of additional components.

The UHV viewports in the multi-port hats are positioned at an angle of nearly 40° with respect to the horizontal plane. To facilitate the integration of optics at this inclination, I have implemented several 30 mm cage systems.

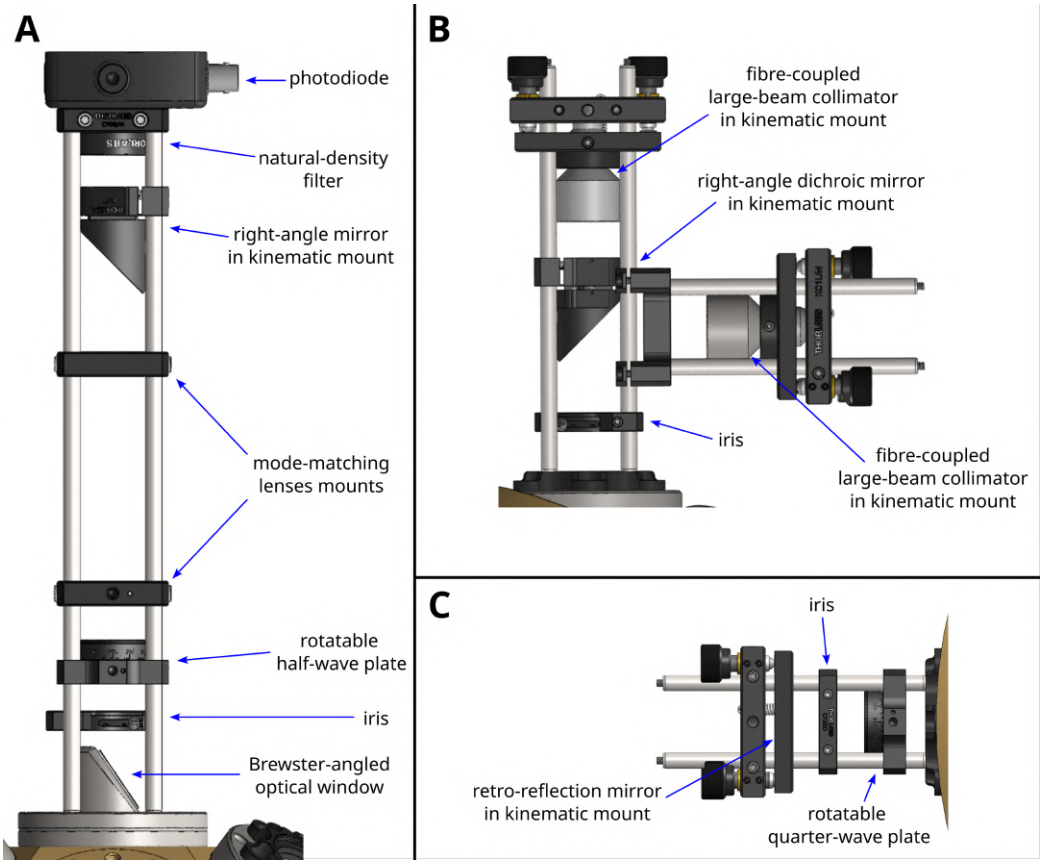

Figure 5.40: 30 mm cage systems used for optical access through the UHV viewports of the new vacuum chamber. **Panel A:** Injection optics for the 362.5 nm lattice beam, including mode-matching lenses, a wave plate, a Brewster-angled optical window, and PDH detection via a photodiode. **Panel B:** Overlap of the 404.7 nm and 546.1 nm repumping beams using a dichroic mirror and fibre-coupled large-beam collimators. **Panel C:** Retro-reflection systems for the vertical MOT beams, each comprising a quarter-wave plate and a mirror in a kinematic mount.

The cage system designed for injecting the 362.5 nm optical lattice beam is shown in panel A of Figure 5.40. It consists of a right-angled kinematic mount holding a back-

polished mirror[99] that directs the beam towards the chamber, two lens mounts for beam shaping, a rotatable mount for a half-wave plate, and an iris. The beam reflected from the cavity retraces the input path, passes partially through the back-polished mirror, and is detected by a photodiode to generate a PDH error signal for the cavity length stabilisation.

Panel B depicts the cage system designed to overlap the 404.7 nm and 546.1 nm repumping beams using a dichroic mirror mounted in a right-angled kinematic holder. Both beams are delivered via optical fibres and collimated using large-beam collimators. For ease of alignment, irises are placed on either side of the chamber.

Panel C shows the cage system intended for retro-reflecting the MOT beams. It consists of a quarter-wave plate in a rotatable mount and a mirror in a kinematic mount. As in the previous case, irises on both sides of the chamber facilitate alignment. Two such cage systems are foreseen, one for the vertical Hg MOT beam and the other for the vertical Rb MOT beam.

All components required for assembling the new UHV chamber have already been bought and shipped. The installation, however, is postponed owing to ongoing experiments in the laboratory.

Forming an MOT requires not only three orthogonal pairs of counter-propagating beams but also a quadrupole magnetic field. This is typically generated by a pair of circular coils in an anti-Helmholtz configuration. Owing to the relatively large dimensions of the designed UHV chamber, the coil carcass must have an inner diameter of at least 254 mm, with the coil centres separated by approximately 150 mm. Such dimensions significantly reduce the achievable magnetic field gradient, which must therefore be compensated for by the number of wire windings and the current.

The coils currently used in the experiment each have 54 windings and provide a magnetic field gradient of 20 Gs/cm at 9 A. For the new UHV chamber, I designed coils with 248 windings of 2 mm diameter insulated copper wire. The winding process, carried out by Janusz Dejewski and me, is shown in the photograph on the left of Figure 5.41. The central wire of the coil has a radius of 150.5 mm, and the separation of the coil centres is also 150.5 mm, forming the anti-Helmholtz configuration. These coils are capable of generating a gradient of 20 Gs/cm at 17 A.

Due to the high number of windings and relatively large current, each coil produces more than 360 W of heat, which must be dissipated. For this reason, the coils are wound on custom-made water-cooled carcasses, with a thermally conductive adhesive applied between every two layers of wire. To minimise the induction of eddy currents in the carcass during coil switching, the carcasses are cut and the gap is filled with an insulating material, as shown in the photograph on the right of Figure 5.41.

Each coil carcass consists of five structural elements fabricated from aluminium[100]:

[99] Edmund Optics #39-209

[100] PA9 (AW-7075)

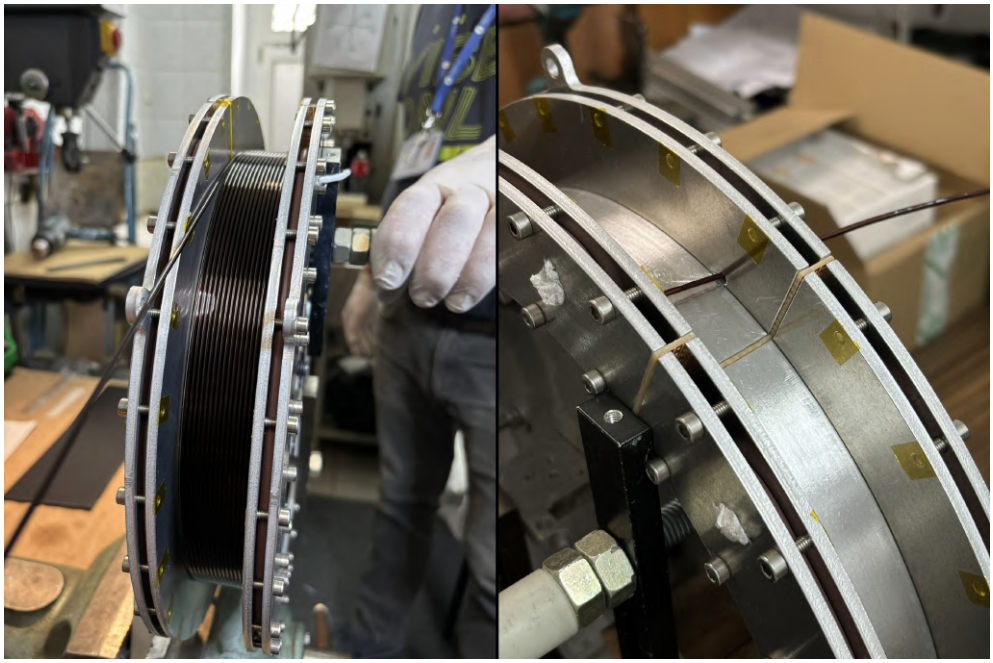

Figure 5.41: Photographs of the MOT coils designed for the new UHV chamber. **Left:** Winding process of the 248 turns of 2 mm insulated copper wire on the custom-made water-cooled carcass. **Right:** Detail of the carcass construction showing the insulating gap introduced to suppress eddy currents.

four 4 mm thick rings forming the side walls and a 35 mm wide cylinder that constitutes the main body. Two rings form each wall of the carcass, with cooling water flowing through the internal cavity between them. The wall is sealed using a 5 mm diameter O-ring[101], compressed to 4.2 mm. The water inlet and outlet are connected via Festo angled plug connectors. Each ring incorporates four brackets that allow the carcasses to be fixed onto the UHV chamber. A photograph of a ring with its fitted seal is shown in Figure 5.42.

Together with Janusz Dejewski, I assembled and wound both coils. We tested them for leak tightness and power dissipation. The coils remain at room temperature when operated at 20 A with circulating water at 20 °C. They are therefore ready to be installed once the new UHV chamber is prepared.

[101] Viton FKM 80 ShA

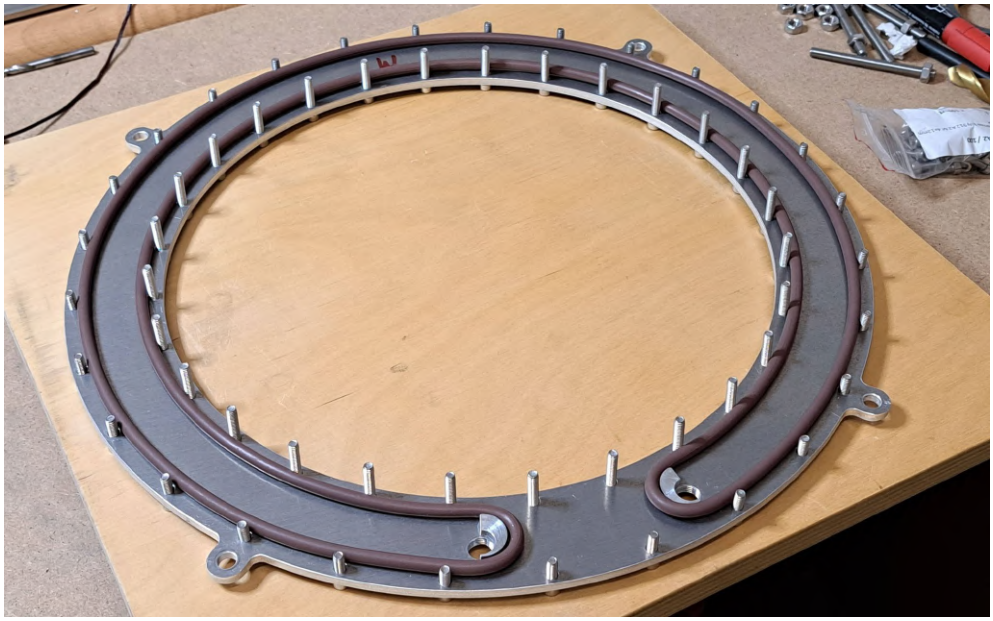

Figure 5.42: Photograph of an aluminium carcass ring used in the MOT coil assembly. The Viton O-ring seal is visible, forming the cooling channel between the paired rings. Mounting brackets for fixing the carcass to the UHV chamber are also visible.

Chapter 6

Experimental Setup at CERN

This chapter describes the experimental apparatus of the AE$\bar{g}$IS experiment at CERN for precision studies of Ps. Although I am not the author of the UHV system and the Ps production chain, I briefly present these setups to provide the context for the reader and allow understanding of the hardware limitations for the Ps spectroscopy.

The main goal of this chapter is to present my design of the CW spectroscopy system for the $1^3S_1 - 2^3S_1$ transition at 486 nm, motivating the use of a power-enhancement cavity and deriving its design targets. I also describe the detection strategies and the digital frequency lock employed to reference the probe laser to the line centre, before compiling the associated uncertainty budget and identifying the dominant systematic effects. Throughout, I emphasise design choices driven by the constraints of the AE$\bar{g}$IS environment and by the requirement to achieve sub-100 kHz accuracy in the absolute frequency measurement.

6.1 Vacuum System and Positronium Formation

The section of the AE$\bar{g}$IS vacuum system dedicated to Ps production is shown in Figure 6.1. The detailed description of the setup can be found here [220]. The Ps production system comprises four main elements: the radioactive positron source, a Surko-type trap and accumulator, a bunching stage, and the spectroscopic chamber in which Ps is created.

We employ a ^{22}Na source as our positron provider. To deliver positrons as pulsed beams suitable for efficient Ps production, the emitted particles must first be moderated, cooled, and guided before accumulating. The source emits positrons with a broad energy distribution and a 4π angular spread, which we reduce using a conical copper moderator [221]. At the inner surface of the cone, we grow a solid neon moderator at 7 K. After moderation, the outgoing flux consists of a continuous, monoenergetic

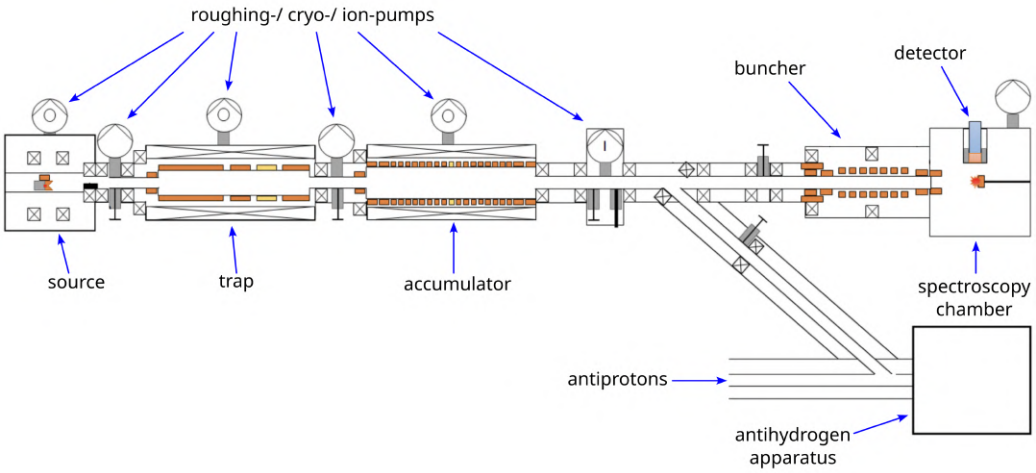

Figure 6.1: Schematic of the vacuum system dedicated to Ps formation in the AE$\bar{g}$IS experiment. Positrons emitted from a ^{22}Na source are moderated and injected into a Surko-type trap and accumulator, where they are cooled and stored. Bunched positron pulses are subsequently shaped in the buncher and directed into the spectroscopic chamber, where they are implanted into a nano-channelled silicon converter to form Ps. The chamber is equipped with μ-metal shielding to suppress residual magnetic fields and a detector system to measure the γ radiation from Ps annihilation. Connections to the antihydrogen apparatus and antiproton beamline are also indicated; however, they remain unused in the context of this work.

beam of positrons with a well-defined energy, which we then guide into the trapping system.

We guide the moderated positron beam magnetically into a Surko-type trap system [222], which comprises a trap stage and an accumulator. Both devices are Penning–Malmberg traps operated with buffer gas, which cools the e^+ with inelastic collisions. By stacking 1000 pulses from the trap, we obtain approximately 1.1×10^7 positrons in the accumulator. The use of a harmonic axial potential compresses the positron plasma as it cools, resulting in a shortened axial length and producing sharper bunch profiles upon release. To extract the positrons, we apply a potential ramp that both releases and accelerates the plasma towards the buncher [223]. The buncher consists of a series of electrodes driven with a time-dependent voltage sequence. As the positron bunch traverses the device, the leading particles are decelerated while the trailing particles are accelerated. This velocity modulation compresses the pulse temporally, yielding a positron bunch with nanosecond duration.

Ps is generated by implanting positron bunches, accelerated to 3.3 keV, into a nano-channelled silicon converter [115, 224]. This target provides a conversion efficiency of roughly 30%, corresponding to a few 10^5 Ps atoms per bunch. The converter is posi-

tioned inside the spectroscopic chamber at an angle of $45°$ with respect to the incoming positron beam. The resulting distributions of both positrons and emitted Ps typically exhibit diameters of about 5 mm.

To minimise residual magnetic fields and ensure a field-free experimental region, the chamber is enclosed in a μ-metal shield, resulting in a measured magnetic field below 1 mT in the Ps production area. Maintaining a magnetic-free environment is crucial for the laser-cooling and spectroscopic experiments [225, 226].

The main observable signal in our experiment is the γ radiation emitted following Ps annihilation. For its detection, we employ a $PbWO_4$ scintillator crystal, positioned above the e^+/Ps converter. The scintillator is optically coupled to a photomultiplier tube[1], which converts the scintillation light into electrical pulses. The resulting signals are recorded using a digital oscilloscope[2], providing the measurement data for further analysis.

6.2 Laser System for Positronium Spectroscopy

Following the approach reported in [50, 51], the highly forbidden $1^3S_1 - 2^3S_1$ transition in Ps can be accessed through two-photon excitation using counter-propagating beams at half the transition frequency, corresponding to a wavelength of 486 nm. This geometry inherently cancels first-order Doppler shifts, which is a major advantage for high-precision spectroscopy. However, it simultaneously imposes the requirement of very high optical intensities. When employing pulsed lasers, these intensities can be accompanied by unwanted non-linearities, such as frequency chirping [47, 227], which complicate the interpretation of the spectra. These difficulties can be avoided by using a CW laser system. The typical optical power used in the previous experiment was on the order of 1 kW [50, 51].

This constraint, however, may be relaxed when a higher-intensity Ps source is employed. The AE$\bar{g}$IS Ps source can produce more than 10^5 Ps per bunch [52], whereas the reference experiment was limited to $4 \cdot 10^3$ Ps per bunch [51]. The typical diameter of a near-spherical Ps cloud is of order a few millimetres. Since the optical beam waist is much smaller, and the corresponding Rayleigh length much larger, than the typical Ps cloud diameter, the laser beam may be treated as collimated within the interaction region. Accordingly, the spectroscopic signal s is proportional to

$$s \propto PNk_{\text{sensitivity}}, \tag{6.2.1}$$

assuming similar Ps cloud sizes across experiments, where P is the beam power, N is the number of Ps atoms, and $k_{\text{sensitivity}}$ is the detection scheme sensitivity. From Eq. (6.2.1),

[1] Hamamatsu R11265-100
[2] Teledyne LeCroy HDO4104A

and assuming comparable detection sensitivity, the estimated power P_{required} required to drive the $1^3\mathrm{S}_1 \rightarrow 2^3\mathrm{S}_1$ transition with an increased number of interacting Ps is

$$P_{\text{required}} \approx 1\,\text{kW} \times \frac{4 \cdot 10^3\,\text{Ps}}{10^5\,\text{Ps}} = 40\,\text{W}. \tag{6.2.2}$$

This value may be lower once the $1^3\mathrm{S}_1 \rightarrow 2^3\mathrm{S}_1$ transition linewidth is taken into account. The measured linewidth is of order 50 MHz [51], whilst the transient-time-limited linewidth for a laser-cooled Ps cloud in the AE$\bar{g}$IS apparatus would be of order 10 MHz. The estimated power needed for spectroscopy would then be reduced by the linewidth ratio to about 8 W. Although these estimates are based on reasonable assumptions, they may be optimistic. Accordingly, a conservative upper limit of 1 kW is adopted for the following calculations.

Reaching such power levels requires the use of a power-enhancement cavity. The design of this cavity must carefully account for its response time, which dictates how rapidly the circulating field builds up once the laser is coupled into the resonator. For spectroscopy of the $1^3\mathrm{S}_1 - 2^3\mathrm{S}_1$ transition, the cavity decay time must be comparable with the natural timescales of the excited state. In particular, the $2^3\mathrm{S}_1$ state has a fluorescence lifetime of approximately 243 ms [97], whereas its annihilation lifetime is limited to 1136 ns. Based on this consideration, I set the design requirement for the cavity decay time to $\tau = 1000$ ns, ensuring compatibility with the physical constraints of the system.

The selection rules governing the two-photon transition [228] applied to the $1^3\mathrm{S}_1 - 2^3\mathrm{S}_1$ case impose $\Delta J = 0$ and $\Delta M_J = 0$. Since the intermediate P states are far detuned from resonance, the influence of the fine and hyperfine spin structure only enters at the $\sim 10^{-6}$ level. As a result, the relevant excitation paths for the $1^3\mathrm{S}_1 - 2^3\mathrm{S}_1$ transition are effectively indistinguishable from those of a hypothetical atom composed of spinless particles. The immediate consequence is that only transitions between identical M_J sublevels are allowed, and all such transitions have equal oscillator strengths.

A further implication is that excitation of the $1^3\mathrm{S}_1 - 2^3\mathrm{S}_1$ transition using $\sigma^+\sigma^+$ circularly polarised photons, such as those naturally present in a build-up cavity driven with circularly polarised light, violates angular momentum conservation and is therefore strongly suppressed. Instead, the excitation beams must be either linearly polarised or circularly polarised such that the counter-propagating photons carry opposite angular momenta ($\sigma^+\sigma^-$). The latter configuration, however, requires the insertion of quarter-wave plates in every retro-reflection path and is at present incompatible with CW excitation in a low-loss power-enhancement cavity. For this reason, the designed cavity has to operate with linearly polarised light.

6.2.1 Optical Lattice Cavity Design

A high-performance power-enhancement cavity is essential for precision spectroscopy of the $1^3S_1 - 2^3S_1$ transition in Ps using a CW 486 nm laser. The design must address two principal challenges, i.e., achieving intra-cavity powers exceeding 1 kW while ensuring that the cavity decay time remains below 1000 ns.

In this section, I present my design of the optical power-enhancement cavity for the AE$\bar{g}$IS experiment, developed with the aim of enabling high-resolution spectroscopy of the $1^3S_1 - 2^3S_1$ transition while ensuring stable long-term operation. The concept follows the implementation of the optical lattice cavity for trapping Hg atoms described in Section 5.6.2.

For the cavity mirrors, I have selected super-polished fused-silica substrates in a plano-concave configuration with a ROC of 500 mm. Each mirror substrate is 12.7 mm in diameter and 6.35 mm thick, with the plane side coated for high transmission at 486 nm and the concave side carrying a custom high-reflectivity coating optimised for the same wavelength. The mirror separation is set to 50 mm, a constraint imposed by the geometry of the Ps source, which also helps to minimise the cavity decay time.

The reflectivity of the coatings at 486 nm has been chosen to maximise the circulating power while ensuring the response time remains within the required limits. According to specifications from the coating manufacturer[3], the total mirror losses, including both absorption and scattering, are expected to be about 15 ppm. In the case of exact impedance matching, where the transmission equals the total loss, Eq. (4.1.14), the cavity would reach a power-enhancement factor of 50000, Eq. (4.1.13), and a finesse exceeding 100000. However, this would correspond to a cavity decay time of more than 5500 ns, far above the annihilation lifetime of the 2^3S_1 state. To reconcile these constraints, I have increased the mirror transmission to 155 ppm. This reduces the power-enhancement factor to 16000 but lowers the cavity response time to about 980 ns, thereby meeting the design requirements. The resulting finesse is on the order of 18500.

With the chosen geometry of $L = 50$ mm, the cavity supports a beam waist radius of approximately 130 μm, in comparison to the 155 μm waist reported in [51]. The corresponding stability parameter is $g = 1 - L/\mathrm{ROC} = 0.9$, giving $g^2 = 0.81 \ll 1$, which confirms that the cavity operates well within the stability regime. This configuration should ensure robust mode stability even in the presence of mechanical vibrations or acoustic noise.

Assuming ideal mode matching, an input power of 100 mW would generate a circulating power in excess of 1.6 kW. While such high intensities raise concerns of potential mirror damage, the estimated linear power density at the cavity waist remains below 190 kW/cm, which is within the safe operational range.

Following the same reason adopted for the optical lattice cavity for Hg described

[3] FiveNine Optics

in Section 5.6.2, I place the cavity mirrors inside the vacuum chamber. Locating the mirrors outside the vacuum would necessitate optical windows within the resonator path, introducing additional losses and significantly reducing the achievable power enhancement. Integrating the mirrors directly into the vacuum, therefore, eliminates this limitation and ensures optimal cavity performance. The cavity mirrors will be mounted from the UHV side onto a custom DN63CF vacuum flange. On the air side, the flange incorporates a one-inch AR-coated optical window, positioned at the Brewster angle of 58.6° to act as a polariser, thereby ensuring linear polarisation of the incoming beam. The flange is also equipped with four threaded holes compatible with the Thorlabs 30 mm cage system, which facilitates integration with standard optomechanical components. On the vacuum side, the flange includes two mounting tabs designed for attaching a vacuum-compatible kinematic mirror mount fitted with a PZT. This configuration allows for coarse alignment through mechanical knobs during installation and fine alignment via PZT actuation once the chamber is under vacuum.

In analogy with the optical lattice cavity design, the cavity mirror substrate will be bonded to a pair of PZT ring chips, which are glued together and then fixed to a 0.5-inch stainless steel ring mounted in the kinematic holder. Each PZT ring provides a maximum displacement of 2.7 μm with a capacitance of 195 nF. Although the first mechanical resonance of a bare chip is specified at 475 kHz, the additional mass of the mirror is expected to reduce this value to approximately 151 kHz. An identical configuration will be implemented on the opposite side of the main vacuum chamber, with the two mirrors aligned face-to-face to form the power-enhancement cavity. The cavity length will be tuned by applying high voltages to the PZT ring chips, enabling precise control of resonance conditions, keeping the cavity referenced to a frequency of the coupled light.

6.2.2 Optical Setup for Positronium Spectroscopy

Achieving sub-100 kHz accuracy in the spectroscopy of the $1^3S_1 - 2^3S_1$ transition requires a spectrally narrow and frequency-stable laser source operating at 486 nm. To access an absolute frequency scale, the laser frequency must be referenced to a known standard. In addition, to meet the requirements of the power enhancement cavity, the source must provide at least 100 mW of optical power coupled into the cavity.

In my design, I ensure frequency stability and absolute referencing of the laser using an OFC. The OFC modes can be stabilised either to an ultra-stable optical reference or to an RF reference, depending on the availability at CERN. For the latter, I envisage either a GPS-disciplined commercial Rb frequency standard or an H-maser disciplined by a Cs standard. For the laser itself, I consider four possible solutions, each with its own advantages and drawbacks. Schematic representations of these laser systems are shown in Figure 6.2.

The most suitable option, shown in Panel A in Figure 6.2, is based on a commercial

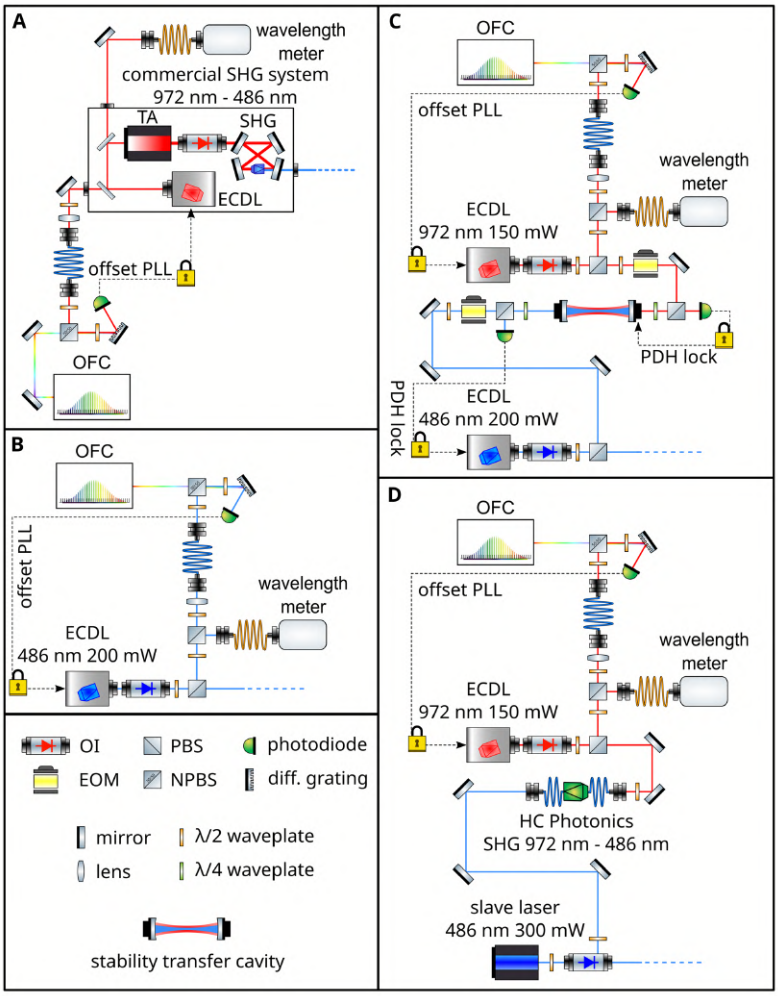

Figure 6.2: Schematic designs of the proposed laser systems for Ps spectroscopy at 486 nm. **Panel A:** Commercial SHG system at 972 nm doubled to 486 nm. **Panel B:** Custom-built ECDL at 486 nm. **Panel C:** Stability transfer cavity linking a 972 nm ECDL to a 486 nm ECDL. **Panel D:** Injection-locking scheme using a 972 nm ECDL doubled in a PPLN waveguide mixer. See text for further details.

SHG laser system. This configuration, closely resembling that employed for Hg laser cooling in Section 5.2.1, consists of an ECDL at 972 nm. The output is amplified with a TA and subsequently frequency-doubled to 486 nm in a bow-tie cavity. Such systems typically deliver more than 1 W at 486 nm, comfortably exceeding the 100 mW threshold. The availability of excess power relaxes the requirements on the mirror coatings of the power enhancement cavity in my design. The fundamental 972 nm radiation is delivered to the OFC via a PM fibre. As in Section 5.2.2, I employ heterodyne detection

between the 972 nm light and the OFC output to obtain a beatnote in the RF domain. This signal is then compared with a LO derived from a DDS, producing an error signal that references the laser frequency to the OFC. Although highly suitable from a technical perspective, such commercial SHG systems are often prohibitively expensive and may exceed the available project budget.

The SHG laser system can be replaced by an ECDL operating directly at 486 nm, as illustrated in panel B of Figure 6.2. The recent availability of high-power single-mode GaN laser diodes[4] enables me to construct a custom ECDL, following the design I have already implemented and tested at 1092.2 nm and 404.7 nm for repumping of metastable states in Hg, as described in Section 5.5.3. Using a 300 mW diode, I can obtain more than 200 mW of usable power after the OI, which comfortably satisfies the cavity coupling requirement. A custom-built ECDL is typically at least an order of magnitude less expensive than a commercial SHG system. The drawback of this approach is that direct lasing at 486 nm necessitates the OFC spectrum to extend into the blue region. Although spectrum extenders exist, their use significantly increases the overall cost of the system.

A more economical approach involves employing a custom-built ECDL operating at 972 nm[5], which can be referenced directly to the OFC without the need for spectrum extension, as illustrated in panels C and D of Figure 6.2. The stability of the 972 nm ECDL can then be transferred to a 486 nm source either by means of a stability transfer optical cavity (panel C) or via injection-locking (panel D).

In the first case, the stability transfer cavity must employ custom high-reflectivity coatings suitable for both 972 nm and 486 nm. One of the mirrors is mounted on a PZT, enabling fine adjustment of the cavity length. Using the PDH technique, the cavity resonance can be stabilised to the frequency of the injected 972 nm light. The custom-built 486 nm ECDL is then referenced to the same cavity via another PDH lock, thereby transferring the stability of the OFC to the 486 nm laser. This approach, however, requires three nested servo-loops, adding significant complexity. Moreover, each ECDL must have RF sidebands imprinted for PDH. While these are conventionally generated with EOMs, they may also be introduced by directly modulating the diode current. The latter method is less costly, but it introduces amplitude modulation in addition to phase modulation. This produces an offset in the PDH error signal, known as RAM, which limits servo stability and causes systematic frequency shifts. In addition, the achievable modulation depth is usually smaller, resulting in a shallower error signal slope [229].

The alternative approach, illustrated in panel D, relies on injection-locking. In this master–slave scheme, the slave diode does not incorporate an external cavity, but instead is forced to oscillate at the frequency of a master laser by injecting a fraction of

[4]For example, Nichia NDS4416

[5]For example, Innolume gain chip

its output. In my implementation, the custom-built 972 nm ECDL is first stabilised to the OFC, and its frequency is then doubled in a PPLN waveguide mixer[6]. This single-pass device is considerably less expensive than a full SHG system and has already been successfully used in the ultra-stable Hg laser system described in Section 5.4.1. According to the specifications, seeding the PPLN mixer with 100 mW of 972 nm light yields more than 5 mW of 486 nm at the fibre output, sufficient for injection-locking. The slave diode, operating without an extended cavity, then provides the full output power of around 300 mW before the OI. I regard this configuration as an optimal compromise, retaining only a single servo-loop while meeting the power requirements in a cost-effective manner.

Regardless of the choice of laser system, the 486 nm light is modulated and delivered via PM fibre to the vicinity of the Ps spectroscopic vacuum chamber, where it is injected into the power enhancement optical cavity. The schematic of this optical system is shown in Figure 6.3.

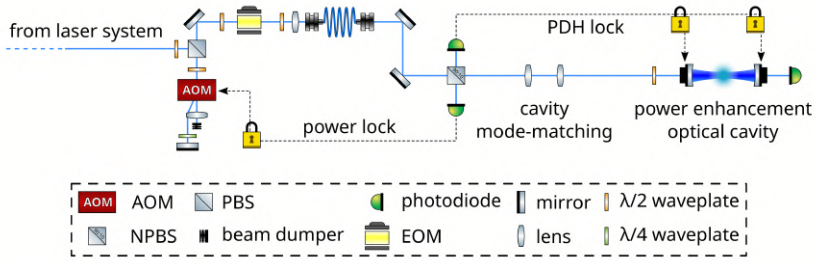

Figure 6.3: Optical setup for delivering 486 nm light into the power enhancement cavity for Ps spectroscopy. The beam is first modulated by a double-pass AOM, providing frequency shifts for the detection scheme and enabling active power stabilisation. An EOM then imprints the sidebands required for PDH locking. After fibre delivery to the spectroscopic chamber, the light is split at an NPBS, with the reflected beam used for power stabilisation and the transmitted beam mode-matched into the cavity. Light reflected from the cavity is directed to an avalanche photodiode for generation of the PDH error signal, which stabilises the cavity length via mirror-mounted PZT. A photodiode placed behind the cavity monitors the transmitted power as an indicator of resonance and mode-matching quality.

The beam is first modulated by an AOM in a double-pass configuration. This arrangement provides the required RF frequency shift for the detection scheme described in Section 6.2.3, while ensuring that the beam direction remains fixed during frequency tuning. In addition, the AOM enables amplitude modulation, which I intend to use for active power stabilisation. The frequency-shifted light is subsequently

[6]HC Photonics

phase-modulated by an EOM, imprinting the RF sidebands required for the PDH technique.

The modulated beam is then delivered through a PM fibre to a breadboard mounted around the spectroscopic chamber. Upon exit, the light is incident on a NPBS with a $T90 : R10$ split ratio. The reflected portion is directed to a photodiode, providing the signal for the active power stabilisation loop. The transmitted beam is mode-matched to the cavity using a pair of spherical lenses to maximise coupling efficiency. Just before entering the power enhancement cavity, a half-wave plate is used to align the light polarisation with the input viewport placed at the Brewster angle.

The light reflected from the cavity retraces the incoming path, and part of it is redirected by the NPBS onto an avalanche photodiode. This signal is used to generate the PDH error signal, which stabilises the cavity resonance to the laser frequency by adjusting the cavity length with mirror-mounted PZTs. This locking scheme enables me to vary the input laser frequency while maintaining resonance, thereby sustaining a high circulating optical power inside the cavity. On the opposite side of the cavity, a photodiode monitors the transmitted power, which serves as an indicator of resonance and mode-matching quality.

6.2.3 Detection and Uncertainty Budget

Detection Methods

In order to detect the $1^3S_1 - 2^3S_1$ transition in Ps, I have considered several complementary approaches. At the present stage, it is not clear which of them will provide the most robust signal, and therefore, I describe them on an equal footing. Each method has its own strengths and drawbacks.

The first method is based on monitoring the optical power transmitted through the power-enhancement cavity. Under normal operating conditions, the transmitted signal simply reflects the balance between the input coupling and the intrinsic cavity losses. However, if Ps atoms interact resonantly with the intracavity field, they introduce an additional loss channel. As a result, the transmitted power should decrease whenever the probe laser is tuned to the resonance. I find this approach particularly attractive because it is technically straightforward and does not require extra hardware beyond the photodiode that is already installed for mode-matching diagnostics. At the same time, I have to acknowledge that the achievable contrast is strongly dependent on the Ps density and on how well the cavity mode overlaps with the spatial distribution of the atoms. These parameters cannot be guaranteed a priori, which means the strength of the signal remains uncertain.

Another possibility is to detect positrons that are released through photoionisation [230]. After resonant excitation of Ps, an additional ionisation laser can remove the bound electron, producing free positrons that are guided to a microchannel plate or

a similar charged-particle detector. The detected counts are then directly proportional to the number of atoms that were excited. I view this approach as highly selective and essentially background-free, since only atoms that have genuinely interacted with the probe contribute to the signal.

A further option is to employ single-shot positron annihilation lifetime spectroscopy (SSPALS) [231]. By detecting the annihilation γ-rays, SSPALS provides a well--established measure of the Ps population and has already been used to resolve sub-Doppler features of the $1^3\mathrm{S}_1 - 2^3\mathrm{P}_j$ transitions. In that case, the contrast in the annihilation spectrum is particularly strong, since the $2^3\mathrm{P}_j$ states exhibit annihilation lifetimes that are several orders of magnitude longer than that of ground-state $1^3\mathrm{S}_1$ Ps. For the $1^3\mathrm{S}_1 - 2^3\mathrm{S}_1$ transition, however, the situation is different: the $2^3\mathrm{S}_1$ state has an annihilation lifetime of 1136 ns, only about one order of magnitude longer than the 142 ns lifetime of $1^3\mathrm{S}_1$. As a consequence, the modification to the SSPALS trace is relatively small, which reduces the signal contrast and renders this technique less suitable as a primary detection method for high-precision spectroscopy. Nevertheless, it remains a valuable diagnostic tool and an independent cross-check of the alternative schemes outlined above.

Digital Frequency Lock

For high-precision spectroscopy, scanning the probe laser across the resonance and fitting the resulting profile is not an optimal strategy. Such an approach is sensitive to statistical noise and systematic offsets arising from asymmetric lineshapes or slow experimental drifts. Instead, I plan to employ a digital lock method, which provides a direct discriminator signal that can be averaged over long timescales, thereby improving the precision of the frequency determination.

The concept of digital locking has been successfully implemented in earlier precision spectroscopy studies. Notably, Morzyński *et al.* demonstrated a digitally locked CW laser for absolute frequency measurements of the Rb $5\mathrm{S} - 7\mathrm{S}$ two-photon transition, attaining sub-kHz frequency uncertainties using an OFC as a reference [232]. Similarly, Witkowski *et al.* used a digital lock to determine the absolute frequency of the $^1\mathrm{S}_0 - {}^3\mathrm{P}_1$ transition in several Hg isotopes [10].

The principle of operation is based on a two-point sampling scheme. In each experimental cycle, a fresh cloud of Ps is prepared. In the first shot, the probe laser frequency is detuned to the low-frequency side of the transition (left wing), and the corresponding signal is recorded. In the following shot, the frequency is shifted by an equal amount to the high-frequency side (right wing), and the signal is measured again. The difference between these two signals forms the error signal of the lock. If the laser is tuned exactly to the resonance, the signals from the two wings are equal and the error signal vanishes. A non-zero error signal indicates an offset from the line centre and provides both the sign and magnitude of the required correction. After the correction is applied,

the laser frequency is set to the centre, where the frequency is logged. The sequence is then repeated, enabling the laser frequency to be continuously tracked with shot-to-shot updates.

In the AE$\bar{g}$IS experiment, the rate at which new Ps bunches can be produced is limited by the positron accumulation and bunching sequence, resulting in a typical repetition rate of about 6.5 Hz. This imposes a natural limit on the update rate of the digital lock: each error signal is available only once every ~ 150 ms. Consequently, the probe laser must remain sufficiently frequency-stable to wait at the chosen detuning until the next Ps bunch is ready. In practice, this requirement is readily met by referencing the laser to an OFC, which ensures sub-kilohertz stability over such timescales.

The choice of frequency jump Δf between the line centre and the sampled wings is critical. For a Lorentzian profile, the maximum sensitivity is obtained when the frequency offset corresponds to half of the linewidth. In the case of the $1^3\mathrm{S}_1 - 2^3\mathrm{S}_1$ transition, the natural linewidth is about 1.2 MHz, as determined from the lifetimes of the involved states. However, strong driving fields in the power-enhancement cavity, together with the short transit time of Ps across the laser mode, are expected to broaden the effective linewidth to the level of several tens of megahertz.

An important advantage of this scheme is that it is independent of the chosen detection method. Any of the observables discussed above: transmission through the cavity, photo-positron detection, or SSPALS, can provide the discriminator signal. This flexibility is especially valuable in the commissioning stage, when different detection channels can be compared and cross-validated.

The technical implementation of the digital lock typically relies on a DDS driving an AOM, with the frequency jumps controlled by a microcontroller. I have previously developed such a system and demonstrated its performance in background-free spectroscopy of Hg [75]. In the context of the Ps experiment, the same concept can be adopted, but integration with the existing ARTIQ/Sinara framework used at CERN is also feasible.

A schematic of the digital lock principle is shown in Figure 6.4. The figure illustrates the frequency switching between the two wings of the resonance by $\pm\Delta f$ around f_{AOM}. The error signal ε is generated from the difference of the corresponding observable signals

$$f_{\mathrm{corr}} = \varepsilon \cdot \mathrm{gain} = (s_1 - s_2) \cdot \mathrm{gain} \tag{6.2.3}$$

and the feedback loop keeps the probe laser referenced to the centre of the transition by applying corrections f_{corr}.

Uncertainty Budget

To assess the ultimate precision of the $1^3\mathrm{S}_1 - 2^3\mathrm{S}_1$ spectroscopy in Ps, it is necessary to consider both systematic and statistical sources of uncertainty. On the systematic side, the most important limitation arises from the residual Doppler effect. While

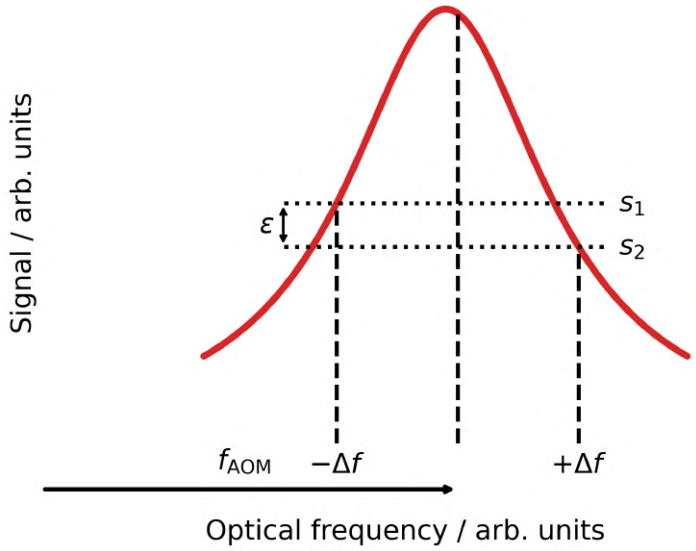

Figure 6.4: Schematic principle of the digital frequency lock. The probe laser frequency is alternately shifted by $\pm\Delta f$ around the central frequency f_{AOM} to probe the two wings of the resonance. The corresponding signals s_1 and s_2 are recorded, and their difference defines the error signal $\varepsilon = s_1 - s_2$. This error signal provides both the sign and magnitude of the correction applied to the laser frequency, thereby keeping it stabilised to the line centre.

the two-photon geometry suppresses the first-order Doppler contribution, the second-order Doppler shift, which results from relativistic time dilation, remains. Thanks to the successful laser cooling of Ps [52], the mean atomic velocity can be substantially reduced, which directly suppresses this contribution.

A further important systematic contribution is the AC Stark shift induced by the intense probe field circulating inside the enhancement cavity. This effect can be characterised experimentally by performing the spectroscopy at different intra-cavity powers and extrapolating to zero intensity. In contrast, the influence of external fields is expected to be negligible. Owing to the use of μ-metal shielding, the residual stray electric and magnetic fields are strongly suppressed, as described in Section 6.1, measurements in the Ps production region confirm that the magnetic field remains below 1 mT. Finally, collisional effects are expected to be minimal, since the Ps cloud produced in the experiment is extremely dilute.

The statistical uncertainty is determined primarily by the signal-to-noise ratio of the chosen detection method and the performance of the digital lock. In practice, the servo error of the lock is expected to remain well below the natural linewidth of the transition, while the OFC provides a reference with sub-kilohertz stability over the timescales of

the experiment.

Taken together, these considerations indicate that the overall uncertainty of the measurement will remain below the 100 kHz level, with the second-order Doppler and AC Stark effects setting the dominant limits. This level of precision is sufficient not only for resolving the $1^3S_1 - 2^3S_1$ transition in Ps, but also for establishing a state-of-the-art absolute frequency value.

Chapter 7

Conclusions

In this thesis, I have explored two distinct yet complementary frontiers of precision atomic physics. The first part focused on neutral Hg atoms, where I developed and characterised an ultra-stable laser system operating at 265.6 nm for high-resolution spectroscopy of the $^1S_0 - {}^3P_0$ transition. The second part concerned my work at CERN, where, together with the AE$\bar{g}$IS collaboration, we achieved the first laser cooling of Ps, paving the way for precision spectroscopy of the $1^3S_1 - 2^3S_1$ transition. Both efforts shared the goal of pushing measurement capabilities to new limits and probing fundamental physics in novel ways.

A core achievement of my work was the design and construction of an ultra-stable FP cavity at 1062.55 nm. The cavity, made from ULE material and operated at its zero-crossing temperature, was installed in a thermally stabilised UHV system with vibration isolation. I engineered multi-layer thermal shielding and temperature control at the millikelvin level. Frequency stability was diagnosed by beating the cavity-stabilised 1062.55 nm laser with two independent reference lasers, namely a 1542 nm cavity laser at KL FAMO and an optical reference from PTB, and analysing the results with the three-cornered-hat and Groslambert covariance methods. I measured a fractional frequency instability of 7.2×10^{-16} at 1 s, which surpassed our secondary laboratory's earlier 1542 nm cavity laser (2.3×10^{-15}) and approached the best reported optical references worldwide. This ultra-stable cavity was a prerequisite for hertz-level interrogation of the $^1S_0 - {}^3P_0$ transition.

Building on this optical reference, I developed the 265.6 nm laser system to probe the $^1S_0 - {}^3P_0$ transition. The fundamental 1062.55 nm source was referenced to the cavity, amplified in a fibre amplifier, and frequency quadrupled using successive SHG stages. This produced several milliwatts at 265.6 nm, sufficient for the interrogation. To preserve phase coherence, I implemented active FNC on the optical fibre links. The FNC suppressed fibre-induced noise below 10^{-16} at 1 s, ensuring the cavity stability was fully transferred to the UV system. I also prepared a tutorial-style description of different FNC schemes, intended as a practical guide for future researchers. The 1062.55 nm

system was referenced to the OFC, enabling absolute frequency comparison against the SI second. Unfortunately, the final spectroscopy of the $^1S_0 - {}^3P_0$ line could not be completed during the time frame of my PhD due to hardware failures of the seed laser, the fibre amplifier, and the SHG waveguide. The latter remains being serviced at the time of completing the thesis. Nevertheless, diagnostics confirmed that the system is capable of resolving the transition once all components are restored.

To enable continuous clock cycle operation in the future, I developed custom repumping lasers for the metastable $^3P_0$ and $^3P_2$ states. I constructed ECDLs at 404.7 nm and 1092.2 nm, with the latter frequency-doubled to 546.1 nm. These lasers were stabilised using digital feedback to a wavelength meter. Both systems delivered sufficient power at the fibre output to exceed the saturation intensities of the respective transitions. This ensured robust repumping from metastable states and reliable preparation of ground-state atoms.

Finally, I designed and partially prepared a new UHV chamber optimised for $^1S_0 - {}^3P_0$ transition spectroscopy and for an optical lattice operating at the magic wavelength of 362.5 nm. I developed a lattice enhancement cavity with in-vacuum mirrors to achieve the high intensities required for tight confinement while cancelling differential Stark shifts. The new chamber included enlarged optical access ports for the lattice beams and water-cooled quadrupole coils for the operation of stable MOT. I also prepared UV-grade high-reflectivity cavity mirrors and mechanical mounts for robust long-term alignment. This upgrade provides the necessary infrastructure for operating a Hg optical lattice clock in the future.

Looking ahead, the Hg apparatus offers exciting opportunities for both precision metrology and searches for new physics. One of the primary future directions is to perform high-accuracy spectroscopy of both the $^1S_0 - {}^3P_0$ transition and the $^1S_0 - {}^3P_2$ intercombination line across multiple Hg isotopes. By measuring isotope shifts in two independent transitions, one can construct King plots to test for nonlinearity, a signature that could indicate physics beyond the Standard Model. If the Hg isotope shift measurements reveal a nonlinearity in the King plot, it would open a window to new physics. If they confirm linearity with improved accuracy, that too would refine our understanding of atomic structure and provide stringent constraints on beyond-Standard-Model effects. In either case, the ultra-stable laser I developed will be the enabling tool for these future high-precision measurements. Beyond fundamental physics tests, a fully realised Hg optical clock could contribute to the broader field of precision timekeeping, complementing existing optical clocks and aiding in tests of general relativity or the temporal variation of fundamental constants.

My research at CERN focused on Ps within the AE$\bar{g}$IS experiment. I proposed a dedicated setup for high-precision Ps spectroscopy that explicitly built on the expertise I gained during the Hg project. This proposal drew directly on my experience developing the Hg MOT and clock laser systems. Critical techniques such as transferring OFC stability to a laser and frequency up-conversion were repurposed in the Ps spectrome-

ter design. The central idea was to perform Doppler-free two-photon spectroscopy of the $1^3S_1 - 2^3S_1$ transition in Ps using a CW 486 nm laser. Achieving this weak two-photon excitation with high resolution requires intense, ultra-stable light, a challenge addressed by transplanting the laser engineering solutions from the neutral Hg clock to this antimatter system.

A key element of the proposed setup was a power-enhancement optical cavity for the 486 nm spectroscopy, directly inspired by the build-up cavity designed for the Hg optical lattice clock. In the Hg experiment, a power-enhancement cavity was employed to boost intra-cavity power at 362.5 nm, and my Ps design followed this principle. The cavity was integrated inside the UHV chamber to avoid losses from viewports and used a short 50 mm spacing with custom high-reflectivity mirrors. By adopting the lattice cavity design from Hg, the Ps resonator could reliably deliver intra-cavity intensities on the order of 1 kW, sufficient to drive the $1^3S_1 - 2^3S_1$ transition. Significantly, I optimised the mirror transmissions to achieve a cavity response time of about 1000 ns. This timing allowed precise synchronisation with the short-lived Ps atoms, ensuring the excitation pulse coincided with both Ps formation and the laser cooling sequence.

Another direct carryover from the Hg project was using an OFC to stabilise and reference the spectroscopy laser. In the Hg system, the clock laser was referenced to an OFC to ensure absolute traceability, and the same strategy was proposed here. The 972 nm fundamental seed laser, frequency-doubled to 486 nm, was phase-locked to an OFC mode, ensuring the 486 nm output inherited sub-100 kHz stability and was traceable to the SI second. I used heterodyne beat detection between the 972 nm light and the OFC output to generate an error signal, as I had implemented for the Hg clock laser. This ensured that the Ps two-photon transition frequency could be measured accurately and directly compared to other frequency standards.

The design of the 486 nm light source itself was also based on my prior work with Hg. Rather than relying on a commercial system, I proposed a custom-built ECDL, following the blueprint of the repumping lasers I had developed for Hg at 1092.2 nm and 404.7 nm. The ECDL design, combined with amplification and frequency doubling from 972 nm, provided single-frequency light with sufficient power to drive the two-photon transition. This approach was technically sound and cost-effective, significantly reducing the system cost compared to a commercial SHG system.

In conclusion, my work in this thesis has advanced the two key areas of precision spectroscopy. On one hand, I delivered a novel ultra-stable laser system for Hg, moving closer to a working optical lattice clock in the deep-UV, an advance with direct implications for time metrology and searches for new physics. On the other hand, I contributed to a landmark achievement in antimatter physics, namely the laser cooling of Ps, which unlocked a pathway toward ultra-precise Ps spectroscopy and unique tests of fundamental laws. A unifying theme is the pursuit of ever greater control over atomic systems, whether to measure time more accurately or to probe nature's symmetries more deeply. There are, of course, remaining challenges and limitations. The Hg clock tran-

sition must still be measured, and the proposed Ps spectroscopy setup awaits implementation. These tasks constitute the natural continuation of my research. The results and experience I have gained during this PhD provide a strong foundation to tackle these challenges. The impact of this work is thus twofold: immediate technical accomplishments and lasting methods and ideas for future exploration. Moving forward, the systems and concepts I have developed will enable sensitive tests for new physics and deeper insights into the behaviour of matter-antimatter systems. From a broader perspective, my doctoral research highlights how progress in precision metrology can drive fundamental physics discovery and vice versa. In closing, my contributions not only solved specific technical problems but also pushed the boundaries of what can be measured and understood, laying the groundwork upon which future scientists will build to expand the frontiers of knowledge further.

Appendices

A: Derivation of Light Transmission and Reflection in Fabry–Pérot Interferometers

This appendix presents the derivation of the electric field amplitudes and the corresponding transmitted and reflected intensities of a plane-parallel FP interferometer, based on geometric series summation and interference analysis.

A plane wave enters a FP cavity formed by two parallel, planar mirrors spaced by the distance d. Each mirror is described by complex reflection and transmission coefficients, denoted r_1, r_2 and t_1, t_2, respectively. These coefficients are complex to account for phase shifts δ_{r_i} and δ_{t_i}introduced during reflection and transmission. In theory, when light reflects off a surface with a higher refractive index, it experiences a phase shift of $180°$. However, the exact phase change can vary depending on specific material properties and geometry [128, 233]. The coefficients are expressed as

$$r_1 = |r_1|e^{i\delta_{r_1}}, \quad r_2 = |r_2|e^{i\delta_{r_2}}, \quad t_1 = |t_1|e^{i\delta_{t_1}}, \quad t_2 = |t_2|e^{i\delta_{t_2}}, \tag{.0.1}$$

where $|r_i|$ and $|t_i|$ are the absolute reflection and transmission coefficients. Moreover, the mirrors may cause some loss of intensity, represented by L_1 and L_2, where each L_i quantifies the fraction of intensity lost upon interaction with the i-th mirror. Defining

$$R_1 = |r_1|^2, \quad R_2 = |r_2|^2, \quad T_1 = |t_1|^2, \quad T_2 = |t_2|^2, \tag{.0.2}$$

the following relations hold

$$R_1 + T_1 = 1 - L_1, \quad R_2 + T_2 = 1 - L_2. \tag{.0.3}$$

For convenience in subsequent calculations, let's introduce the quantity

$$R = |r_1 r_2|, \tag{.0.4}$$

which will streamline later expressions.

A plane wave with electric field amplitude E_0 is incident upon the first mirror. A fraction $r_1 E_0$ of the incoming wave is reflected, while $t_1 E_0$ is transmitted through the

mirror. Upon reaching the second mirror, the transmitted component $t_2 t_1 E_0$ passes through, and $r_2 t_1 E_0$ is reflected back towards the first mirror. Within the cavity, the reflected wave interacts again with the first mirror, leading to a transmitted component $r_2 t_1^2 E_0$ and a reflected component $r_1 r_2 t_1 E_0$. This sequence of reflections and transmissions continues indefinitely. A schematic illustration of this propagation process is presented in Figure 1.

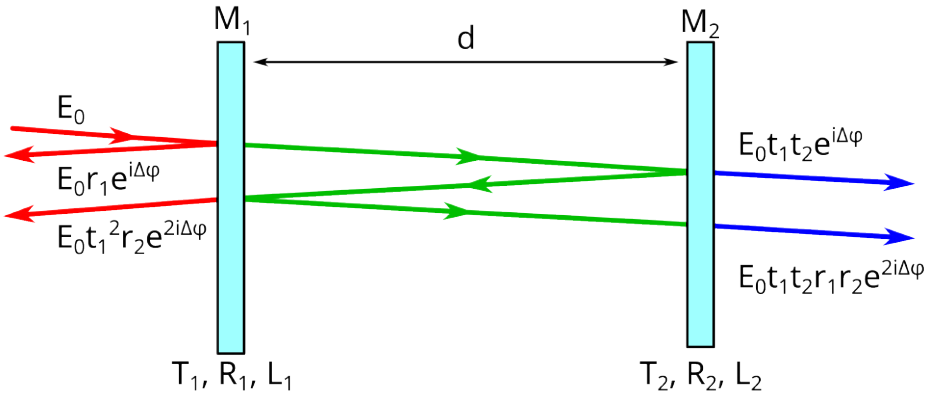

Figure 1: Simplified scheme of the light propagation within a plane-parallel FP interferometer. The mirrors M_1, M_2 are characterised by the transmission T_i, reflection R_i and losses L_i, and are spaced by the distance d. The incoming E_0 and reflected electric field are depicted in red, the circulating electric field in green, and the transmitted electric field in blue. The beams are depicted at a small angle for better visibility. However, within the text, the parallel beams are considered.

The focus here is on determining the light intensity reflected and transmitted by the cavity. Due to the effects of interference, evaluating the phase difference between successive reflected and transmitted waves is necessary. Assuming that the cavity is placed in a UHV and there is no medium inside the cavity, the space-dependent phase term for a propagating wave is expressed as

$$E_0 \exp(ikx) = E_0 \exp\left(i\frac{2\pi}{\lambda}x\right), \tag{.0.5}$$

where k is the wave vector, and λ denotes the wavelength of the incident wave in vacuum.

The optical path difference determines the phase shift associated with beam propagation through space. Assuming the beam is incident on the mirror normally, after a full round-trip, it accumulates the phase shift

$$\Delta\phi = 2kd = \frac{4\pi d}{\lambda}. \tag{.0.6}$$

The transmitted electric field E_T can be expressed as a geometric series of the transmitted components

$$\begin{aligned} E_T &= E_0 t_1 t_2 + E_0 t_1 t_2 r_1 r_2 e^{i\Delta\phi} + E_0 t_1 t_2 (r_1 r_2)^2 e^{i2\Delta\phi} + \dots \\ &= E_0 t_1 t_2 \sum_{n=0}^{\infty} (r_1 r_2 e^{i\Delta\phi})^n = \frac{E_0 t_1 t_2}{1 - r_1 r_2 e^{i\Delta\phi}} = E_0 \frac{\sqrt{T_1 T_2} e^{i(\delta_{t_1} + \delta_{t_2})}}{1 - R e^{i\Delta\phi'}}, \end{aligned} \tag{.0.7}$$

where $\Delta\phi' = \Delta\phi + \delta_{r_1} + \delta_{r_2}$. Similarly, the reflected electric field E_R is given by

$$\begin{aligned} E_R &= E_0 r_1 + E_0 t_1^2 r_2 e^{i\Delta\phi} + E_0 t_1^2 r_1 r_2^2 e^{i2\Delta\phi} + \dots \\ &= E_0 r_1 + E_0 t_1^2 r_2 e^{i\Delta\phi} \sum_{n=0}^{\infty} (r_1 r_2 e^{i\Delta\phi})^n = \\ &= E_0 \left(r_1 + \frac{t_1^2 r_2 e^{i\Delta\phi}}{1 - r_1 r_2 e^{i\Delta\phi}} \right) = E_0 \left(r_1 + \frac{t_1^2 r_2 e^{i\Delta\phi}}{1 - R e^{i\Delta\phi'}} \right). \end{aligned} \tag{.0.8}$$

In experiments, the observable is not the electric field but the light intensity $I = \frac{1}{2}\varepsilon_0 c E_0^2$ [234, 235]. The transmitted intensity is

$$\begin{aligned} I_T &= \frac{\epsilon_0 c}{2} |E_T|^2 = I_0 \frac{T_1 T_2}{(1 - R e^{i\Delta\phi'})(1 - R e^{-i\Delta\phi'})} = \\ &= I_0 \frac{T_1 T_2}{1 + R^2 - 2R\cos\Delta\phi'} = I_0 \frac{T_1 T_2}{(1-R)^2 + 4R\sin^2\left(\frac{\Delta\phi'}{2}\right)}. \end{aligned} \tag{.0.9}$$

The coefficient of finesse F is often introduced [127]

$$F = \frac{4R}{(1-R)^2}, \tag{.0.10}$$

which allows the transmitted intensity to be written as [126]

$$\boxed{I_T = I_0 \frac{T_1 T_2}{(1-R)^2} \frac{1}{1 + F\sin^2\left(\frac{\Delta\phi'}{2}\right)}.} \tag{.0.11}$$

The reflected light intensity I_R is given by

$$
\begin{aligned}
I_R &= I_0 \left(r_1 + \frac{t_1^2 r_2 e^{i\Delta\phi}}{1 - R e^{i\Delta\phi'}} \right) \left(r_1^* + \frac{(t_1^*)^2 r_2^* e^{-i\Delta\phi}}{1 - R e^{-i\Delta\phi'}} \right) = \\
&= I_0 \left(|r_1|^2 + r_1 \frac{(t_1^*)^2 r_2^* e^{-i\Delta\phi}}{1 - R e^{-i\Delta\phi'}} + r_1^* \frac{t_1^2 r_2 e^{i\Delta\phi}}{1 - R e^{i\Delta\phi'}} + \left| \frac{t_1^2 r_2 e^{i\Delta\phi}}{1 - R e^{i\Delta\phi'}} \right|^2 \right) = \\
&= I_0 \left(R_1 + 2\,\Re \left(r_1^* \frac{t_1^2 r_2 e^{i\Delta\phi}}{1 - R e^{i\Delta\phi'}} \right) + \frac{|t_1|^4 |r_2|^2}{1 - 2R\cos(\Delta\phi') + R^2} \right) = \\
&= I_0 \left(R_1 + \frac{2\,\Re \left(t_1^2 r_1^* r_2 (e^{i\Delta\phi} - R e^{i(\Delta\phi - \Delta\phi')}) \right)}{1 - 2R\cos(\Delta\phi') + R^2} + \frac{|t_1|^4 |r_2|^2}{1 - 2R\cos(\Delta\phi') + R^2} \right) = \\
&= I_0 \left(R_1 + \frac{2 t_1^2 r_1^* r_2 \left(\cos(\Delta\phi) - R\cos(\Delta\phi - \Delta\phi') \right) + |t_1|^4 |r_2|^2}{1 - 2R\cos(\Delta\phi') + R^2} \right),
\end{aligned}
\tag{.0.12}
$$

what can be written as [126]

$$
\boxed{I_R = I_0 \frac{R_1 + (1 - L_1) \left(R^2 - 2R + 4R \sin^2 \left(\frac{\Delta\phi'}{2} \right) \right) + T_1 \left(R^2 + T_1 R_2 \right)}{(1 - R)^2 + 4R \sin^2 \left(\frac{\Delta\phi'}{2} \right)}.}
\tag{.0.13}
$$

B: Derivation of Transmission and Reflection for Realistic Mirror Model

This appendix presents the derivation of the transmitted and reflected light intensities in a FP interferometer constructed using realistic multi-layer dielectric mirrors. These mirrors introduce distinct loss mechanisms for reflected and transmitted components, necessitating modifications to the idealised model presented previously.

The realistic model, illustrated in Figure 2, assumes that the reflective surface consists of a dielectric coating deposited on an optical substrate, such as glass. The coating comprises multiple layers with varying refractive indices. By appropriately selecting the refractive indices and thicknesses of these layers, constructive or destructive interference can be engineered to achieve the desired transmission T_i' or reflectivity R_i' [236]. Consequently, it is not possible to define a distinct surface at which reflection occurs. The structure of the coating is determined by the manufacturer based on the desired reflectance, typically using numerical optimisation tools. However, such calculations

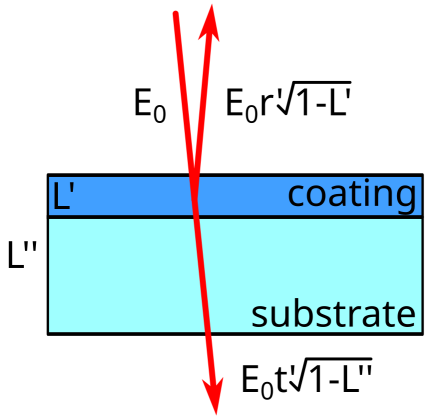

Figure 2: Model of a realistic mirror used in FP interferometer construction. The transmitted and reflected beams are modified by loss factors, as the manufacturer typically defines the relation $R' + T' = 1$. The loss factors are applied differently to transmitted and reflected components due to the complexity of multi-layer dielectric coatings.

often neglect absorption and other losses within the coating. As a result, the relation

$$R'_i + T'_i = 1 \tag{.0.14}$$

holds. To account for the losses introduced by the dielectric coating and the substrate, the electric field must be multiplied by the scaling factors. Due to the absence of a single reflective interface and the complex multilayer structure, the losses associated with reflection and transmission differ. The electric field is multiplied by $\sqrt{1 - L'_i}$ and $\sqrt{1 - L''_i}$ factors, while reflected by the dielectric coating and while transmitted through the substrate and dielectric coating. In this model, reflections at the glass–vacuum interface on the rear side of the substrate are assumed negligible. If such reflections were significant, the substrate would itself behave as an interferometer, etalon, complicating the interference pattern [237]. Minimisation of these reflections can be obtained either by using the wedged substrate or by applying an additional anti-reflection coating at the rear side [136].

It is assumed that the phase shifts $\delta'_{r_i}, \delta'_{t_i}$ introduced by the mirrors are negligible, and

$$r'_1 = \sqrt{R'_1}, \quad r'_2 = \sqrt{R'_2}, \quad t'_1 = \sqrt{T'_1}, \quad t'_2 = \sqrt{T'_2}. \tag{.0.15}$$

The electric field transmitted by the FP constructed with such mirrors can be expressed as

$$\begin{aligned} E_T &= E_0 \sqrt{(1 - L''_1)(1 - L''_2)} t'_1 t'_2 \\ &\quad + E_0 \sqrt{(1 - L'_1)(1 - L'_2)} \sqrt{(1 - L''_1)(1 - L''_2)} t'_1 t'_2 r'_1 r'_2 e^{i\Delta\phi} \\ &\quad + E_0 (1 - L'_1)(1 - L'_2) \sqrt{(1 - L''_1)(1 - L''_2)} t'_1 t'_2 (r'_1 r'_2)^2 e^{2i\Delta\phi} + \dots \\ &= E_0 \sqrt{(1 - L''_1)(1 - L''_2)} t'_1 t'_2 \sum_{n=0}^{\infty} \left(r'_1 r'_2 \sqrt{(1 - L'_1)(1 - L'_2)} e^{i\Delta\phi} \right)^n \qquad (.0.16) \\ &= \frac{E_0 \, t'_1 t'_2 \sqrt{(1 - L''_1)(1 - L''_2)}}{1 - r'_1 r'_2 \sqrt{(1 - L'_1)(1 - L'_2)} e^{i\Delta\phi}}. \qquad (.0.17) \end{aligned}$$

To simplify notation, the following definitions are introduced:

$$\tilde{T}_i = (1 - L''_i) T'_i, \tag{.0.18}$$

$$\tilde{R}_i = (1 - L'_i) R'_i, \tag{.0.19}$$

$$\tilde{R} = \sqrt{\tilde{R}_1 \tilde{R}_2}. \tag{.0.20}$$

Using these quantities, the transmitted electric field becomes

$$E_T = E_0 \frac{\sqrt{\tilde{T}_1 \tilde{T}_2}}{1 - \tilde{R} e^{i\Delta\phi}}, \tag{.0.21}$$

and the corresponding transmitted intensity is

$$I_T = I_0 \frac{\tilde{T}_1 \tilde{T}_2}{(1-\tilde{R})^2 + 4\tilde{R}\sin^2\left(\frac{\Delta\phi}{2}\right)}. \tag{.0.22}$$

This expression can be further written in the standard form:

$$\boxed{I_T = I_0 \frac{\tilde{T}_1 \tilde{T}_2}{(1-\tilde{R})^2} \cdot \frac{1}{1+\tilde{F}\sin^2\left(\frac{\Delta\phi}{2}\right)},} \tag{.0.23}$$

where the generalised coefficient of finesse is defined as

$$\tilde{F} = \frac{4\tilde{R}}{(1-\tilde{R})^2}, \tag{.0.24}$$

and for high values of $\tilde{R}$, the finesse may be approximated by

$$\tilde{\mathcal{F}} \approx \frac{\pi\sqrt{\tilde{R}}}{1-\tilde{R}}. \tag{.0.25}$$

The reflected intensity in this more complete model takes the form

$$\boxed{I_R = I_0 \cdot \frac{\tilde{R}_1 + (\tilde{R}_1 + \tilde{T}_1)\left(\tilde{R}_2 - 2\tilde{R} + 4\tilde{R}\sin^2\left(\frac{\Delta\phi}{2}\right)\right) + \tilde{T}_1\left(\tilde{R}^2 + \tilde{T}_1\tilde{R}_2\right)}{(1-\tilde{R})^2 + 4\tilde{R}\sin^2\left(\frac{\Delta\phi}{2}\right)}.} \tag{.0.26}$$

C: Derivation of Intra-Cavity Intensity and Impedance Matching

This appendix provides the full derivation of the intra-cavity electric field distribution in a FP interferometer constructed using realistic multi-layer dielectric mirrors. It also includes the analytic optimisation of mirror transmission to maximise the intra-cavity intensity under the impedance matching condition.

The electromagnetic field within the FP interferometer comprises two components: a forward-propagating wave, denoted as E_{circ}, and a backwards-propagating wave, referred to as $E_{\text{b-circ}}$. Both components within the FP interferometer can be derived analogously to the expressions for the transmitted and reflected fields.

The forward-propagating field is given by

$$\begin{aligned} E_{\text{circ}} &= E_0 t_1' \sqrt{1-L_1''} + E_0 t_1' r_1' r_2' \sqrt{1-L_1''}\sqrt{1-L_1'}\sqrt{1-L_2'} e^{i\Delta\phi} \\ &\quad + E_0 t_1' (r_1' r_2')^2 \sqrt{1-L_1''}(1-L_1')(1-L_2') e^{2i\Delta\phi} + \dots \\ &= E_0 t_1' \sqrt{1-L_1''} \sum_{n=0}^{\infty} \left(r_1' r_2' \sqrt{1-L_1'}\sqrt{1-L_2'} e^{i\Delta\phi} \right)^n \\ &= E_0 \sqrt{\tilde{T}_1} \frac{1}{1-\tilde{R} e^{i\Delta\phi}}. \end{aligned} \tag{.0.27}$$

The backwards-propagating field results from the reflection at the second mirror and is given by

$$\begin{aligned} E_{\text{b-circ}} &= E_0 t_1' r_2' \sqrt{1-L_1''}\sqrt{1-L_2'} e^{\frac{1}{2}i\Delta\phi} \\ &\quad + E_0 t_1' r_1' r_2'^2 \sqrt{1-L_1''}\sqrt{1-L_1'}(1-L_2') e^{\frac{3}{2}i\Delta\phi} \\ &\quad + E_0 t_1' r_1'^2 r_2'^3 \sqrt{1-L_1''}(1-L_1')(1-L_2')^{3/2} e^{\frac{5}{2}i\Delta\phi} + \dots \\ &= E_0 t_1' r_2' \sqrt{1-L_1''}\sqrt{1-L_2'} e^{\frac{1}{2}i\Delta\phi} \sum_{n=0}^{\infty} \left(r_1' r_2' \sqrt{1-L_1'}\sqrt{1-L_2'} e^{i\Delta\phi} \right)^n \\ &= E_0 \sqrt{\tilde{T}_1}\sqrt{\tilde{R}_2} e^{\frac{1}{2}i\Delta\phi} \frac{1}{1-\tilde{R} e^{i\Delta\phi}}. \end{aligned} \tag{.0.28}$$

The interference between the forward propagating E_{circ} and backwards-propagating electric field $E_{\text{b-circ}}$ results in space-dependent intensity modulation

$$\begin{aligned} I_{\text{ins}}(x) &= \frac{\varepsilon_0 c}{2}\left|E_{\text{circ}}e^{i\frac{2\pi}{\lambda}x} + E_{\text{b-circ}}e^{-i\frac{2\pi}{\lambda}x}\right|^2 \\ &= \frac{\varepsilon_0 c}{2}\left[|E_{\text{circ}}|^2 + |E_{\text{b-circ}}|^2 + 2|E_{\text{circ}}E_{\text{b-circ}}|\cos\left(\frac{4\pi}{\lambda}x\right)\right]. \end{aligned} \tag{.0.29}$$

The light intensity at the maxima of light intensity (anti-node) is

$$\begin{aligned} I^{\text{anti-node}} &= \frac{\varepsilon_0 c}{2}\left(|E_{\text{circ}}|^2 + |E_{\text{b-circ}}|^2 + 2|E_{\text{circ}}E_{\text{b-circ}}|\right) \\ &= I_0\frac{\tilde{T_1}}{(1-\tilde{R})^2}\frac{1}{1+\tilde{F}\sin^2\left(\frac{\Delta\phi}{2}\right)}\left(1+\tilde{R_2}+\sqrt{\tilde{R_2}}\right). \end{aligned} \tag{.0.30}$$

The light intensity at the anti-node when the FP interferometer is pumped with the light of frequency matching the cavity resonance

$$I^{\text{anti-node}}_{\text{max}} = I_0\frac{\tilde{T_1}}{(1-\tilde{R})^2}\left(1+\tilde{R_2}+\sqrt{\tilde{R_2}}\right). \tag{.0.31}$$

Assuming identical mirrors and low transmission losses, $\tilde{T} \approx T'$, the optimal mirror transmission can be derived through differentiation to maximise the light intensity at the anti-node. The maximisation of the leading part

$$I^{\text{anti-node}}_{\text{max}} \propto \frac{\tilde{T}}{(1-\tilde{R})^2} \approx \frac{T'}{\left(L'+(1-L')T'\right)^2} \tag{.0.32}$$

results in

$$T'_{\text{opt}} = \frac{L'}{1-L'}. \tag{.0.33}$$

Typically, the losses are very low. Hence, for the FP interferometer with identical mirrors, the maximum intra-cavity power can be achieved when the transmission of the mirror is equal to the total losses during reflection

$$\boxed{T'_{\text{opt}} \approx L'.} \tag{.0.34}$$

Bibliography

[1] H. Hachisu, K. Miyagishi, S. G. Porsev, A. Derevianko, V. D. Ovsiannikov, V. G. Pal'chikov, M. Takamoto, and H. Katori, "Trapping of neutral mercury atoms and prospects for optical lattice clocks", Phys. Rev. Lett. **100**, 053001 (2008).

[2] M. Petersen, R. Chicireanu, S. T. Dawkins, D. V. Magalhães, C. Mandache, Y. Le Coq, A. Clairon, and S. Bize, "Doppler-free spectroscopy of the $^1S_0$–$^3P_0$ optical clock transition in laser-cooled fermionic isotopes of neutral Hg", Phys. Rev. Lett. **101**, 183004 (2008).

[3] C. Sanner, N. Huntemann, R. Lange, C. Tamm, E. Peik, M. S. Safronova, and S. G. Porsev, "Optical clock comparison for Lorentz symmetry testing", Nature **567**, 204–208 (2019).

[4] P. Delva, J. Lodewyck, S. Bilicki, E. Bookjans, G. Vallet, R. Le Targat, P.-E. Pottie, C. Guerlin, F. Meynadier, C. Le Poncin-Lafitte, O. Lopez, A. Amy-Klein, W.-K. Lee, N. Quintin, C. Lisdat, A. Al-Masoudi, S. Dörscher, C. Grebing, G. Grosche, A. Kuhl, S. Raupach, U. Sterr, I. R. Hill, R. Hobson, W. Bowden, J. Kronjäger, G. Marra, A. Rolland, F. N. Baynes, H. S. Margolis, and P. Gill, "Test of special relativity using a fiber network of optical clocks", Physical Review Letters **118**, 221102 (2017).

[5] T. Rosenband, D. B. Hume, P. O. Schmidt, C. W. Chou, A. Brusch, L. Lorini, W. H. Oskay, R. E. Drullinger, T. M. Fortier, J. E. Stalnaker, S. A. Diddams, W. C. Swann, N. R. Newbury, W. M. Itano, D. J. Wineland, and J. C. Bergquist, "Frequency ratio of Al^+ and Hg^+ single-ion optical clocks: metrology at the 17th decimal place", Science **319**, 1808–1812 (2008).

[6] E. Peik, B. Lipphardt, H. Schnatz, T. Schneider, C. Tamm, and S. G. Karshenboim, "Limit on the present temporal variation of the fine-structure constant", Phys. Rev. Lett. **93**, 170801 (2004).

[7] T. M. Fortier, N. Ashby, J. C. Bergquist, M. J. Delaney, S. A. Diddams, T. P. Heavner, L. Hollberg, W. M. Itano, S. R. Jefferts, K. Kim, F. Levi, L. Lorini, W. H. Oskay, T. E. Parker, J. Shirley, and J. E. Stalnaker, "Precision atomic

spectroscopy for improved limits on variation of the fine-structure constant and local position invariance", Phys. Rev. Lett. **98**, 070801 (2007).

[8] A. Derevianko and M. Pospelov, "Hunting for topological dark matter with atomic clocks", Nat. Phys. **10**, 933–936 (2014).

[9] P. Wcisło, P. Morzyński, M. Bober, A. Cygan, D. Lisak, R. Ciuryło, and M. Zawada, "Experimental constraint on dark matter detection with optical atomic clocks", Nat. Astron. **1**, 0009 (2016).

[10] M. Witkowski, G. Kowzan, R. Munoz-Rodriguez, R. Ciuryło, P. S. Żuchowski, P. Masłowski, and M. Zawada, "Absolute frequency and isotope shift measurements of mercury $^1S_0$–$^3P_1$ transition", Opt. Express **27**, 11069–11083 (2019).

[11] M. J. Martin, M. Bishof, M. D. Swallows, X. Zhang, C. Benko, J. von-Stecher, A. V. Gorshkov, A. M. Rey, and J. Ye, "A quantum many-body spin system in an optical lattice clock", Science **341**, 632–636 (2013).

[12] A. J. Daley, M. M. Boyd, J. Ye, and P. Zoller, "Quantum computing with alkaline-earth-metal atoms", Phys. Rev. Lett. **101**, 170504 (2008).

[13] A. V. Gorshkov, A. M. Rey, A. J. Daley, M. M. Boyd, J. Ye, P. Zoller, and M. D. Lukin, "Alkaline-earth-metal atoms as few-qubit quantum registers", Phys. Rev. Lett. **102**, 110503 (2009).

[14] A. V. Gorshkov, M. Hermele, V. Gurarie, C. Xu, P. S. Julienne, J. Ye, P. Zoller, E. Demler, M. D. Lukin, and A. M. Rey, "Two-orbital SU(N) magnetism with ultracold alkaline-earth atoms", Nature Physics **6**, 289–295 (2010).

[15] K. Shibata, S. Kato, A. Yamaguchi, S. Uetake, and Y. Takahashi, "A scalable quantum computer with ultranarrow optical transition of ultracold neutral atoms in an optical lattice", Appl. Phys. B **97**, 753–758 (2009).

[16] K. Yamanaka, N. Ohmae, I. Ushijima, M. Takamoto, and H. Katori, "Frequency ratio of ^{199}Hg and ^{87}Sr optical lattice clocks beyond the SI limit", Physical Review Letters **114**, 230801 (2015).

[17] S. Kolkowitz, I. Pikovski, N. Langellier, M. D. Lukin, R. L. Walsworth, and J. Ye, "Gravitational wave detection with optical lattice atomic clocks", Phys. Rev. D **94**, 124043 (2016).

[18] M. Takamoto, I. Ushijima, N. Ohmae, T. Yahagi, K. Kokado, H. Shinkai, and H. Katori, "Test of general relativity by a pair of transportable optical lattice clocks", Nature Photonics **14**, 411–415 (2020).

[19] A. Derevianko, K. Gibble, L. Hollberg, N. R. Newbury, C. Oates, M. S. Safronova, L. C. Sinclair, and N. Yu, "Fundamental physics with a state-of-the-art optical clock in space", Quantum Sci. Technol. **7**, 044002 (2022).

[20] A. Golovizin, E. Fedorova, D. Tregubov, D. Sukachev, K. Khabarova, V. Sorokin, and N. Kolachevsky, "Inner-shell clock transition in atomic thulium with a small blackbody radiation shift", Nat. Commun. **10**, 1724 (2019).

[21] S. G. Porsev and A. Derevianko, "Multipolar theory of blackbody radiation shift of atomic energy levels and its implications for optical lattice clocks", Physical Review A **74**, 020502 (2006).

[22] K. Ono, Y. Saito, T. Ishiyama, T. Higomoto, T. Takano, Y. Takasu, Y. Yamamoto, M. Tanaka, and Y. Takahashi, "Observation of nonlinearity of generalized King plot in the search for new boson", Physical Review X **12**, 021033 (2022).

[23] C. Solaro, S. Meyer, K. Fisher, J. C. Berengut, E. Fuchs, and M. Drewsen, "Improved isotope-shift-based bounds on bosons beyond the standard model through measurements of the $^2D_{3/2} - {}^2D_{5/2}$ interval in Ca^+", Phys. Rev. Lett. **125**, 123003 (2020).

[24] W. H. King, *Isotope shifts in atomic spectra*, Physics of Atoms and Molecules (Springer, Boston, MA, 1984).

[25] K. Ono, Y. Saito, T. Ishiyama, T. Higomoto, T. Takano, Y. Takasu, Y. Yamamoto, M. Tanaka, and Y. Takahashi, "Observation of nonlinearity of generalized King plot in the search for new boson", Phys. Rev. X **12**, 021033 (2022).

[26] C. Delaunay, R. Ozeri, G. Perez, and Y. Soreq, "Probing atomic Higgs-like forces at the precision frontier", Physical Review D **96**, 093001 (2017).

[27] B. L. Wexler, B. E. Wilcomb, and N. Djeu, "6^1S_0–6^3P_0 transition in ^{199}Hg: determination of the A coefficient and self–pressure broadening", Journal of the Optical Society of America **70**, 863–865 (1980).

[28] E. J. Angstmann, V. A. Dzuba, and V. V. Flambaum, "Relativistic effects in two valence-electron atoms and ions and the search for variation of the fine-structure constant", Phys. Rev. A **70**, 014102 (2004).

[29] M. Petersen, J. Millo, D. Magalhaes, C. Mandache, S. Dawkins, R. Chicireanu, Y. Lecoq, O. Acef, G. Santarelli, A. Clairon, and S. Bize, "Magneto-optical trap of neutral mercury for an optical lattice clock", in Proc. 2008 IEEE int. frequency control symposium (2008), pp. 451–454.

[30] M. Petersen, "Laser cooling of neutral mercury and laser spectroscopy of the $^1S_0$–$^3P_0$ optical clock transition", PhD thesis (Université Pierre et Marie Curie – Paris VI, Paris, France, 2009).

[31] L. Yi, S. Mejri, J. J. McFerran, Y. Le Coq, and S. Bize, "Optical lattice trapping of ^{199}Hg and determination of the magic wavelength for the ultraviolet $^1S_0 \leftrightarrow {}^3P_0$ transition", Phys. Rev. Lett. **106**, 073005 (2011).

[32] S. Mejri, J. J. McFerran, L. Yi, Y. Le Coq, and S. Bize, "Ultraviolet laser spectroscopy of neutral mercury in a one-dimensional optical lattice", Physical Review A **84**, 032507 (2011).

[33] J. J. McFerran, D. V. Magalhães, C. Mandache, J. Millo, W. Zhang, Y. Le Coq, G. Santarelli, and S. Bize, "Laser locking to the ^{199}Hg ^{1}S$_0$–^{3}P$_0$ clock transition with $5.4 \times 10^{-15}/\sqrt{\tau}$ fractional frequency instability", Optics Letters **37**, 3477–3479 (2012).

[34] S. Mejri, J. J. McFerran, L. Yi, and S. Bize, "Towards an optical lattice clock based on mercury: Loading of a dipole trap", in Proceedings of the 2010 european frequency and time forum (eftf 2010) (2010).

[35] J. J. McFerran, L. Yi, S. Mejri, W. Zhang, S. Di Manno, M. Abgrall, J. Guéna, Y. Le Coq, and S. Bize, "Statistical uncertainty of 2.5×10^{-16} for the ^{199}Hg ^{1}S$_0$–^{3}P$_0$ clock transition against a primary frequency standard", Physical Review A **89**, 043432 (2014).

[36] R. Tyumenev, "Mercury Lattice Clock: From the Lamb-Dicke Spectroscopy to Stable Clock Operation", PhD thesis (Université Pierre et Marie Curie (Paris VI), Paris, France, 2015).

[37] R. Tyumenev, M. Favier, S. Bilicki, E. Bookjans, R. Le Targat, J. Lodewyck, D. Nicolodi, Y. Le Coq, M. Abgrall, J. Guéna, L. De Sarlo, and S. Bize, "Comparing a mercury optical lattice clock with microwave and optical frequency standards", New Journal of Physics **18**, 113002 (2016).

[38] H. S. Margolis, G. Panfilo, G. Petit, C. Oates, T. Ido, and S. Bize, "The CIPM list 'Recommended values of standard frequencies': 2021 update", Metrologia **61**, 035005 (2024).

[39] J. R. Paul, "Construction and characterization of a neutral Hg magneto-optical trap and precision spectroscopy of the 6^1S$_0$–6^3P$_0$ ^{199}Hg clock transition", PhD Thesis (University of Arizona, Tucson, Arizona, USA, 2015).

[40] X. Fu, S. Fang, R. Zhao, Y. Zhang, J. Huang, J. Sun, Z. Xu, and Y. Wang, "Observation of the ^{1}S$_0$–^{3}P$_0$ optical clock transition in cold ^{199}Hg atoms", Chinese Optics Letters **16**, 060202 (2018).

[41] J. S. Schelfhout and J. J. McFerran, "Multiconfiguration Dirac-Hartree-Fock calculations for Hg and Cd with estimates for unknown clock-transition frequencies", Physical Review A **105**, 022805 (2022).

[42] A. Rich, "Recent experimental advances in positronium research", Reviews of Modern Physics **53**, 127–165 (1981).

[43] S. Berko and H. N. Pendleton, "Positronium", Annual Review of Nuclear and Particle Science **30**, 543–581 (1980).

[44] W. E. Caswell and G. P. Lepage, "Effective lagrangians for bound state problems in qed, qcd, and other field theories", Physics Letters B **167**, 437–442 (1986).

[45] R. Barbieri and E. Remiddi, "Electronic transition probabilities in positronium: one- and two-photon decays", Il Nuovo Cimento A **77**, 519–535 (1983).

[46] D. B. Cassidy, "Experimental progress in positronium laser physics", The European Physical Journal D **72**, 53 (2018).

[47] M. W. Heiss, L. de Sousa Borges, A. Golovizin, and P. Crivelli, "Measurement of the $1^3S_1 \rightarrow 2^3S_1$ interval in positronium using field-ionization of Rydberg states", Physical Review A **111**, 012810 (2025).

[48] S. Chu and J. Mills Allen P., "Excitation of the positronium two-photon transition", Physical Review Letters **48**, 1333–1336 (1982).

[49] J. Mills Allen P., S. Chu, and J. L. Hall, in *Coherence and quantum optics v*, edited by L. Mandel and E. Wolf (Springer, Boston, MA, 1984), pp. 1001–1008.

[50] M. S. Fee, J. Mills A. P., S. Chu, E. D. Shaw, K. Danzmann, R. J. Chichester, and D. M. Zuckerman, "Measurement of the positronium $1^3S_1 \rightarrow 2^3S_1$ interval by continuous-wave two-photon excitation", Physical Review Letters **70**, 1397–1400 (1993).

[51] M. S. Fee, S. Chu, J. Mills A. P., R. J. Chichester, D. M. Zuckerman, E. D. Shaw, and K. Danzmann, "Measurement of the positronium $1^3S_1 \rightarrow 2^3S_1$ interval by continuous-wave two-photon excitation", Physical Review A **48**, 192–219 (1993).

[52] L. T. Glöggler, N. Gusakova, B. Rienäcker, A. Camper, R. Caravita, S. Huck, M. Volponi, T. Wolz, L. Penasa, V. Krumins, F. P. Gustafsson, D. Comparat, M. Auzins, B. Bergmann, P. Burian, R. S. Brusa, F. Castelli, G. Cerchiari, R. Ciuryło, G. Consolati, M. Doser, Ł. Graczykowski, M. Grosbart, F. Guatieri, S. Haider, M. A. Janik, G. Kasprowicz, G. Khatri, Ł. Kłosowski, G. Kornakov, L. Lappo, A. Linek, J. Malamant, S. Mariazzi, V. Petracek, M. Piwinski, S. Pospíšil, L. Povolo, F. Prelz, S. A. Rangwala, T. Rauschendorfer, B. S. Rawat, V. Rodin, O. M. Røhne, H. Sandaker, P. Smolyanskiy, T. Sowiński, D. Tefelski, T. Vafeiadis, C. P. Welsch, M. Zawada, J. Zielinski, and N. Zurlo (AEgIS Collaboration), "Positronium laser cooling via the 1^3S–2^3P transition with a broadband laser pulse", Phys. Rev. Lett. **132**, 083402 (2024).

[53] A. Derevianko and H. Katori, "Colloquium: physics of optical lattice clocks", Rev. Mod. Phys. **83**, 331–347 (2011).

[54] A. D. Ludlow, M. M. Boyd, J. Ye, E. Peik, and P. O. Schmidt, "Optical atomic clocks", Rev. Mod. Phys. **87**, 637–701 (2015).

[55] National Institute of Standards and Technology (NIST), *NIST chemistry webbook: mercury*, `https://webbook.nist.gov/chemistry/`, 2023.

[56] M. L. Huber, A. Laesecke, and D. G. Friend, "Correlation for the vapor pressure of mercury", Ind. Eng. Chem. Res. **45**, 7351–7361 (2006).

[57] S. Falke, N. Lemke, C. Grebing, B. Lipphardt, S. Weyers, V. Gerginov, N. Huntemann, C. Hagemann, F. Riehle, E. Peik, and U. Sterr, "A strontium lattice clock with 3×10^{-17} inaccuracy and its frequency", New J. Phys. **16**, 073023 (2014).

[58] Z. W. Barber, C. W. Hoyt, J. E. Stalnaker, N. Lemke, C. W. Oates, T. M. Fortier, S. A. Diddams, and L. Hollberg, "Lattice-based optical clock using an even isotope of Yb", in Proc. spie, Vol. 6673 (2007), 66730E.

[59] Q. Lavigne, T. Groh, and S. Stellmer, "Magneto-optical trapping of mercury at high phase-space density", Phys. Rev. A **105**, 033106 (2022).

[60] W. M. Haynes, *CRC handbook of chemistry and physics*, 97th ed. (CRC Press, 2016).

[61] L. F. Livi, G. Cappellini, M. Diem, L. Franchi, C. Clivati, M. Frittelli, F. Levi, D. Calonico, J. Catani, M. Inguscio, and L. Fallani, "Synthetic dimensions and spin-orbit coupling with an optical clock transition", Phys. Rev. Lett. **117**, 220401 (2016).

[62] S. L. Bromley, S. Kolkowitz, T. Bothwell, D. Kedar, A. Safavi-Naini, M. L. Wall, C. Salomon, A. M. Rey, and J. Ye, "Dynamics of interacting fermions under spin–orbit coupling in an optical lattice clock", Nat. Phys. **14**, 399–404 (2018).

[63] N. R. Cooper and A. M. Rey, "Adiabatic control of atomic dressed states for transport and sensing", Phys. Rev. A **92**, 021401 (2015).

[64] J. P. Covey, I. S. Madjarov, A. Cooper, and M. Endres, "2000-times repeated imaging of strontium atoms in clock-magic tweezer arrays", Phys. Rev. Lett. **122**, 173201 (2019).

[65] M. A. Norcia, H. Kim, W. B. Cairncross, M. Stone, A. Ryou, M. Jaffe, M. O. Brown, K. Barnes, P. Battaglino, T. C. Bohdanowicz, A. Brown, K. Cassella, C.-A. Chen, R. Coxe, D. Crow, J. Epstein, C. Griger, E. Halperin, F. Hummel, A. M. W. Jones, J. M. Kindem, J. King, K. Kotru, J. Lauigan, M. Li, M. Lu, E. Megidish, J. Marjanovic, M. McDonald, T. Mittiga, J. A. Muniz, S. Narayanaswami, C. Nishiguchi, T. Paule, K. A. Pawlak, L. S. Peng, K. L. Pudenz, D. Rodríguez Pérez, A. Smull, D. Stack, M. Urbanek, R. J. M. van de Veerdonk, Z. Vendeiro, L. Wadleigh, T. Wilkason, T.-Y. Wu, X. Xie, E. Zalys-Geller, X. Zhang, and B. J. Bloom, "Iterative assembly of ^{171}Yb atom arrays with cavity-enhanced optical lattices", PRX Quantum **5**, 030316 (2024).

[66] N. Yu and M. Tinto, "Gravitational wave detection with single-laser atom interferometers", Gen. Relativ. Gravit. **43**, 1943–1952 (2011).

[67] P. W. Graham, J. M. Hogan, M. A. Kasevich, and S. Rajendran, "New method for gravitational wave detection with atomic sensors", Phys. Rev. Lett. **110**, 171102 (2013).

[68] P. Villwock, S. Siol, and T. Walther, "Magneto-optical trapping of neutral mercury", Eur. Phys. J. D **65**, 251–256 (2011).

[69] Y. Zhang, Q.-X. Liu, J.-F. Sun, Z. Xu, and A. Wang, "Enhanced cold mercury atom production with two-dimensional magneto-optical trap", Chin. Phys. B **31**, 073701 (2022).

[70] C. Guo, V. Cambier, J. Calvert, M. Favier, M. Andia, L. de Sarlo, and S. Bize, "Exploiting the two-dimensional magneto-optical trapping of ^{199}Hg for a mercury optical lattice clock", Phys. Rev. A **107**, 033116 (2023).

[71] B. Wang, D.-S. Lü, J.-G. Wang, Z.-Y. Wang, and Y.-Z. Wang, "A single folded beam magneto-optical trap system for neutral mercury atoms", in Proc. 2011 int. conf. on manipulation, manufacturing and measurement on the nanoscale (2011), pp. 275–278.

[72] B. Wang, D.-S. Lü, J.-G. Wang, Z.-Y. Wang, and Y.-Z. Wang, "Magneto-optical trap for neutral mercury atoms", Chin. Phys. B **20**, 073701 (2011).

[73] M. Witkowski, B. Nagórny, R. Munoz-Rodriguez, R. Ciuryło, P. S. Żuchowski, S. Bilicki, M. Piotrowski, P. Morzyński, and M. Zawada, "Dual Hg–Rb magneto-optical trap", Opt. Express **25**, 3165–3179 (2017).

[74] S. Gravina, N. A. Chishti, S. Di Bernardo, E. Fasci, A. Castrillo, A. Laliotis, and L. Gianfrani, "Comb-referenced doppler-free spectrometry of the ^{200}Hg and ^{202}Hg intercombination line at 254 nm", Phys. Rev. Lett. **132**, 213001 (2024).

[75] A. Linek, P. Morzyński, and M. Witkowski, "Absolute frequency measurement of the $6s^2\,{}^1S_0 \rightarrow 6s6p\,{}^3P_1$ F = 3/2 → F′ = 5/2 ^{201}Hg transition with background-free saturation spectroscopy", Opt. Express **30**, 44103–44117 (2022).

[76] C. Clivati, S. Gravina, A. Castrillo, G. A. Costanzo, F. Levi, and L. Gianfrani, "Tunable UV spectrometer for doppler broadening thermometry of Mercury", Optics Letters **45**, 3693–3696 (2020).

[77] B. Lu, Y. Wang, J. Han, S. Zhang, J. Li, and H. Chang, "Exploration of the magnetic-field-induced $5s5p\,{}^3P_0$–$5s^2\,{}^1S_0$ forbidden transition in bosonic Sr atoms", Journal of Physics Communications **1**, 055017 (2017).

[78] A. V. Taichenachev, V. I. Yudin, C. W. Oates, C. W. Hoyt, Z. W. Barber, and L. Hollberg, "Magnetic field-induced spectroscopy of forbidden optical transitions with application to lattice-based optical atomic clocks", Physical Review Letters **96**, 083001 (2006).

[79] X. Lu, M. Yin, T. Li, Y. Wang, and H. Chang, "An evaluation of the Zeeman shift of the ^{87}Sr optical lattice clock at the national time service center", Applied Sciences **10**, 1440 (2020).

[80] H. Katori, K. Hashiguchi, E. Y. Il'inova, and V. D. Ovsiannikov, "Magic wavelength to make optical lattice clocks insensitive to atomic motion", Phys. Rev. Lett. **103**, 153004 (2009).

[81] N. Ohmae, F. Bregolin, N. Nemitz, and H. Katori, "Direct measurement of the frequency ratio for Hg and Yb optical lattice clocks and closure of the Hg/Yb/Sr loop", Optics Express **28**, 15112–15121 (2020).

[82] D. S. Barker, B. J. Reschovsky, N. C. Pisenti, and G. K. Campbell, "Enhanced magnetic trap loading for atomic strontium", Physical Review A **92**, 043418 (2015).

[83] K. Blagoev, V. Pentchev, E. Biémont, Z. G. Zhang, C.-G. Wahlström, and S. Svanberg, "Radiative lifetimes of $6s\,ns\,^3S_1$ and $6s\,nd\,^3D_1$ excited states of Hg I", Physical Review A **66**, 032509 (2002).

[84] R. D. Cowan, *The theory of atomic structure and spectra* (University of California Press, 1981).

[85] D. M. Harber and M. V. Romalis, "Measurement of the scalar Stark shift of the $6\,^1S_0 \rightarrow 6\,^3P_1$ transition in Hg", Physical Review A **63**, 013402 (2000).

[86] C. J. Foot, *Atomic physics* (Oxford University Press, 2005).

[87] J. Li, Y. Yao, and X. Zhang, "Role of hyperfine interaction in Landé g-factors of $^3P_0$ clock states", Journal of Quantitative Spectroscopy and Radiative Transfer **255**, 107263 (2020).

[88] F. M. Fernández, *Introduction to perturbation theory in quantum mechanics* (CRC Press, Boca Raton, 1999).

[89] V. Devanathan, *Angular momentum techniques in quantum mechanics* (Springer, Dordrecht, 2002).

[90] M. Deutsch, "Evidence for the formation of positronium in gases", Physical Review **82**, 455–456 (1951).

[91] G. Adkins, D. Cassidy, and J. Pérez-Ríos, "Precision spectroscopy of positronium: testing bound-state qed theory and the search for physics beyond the standard model", Physics Reports **975**, 1–61 (2022).

[92] S. G. Karshenboim, "Precision study of positronium: testing bound state qed theory", International Journal of Modern Physics A **19**, 3879–3896 (2004).

[93] J.-L. Basdevant and J. Dalibard, in *The quantum mechanics solver* (Springer, Cham, 2019), pp. 51–59.

[94] P. A. M. Dirac, "On the annihilation of electrons and protons", Mathematical Proceedings of the Cambridge Philosophical Society **26**, 361–375 (1930).

[95] A. Ore and J. L. Powell, "Three-photon annihilation of an electron-positron pair", Physical Review **75**, 1696–1699 (1949).

[96] P. Wallyn, W. A. Mahoney, P. Durouchoux, and C. Chapuis, "The positronium radiative recombination spectrum: calculation in the limit of thermal positrons and low densities", The Astrophysical Journal **465**, 473 (1996).

[97] J. Shapiro and G. Breit, "Metastability of states of hydrogenic atoms", Physical Review **113**, 179–188 (1959).

[98] A. I. Alekseev, "Two-quantum annihilation of positronium in the p-state", Soviet Physics JETP **7**, 826–829 (1958).

[99] H. A. Bethe and E. E. Salpeter, *Quantum mechanics of one- and two-electron atoms* (Springer, Berlin, 1957).

[100] A. I. Alekseev, "Three-quantum annihilation of positronium in the p-state", Soviet Physics JETP **9**, 1312–1315 (1959).

[101] G. S. Adkins, R. N. Fell, and J. Sapirstein, "Order α^2 corrections to the decay rate of orthopositronium", Physical Review Letters **84**, 5086–5089 (2000).

[102] P. A. Vetter and S. J. Freedman, "Branching-ratio measurements of multiphoton decays of positronium", Physical Review A **66**, 052505 (2002).

[103] A. Badertscher, P. Crivelli, A. Curioni, A. Gendotti, A. Rubbia, P. Sala, and R. Treichel, "Improved limit on invisible decays of positronium", Physical Review D **75**, 032004 (2007).

[104] M. T. Yamashita, T. Frederico, and L. Tomio, "Intrinsic properties of positronium: testing qed in the simplest bound system", Entropy **20**, 721 (2018).

[105] J. Pirenne, "Ph.d. thesis", PhD thesis (University of Paris, 1944).

[106] A. P. Mills, "Precision spectroscopy of positronium: present and future", Contemporary Physics **55**, 115–136 (2014).

[107] G. S. Adkins, R. N. Fell, and A. Mitrikov, "Two-loop corrections to positronium fine structure", Physical Review A **66**, 052505 (2002).

[108] D. Hagena, R. Ley, D. Weil, G. Werth, W. Arnold, and H. Schneider, "Precise measurement of $n = 2$ positronium fine-structure intervals", Physical Review Letters **71**, 2887–2890 (1993).

[109] K. Pachucki and S. G. Karshenboim, "Complete result for positronium energy levels at order $m\alpha^6$", Physical Review Letters **80**, 2101–2104 (1998).

[110] C. Amsler, et al., and P. D. Group, "Review of particle physics", Physics Letters B **667**, 1–1340 (2008).

[111] S. G. Karshenboim, "Positronium, antihydrogen, light, and the equivalence principle", Journal of Physics B: Atomic, Molecular and Optical Physics **49**, 144001 (2016).

[112] D. A. Cooke, P. Crivelli, J. Alnis, A. Antognini, B. Brown, S. Friedreich, A. Gabard, T. W. Hänsch, K. Kirch, A. Rubbia, and V. Vrankovic, "Observation of positronium annihilation in the 2S state: towards a new measurement of the 1S–2S transition frequency", Hyperfine Interactions **233**, 67–73 (2015).

[113] D. B. Cassidy, P. Crivelli, T. H. Hisakado, L. Liszkay, V. E. Meligne, P. Perez, H. W. K. Tom, and A. P. J. Mills, "Positronium cooling in porous silica measured via doppler spectroscopy", Physical Review A **81**, 012715 (2010).

[114] M. Antonello, A. Belov, G. Bonomi, R. S. Brusa, M. Caccia, A. Camper, R. Caravita, F. Castelli, D. Comparat, G. Consolati, L. Di Noto, M. Doser, M. Fanì, R. Ferragut, J. Fesel, S. Gerber, A. Gligorova, L. T. Glöggler, F. Guatieri, S. Haider, A. Hinterberger, O. Khalidova, D. Krasnický, V. Lagomarsino, C. Malbrunot, S. Mariazzi, V. Matveev, S. R. Müller, G. Nebbia, P. Nedelec, L. Nowak, M. Oberthaler, E. Oswald, D. Pagano, L. Penasa, V. Petracek, F. Prelz, B. Rienäcker, O. M. Røhne, A. Rotondi, H. Sandaker, R. Santoro, G. Testera, I. C. Tietje, T. Wolz, C. Zimmer, and N. Zurlo (AEgIS Collaboration), "Rydberg-positronium velocity and self-ionization studies in a 1 T magnetic field and cryogenic environment", Physical Review A **102**, 013101 (2020).

[115] S. Mariazzi, R. Caravita, C. Zimmer, B. Rienäcker, A. Camper, A. Belov, G. Bonomi, R. S. Brusa, F. Castelli, G. Consolati, M. Doser, H. Gjersdal, L. T. Glöggler, F. Guatieri, S. Haider, V. Matveev, G. Nebbia, P. Nedelec, D. Pagano, L. Penasa, V. Petracek, F. Prelz, L. Povolo, O. M. Rhøne, A. Rotondi, H. Sandaker, N. Zurlo, and A. Collaboration, "High-yield thermalized positronium at room temperature emitted by morphologically tuned nanochanneled silicon targets", Journal of Physics B: Atomic, Molecular and Optical Physics **54**, 085004 (2021).

[116] E. P. Liang and C. D. Dermer, "Laser cooling of positronium", Optics Communications **65**, 419–424 (1988).

[117] W. D. Phillips, "Nobel lecture: laser cooling and trapping of neutral atoms", Reviews of Modern Physics **70**, 721–741 (1998).

[118] T. Kumita, T. Hirose, M. Irako, K. Kadoya, B. Matsumoto, K. Wada, N. N. Mondal, H. Yabu, K. Kobayashi, and M. Kajita, "Study on laser cooling of ortho-positronium", Nuclear Instruments and Methods in Physics Research Section B: Beam Interactions with Materials and Atoms **192**, 171–175 (2002).

[119] K. Shu, Y. Tajima, R. Uozumi, N. Miyamoto, S. Shiraishi, T. Kobayashi, A. Ishida, K. Yamada, R. W. Gladen, T. Namba, S. Asai, K. Wada, I. Mochizuki, T. Hyodo, K. Ito, K. Michishio, B. E. O'Rourke, N. Oshima, and K. Yoshioka, "Cooling positronium to ultralow velocities with a chirped laser pulse train", Nature **633**, 793–797 (2024).

[120] D. B. Cassidy, H. W. K. Tom, and A. P. Mills, "Fundamental physics with cold positronium", in Aip conference proceedings, Vol. 1037 (Aug. 2008), pp. 66–83.

[121] P. M. Platzman and A. P. J. Mills, "Possibilities for bose condensation of positronium", Physical Review B **49**, 454–458 (1994).

[122] R. W. P. Drever, J. L. Hall, F. V. Kowalski, J. Hough, G. M. Ford, A. J. Munley, and H. Ward, "Laser phase and frequency stabilization using an optical resonator", Appl. Phys. B **31**, 97–105 (1983).

[123] H. Katori, M. Takamoto, V. G. Pal'chikov, and V. D. Ovsiannikov, "Ultrastable optical clock with neutral atoms in an engineered light shift trap", Phys. Rev. Lett. **91**, 173005 (2003).

[124] A. E. Siegman, *Lasers* (University Science Books, Mill Valley, CA, USA, 1986).

[125] H. Kogelnik and T. Li, "Laser beams and resonators", Appl. Opt. **5**, 1550–1567 (1966).

[126] B. E. A. Saleh and M. C. Teich, *Fundamentals of photonics* (Wiley-Interscience, New York, USA, 1991).

[127] A. Yariv, *Quantum electronics*, 3rd ed. (Wiley, New York, USA, 1989).

[128] E. Hecht, *Optics*, 4th ed. (Addison-Wesley, San Francisco, USA, 2002).

[129] W. Demtröder, *Laser spectroscopy, vol. 1: basic principles*, 4th ed. (Springer, Berlin, Heidelberg, 2008).

[130] B. E. A. Saleh and M. C. Teich, *Fundamentals of photonics*, 2nd ed. (Wiley-Interscience, Hoboken, NJ, USA, 2007).

[131] E. D. Black, "An introduction to Pound–Drever–Hall laser frequency stabilization", Am. J. Phys. **69**, 79–87 (2001).

[132] D. G. Matei, T. Legero, S. Häfner, C. Grebing, R. Weyrich, W. Zhang, L. Sonderhouse, J. M. Robinson, J. Ye, F. Riehle, and U. Sterr, "1.5 μm lasers with sub-10 mHz linewidth", Phys. Rev. Lett. **118**, 263202 (2017).

[133] R. V. Pound, "Electronic frequency stabilization of microwave oscillators", Rev. Sci. Instrum. **17**, 490–505 (1946).

[134] M. Zeyen, M. Rautenberg, and M. C. Suhm, "Pound–Drever–Hall locking scheme free from Trojan operating points", Rev. Sci. Instrum. **94**, 013001 (2023).

[135] W. Wang, S. Subhankar, and J. W. Britton, "A practical guide to feedback control for Pound–Drever–Hall laser linewidth narrowing", Appl. Phys. B **131**, 146 (2025).

[136] J. A. Dobrowolski, in *Handbook of optics, vol. i*, edited by M. Bass, 2nd ed. (McGraw-Hill, New York, USA, 1995).

[137] R. Grimm, M. Weidemüller, and Y. B. Ovchinnikov, "Optical dipole traps for neutral atoms", Adv. At. Mol. Opt. Phys. **42**, 95–170 (2000).

[138] S. Chu, "Nobel Lecture: the manipulation of neutral particles", Rev. Mod. Phys. **70**, 685–706 (1998).

[139] A. Yariv, "Critical coupling and its control in optical waveguide–ring resonator systems", IEEE Photon. Technol. Lett. **14**, 483–485 (2002).

[140] J. Chow, M. Gray, and D. McClelland, "Experimental demonstration of impedance match locking and tuning in optical cavities", Opt. Express **18**, 9314–9323 (2010).

[141] S. Kim and J. Rho, "Critically coupled Fabry–Perot cavity with high signal contrast for refractive index sensing", Sci. Rep. **11**, 19515 (2021).

[142] A. D. Boardman, N. King, Y. Rapoport, V. Grimalsky, and S. V. Koshevaya, "Critical coupling in a Fabry–Pérot cavity with metamaterial mirrors", Opt. Commun. **283**, 5271–5278 (2010).

[143] M. Afzelius and C. Simon, "Impedance-matched cavity quantum memory", Phys. Rev. A **82**, 022310 (2010).

[144] A. A. Fedyanin, A. A. Lisyansky, and J. L. Birman, "Asymmetrical properties of the optical reflection response of a Fabry–Pérot interferometer", J. Opt. Soc. Am. A **17**, 1092–1097 (2000).

[145] J. A. Barnes, A. R. Chi, L. S. Cutler, D. J. Healey, D. B. Leeson, T. E. McGunigal, J. A. Mullen, W. L. Smith, R. L. Sydnor, R. F. C. Vessot, and G. M. R. Winkler, "Characterization of frequency stability", IEEE Trans. Instrum. Meas. **IM-20**, 105–120 (1971).

[146] E. Rubiola and R. Boudot, "The effect of AM noise on correlation phase noise measurements", in Proc. 2007 IEEE int. frequency control symposium joint with the 21st european frequency and time forum (2007), pp. 1099–1105.

[147] D. J. Fraser, *Electronic engineering applications of two-port networks* (Pergamon Press, New York, USA, 1970).

[148] D. Halford, A. E. Wainwright, and J. A. Barnes, in *Proc. 22nd annual symposium on frequency control* (IEEE, Fort Monmouth, NJ, 1968), pp. 340–341.

[149] E. Rubiola and F. Vernotte, "The companion of enrico's chart for phase noise and two-sample variances", IEEE Trans. Microw. Theory Tech. **71**, 2996–3025 (2023).

[150] A. Aeppli, K. Kim, W. Warfield, M. S. Safronova, and J. Ye, "Clock with 8×10^{-19} systematic uncertainty", Phys. Rev. Lett. **133**, 023401 (2024).

[151] IEEE, *IEEE Standard Definitions of Physical Quantities for Fundamental Frequency and Time Metrology—Random Instabilities*, tech. rep. IEEE Std 1139-1999 (Institute of Electrical and Electronics Engineers, 1999).

[152] D. W. Allan and M. A. Weiss, *Characterization of frequency and phase noise*, tech. rep. NIST Technical Note 1337 (National Institute of Standards and Technology (NIST), 1980).

[153] National Institute of Standards and Technology (NIST), *Power-law noise processes*, (2025) `https://tf.nist.gov/phase/Properties/nine.htm`.

[154] Analog Devices, *The power spectral density of phase noise and jitter*, tech. rep. Application Note AN-1067 (Analog Devices, 2005).

[155] D. W. Allan, "Statistics of atomic frequency standards", Proc. IEEE **54**, 221–230 (1966).

[156] A. E. Wallin, *Allan Tools: a Python library for time and frequency statistics* (2023).

[157] N. J. Kasdin and T. Walter, "Discrete simulation of power-law noise for oscillator stability evaluation", in Proc. 1992 IEEE frequency control symposium (1992), pp. 274–283.

[158] W. J. Riley, *Handbook of frequency stability analysis*, tech. rep. NIST Special Publication 1065 (National Institute of Standards and Technology (NIST), Gaithersburg, MD, USA, 2008).

[159] D. W. Allan and J. A. Barnes, "A modified Allan variance with increased oscillator characterization ability", in Proc. 35th annual frequency control symposium (1981), pp. 470–473.

[160] F. Conte, S. Massucco, M. Paolone, G. P. Schiapparelli, F. Silvestro, and Y. Zuo, "Frequency stability assessment of modern power systems: models definition and parameters identification", Sustainable Energy, Grids Netw. **23**, 100384 (2020).

[161] C. A. Greenhall, "Recipes for degrees of freedom of frequency stability estimators", IEEE Transactions on Instrumentation and Measurement **40**, 994–999 (1991).

[162] J. E. Gray and D. W. Allan, *A method for estimating the frequency stability of an individual oscillator*, tech. rep. NBS Technical Note 394 (National Bureau of Standards (NBS), Boulder, CO, USA, 1974).

[163] F. Vernotte, M. Addouche, M. Delporte, and M. Brunet, "The three-cornered hat method: an attempt to identify some clock correlations", in Proc. 2004 IEEE int. frequency control symposium and exposition (2004), pp. 482–488.

[164] J. Groslambert, D. Fest, M. Olivier, and J. J. Gagnepain, "Characterization of frequency fluctuations by cross-correlations and by using three or more oscillators", in Proc. 35th annual frequency control symposium (1981), pp. 458–463.

[165] F. Vernotte, C. E. Calosso, and E. Rubiola, "Three-cornered hat versus Allan covariance", in Proc. 2016 IEEE int. frequency control symposium (IFCS) (2016), pp. 1–6.

[166] É. Lantz, C. E. Calosso, E. Rubiola, V. Giordano, C. Fluhr, B. Dubois, and F. Vernotte, "KLTS: a rigorous method to compute the confidence intervals for the three-cornered hat and for groslambert covariance", IEEE Trans. Ultrason., Ferroelectr., Freq. Control **66**, 1942–1949 (2019).

[167] E. Rubiola, "On the measurement of frequency and of its sample variance with high-resolution counters", Review of Scientific Instruments **76**, 054703 (2005).

[168] F. L. Walls and D. A. Howe, "Measurement of frequency, phase noise, and amplitude noise", Proc. IEEE **74**, 162–168 (1986).

[169] S. T. Dawkins, J. J. McFerran, and A. N. Luiten, "Considerations on the measurement of the stability of oscillators with frequency counters", IEEE Trans. Ultrason., Ferroelectr., Freq. Control **54**, 918–925 (2007).

[170] D. A. Howe, "The total variance: a new measure of frequency stability", in Proc. 1995 IEEE int. frequency control symposium (1995), pp. 38–42.

[171] K+K Messtechnik GmbH, *FXE65 high-resolution frequency counter: product datasheet*, `https://www.kplusk.de/en/products/fxe65/`, 2020.

[172] B. Nagórny, "Podwójna pułapka magneto-optyczna dla atomów rtęci i rubidu", PhD thesis (Nicolaus Copernicus University in Torun, 2019).

[173] L. Krzemień, K. Brzozowski, A. Noga, M. Witkowski, J. Zachorowski, M. Zawada, and W. Gawlik, "Laser frequency stabilization by magnetically assisted rotation spectroscopy", Optics Communications **284**, 1247–1253 (2011).

[174] S. Pustelny, V. Schultze, T. Scholtes, and D. Budker, "Dichroic atomic vapor laser lock with multi-gigahertz stabilization range", Review of Scientific Instruments **87**, 063107 (2016).

[175] G. Wasik, W. Gawlik, J. Zachorowski, and W. Zawadzki, "Laser frequency stabilization by doppler-free magnetic dichroism", Applied Physics B **75**, 613–619 (2002).

[176] J. L. Hall, "Nobel lecture: defining and measuring optical frequencies", Reviews of Modern Physics **78**, 1279–1295 (2006).

[177] T. W. Hänsch, "Nobel lecture: passion for precision", Reviews of Modern Physics **78**, 1297–1309 (2006).

[178] P. Krehlik, Ł. Śliwczyński, Ł. Buczek, J. Kołodziej, and M. Lipiński, "ELSTAB—fiber-optic time and frequency distribution technology: a general characterization and fundamental limits", IEEE Transactions on Ultrasonics, Ferroelectrics, and Frequency Control **63**, 993–1004 (2016).

[179] J. Azoubib, J. Nawrocki, and W. Lewandowski, "Independent atomic timescale in poland—organization and results", Metrologia **40**, S245 (2003).

[180] Ł. Śliwczyński, P. Krehlik, Ł. Buczek, and M. Lipiński, "Multipoint dissemination of RF frequency in delay-stabilized fiber-optic link in a side-branch configuration", in 2013 joint european frequency and time forum (eftf) and international frequency control symposium (ifcs) (2013), pp. 876–878.

[181] J. E. Volder, "The CORDIC trigonometric computing technique", IRE Transactions on Electronic Computers **EC-8**, 330–334 (1959).

[182] J. E. Volder, "The birth of CORDIC", Journal of VLSI Signal Processing Systems for Signal, Image and Video Technology **25**, 101–105 (2000).

[183] P. K. Meher, J. Valls, T.-B. Juang, K. Sridharan, and K. Maharatna, "50 years of CORDIC: algorithms, architectures, and applications", IEEE Transactions on Circuits and Systems I: Regular Papers **56**, 1893–1907 (2009).

[184] T. Nazarova, F. Riehle, and U. Sterr, "Vibration-insensitive reference cavity for an ultra-narrow-linewidth laser", Applied Physics B **83**, 531–536 (2006).

[185] L. Chen, J. L. Hall, J. Ye, T. Yang, E. Zang, and T. Li, "Vibration-induced elastic deformation of Fabry–Perot cavities", Physical Review A **74**, 053801 (2006).

[186] S. Häfner, S. Falke, C. Grebing, S. Vogt, T. Legero, M. Merimaa, C. Lisdat, and U. Sterr, "8×10^{-17} fractional laser frequency instability with a long room-temperature cavity", Optics Letters **40**, 2112–2115 (2015).

[187] J. Keller, S. Ignatovich, S. A. Webster, and T. E. Mehlstäubler, "Simple vibration-insensitive cavity for laser stabilization at the 10^{-16} level", Applied Physics B **116**, 203–210 (2014).

[188] Corning Incorporated, *Corning® ULE® 7973 Low Expansion Glass: Optical Materials Product Information*, Sept. 2019.

[189] T. Legero, T. Kessler, and U. Sterr, "Tuning the thermal expansion properties of optical reference cavities with fused silica mirrors", Journal of the Optical Society of America B **27**, 914–919 (2010).

[190] K. P. Birch and M. J. Downs, "An updated Edlén equation for the refractive index of air", Metrologia **30**, 155 (1993).

[191] K. P. Birch and M. J. Downs, "Correction to the updated Edlén equation for the refractive index of air", Metrologia **31**, 315 (1994).

[192] A. Linek, *Temperature Control Script for Ultra-Stable Optical Cavity*, version V1, 2025.

[193] G. Berden, R. Peeters, and G. Meijer, "Cavity ring-down spectroscopy: experimental schemes and applications", International Reviews in Physical Chemistry **19**, 565–607 (2000).

[194] P. G. Cielo, "Fiber optic hydrophone: improved strain configuration and environmental noise protection", Applied Optics **18**, 2933–2937 (1979).

[195] A. Masoudi and T. P. Newson, "High spatial resolution distributed optical fiber dynamic strain sensor with enhanced frequency and strain resolution", Optics Letters **42**, 290–293 (2017).

[196] L.-S. Ma, P. Jungner, J. Ye, and J. L. Hall, "Accurate cancellation (to millihertz levels) of optical phase noise due to vibration or insertion phase in fiber-transmitted light", in Laser frequency stabilization and noise reduction, SPIE proceedings, Vol. 2378 (1995), pp. 165–172.

[197] C. E. Calosso, E. K. Bertacco, D. Calonico, F. Levi, S. Micalizio, A. Mura, C. Clivati, and G. A. Costanzo, "Tracking DDS for coherent optical links", in 2013 joint european frequency and time forum (EFTF) & international frequency control symposium (IFCS) (2013), pp. 885–888.

[198] P. A. Williams, W. C. Swann, and N. R. Newbury, "High-stability transfer of an optical frequency over long fiber-optic links", Journal of the Optical Society of America B **25**, 1284–1293 (2008).

[199] C. E. Calosso, E. K. Bertacco, D. Calonico, C. Clivati, G. A. Costanzo, M. Frittelli, F. Levi, S. Micalizio, A. Mura, and A. Godone, "Doppler-stabilized fiber link with 6 dB noise improvement below the classical limit", Optics Letters **40**, 131–134 (2015).

[200] C. Clivati, R. Aiello, G. Bianco, C. Bortolotti, P. De Natale, V. Di Sarno, P. Maddaloni, G. Maccaferri, A. Mura, M. Negusini, F. Levi, F. Perini, R. Ricci, M. Roma, L. Santamaria Amato, M. Siciliani de Cumis, M. Stagni, A. Tuozzi, and D. Calonico, "Common-clock very long baseline interferometry using a coherent optical fiber link", Optica **7**, 1031–1037 (2020).

[201] S. Droste, F. Ozimek, T. Udem, K. Predehl, T. W. Hänsch, H. Schnatz, G. Grosche, and R. Holzwarth, "Optical-frequency transfer over a single-span 1840 km fiber link", Physical Review Letters **111**, 110801 (2013).

[202] C. Clivati, A. Tampellini, A. Mura, F. Levi, G. Marra, P. Galea, A. Xuereb, and D. Calonico, "Optical frequency transfer over submarine fiber links", Optica **5**, 893–901 (2018).

[203] F. Stefani, O. Lopez, A. Bercy, W.-K. Lee, C. Chardonnet, G. Santarelli, P.-E. Pottie, and A. Amy-Klein, "Tackling the limits of optical fiber links", Journal of the Optical Society of America B **32**, 787–797 (2015).

[204] D. Xu, O. Lopez, A. Amy-Klein, and P.-E. Pottie, "Non-reciprocity in optical fiber links: experimental evidence", Optics Express **29**, 17476–17490 (2021).

[205] J. L. Hall, M. S. Taubman, S. A. Diddams, B. Tiemann, J. Ye, L.-S. Ma, D. Jones, and S. Cundiff, "Stabilizing and measuring optical frequencies", in Proceedings of the 14th international conference on laser spectroscopy, edited by R. Blatt (1999), pp. 315–320.

[206] G. Roberts, *About time? (nordunet 2024 presentation)*, (Sept. 13, 2024) `https://nordu.net/ndn2024/static/presentations/ndn2024/11th/track1/optical/3-About_Time-Guy_Roberts_NDN2024.pdf`.

[207] *Pathfinder – a brand new fibre optic link between ptb and psnc*, Poznań Supercomputing and Networking Center (PSNC), (Nov. 1, 2024) `https://www.psnc.pl/pathfinder-a-brand-new-fibre-optic-link-between-ptb-and-psnc/`.

[208] K. Turza, "Pathfinder update (1st sig-tfn meeting)" (Oct. 16–17, 2024).

[209] D. Kushary, "Bootstrap methods and their application", Technometrics **42**, 216–217 (2000).

[210] T. J. DiCiccio and B. Efron, "Bootstrap confidence intervals", Statistical Science **11**, 189–228 (1996).

[211] A. Linek, *Python PI Control Script for Laser Wavelength Stabilisation*, version V1, 2025.

[212] C. J. Hawthorn, K. P. Weber, and R. E. Scholten, "Littrow configuration tunable external cavity diode laser with fixed direction output beam", Review of Scientific Instruments **72**, 4477–4479 (2001).

[213] P. McNicholl and H. J. Metcalf, "Synchronous cavity mode and feedback wavelength scanning in dye laser oscillators with gratings", Applied Optics **24**, 2757–2761 (1985).

[214] A. Linek, *Projekt mechaniczny głowicy lasera ECDL — modele CAD i rysunki*, version V1, 2025.

[215] S. L. Campbell, R. B. Hutson, G. E. Marti, A. Goban, N. Darkwah Oppong, R. L. McNally, L. Sonderhouse, J. M. Robinson, W. Zhang, B. J. Bloom, and J. Ye, "A Fermi-degenerate three-dimensional optical lattice clock", Science **358**, 90–94 (2017).

[216] H. Katori, "Spectroscopy of strontium atoms in the Lamb–Dicke confinement", in *Frequency standards and metrology* (2002), pp. 323–330.

[217] M. Takamoto and H. Katori, "Spectroscopy of the $^1S_0$–$^3P_0$ clock transition of ^{87}Sr in an optical lattice", Physical Review Letters **91**, 223001 (2003).

[218] M. Favier, "Mercury optical lattice clock: from high-resolution spectroscopy to frequency ratio measurements", PhD Thesis (Université Pierre et Marie Curie, Paris, France, 2017).

[219] The Engineering Toolbox, *Emissivity coefficients of common materials: data & reference guide*, 2003.

[220] I. C. Tietje, C. Amsler, M. Antonello, A. Belov, G. Bonomi, R. S. Brusa, M. Caccia, A. Camper, R. Caravita, F. Castelli, P. Cheinet, D. Comparat, G. Consolati, A. Demetrio, L. D. Noto, M. Doser, M. Fani, R. Ferragut, J. Fesel, S. Gerber, M. Giammarchi, A. Gligorova, L. T. Glöggler, F. Guatieri, S. Haider, A. Hinterberger, A. Kellerbauer, O. Khalidova, D. Krasnický, V. Lagomarsino, C. Malbrunot, L. Nowak, S. Mariazzi, V. Matveev, S. R. Müller, G. Nebbia, P. Nedelec, M. Oberthaler, E. Oswald, D. Pagano, L. Penasa, V. Petracek, L. Povolo, F. Prelz, M. Prevedelli, B. Rienäcker, O. M. Røhne, A. Rotondi, H. Sandaker, R. Santoro, G. Testera, V. Toso, T. Wolz, P. Yzombard, C. Zimmer, and N. Zurlo, "Protocol for pulsed antihydrogen production in the AEgIS apparatus", in Journal of physics: conference series, Vol. 1612 (2020), p. 012025.

[221] R. Khatri, M. Charlton, P. Sferlazzo, K. G. Lynn, A. P. J. Mills, and L. O. Roellig, "Improvement of rare-gas solid moderators by using conical geometry", Applied Physics Letters **57**, 2374–2376 (1990).

[222] C. M. Surko, M. Leventhal, and A. Passner, "Positron plasma in the laboratory", Physical Review Letters **62**, 901–904 (1989).

[223] S. Aghion, C. Amsler, A. Ariga, T. Ariga, A. S. Belov, G. Bonomi, P. Bräunig, J. Bremer, R. S. Brusa, L. Cabaret, M. Caccia, R. Caravita, F. Castelli, G. Cerchiari, K. Chlouba, S. Cialdi, D. Comparat, G. Consolati, A. Demetrio, L. Di Noto, M. Doser, A. Dudarev, A. Ereditato, C. Evans, J. Fesel, A. Fontana, O. K. Forslund, S. Gerber, M. Giammarchi, A. Gligorova, S. Gninenko, F. Guatieri, S. Haider, H. Holmestad, T. Huse, I. L. Jernelv, E. Jordan, A. Kellerbauer, M. Kimura, T. Koettig, D. Krasnický, V. Lagomarsino, P. Lansonneur, P. Lebrun, S. Lehner, J. Liberadzka, C. Malbrunot, S. Mariazzi, L. Marx, V. Matveev, Z. Mazzotta, G. Nebbia, P. Nedelec, M. Oberthaler, N. Pacifico, D. Pagano, L. Penasa, V. Petracek, C. Pistillo, F. Prelz, M. Prevedelli, L. Ravelli, L. Resch, B. Rienäcker, J. Robert, O. M. Røhne, A. Rotondi, M. Sacerdoti, H. Sandaker, R. Santoro, P. Scampoli, M. Simon, L. Smestad, F. Sorrentino, G. Testera, I. C. Tietje, E. Widmann, P. Yzombard, C. Zimmer, and N. Zurlo, "Positron bunching and electrostatic transport system for the production and emission of dense positronium clouds into vacuum", Nuclear Instruments and Methods in Physics Research Section B: Beam Interactions with Materials and Atoms **362**, 86–92 (2015).

[224] S. Mariazzi, P. Bettotti, S. Larcheri, L. Toniutti, and R. S. Brusa, "High positronium yield and emission into the vacuum from oxidized tunable nanochannels in silicon", Physical Review B **81**, 235418 (2010).

[225] C. Zimmer, P. Yzombard, A. Camper, and D. Comparat, "Positronium laser cooling in a magnetic field", Physical Review A **104**, 023106 (2021).

[226] K. P. Ziock, C. D. Dermer, R. H. Howell, F. Magnotta, and K. M. Jones, "Optical saturation of the 1^3s–2^3p transition in positronium", Journal of Physics B: Atomic, Molecular and Optical Physics **23**, 329–335 (1990).

[227] M. S. Fee, K. Danzmann, and S. Chu, "Frequency measurements of the $^1S_0$-$^3P_1$ intercombination line in magnesium, calcium, and strontium", Physical Review A **45**, 4911–4924 (1992).

[228] B. Cagnac, G. Grynberg, and F. Biraben, "Spectroscopie d'absorption multiphotonique sans effet doppler", Journal de Physique (Paris) **34**, 845–858 (1973).

[229] R. W. Fox, C. W. Oates, and L. W. Hollberg, in *Cavity-enhanced spectroscopies*, Vol. 40, edited by R. D. van Zee and J. P. Looney, Experimental Methods in the Physical Sciences (Elsevier, New York, 2003), pp. 1–46.

[230] C. Amsler, M. Antonello, A. Belov, G. Bonomi, R. S. Brusa, M. Caccia, A. Camper, R. Caravita, F. Castelli, G. Cerchiari, D. Comparat, G. Consolati, A. Demetrio, L. Di Noto, M. Doser, M. Fanì, S. Gerber, A. Gligorova, F. Guatieri, P. Hackstock, S. Haider, A. Hinterberger, H. Holmestad, A. Kellerbauer, O. Khalidova, D. Krasnický, V. LagoMarsino, P. Lansonneur, P. Lebrun, C. Malbrunot, S. Mariazzi, V. Matveev, S. R. Müller, G. Nebbia, P. Nedelec, M. Oberthaler,

D. Pagano, L. Penasa, V. Petracek, F. Prelz, M. Prevedelli, B. Rienäcker, J. Robert, O. M. Røhne, A. Rotondi, H. Sandaker, R. Santoro, L. Smestad, F. Sorrentino, G. Testera, I. C. Tietje, E. Widmann, P. Yzombard, C. Zimmer, and N. Zurlo (AEgIS Collaboration), "Velocity-selected production of $2\,^3S$ metastable positronium", Phys. Rev. A **99**, 033405 (2019).

[231] D. B. Cassidy, S. H. M. Deng, H. K. M. Tanaka, and A. P. J. Mills, "Single shot positron annihilation lifetime spectroscopy", Applied Physics Letters **88**, 194105 (2006).

[232] P. Morzyński, P. Wcisło, P. Ablewski, R. Gartman, W. Gawlik, P. Masłowski, B. Nagórny, F. Ozimek, C. Radzewicz, M. Witkowski, R. Ciuryło, and M. Zawada, "Absolute frequency measurement of rubidium 5S–7S two-photon transitions", Opt. Lett. **38**, 4581–4584 (2013).

[233] M. Born and E. Wolf, *Principles of Optics*, 7th ed. (Cambridge University Press, 1999).

[234] D. J. Griffiths, *Introduction to electrodynamics*, 4th ed. (Pearson, 2012).

[235] J. D. Jackson, *Classical electrodynamics*, 3rd ed. (Wiley, 1998).

[236] A. Thelen, *Design of optical interference coatings* (McGraw-Hill, 1989).

[237] H. E. Bennett and E. J. Ashley, "Interference effects in thick glass substrates", Appl. Opt. **6**, 623–630 (1967).